

INVESTIGATIONS ON INFLUENCES OF FAULTS AND RELATED STRESS
FIELDS ON NATURALLY FRACTURED RESERVOIRS IN ADIYAMAN
AREA, EASTERN TURKEY

A THESIS SUBMITTED TO
THE GRADUATE SCHOOL OF NATURAL AND APPLIED SCIENCES
OF
MIDDLE EAST TECHNICAL UNIVERSITY

BY

GÖKTÜRK MEHMET DİLCİ

IN PARTIAL FULFILLMENT OF THE REQUIREMENTS
FOR
THE DEGREE OF DOCTOR OF PHILOSOPHY
IN
GEOLOGICAL ENGINEERING

SEPTEMBER 2019

Approval of the thesis:

**INVESTIGATIONS ON INFLUENCES OF FAULTS AND RELATED
STRESS FIELDS ON NATURALLY FRACTURED RESERVOIRS IN
ADIYAMAN AREA, EASTERN TURKEY**

submitted by **GÖKTÜRK MEHMET DİLCİ** in partial fulfillment of the
requirements for the degree of **Doctor of Philosophy in Geological Engineering
Department, Middle East Technical University** by,

Prof. Dr. Halil Kalıpçılar
Dean, Graduate School of **Natural and Applied Sciences**

Prof. Dr. Erdin Bozkurt
Head of Department, **Geological Engineering**

Prof. Dr. Erdin Bozkurt
Supervisor, **Geological Engineering, METU**

Examining Committee Members:

Prof. Dr. Erdinç Yiğitbaş
Geological Engineering, Çanakkale Onsekiz Mart University

Prof. Dr. Erdin Bozkurt
Geological Engineering, METU

Prof. Dr. Gürol Seyitoğlu
Geological Engineering, Ankara University

Prof. Dr. Kadir Dirik
Geological Engineering, Hacettepe University

Prof. Dr. Bora Rojay
Geological Engineering, METU

Date: 13.09.2019

I hereby declare that all information in this document has been obtained and presented in accordance with academic rules and ethical conduct. I also declare that, as required by these rules and conduct, I have fully cited and referenced all material and results that are not original to this work.

Name, Surname: GÖKTÜRK MEHMET DİLCİ

Signature:

ABSTRACT

INVESTIGATIONS ON INFLUENCES OF FAULTS AND RELATED STRESS FIELDS ON NATURALLY FRACTURED RESERVOIRS IN ADIYAMAN AREA, EASTERN TURKEY

Dilci, Göktürk Mehmet

Doctor of Philosophy, Geological Engineering

Supervisor: Prof. Dr. Erdin Bozkurt

September 2019, 181 pages

Northern Margin of the Arabian Plate is a novel area to study the effects of faults on fracture corridors since the region has heavily been subjected to reverse and strike-slip faulting regimes beginning with Eocene and Miocene, respectively. In Adiyaman province especially, verified discovery of a naturally fractured reservoir (NFR), Şambayat oilfield, necessitates more comprehensive explanations concerning to association of the fractured reservoir with the nearby Samsat Fault. Isolated effects of the fractures on reservoir qualities could be adequately measured within non-porous rocks. Therefore, this study has focused on initially non-porous NFR host rock of the Şambayat oilfield, the Campanian argillaceous limestone of Sayındere Formation. In the extent of this study, fractures within the Sayındere Formation were also investigated at outcrops close to Bozova Fault, which has analogous tectonic settings with the Samsat Fault. Main goals of this research are to explore the role of faults and stress fields on the formation of NFR's and to determine best directional drilling trajectories to produce oil from as much fracture porosity as possible. To achieve these goals, I suggested a new methodology comprising combination of surface and subsurface data as well as rock deformation experiments, in-situ stress measurements and slip-tendency analyses. In conclusion, (i) the Sayındere Formation was proven to have the lowest strength for brittle deformation among brittle rocks exposed in the basin. Therefore, it preferentially gets fractured first. (ii) Volumetric dilatational strain that forms on the fault bending domains can be distributed among shear and tension fractures and provides up to %10 fracture porosity as measured at outcrops (iii) Local stress intensification related to fault activity seems necessary and sufficient to fracture

intact the Sayıdere Formation. Therefore slip tendency of the existing faults must be studied to predict the localization of fault-related NFR's.

Keywords: Naturally Fractured Reservoirs, Rock Strength, Slip Tendency, Distributed Opening

ÖZ

DOĞAL ÇATLAKLI REZERVUARLARA FAYLAR VE İLİŞKİLİ GERİLME ALANLARININ ETKİLERİNİN İNCELENMESİ, TÜRKİYE’NİN GÜNEYDOĞUSUNDA YER ALAN ADIYAMAN CİVARINDAN BİR ÖRNEK ÇALIŞMA

Dilci, Göktürk Mehmet

Doktora, Jeoloji Mühendisliği

Tez Danışmanı: Prof. Dr. Erdin Bozkurt

Eylül 2019, 181 sayfa

Arap Kıtası’nın Kuzey kenarı, fayların doğal çatlaklı rezervuarların oluşmasındaki etkilerini incelemek için örnek bir bölgedir. Zira bu bölge Eosen ve Miyosen’den itibaren sırasıyla ters ve doğrultu atımlı faylanmalara maruz kalmıştır. Özellikle Adıyaman civarında Şambayat petrol sahasındaki kanıtlanmış doğal çatlaklı rezervuar (DÇR) keşfi, bu yapıların komşu Samsat Fayı ile ilişkisi hakkında kapsamlı açıklama getirilmesini gerekli kılmıştır. Rezervuar özelliklerine çatlakların olası etkileri (ilksel olarak) gözeneksiz kayalarda daha doğru ölçülebilir. Bu nedenle, bu çalışmada, ilksel olarak gözeneksiz olup Şambayat petrol sahasının çatlaklı rezervuar kayacı olan Kampaniyen yaşlı killi kireçtaşı litolojisindeki Sayındere Formasyonu’na odaklanılmıştır. Ayrıca Sayındere Formasyonu’ndaki çatlaklar Samsat Fayı ile tektonik benzerlik sergileyen Bozova Fayı’nın yakınlarındaki yüzleklerde de çalışılmıştır. Bu çalışmanın ana amaçları; faylar ve gerilme alanlarının DÇR’ların oluşumundaki rolünü araştırmak ve en yüksek çatlak gözeneginin kesilmesi için gereken yönlü sondaj tasarımlarını belirlemektir. Bu amaçları gerçekleştirmek için yüzey ve yeraltı verilerinin birleştirilmesi kadar kayaç deformasyon deneyleri, yerinde gerilme ölçümleri ve kayma eğilimi analizlerini de içeren yeni bir yöntem önermekteyim. Sonuç olarak, (i) Sayındere Formasyonu’nun Adıyaman sahasındaki diğer gevrek kayalardan daha düşük bir kırılğan deformasyon dayanımına sahip olduğu ve bu nedenle tercihen daha önce çatlaklandığı tespit edilmiştir. (ii) Yüzlek ölçümleri, fayların büküm gösterdiği alanlarda hacimsel açılma deformasyonunun, makaslama ve gerilme çatlakları arasında dağıldığını ve %10’a varan oranlarda çatlak

gözenekliliği oluşturduğunu göstermiştir. (iii) Örselenmemiş Sayındere Formasyonu kayacının çatlayabilmesi için fay etkinliğiyle ilişkili yerel (lokal) gerilme artışlarının yeterli ve gerekli olduğu anlaşılmıştır. Bu nedenle, doğal çatlaklı rezervuarların oluşacağı lokasyonları tahmin edebilmek için mevcut fayların kayma eğilimleri incelenmelidir.

Anahtar Sözcükler: Çatlaklı Rezervuar, Kayaç Dayanımı, Kayma Eğilimi, Açılma Çatlakları

To Gümüş, Asya, Gülşah, Meral, Ejder, Göksel, Gökberk, Gökarp and Gökçen

ACKNOWLEDGEMENTS

I would like to express the deepest appreciation to my supervisor, Professor Erdin Bozkurt, for his inspiring attitude, sincere guidance and valuable support during the entire process of this thesis.

I wish to thank my thesis committee members: Kadir Dirik, Gürol Seyitoğlu, Bora Rojay and Erdinç Yiğitbaş for generously offering their time, care and guidance throughout the preparation and review of this document.

I would like to thank to my former project manager, Kadri Yapan for his precious contributions to come up with the idea of trying to decipher the mystery of fault related fractures in the Adıyaman region.

I convey my respectable thanks to Turkish Petroleum for encouraging me to conduct this research that is attributable to the needs of the exploration projects and also for providing precious non-confidential data to make this research possible.

Special thanks to my talented brother, and also my colleague Gökalp Dilci, for his comments, observations, and suggestions helped me make this thesis better.

Finally, I can never thank enough my wife and daughter for their love and constant support during my entire life.

TABLE OF CONTENTS

ABSTRACT.....	v
ÖZ	vii
ACKNOWLEDGEMENTS	x
TABLE OF CONTENTS	xi
LIST OF TABLES	xv
LIST OF FIGURES	xvi
LIST OF ABBREVIATIONS.....	xxiv
LIST OF SYMBOLS	xxvi
CHAPTERS	
1. INTRODUCTION.....	1
1.1. Purpose and Scope	1
1.1.1. Conceptual Problems.....	4
1.1.2. Regional Problems.....	4
1.2. The Study Area.....	6
1.3. Regional Stratigraphy	9
1.3.1. Pre-Cambrian, Paleozoic and Early Mesozoic Rocks.....	10
1.3.2. Early Cretaceous to Present-Day Rocks	18
1.4. Regional Tectonics	32
1.5. Methodology	33
2. GEOLOGICAL STRUCTURES AND PETROLEUM SYSTEM OF THE STUDY AREA	39
2.1. Faults	49

2.1.1. Normal Faults.....	50
2.1.1.1. Type-1 Paleozoic Normal Faults	50
2.1.1.2. Type-2 Early Campanian Normal Faults	51
2.1.2. Thrust Faults	52
2.1.3. Reverse Faults	55
2.1.4. Strike-Slip Faults.....	56
2.1.4.1. Strike-Slip Reactivation of the Bozova Fault	58
2.1.4.2. Kemerli Strike-Slip Fault	60
2.2. Folds	63
2.2.1. Asymmetric Folds	64
2.2.2. Symmetric Folds	64
2.3. Fractures and Veins.....	65
2.3.1. Tension Joints/Veins.....	66
2.3.2. Pressure Solution Seams (PSSs).....	66
2.3.3. Shear Fractures.....	71
3. ANALYSES AND INTERPRETATION OF FRACTURES.....	73
3.1. Introduction and Background.....	73
3.2. Methodology	80
3.3. Fracture Data Collected at Structural Stations	80
3.3.1. Station 1: Wall Damage Zone of Left-Lateral Strike-slip Kemerli Fault.....	83
3.3.2.-Station-2:-Triangular Area Close to Bozova and Kemerli Faults' Intersection.....	84
3.3.3. Station 3: Precursory Fractures to Folding and the Fractures Associated with the Strike-slip Activation of the Bozova Fault Plane	86

3.3.4. Station 4: Fractures Formed Around P-Shear Segment of the Bozova Fault.....	89
3.3.5. Station 5: Fractures Formed at Outer Damage Zone of the Bozova Fault and Hinge Zone to Back Limb of the Gemrik Anticline.....	91
3.3.6. Station 6: Kuyulu Low as an Exhumed Fractured Reservoir Formed at the Extensional Step-over of the Bozova Fault.....	92
4. SAYINDERE ROCK UNIT'S STRENGTH AND POLY-AXIAL STRESS CONDITIONS REQUIRED FOR ITS FAILURE.....	97
4.1. Methodology	98
4.2. Determination of Strength & Frictional Parameters of the Sayindere Formation.....	99
4.3. Determination of Elastic Parameters of the Sayindere Formation.....	103
4.4. Poly-Axial Failure Criterion and Stress Conditions Required to Yield the Sayindere Formation.....	106
4.5. Stress Perturbation Analyses & Estimating the Scale of Magnitude Buildups.....	111
5. IN-SITU STRESS ESTIMATIONS AND MEASUREMENTS	113
5.1. In-Situ Stress Estimations	113
5.1.1. Local Earthquakes as Natural Confirmations of Strike-slip Faulting.....	115
5.1.2. Upper & Lower Bound Estimations for Lateral Stress Coefficient, K.....	116
5.1.3. Estimations of Tectonic Stress Ratio (σ_h/σ_H).....	118
5.2. In-Situ Stress Measurements	120
5.2.1. Determination of the Least Principal Stress (σ_3) from Leak-Off Tests.....	120
5.2.2. Constraining σ_H from Borehole Breakouts	122

5.3. Extrapolated Vertical Profiles of Coefficient of Friction, Principal Stresses and Hydrostatic Pressure.....	135
6. SLIP TENDENCY ANALYSES	139
7. SLIP TENDENCY ANALYSIS: DELINEATION AND FILTERING OF CONDUCTIVE FAULTS ON 3D SEISMIC SURVEY.....	147
8. DISCUSSION AND CONCLUSION.....	155
8.1. Combination of Slip Tendency and Stress Perturbation Analyses.....	155
8.2. Mechanical Stratigraphy.....	160
8.3. Incorporation of Oil Expulsion Timing into Fracture Oiliness Predictions.....	166
8.4. Localization Mechanism and Orientation of the Oil Filled Fractures	166
8.5. Conclusive Remarks.....	167
REFERENCES.....	169
CURRICULUM VITAE.....	181

LIST OF TABLES

TABLES

Table 2.1. Ages and descriptions of major tectonic events and related depositional units.....	49
Table 4.1. Sayındere Fm. rock specimens' dimensions, densities and seismic wave velocities that were derived from ultrasonic velocity measurements.....	104
Table 4.2. Elastic properties of Sayındere argillaceous limestone specimens derived from ultrasonic velocity measurements.	105
Table 4.3. Critical principal stress magnitudes that must be realized due to perturbation of stress field near fault tips to form new fractures and subsidiary faults within a theoretically intact and cohesive blocks of the Sayındere argillaceous limestone.....	108
Table 5.1. Parameters, magnitudes and conditions for the formation of a borehole breakout at the depth of 1882 m. on the wellbore wall of the Well-1 drilled in Şambayat Oilfield.....	127
Table 5.2. Parameters, magnitudes and conditions for the formation of a borehole breakout at the depth of 1786 m. on the wellbore wall of the Well-2 drilled in the Şambayat Oilfield.....	130
Table 5.3. Parameters, magnitudes and conditions for the formation of a borehole breakout at the depth of 1813 m. on the wellbore wall of the Well-3 drilled in the Şambayat Oilfield.....	133

LIST OF FIGURES

FIGURES

Figure 1-1 (a) Regional Tectonic Map (b) Location Map (c) Updated geological and structural map of the study area.....	7
Figure 1-2 Generalized stratigraphic section of the southeast Turkey	19
Figure 1-3 Generalized stratigraphic section of the Adıyaman Region.....	20
Figure 1-4 Cross-section of the Adıyaman-Mardin-Kahta paleo-high.....	21
Figure 1-5 Late Early Permian palinspatic reconstruction map of continents.....	23
Figure 1-6 Outcrop view of the Sayındere Formation.....	27
Figure 1-7 Southward advancement of the intra-oceanic Neo-Tethys subduction front over the submerged hyperextension of the Arabian Plate.....	29
Figure 2-1 a) Measured stratigraphic section of the Lower member of the Kastel Formation and b) Sequence stratigraphic interpretation of the para-sequences.....	43
Figure 2-2 Tectonic faulting regime alternations affected the study numbered by chronological orders.....	47
Figure 2-3 A seismic section taken from SE Turkey illustrating the type-1 normal faults, that are interpreted as associated with the opening of Neo-Tethys.....	53
Figure 2-4 (a) Riedel-type slip surfaces near the Bozova Fault's trajectory (b) A sheared tensional fault formed on an E-W elongated Anticline.....	54
Figure 2-5 A seismic section from Adıyaman Province illustrating steeply dipping reverse faults which are considered to have used normal fault remnants of earlier extensional tectonic regimes.....	57
Figure 2-6 Sketch cross section illustrating relationship between the Bozova Fault and the Gemrik Anticline.....	59

Figure 2-7 Sketch cross section illustrating relationship between the Bozova Fault and the Karababa Anticline.....	60
Figure 2-8 (a, b) Quasilinearly arranged isolated lenses of exhumed, deformed blocks of steeply dipping Şelmo Formation associated with the Bozova Fault.....	61
Figure 2-9 (a, b) Subsidiary slip surfaces from damage zone of the Bozova Fault....	62
Figure 2-10 A striated slip surface along the trace of the Bozova Fault.....	63
Figure 2-11 (a) Tension joints from the structural station located at the back limb of the Gemrik Anticline (b) a close-up view from 3-cm-width calcite filled vein.....	67
Figure 2-12 (a) A close-up view from a shallower facies of the Sayındere Formation which consists of anti-cracked Campanian aged Ammonite fossils.....	68
Figure 2-13 (a) A close-up view of a slipped antithetic shear fracture that crosscuts an anti-crack (b) A set of synthetic shear fractures and slip surfaces that crosscut a tension vein.....	69
Figure 3-1 (a,b) Geometrical relations of shear band fractures with principal shear zone (PSZ) and maximum principal stress direction for right and left lateral strike-slip faults.....	75
Figure 3-2 “Bookshelf” type rotation of micro-blocks between R’ bands.....	78
Figure 3-3 Primary and secondary hierarchy Riedel shear fractures formed by remote and reoriented local maximum stress directions respectively.....	79
Figure 3-4 Perturbation of σ_1 trajectories around an active fault segment.....	79
Figure 3-5 Map of structural stations for field data collections.....	81
Figure 3-6 (a) Stereographic representation of fractures at the station-1 (b) Poles to bedding planes and their mean circle (c) Rose diagram of fracture strikes (d) Simplified sketch representing local fracture types.....	84

Figure 3-7 (a) Stereographic representation of fractures at the station-2 **(b)** Poles to bedding planes and their mean circle **(c)** Rose diagram of fracture strikes **(d)** Fracture sets associated with the Kemerli Fault **(e)** Fracture sets associated with the Bozova Fault **(f)** fracture set as a product of the perturbed stress field..... 85

Figure 3-8 (a) Stereographic representation of fractures located at the station-3 **(b)** Rose diagram of fracture strikes **(c)** Poles to bedding planes and their mean circle **(d)** Shear fractures related to the Bozova Fault **(e)**, TJs and PSSs that predate Gemrik anticline.....87

Figure 3-9 (a-e) Disc shape representations of fracture sets in one meter scanlines located in the station-3. **(f)** Calculation of the resultant vector (red arrow) representing best directional drilling trajectory to cut maximum amount of total linear fracture thickness.....88

Figure 3-10 (a) Stereographic representation of fractures located at the station-4 **(b)** Rose diagram of fracture strikes **(c)** Poles to bedding planes and their mean circle **(d)** TJs and PSSs that predate Gemrik anticline **(e)** TJs and PSSs that formed at the compressional quadrant of lately SS reactivated Bozova Fault. **(f)** Antithetic R' and P' shear fractures89

Figure 3-11 (a-d) Disc shape representations of fracture sets in one meter scanlines located in the station-3. **(f)** Calculation of the resultant vector (red arrow) representing best directional drilling trajectory to cut maximum amount of total linear fracture thickness.....90

Figure 3-12 (a) the mean circles of the systematic fracture sets located at the station 5. **(b)** Rose diagram of fracture strikes **(c)** Poles to bedding planes and their mean circle **(d)** TJs and PSSs that predate the Gemrik anticline. **(e)** Preferred strike orientation of the fold related extensional outer arc cleavages parallel to the strikes of the bedding planes at the longitudinally plunging hinge zone of the Gemrik Anticline. **(f)** R-shear fractures and TJs.....91

Figure 3-13 (a-e) Disc shape representations of fracture sets in one meter scanlines located in the station-5. (f) Calculation of the resultant vector (red arrow) representing best directional drilling trajectory to cut maximum amount of total linear fracture thickness.....	93
Figure 3-14 (a, b) Photos from outcropped asphaltite-filled fractures within Campanian argillaceous limestones (c) Geo-located rose diagram for the asphaltite-filled fractures.....	94
Figure 3-15 (a) the mean circles of the systematic fracture sets located at the station 6. (b) Rose diagram of fracture strikes (c) Poles to bedding planes and their mean circle (d) Preferred orientations of the TJs, Riedel shear, P'-shear and Y shear fractures.....	95
Figure 3-16 (a-d) Disc shape representations of fracture sets in one meter scanlines located in the station-6. (e) The intercepting discs with varying thicknesses indicate total anisotropic, oil filled fracture porosity values originated from different set of fractures. Calculation of the resultant vector (red arrow) representing best directional drilling trajectory to cut maximum amount of total linear fracture porosity.....	96
Figure 4-1 Mohr circles drawn for 6 compressive tests for strengths of bedding-parallel samples. While the three of them were subjected to unconfined compression (UH-1, 2, 3), the other three (CH-4, 5, 6) of the six samples were subjected to compression with three different confining pressures.....	100
Figure 4-2 Mohr circles drawn for 6 compressive tests for strengths of vertically (perpendicular to bedding) taken samples. While the three of them were subjected to unconfined compression (UH-1, 2, 3), the other three (CH-4, 5, 6) of the six samples were subjected to compression with three different confining pressures.....	101
Figure 4-3 Griffith failure criterion of brittle fracture in tensile domain expressed as the equation of a Mohr envelope, modified by Murrell (1963).....	102

Figure 4-4 (a-b) 3-dimensional Mohr diagrams showing failure envelopes to create slip on existing surfaces and to yield intact rock. (a) The 1st case corresponds to an amplified (2-fold increase) S_H component. (b) The 2nd case corresponds to a moderately decreased S_H and moderately (50%) increased S_H component.....	109
Figure 4-5 (a) Local maximum principal stress (σ_{1L}) trajectories form around a single, cohesionless defect. (b) Modified contours for amplifications of maximum principal stress magnitudes around the leading fault tip of a fault derived from photoelastic and numerical experiments conducted by Joussineau et al. (c) Contours of amplification and drops of remote minimum horizontal stress around the leading fault tip.....	112
Figure 5-1 Domain of variation for K values in different tectonic regimes.....	114
Figure 5-2 Location map of earthquake epicenters, main fault trajectories, Şambayat Oilfield and outcrop data collection site of this study.....	115
Figure 5-3 Stages of a fully-fledged XLOT, the extended leak-off test.....	122
Figure 5-4 Trajectories of principal stress around a cylindrical opening in a bi-axial stress field based on Kirsch equations (Kirsch, 1898).....	123
Figure 5-5 Tectonic faulting regimes polygons, customized by the stress magnitudes, that are calculated and measured for Well-1	128
Figure 5-6 (a) Circumferential, $\sigma_{\theta\theta}$, vertical, σ_{zz} and radial, σ_{rr} stresses acting on the wellbore wall of the Well-1 in a cylindrical coordinate system (b) Image log of the wellbore wall at 1882 m. where a part of a series of breakouts is observed.....	129
Figure 5-7 Failure envelope drawn for the Sayındere Formation and three effective principal stresses, $\sigma_{\theta\theta}$, σ_{rr} and σ_{zz} at the wellbore of Well-1 shown as three dimensional Mohr diagrams.....	130
Figure 5-8 Tectonic faulting regimes polygons, customized by the stress magnitudes, that are calculated and measured for Well-2.....	131

Figure 5-9 (a) Circumferential, $\sigma_{\theta\theta}$, vertical, σ_{zz} and radial, σ_{rr} stresses acting on the wellbore wall of the Well-2 in a cylindrical coordinate system (b) Image log of the wellbore wall at 1786 m. where a part of a series of breakouts is observed.....	131
Figure 5-10 Failure envelope drawn for the Sayındere Formation and three effective principal stresses, $\sigma_{\theta\theta}$, σ_{rr} and σ_{zz} at the wellbore of Well-2 shown as three dimensional Mohr diagrams.....	132
Figure 5-11 Tectonic faulting regimes polygons, customized by the stress magnitudes, that are calculated and measured for Well-3.....	134
Figure 5-12 (a) Circumferential, $\sigma_{\theta\theta}$, vertical, σ_{zz} and radial, σ_{rr} stresses acting on the wellbore wall of the Well-3 in a cylindrical coordinate system (b) Image log of the wellbore wall at 1813 m. where a part of a series of breakouts is observed.....	134
Figure 5-13 Failure envelope drawn for the Sayındere Formation and three effective principal stresses, $\sigma_{\theta\theta}$, σ_{rr} and σ_{zz} at the wellbore of Well-3 shown as three dimensional Mohr diagrams.....	136
Figure 5-14 Change of in-situ effective stress magnitudes by depth over Adıyaman Province.....	137
Figure 5-15 K values derived from in situ stress measurements (red ellipses) within Şambayat Oilfield. Upper (black) and lower bound (blue) curves derived using corresponding expressions for bounds of K elaborated in the text and inverse solution of an earthquake focal mechanism (purple ellipse).....	138
Figure 6-1 Geometrical relation between direction cosines and the angles that the principal stresses make with the normal vector to any arbitrary surface (modified from Allmendinger et al., 2012).....	141
Figure 6-2 (a) Arbitrary distribution of pre-existing faults and fractures under compression (b) The relationship between static friction and the angle of "expected to reactivate" faults. (c) Orientation interval of optimally oriented, high-slip tendency faults with respect to maximum principal stress direction.....	144

Figure 6-3 Pole demonstration of slip tendency values for every possible integer strike and dip combination. This plot was generated based on in-situ stress measurements for 1600 m in Şambayat Oilfield.....	145
Figure 6-4 (a-f) Slip tendency plots of lower hemisphere, equal area projection of poles to slip planes for various depths were created according to changing poly-axial stress states. (g) The stress conditions of selected depths at which slip tendencies were analyzed.....	146
Figure 7-1 A shear stress to normal stress binary plot illustrating fractures whose geometry and hydraulic connectivity properties are identified with borehole imaging techniques in Cajon Pass (triangles), Long Valley (circles), and Nevada Test Site (squares) boreholes. Taken from Townend and Zoback (2000) based on original data of Zoback et al. (1995).....	148
Figure 7-2 (a) A cropped ant-tracking depth slice of the -1100 m corresponding to an average regional burial depth of 1600 m of the Sayındere Formation from the Şambayat 3D seismic coverage area. (b) The stereonet polar plot showing slip tendency fraction of accordingly color coded fault segments on the depth slice. (c) A closer view to the Şambayat NFR oilfield and its production wells. The contours show elevation of the Sayındere Formation tops from the wells drilled into the Şambayat antiformal structure.....	151
Figure 7-3 (a,b) Maps showing highest-slip tendency, red color-coded principal shear zone segments of the Samsat Fault and envisaged damage zone extents for each one of those segments based on bilaterally growing fault models of Faulkner et al. (2011).....	152
Figure 8-1 Dually color-coded (red and blue) faults are considered to show induced mechanic and hydraulic activity; these are in fact inactive relict faults, as depicted in the Figure 8.4, and are subjected to reactivation.....	157

Figure 8-2 Image log showing drilling-induced fractures. The log belongs to Well-10, which is located at the north of the northwestern end of the hydraulically active and HST segments of the Samsat strike-slip fault strand.....	158
Figure 8-3 Log-log plot illustrating pressure change and derivative values with respect to elapsed time during the 2nd buildup phase of a drilling stem test conducted in Sayindere Formation at well S-14.....	159
Figure 8-4 Binary plot showing gradients of mineral compositions from foredeep to distal foreland sediments of the syn-obduction upper Campanian Upper Kastel Formation and its contemporaneous distal counterpart, the Bozova Formation.....	160
Figure 8-5 Conceptual model for changing heights of the oil column related to facies and mechanical stratigraphy of the supposedly cover rocks deposited over different oilfields.....	163
Figure 8-6 Field views from the Kastel and Bozova Formation outcrops.....	165
Figure 8-7 A binary plot illustrating oil generation and expulsion rates versus time for Adıyaman province foreland basins in general, including the Şambayat NFR oilfield.....	166

LIST OF ABBREVIATIONS

ABBREVIATIONS

BSL: Below sea level

CFF: Coulomb failure function

CH: Confined tested horizontal layer parallel rock samples

CV: Confined tested rock samples that were cored vertically to the layer

DITF-DIF: Drilling induced tensile fracture

DST: Drilling stem test

FBP: Formation breakdown pressure

FCP: Fracture closure pressure

FIT: Formation integrity test

FPP: Fracture propagation pressure

HST: High slip tendency

ISIP: Instantaneous shut-in pressure

LD: Linear density

LFP: Linear fracture porosity

LHFT: Linear healed fracture thickness

LOP: Leak-off point

LOT: Leak-off Test

MEM: Mechanical earth model

MFS: Maximum flooding surface

NF: Normal faulting

NFR: Naturally fractured reservoir

PMMA: Polymethylmethacrylate (birefringent material)

PSSs: Pressure solution seams

PSZ: Principal shear zone

R'-Shear: Antithetical Riedel shear fracture

RF: Reverse faulting

R-Shear: Riedel shear fractures

SS: Strike-slip

TJs: Tension joints

TLFP: Total linear fracture porosity

TLFT: Total linear fracture thickness

UCS: Unconfined compressive strength

UH: Unconfined tested horizontal layer parallel rock samples

UTS: Unconfined tensile strength

UV: Ultrasonic velocity

UV: Unconfined tested rock samples that were cored vertically to the layer

WBO: Break-out width

XLOT: Extended leak-off test

Y-Shear: Fractures form parallel with the principal shear zone

LIST OF SYMBOLS

SYMBOLS

C-C0: Cohesion

d: Displacement

E: Modulus of elasticity (Young Modulus)

G: Shear modulus

g: Gravitational acceleration constant

k: Stress division ratio

K: Lateral stress coefficient

l,m,n: Direction cosines

P_C: Confining pressure

P_P, P₀: Reservoir pore pressure

r: Radius of the wellbore

R: Stress difference ratio

R_r: Secondary hierarchy Riedel fractures

s: Spacing

S': Effective stress

S₁: Maximum principal stress

S₂: Intermediate principal stress

S₃: Minimum principal stress

S_H, σ_H: Maximum horizontal stress

S_h, σ_h: Minimum horizontal stress

S_v, σ_v : Vertical stress

t : Interval transit time in μs

T_s : Tendency of Slip, Slip Tendency

T_s' : Normalized slip tendency

$T_{s_{max}}$: Maximum slip tendency

V_P : P-Wave Velocity

V_S : S-Wave Velocity

z : Depth

α, β, γ : Angles of the arbitrary planes with respect to principal stress axes in a Cartesian coordinate system

β : Modified angle from R-shear and R'-Shear fractures

β_0 : Original angle from R-shear and R'-Shear fractures

ΔP : Pressure difference between circulation and reservoir fluids

Δt : Sonic wave slowness in $\mu s/ft$

θ : Angle measured from the azimuth of maximum principal stress

μ, μ_i : Internal friction coefficient

μ_s : Static friction coefficient; highest allowable coefficient of static friction for pre-existing surfaces for certain stress conditions

ρ : Density

ρ_{Mud} : Mud pressure

σ_{1L} : Local maximum principal stress

σ_{1r} : Reoriented maximum principal stress

σ_n : Normal stress

σ_{rr} : Effective radial stress around a vertical wellbore of radius R

$\sigma_{x,y,z}$: Principal stresses in a Cartesian coordinate system

σ_{zz} : Effective stress acting parallel to the wellbore axis

$\sigma_{\theta\theta}$: Effective circumferential (Hoop) stress around a vertical wellbore

σ_{τ}, τ : Shear stress

$\phi_s, \varphi_s, \phi_s$: Static friction angle; highest allowable static friction angle for pre-existing surfaces for certain stress conditions

ϕ, φ_i, ϕ_i : Internal friction angle

Ω : Pitch angle

ν : Poisson ratio

$\sigma_{\Delta T}, S_{\Delta T}$: Thermal stress

CHAPTER 1

INTRODUCTION

1.1. Purpose and Scope

Naturally fractured reservoirs (NFRs) comprises at least 60% of the world's petroleum reserves (e.g., Waldren and Corrigan, 1985; Beydoun, 1998; Roxar, 2009). Because of their highly complicated nature, compared to traditional reservoirs, proper evaluation of NFRs necessitates more data and effort (time). As most traditional reserves worldwide tend to decline in the last decades, attention of the producers in the petroleum industry has drawn to non-traditional NFRs (cf. Niven and Deutsch, 2009) despite of their complexities. Because of increasing economic significance, it has become rather important to decrypt complexity of NFRs by understanding conditions under which they form and bear reservoir fluids. In most NFRs, fractures and matrices support reservoir properties at different proportions (Nelson, 2001). Fractures as structural heterogeneities are considered critical for hydrocarbon migration and fluid flow (Aydin, 2000). Especially in cases where rocks have negligible initial matrix porosity, fracture's role becomes essential on the formation of reservoirs and fluid flow. A fractured reservoir, called Şambayat NFR oilfield, was discovered by Turkish Petroleum (TPAO) National Oil Company in Adıyaman province of SE Turkey in 2008 (Figure 1.1a, b). There, fractures are considered responsible for the most oil containment within Campanian argillaceous limestones of the Sayındere Formation; it is important to note that this formation had long been considered as a cap rock in the petroleum system of the Adıyaman province. The oilfield is discovered by utilization of 3D seismics and production wells; this dataset constitutes the main source of subsurface data of this research with permission of TPAO. The Sayındere Formation in the Şambayat oilfield is folded (an anticline) and is demarcated by a NW–SE-trending strike-slip fault, namely Samsat Fault. With its initially non-porous and impermeable nature, and with its fracture prone nature owing to its relatively weak strength to brittle failure

(as compared to underlying pure limestone units), the argillaceous limestones of the Sayındere Formation can be considered as the best rock type to investigate isolated effects of fractures on reservoir qualities. The Sayındere Formation crops out around a site located at about 20 km SSE of the Şambayat oilfield. Major structures in the outcrop site comprise WNW–ESE-trending anticline, WNW–ESE-trending strike-slip Bozova Fault and a NE–SW-trending strike-slip Kemerli Fault. There, the formation is therefore intensely deformed and highly fractured; field data concerning fractures, faults and fluid circulation is collected in this particular locality (Figure 1.1c).

Within the context of field studies of this research, I discovered an exhumed domain of mostly asphaltite and heavy oil filled interconnected arrays of fractures around the Bozova Fault and denoted the domain as “*exhumed fractured reservoir*” whereas at many other domains along the same fault, the vast majority of the fracture population are either unfilled or filled with calcite (see Chapter 3 for more detail information). This discovery and supportive observations led to investigate hydraulic activity of the fractures and faults in the study area. According to critically stressed fault hypothesis proposed by Zoback et al. (1995) and slip tendency concept introduced by Morris et al. (1996) hydraulic activity of a planar discontinuity is directly proportional to its mechanical activity, and thence its slip tendency. To calculate mechanic or hydraulic activity of existing surfaces, one must have knowledge about orientation and magnitude of these surfaces as well as directions of three natural principal stresses acting on them with a decent level of confidence. Therefore, in this research, I respectively included (i) construction of a vertical profile of the three principal stresses via in-situ stress measurements, (ii) delineation of whole existing population of major and subsidiary faults within 3D seismic data by applying seismic volume attributes (e.g., ant tracking) and (iii) polar filtering of mechanically and hydraulically active faults amongst the whole population of discontinuities, based on slip-tendency analysis and measured principal stresses.

Most of the natural fractures are confined within spatial volumes below seismic resolution and especially around faulted areas, quality of seismic reflections might so

deteriorate that even the major structures may turn out to be uninterpretable. To be able to speculate about the presence of oil-bearing fractures in such areas as depicted above or areas with no seismic data, construction of a vertical stress profile, determination of the strength parameters of NFR candidate rock and utilization of poly-axial failure criterion can be used as powerful tools. Since the fractures are planar discontinuities resulted from natural stresses exceeding the rupture strength of the rocks, I determined strength parameters of the Sayındere Formation via laboratory experiments and made deductive calculations for critical natural stress magnitudes that would have ever fractured the Sayındere Formation; and this is based on a modified Mohr-Coulomb poly-axial criteria proposed by Singh et al. (2011). As I compared the calculated critical magnitudes to yield the Sayındere Formation with the in-situ stress magnitudes that are measured from wells, I realized that the measured magnitudes were not sufficient, instead, a significant increase in differential stress was required to create new fractures within an intact medium of Sayındere Formation. The result of this comparison has led me to consider how the natural stresses could amplify up to the magnitudes to fracture rocks in the first place. Therefore, in this research, I also included the concept of stress field perturbation to explain how the critical stress conditions are reached in natural settings.

Despite of a few research over the last decades (Akyol et al., 2013; Türkmen and Gözel, 2014; Özkaya et al., 2019), there are still several conceptual and local (for Adıyaman region) problems about formation, evolution and extend of fractured reservoir(s). The purpose of this research is therefore to address these questions (see sections 1.1.1 and 1.1.2). The Adıyaman region, which is located at the collision zone between Anatolian and Arabian plates since late Cretaceous with short-term intervening tectonic quiescence period, is chosen as target area during this research. It is a region of intense deformation as manifested by several reverse and strike-slip faults, and associated deformation zones. The Adıyaman region is therefore considered as one of the key/novel areas to investigate the effects of faulting on the formation, evolution and extent of NFRs.

1.1.1. Conceptual Problems

Major objectives of the present thesis are therefore to address following conceptual and regional (unique to Adiyaman region) questions, awaiting for answers and clarification:

(a) What is the role of faults and stress field perturbation along fault trajectories on properties of fracture networks?

(b) Where do hydraulically active fracture corridors localized around faults? Why exactly there?

(c) What would be the best directional drilling trajectories to cut and produce hydrocarbon from as many fractures and as much fracture porosity as possible?

(d) What is the relationship of individual set of fractures with local and regional stress field and major structures, e.g., proximal master faults or folds.

(e) How brittle damage is distributed over the extent of major structures?

(f) What respective steps should a fully-fledged reproducible work-flow comprise to implement in any other potentially fractured reservoir oilfield for development and/or in uncharted areas for exploration purposes?

1.1.2. Regional Problems

(1) Why is the Sayindere Formation a Decent NFR Forming Rock Unit?

In a regional scope, it is not well received that which property of the Sayindere Formation makes it to come into prominence as a good naturally fractured reservoir.

(2) Unknown Strength Parameters of the Host Rock, The Sayindere Formation

Though it is well received that the natural fractures are formed mostly by poly-axial natural stresses whose resultant values exceed the failure strength of the host

rock units, neither the local stress magnitudes in the Adıyaman region, nor the failure strength parameters of the host rocks have been the subject of any research.

(3) Poorly Studied Mechanical Genesis of Fracture Incipience

Although the importance of the hydrocarbon-bearing fractures and their potential contribution to overall recoverable reserves are of matters of consensus, their mechanical formation conditions, on the other hand, have not yet properly studied exclusively for the SE Anatolian oilfields. Thus, remote and local stress magnitudes around NFR's as well as mechanical strength parameters of the only proven fractured reservoir host rock of the Adıyaman region (the Sayındere Formation) must have been studied in order to (i) bring a mechanical approach, (ii) explain genesis of fracturing in regional NFR's and (iii) emphasize the fact that most of the natural fractures are products of poly-axial natural stresses, which surpass brittle failure strengths of rocks at depths.

(4) Lack of Incorporation of Slip Tendency and Hydraulic Activity Concepts on Pre-existing Discontinuities

The problem of 'Why some fractures are oil filled, while others not?' has not been sufficiently addressed yet. Due to lack of research on the stress field and its implications on the fluid flow, the mechanical and hydraulic activity, which allow existent fluids to flow through planar discontinuities, within the study area have not become an issue of debate so far. According to critically stressed faults and slip-tendency concepts proposed by Zoback et al. (1995) and Morris et al. (1996), hydraulic activity of any planar discontinuity is directly proportional to their mechanical properties and tectonic activity. Basically all rocks at depth may include pre-existing faults and fractures with various orientations. Among the whole population of existing faults and fractures, however, only the ones that are oriented within specific interval of dip and strike combinations with respect to maximum natural principal stress direction, can accumulate stress on their bodies and bear a high slip tendency, thus a hydraulic activity.

(5) Leaving Timing out of Account

In order for any fractured reservoir to become oily and thus not filled with any other circulating fluids (which may include dissolved minerals, such as calcite or quartz) at the time of opening, the tectonic, hydraulic and mechanical activity periods of fractures and faults should coincide with timing of oil expulsion for any oilfield. In order to determine which faults and fractures might bear oil, the timing of regional oil expulsion peak and, mechanic and hydraulic activity periods of the faults and related fractures should be incorporated.

(6) Water-flooding Phenomenon

Despite the discovery of the Şambayat oilfield, fractures within the rest of the oilfields in the SE Turkey are because of actualization risk of the water flooding phenomenon (cf. De Swaan, 1978; Li, 1997, 2003; Yuan et al., 2004). This phenomenon, however, entails shallower accommodation spaces interconnected with the fractured reservoir horizons by veins, faults or penetrative fractures for the reservoir fluids to be transferred. On the other hand, as will be elaborated in the Discussion Chapter, field observations and mineralogical analyses of the host rocks (the Sayındere Formation) that enable deductions on the mechanical stratigraphy of the overlying rock units, the geographical extent of the regions of the water-flooding can be anticipated.

1.2. The Study Area

The study area is located at the northern margin of the African-Arabian tectonic plate in Adıyaman province of southeast Turkey. The Sayındere Formation forms the key lithological association and is exhumed and deformed by a strike-slip fault around Gemrik and Karababa anticlines and Kuyulu low located along the Bozova Fault trace. The field studies were carried out around these outcrops. The field survey site is located at about 20 km SE of the Şambayat seismic survey site where the Sayındere Formation is buried and fractured in similar tectonic settings (Figure 1.1c).

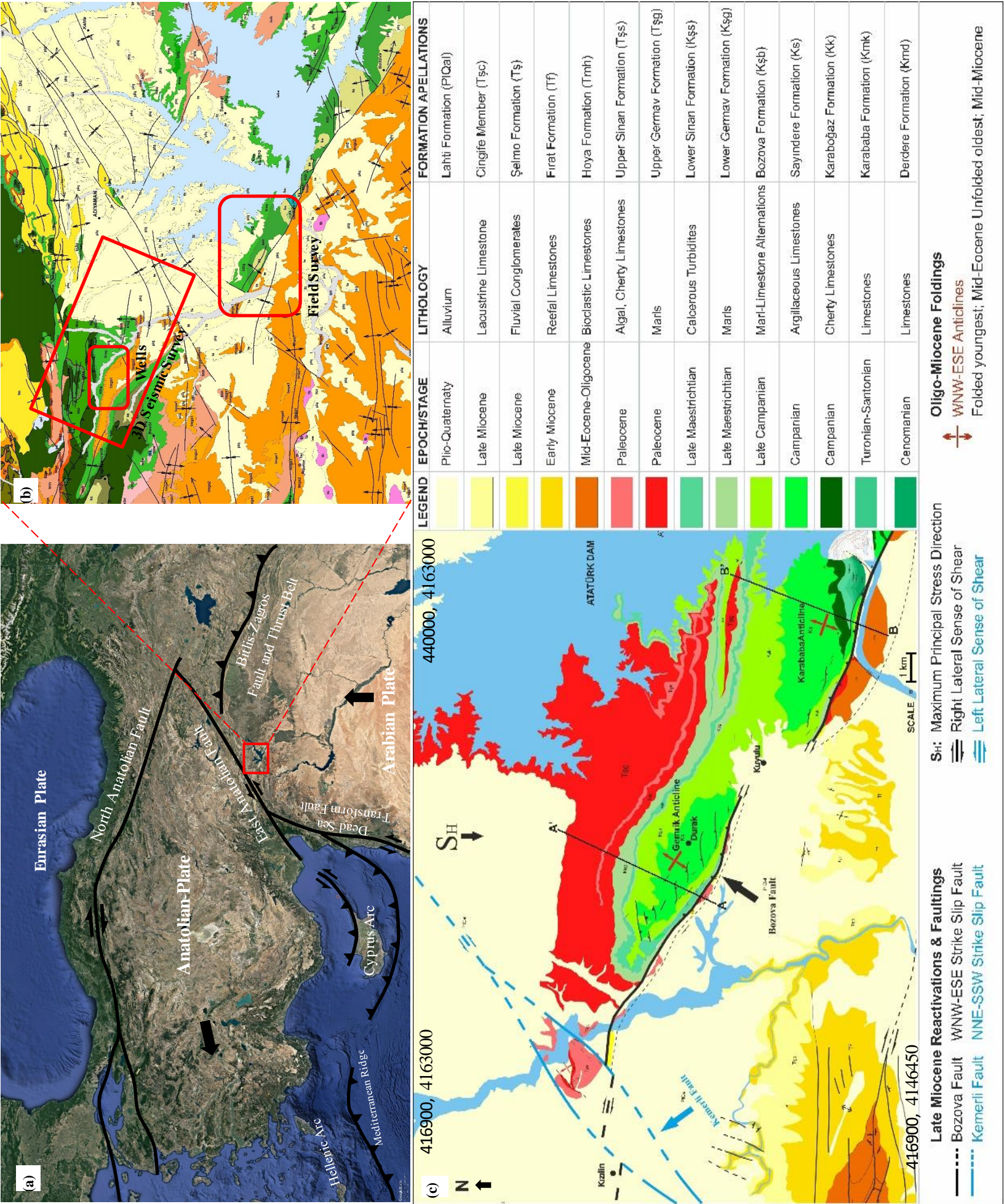


Figure 1.1 (a) Regional Tectonic Map showing main plate boundaries (convergent and transfer). The red rectangle shows the location of the study area which is located onto northwestern margin of the Arabian plate. (b) Location map of seismic and field survey areas within the study area. Bigger rounded rectangle shows the field survey site whereas the smaller rounded rectangle show the Şambayat NFR oilfield, which was covered by 3D seismic survey (The biggest rectangle) (c) Updated geological and structural map of the study area located around the Bozova Fault and its adjacent culminations and depression domains. Sayındere and Bozova formations are the light and yellowish green colored units in the legend and crops out at the hinge of the highs and the lows. Black circle shows the surroundings where asphaltite-filled fracture corridors were discovered. The straight black lines show line of cross sections that will be illustrated in Figures 2.6 and 2.7.

1.3. Regional Stratigraphy

Throughout the southeast Turkey, pre-Cambrian to recent sedimentary successions are discontinuously preserved as evidenced either from drilled wells or from the outcropped field sites (Figure 1.2). The preserved sedimentary sequence around the study area, the Adıyaman province is composed of so-called Precambrian to Ordovician basement sediments and Early Cretaceous to recent cover sediments (Figure 1.3) deposited in continental, shallow-marine or deep ocean paleo-environments along Tethyan margins (Proto-Tethys, Paleo-Tethys, Neo-Tethys) of the Gondwana and the Arabian Plate chronologically (e.g., Dercourt et al., 1986; Şengör, 1990; Stampfli and Borel, 2002; Stampfli and Kozur, 2004; Rolland et al., 2011). Early Ordovician to Late Jurassic successions were either eroded after deposition or not deposited around the study area. Local absence of post-Cambrian to pre-Cretaceous stratigraphic units around Adıyaman region is associated with one of the most pronounced uplifts of the Northern Arabian Plate; it is known as Mardin-Kahta High whose long axis lies in a ESE–WNW direction in the area between Kahta and Mardin provinces (Figure 1.4). Mardin-Kahta uplift is considered to have been constructed during by a number of orogenic events; main phases are Caledonian, Hercynian (Variscan) and Early Alpine orogeny. Erosional (and consequent hiatus) events, which generally accompany with relative sea level falls, are attributed to orogenic processes. Besides, some of the unconformity surfaces are considered as related to glaciation and post-glaciation events, especially those reported in the narrower extent of the study area including the Mardin-Kahta High. The pre-Aptian units include varying ages of rocks from pre-Cambrian volcanoclastics to Jurassic shallow-marine carbonates. Towards to the central localities within Mardin-Kahta High, all unconformity surfaces merge, whereas at its distant, marginal areas, unconformity surfaces get separated with an increased preservation in the number and thickness of intercalating units (Figure 1.4). Accordingly, at places away from paleo-highs where the effects of global orogenic events are sensed mildly, the entire Paleozoic and Mesozoic successions were deposited and well preserved. In the following sub-sections, the geological history of the whole northeastern Arabian Plate since pre-Cambrian times will be summarized.

1.3.1. Pre-Cambrian, Paleozoic and Early Mesozoic Rocks

These successions are discontinuously preserved throughout the entire region of the southeast Turkey. Post-Cambrian Paleozoic units along with Triassic, Jurassic and the earliest Cretaceous units (pre-Aptian), which are described in this section, are missing in the Adıyaman province including the field and underground survey sites of this research. Post-Cambrian–pre-Aptian units are proven to have preserved somewhere else in the southeast Turkey, such as around Diyarbakır, Batman or Gaziantep provinces. Investigating how they become locally missing in the study area, however, may shed light on the tectonic and stratigraphic history of the region as a whole. The late Cambrian Sosink Formation and older units, which constitute the local basement, are overlain by Aptian Areban Formation of the Mardin Group around the Adıyaman Province (Figure 1.3).

The Cenomanian and Turonian Derdere and Karababa formations within the Mardin Group, on the other hand, form essential source rocks of the regional petroleum system in the study area (see Section 1.3.2.). Nevertheless, locally absent Silurian Dadaş Formation and Triassic–Jurassic Cudi Group’s source rocks contribute the petroleum system additionally to the Mardin Group source rocks elsewhere in the southeast Turkey.

- **Pre-Cambrian Telbesmi Formation**

Late Proterozoic (Edicaran) Telbesmi Formation, the oldest rock in the studied region, is composed of intensely fractured and faulted volcanic and volcanoclastic rocks, shale and sandstone; there are reports of granitic blocks within the clastic sediments (Şenalp et al., 2018). The formation is interpreted to constitute the basement of the Paleozoic succession in Southeast Turkey. It is exposed around Derik (Mardin) province and interpreted at some deep wells drilled in the region.

Telbesmi Formation is also considered by Şenalp et al. (2018) to have supplied some polished and scratched rock particles along with post-glacial cap carbonate particles to its posterior and overlying fluvial deposits of Early Cambrian Sadan

Formation, indicating the existence of the effects of Marinoan glaciation that prevailed globally between 650–635 Ma. The unconformity is considered to be associated with the combined effects of glacial incisions, post-glacial isostatic rebound and de-glacially induced global sea-level rise (Knoll et al., 2006). Some other researchers, who investigated the age of the Telbesmi Formation, however, remarks that the geochronological (zircon LA-ICP-MS) data from the oldest volcanics of the formation exhumed in Derik, SE Turkey, provide crystallization ages ranging between 559.2 ± 3.2 Ma & 581.4 ± 0.5 Ma (Gürsu et al., 2016), which postdates the Marinoan glaciation. Accordingly, the indications that may be associated with the Marinoan glaciation in SE Turkey may not be considered as substantial.

The Telbesmi Formation is unconformably overlain by thick and widespread Cambrian Derik Group. The group comprises, from the oldest to the youngest, marine clastic rocks of the Sadan Formation, shelf carbonates of the Koruk Formation and, shallow-marine shale and sandstone alternation of the Sosink Formation.

- **Early Cambrian Sadan Formation**

Beginning with the retreat of the Marinoan global ice cap 635 million years ago, a steady global sea-level rise began and lasted for a long time including the Cambrian and Middle Ordovician. Accompanying the sub-aerial exposure of the Gondwanan continental crust with the contribution of the post-glacial rebound of the continental interiors, previously faulted and fractured Telbesmi Formation became an exposed provenance of terrigenous sediments either of alluvial and fluvial deposits at proximal localities or shallow-marine deposits on its distal peripheries where the study area of this research is located. As the global eustatic sea level increased, Early Cambrian (Fortunian) shallow-marine clastic sediments of the Sadan Formation unconformably overlie the Telbesmi Formation because of the further encroachment of the proto-Tethys (Berra and Angiolini, 2014).

- **Late Early Cambrian Zabuk Formation**

Though the Cambrian, global sea-level rise was continuing with some third order sea-level fluctuations. A significant regional relative sea-level drop related to a possible upward movement has taken place at the Northern Gondwana by the end of Fortunian (529 Ma) and, the source area of the sedimentary infill materials and the depositional environments have therefore suddenly shifted thereafter. Thus, the braided river sandstone facies of the Zabuk Formation (firstly defined by Schmidt, 1965) was deposited conformably above the Sadan shallow-marine clastics. The type section is located in the Zabuk valley near the town of Derik of Mardin province in SE Turkey. The Zabuk Formation ends with foreshore sandstones in transgressive settings in accordance with the overall Cambrian transgression event.

- **Middle Cambrian Koruk Formation**

Koruk Formation (Ketin, 1964) is originally made up of algal bioclastic limestones (now occur as dolomitic limestones) of tidal flat depositional environment (Aydemir, 2011). It conformably overlies the shallow-marine sandstones of the Zabuk Formation. The type section is located near Koruk village in Mardin province of SE Turkey. Koruk Formation is the only carbonate sequence of the Cambrian deposits of SE Turkey. Medium- to thin-bedded marl and fine-grained sandstone intercalations of the upper para-sequences of the Koruk Formation is conformable with the overlying the Sosink Formation.

- **Late Cambrian Sosink Formation**

Sosink Formation is composed of mainly a wave-dominated delta sequence deposited in continental shelf environment. Both coarsening- and fining-upward para-sequences are observed within the formation in response to short-term eustatic sea-level fluctuations and, consequent sea- and basin-ward migration of the coastline during late Cambrian (Şenalp et al., 2018). The most prominent lithology of the Sosink Formation is pro-delta shale alternating with siltstone and sandstone. The

depositional environment of the Sosink Formation was mainly controlled by two competing dynamics: global eustatic sea-level changes and rate of sediment influx.

- **Early Ordovician Konur Formation**

Konur Formation was firstly denoted by Şenalp et al. (2015) referring to its type locality near the Konur village, Derik town of Mardin province in SE Turkey; it is interpreted as a chronological, stratigraphical and sedimentological equivalent of the Upper Cambrian–Early Ordovician Seydişehir Formation. Konur Formation consists of deltaic sandstone, pro-delta shale and transition facies along with deltaic mouth bar facies at its upper sections. Those mouth-bar facies are incised by submarine distributary channels which form as extensions of fluvial system (Şenalp et al., 2016). During the shallow- and deep-marine clastics was cyclically deposited along the margin of the Gondwanaland due to global sea-level fluctuations of the time (Vail et al., 1977a).

- **Middle to Late Ordovician Bedinan and Yurteri Formations**

The Bedinan Formation was firstly defined by Cobb (1957) at its type locality near Bedinan village in Derik town of Mardin (SE Turkey). Its lower, coarsening-upward parasequences are composed of open-marine shales interbedded with sandstone, and transgressively overlie sandstone-dominated upper sections of the Konur Formation.

In the latest Ordovician (Hirnantian, 446 Ma), glaciation prevailed over the Northern Gondwana since the continent was located at the South Pole and the present day SE Turkey was at the northern periphery of the ice cap at that time. Upper sequences of the Bedinan Formation are incised and thus unconformably overlain by glacial valley-fill deposits of the Hirnantian Yurteri Formation (Şenalp et al., 2018).

The Yurteri Formation overlies older units at the localities where the glacial valleys scratch deeper sporadically. The valley-fill deposits is composed of fining-upward sequences of clastic units whose grain dimensions ranges from

conglomerate to fine-grained sandstone. Pebbles are polished and include striations recording the advancement of the ice sheet. Glacio-fluvial finer parts of the sequences are formed by glacial retreats.

- **Silurian Dadaş and Hazro Formations**

Shaly, lowermost part of the Silurian Dadaş Formation transgressively overlies Yurteri and Bedinan formations in response to de-glacially formed sea-level rise at the end of the Ordovician. In the petroleum industry, this unit is denoted as “*hot shale*” because of its high source rock potential. As global sea level stabilizes with the termination of additional water input originated from the melting down of the ice sheets, cap carbonates (limestone and dolostones) form and conformably overlie the first post-glacial flooding products (e.g., hot shales). Formation mechanism of the cap carbonates is still a hot topic of research and there are different explanations proposed; these include carbonate and silicate weathering (Fairchild, 1993; Higgins and Schrag, 2003), breakdown of permafrost and gas-hydrates (Kennedy et al., 2001b), upwelling of alkali oceanic deep waters (Grotzinger and Knoll, 1995; Ridgwell et al., 2003). After the deposition of cap carbonates, platform shales and sandstone units in progradational coarsening-upward sequences was deposited and formed the uppermost sections of the Dadaş Formation. The formation is acknowledged as a separate formation named Hazro Formation by some researchers.

The progradation of the Silurian sequences was in its most severe stage during Ludfordian short-term sea-level drop at about 80 m, which was then succeeded by a 70 m rise (Haq and Schutter, 2008). When the sea-level was at its lowest for the Silurian, the deltaic mouth-bar facies of the upper Dadaş Formation (or of the Hazro Formation) was deposited; the sedimentation was continued with deposition of offshore marine shales. Continuation of the first order eustatic global sea-level drop of the late Silurian, along with a possible contribution of the influence of the Caledonian orogeny (Early Devonian), causes a slight sub-aerial exposure of the shelf and created an unconformity surface between Silurian and Devonian deposits around the study area. This upward movement did not trigger the formation of a

continental sedimentary sequence, except for paleo-soils at the bottom of the overlying Devonian Kayayolu Formation.

Towards interior of the Mardin-Kahta axis, which includes the study area of this research, influence of the Caledonian and succeeding orogenic events are prominent, since we observe missing parts of the Dadaş Formation and some preceding succeeding units in the exploration wells drilled in that region.

- **Early Devonian Kayayolu Formation**

A robust short-termed eustatic sea-level fall (Haq and Schutter, 2008) coupled with a slight effect of Caledonian Orogeny in the Early Lochkovian (earliest Devonian) caused sub-aerial exposure of the Gondwana continental shelf via coastline progradation and triggered deposition of continental (playa or) flood plain mudstone unit as an indication of unconformity. Subsequently, a short-term global sea-level rise occurred in an equivalent severity (Haq and Schutter, 2008) causing offshore marine shales to overlie transgressively the older mudstone facies. After the end of the strong sea-level fluctuation events, during the rest of the Lochkovian period, a slight sea-level fall period prevailed. This led the deposition of interbedded shallow-marine limestone, algal dolomite and evaporite facies with shale intercalations. In Praghian stage of the late Early Devonian (411 Ma), by courtesy of another high frequency eustatic sea-level cycle, which begins with a robust sea-level fall, red colored mudstone with siltstone and evaporite alternations was deposited in a playa environment (Senalp et al., 2018).

Kayayolu Formation was overlain by Hercynian unconformity surface particularly in the Hazro area of Diyarbakır, SE Turkey. The rest of the Devonian successions just as the Carboniferous and Early Permian units are missing outcrops in the present-day Mardin-Kahta axis or in wells, since they had not been preserved due to tectonic events associated with mainly the Hercynian Orogeny. Elsewhere in the SE Turkey, at the places away from major Paleozoic highs (e.g., Mardin-Kahta, Siirt or Hakkari), intensity of erosive influence of the Hercynian orogeny appears

minimum as indicated by the reduced thickness of the missing Paleozoic successions beneath Permian.

- **Middle Permian Kaş Formation and Hercynian Orogeny**

Carboniferous and Lower Permian units are either not exposed at the outcrop sites in SE Turkey or penetrated in boreholes since Late Carboniferous Hercynian (Variscan) Orogeny, its regional implications and associated compressional tectonic events became highly influential until Wordian (269 Ma; middle Middle Permian) over the present-day SE Turkey. Accordingly Hercynian unconformity surface beneath the Middle Permian Kaş Formation directly overlies Ordovician to Carboniferous units in the SE Turkey (Figure 1.4). After the onset of Hercynian Orogeny, which commenced with the collision of Laurassia and Gondwana in the Late Carboniferous (Figure 1.5), the present-day SE Turkey as a margin of the newly united supercontinent Pangea turned into a locally emerged, erosion prevalent region with an undulated topography. Most of the pre-Permian successions were therefore eroded at some places down to Carboniferous units and at some places down to Ordovician units.

In the Late Early Permian, Neo-Tethys rifting started as a continental-scale NNE to SSW lateral lengthening to accommodate unilaterally progressing NW to SE shortening effects of Hercynian Orogeny (Figure 1.5). With the onset of the Neo-Tethys opening, northern margin of the Pangean Gondwana underwent subsidence via north-dipping normal faults, stair-stepping towards contemporaneously forming Neo-Tethys Ocean. This tectonic basement subsidence caused coastline to prograde landward; first nearshore deposits of the Kaş Formation were deposited unconformably (transgressively) over locally eroded and locally normal-faulted Paleozoic successions (Figure 1.4). This unconformity surface therefore marks a merged horizon of the erosional events of Hercynian Orogeny and Neo-Tethys subsidence. Kaş Formation mostly consists of shale and sandstone alternations with thin coal-bed intercalations, deposited in shallow-marine, coastal plain and estuarine environments. Tectonic subsidence continued to be the dominant factor to control relative sea level in the active continental margin until Jurassic as the Neo-Tethys

reached its upmost widening through normal faulting. Maximum flooding surface is reached in the late Permian, and Gomaniibrik carbonates overlie the Kaş Formation transgressively.

- **Late Permian Gomaniibrik Formation**

With the initiation of a divergent movement and the opening of Neo-Tethys tectonic subsidence continued to be the dominant factor to control relative sea level in the active continental margin until Jurassic as the Neo-Tethys reached its upmost widening through normal faulting. Maximum flooding surface is reached in the late Permian, and Gomaniibrik carbonates overlie the Kaş Formation transgressively. Ocean in Late Permian, Cimmerian terranes parted from Pangean Gondwana (Figure 1.5). The study area was located at the northeastern passive margin of the Pangean Gondwana at the time of the opening. Continued Neo-Tethyan opening in the Late Permian caused tectonic subsidence at the passive margin of the Pangean Gondwana and triggered a rise at the regional relative sea level.

Peneplenization of the formerly aerially exposed areas and termination of terrigenous sedimentary influx towards the Neo-Tethys facilitated the carbonates of the Gomaniibrik Formation to transgressively surpass nearshore sequences of the Kaş Formation conformably. Gomaniibrik carbonates deposited at shallow-marine environment and its base corresponds to a major MFS P20 261 Ma as redefined by Gradstein and his colleagues (2004).

- **Triassic and Jurassic Sequences, Çığlı and Cudi Groups**

After the Hercynian Orogeny and contemporary onset of the Neo-Tethys opening (Figure 1.5), which began in the late early Permian and continued in the Triassic, the northeastern margin of the Pangean Gondwana turned into an active subsidence margin where Early Triassic clastic sediments and Triassic and Jurassic platform carbonates were deposited. Nevertheless, Adıyaman, Mardin and Kahta regions were located over an emerged, sub-aerially exposed landmass surrounded by Neo-Tethys waters at the time. The entire Triassic–Jurassic platform carbonates were not therefore deposited over these emerged areas, but deposited over their peripheries,

beyond their shorelines and at the lows in between them, as evidenced by the drilled exploration wells in the surrounding areas or as observed at the outcrops in Hazro area of Diyarbakır province. Although Triassic first-order global eustatic sea level was moderately stationary, tectonic subsidence associated with the temporal opening of the Neo-Tethys has caused a general increase in the relative regional sea level. Accordingly, the carbonate successions were deposited as a generally retro-gradational sequence and with onlap geometry towards the margins of emerged lands. On the other hand, the upper boundary of the Jurassic sequence is overlain by pre-Aptian unconformity surface, which overlies pre-Aptian units and merges with earlier unconformity surfaces at particular localities of the present-day SE Turkey. The pre-Aptian unconformity surface includes erosional hiatus associated with Cimmerian phase and a subsequent transgression corresponding to the Aptian maximum flooding surface, MFS K70 as defined by Sharland et al. (2004) and recalibrated by Gradstein et al. (2004).

1.3.2. Early Cretaceous to Present-Day Rocks

During the pre-Aptian Cimmerian Orogenic phase, the previously emerged lands (e.g., Mardin-Kahta high and Siirt High) had uplifted more and were subjected to further erosion till their peneplenization. The autochthonous stratigraphic units which constitute the most of the Aptian–Campanian units encountered at present-day Southeast Anatolia, Turkey were located at the north facing passive Arabian margin of the southern branch of the Neotethys Ocean (Şengör and Yılmaz, 1981; Harris et al., 1984). After the end of the Cimmerian phase, the Arabian margin experienced an extensional regime accompanying the opening of the Neotethys Ocean, which caused an uneven bathymetry with structural highs and lows (Sungurlu, 1974; Ala and Moss, 1979; Sass and Bein, 1980). The direction of the extension was roughly in the N–S; whereas the direction of topographic highs and lows was roughly E–W (Yılmaz, 1993).

AUTOCHTHONOUS LITHOSTRATIGRAPHIC UNITS OF SOUTHEAST TURKEY											
AGE			ROCK UNITS		LITHOLOGY	THICKNESS (m)	ENVIRONMENT				
PLIO-QUATERNARY			GROUP	FORMATION							
TERTIARY	MIOCENE	LOWER UPPER	SİLİVAN (Ts)	ŞELMO (Ts)			200-800	CONTINENTAL			
				LİCE (Ti)			300-800	OPEN MARINE - SLOPE			
				FIRAT (Ti)			100-200	SHALLOW PLATFORM			
		OLIGOCENE	MIDYAT (Tm)	GERMİK (Tmg)			200-1200	FLAT/SHALLOW MARINE	SUPRA-TIDAL CONTINENTAL		
	HOVA (Tmh)										
	EOCENE	KİŞİ	GAZİANTEP (Tkg)			500-1000	DEEP MARINE - SLOPE	SHALLOW PLATFORM			
			BEYEREN (Tbg)					CONTINENTAL			
	PALEOCENE	ŞİRİNAK (Ks)	ÜST GERMAY (Tkg)			500-1000		DEEP MARINE - SLOPE	SHALLOW PLATFORM		
			ALT GERMAY (Ksg)						CONTINENTAL		
	UPPER	MAASTRICHTIAN	MARDİN (Km)	BESNİ (Kbs)			500-1500		DEEP MARINE - SLOPE	SHALLOW PLATFORM	
TERRÜZEK (Kts)					CONTINENTAL						
CAMPANIAN	SANTONIAN	MARDİN (Km)	KOÇALI (Kks)			500-1500	DEEP MARINE - SLOPE	SHALLOW PLATFORM			
			KASTEL (Kks)					CONTINENTAL			
TURONIAN	CENOMANIAN	MARDİN (Km)	DOZOVA (Kds)			500-1500		DEEP MARINE - SLOPE	SHALLOW PLATFORM		
			KARABOĞAZ (Kkb)						CONTINENTAL		
ALBIAN	APTIAN	MARDİN (Km)	SAVİNDERE (Ksa)			500-1500	DEEP MARINE - SLOPE		SHALLOW PLATFORM		
			KARABABA (Kmk)						CONTINENTAL		
JURASSIC	UPPER	LOWER UPPER	ÇANDAKLI (Rc)	KARABOĞAZ (Kkb)				30-200	DEEP MARINE	SHALLOW MARINE - TIDAL FLAT	
				ORTABAĞ (Kot)				30-100		SHALLOW MARINE - TIDAL FLAT	
	UPPER	LOWER MIDDLE	ÇANDAKLI (Rc)	KARABABA (Kmk)			180	SHALLOW MARINE - TIDAL FLAT	SHALLOW MARINE - TIDAL FLAT		
				DERDERE (Kmd)			50-275		SHALLOW MARINE - TIDAL FLAT		
	UPPER	LOWER MIDDLE	ÇANDAKLI (Rc)	SABUNSUYU (Kms)			40-425	SHALLOW MARINE - TIDAL FLAT	SHALLOW MARINE - TIDAL FLAT		
				AREBAN (Kma)			50		SHALLOW MARINE - TIDAL FLAT		
	UPPER	LOWER MIDDLE	ÇANDAKLI (Rc)	LATDAĞI (JKcl)			350-750	SHALLOW MARINE - TIDAL FLAT	SHALLOW MARINE - TIDAL FLAT		
				YOLAÇAN (Jcy)			50-400		SHALLOW MARINE - TIDAL FLAT		
	UPPER	LOWER MIDDLE	ÇANDAKLI (Rc)	KOZLUCA (Rck)			50	SHALLOW MARINE - TIDAL FLAT	SHALLOW MARINE - TIDAL FLAT		
				DİNÇER (Rcd)			80		SHALLOW MARINE - TIDAL FLAT		
UPPER	LOWER MIDDLE	ÇANDAKLI (Rc)	TELHASAN (Rct)			80	SHALLOW MARINE - TIDAL FLAT	SHALLOW MARINE - TIDAL FLAT			
			ÇAMURLU (Rcp)			100-150		SHALLOW MARINE - TIDAL FLAT			
UPPER	LOWER MIDDLE	ÇANDAKLI (Rc)	GİRMELİ (Rcg)			50	SHALLOW MARINE - TIDAL FLAT	SHALLOW MARINE - TIDAL FLAT			
			BAKÜK (Rcb)			300-400		SHALLOW MARINE - TIDAL FLAT			
TRIASSIC	UPPER	LOWER MIDDLE	ÇANDAKLI (Rc)	UZUNGEÇİT (Rcz)			200-400	SHALLOW MARINE - TIDAL FLAT	SHALLOW MARINE - TIDAL FLAT		
				ULUDERE (Rcu)			100-200		SHALLOW MARINE - TIDAL FLAT		
	UPPER	LOWER MIDDLE	ÇANDAKLI (Rc)	YONCALLI (Rcy)			100-150	SHALLOW MARINE - TIDAL FLAT	SHALLOW MARINE - TIDAL FLAT		
				GOMANİBRİK (Prg)			300-400		SHALLOW MARINE - TIDAL FLAT		
	UPPER	LOWER MIDDLE	ÇANDAKLI (Rc)	KAŞ (Ptk)			30-80	SHALLOW MARINE - TIDAL FLAT	SHALLOW MARINE - TIDAL FLAT		
				KÖPRÜLÜ (DKb)			50-125		SHALLOW MARINE - TIDAL FLAT		
	UPPER	LOWER MIDDLE	ZAP (DCz)	BELEK (Cbn)			150-200	SHALLOW MARINE - TIDAL FLAT	SHALLOW MARINE - TIDAL FLAT		
				YIĞINLI (Dy)			200-300		SHALLOW MARINE - TIDAL FLAT		
	UPPER	LOWER MIDDLE	ZAP (DCz)	KAYAYOLU (Dk)			50+?	SHALLOW MARINE - TIDAL FLAT	SHALLOW MARINE - TIDAL FLAT		
				HAZRO (Dh)			100-250		SHALLOW MARINE - TIDAL FLAT		
DEVONIAN	UPPER	LOWER MIDDLE	DİYARBAKIR (Sdd)	DADAŞ (Sdd)			200-400	SHALLOW MARINE - TIDAL FLAT	SHALLOW MARINE - TIDAL FLAT		
				BEDİNAN (Ob)			500-1500		SHALLOW MARINE - TIDAL FLAT		
	UPPER	LOWER MIDDLE	HABUR (Ob)	SEYDİŞEHİR (Os)			500-1000	SHALLOW MARINE - TIDAL FLAT	SHALLOW MARINE - TIDAL FLAT		
				SOSİNK (Edso)			100-300		SHALLOW MARINE - TIDAL FLAT		
	UPPER	LOWER MIDDLE	HABUR (Ob)	KORUK (Edk)			50-200	SHALLOW MARINE - TIDAL FLAT	SHALLOW MARINE - TIDAL FLAT		
				SADAN (Eds)			200-500		SHALLOW MARINE - TIDAL FLAT		
	UPPER	LOWER MIDDLE	DERİK (Ed)	TELBEŞMİ (Edt)			500+?	SHALLOW MARINE - TIDAL FLAT	SHALLOW MARINE - TIDAL FLAT		
							500+?		SHALLOW MARINE - TIDAL FLAT		
	UPPER	LOWER MIDDLE	DERİK (Ed)				500+?	SHALLOW MARINE - TIDAL FLAT	SHALLOW MARINE - TIDAL FLAT		
							500+?		SHALLOW MARINE - TIDAL FLAT		
UPPER	LOWER MIDDLE	DERİK (Ed)				500+?	SHALLOW MARINE - TIDAL FLAT	SHALLOW MARINE - TIDAL FLAT			
						500+?		SHALLOW MARINE - TIDAL FLAT			
UPPER	LOWER MIDDLE	DERİK (Ed)				500+?	SHALLOW MARINE - TIDAL FLAT	SHALLOW MARINE - TIDAL FLAT			
						500+?		SHALLOW MARINE - TIDAL FLAT			
UPPER	LOWER MIDDLE	DERİK (Ed)				500+?	SHALLOW MARINE - TIDAL FLAT	SHALLOW MARINE - TIDAL FLAT			
						500+?		SHALLOW MARINE - TIDAL FLAT			
UPPER	LOWER MIDDLE	DERİK (Ed)				500+?	SHALLOW MARINE - TIDAL FLAT	SHALLOW MARINE - TIDAL FLAT			
						500+?		SHALLOW MARINE - TIDAL FLAT			
UPPER	LOWER MIDDLE	DERİK (Ed)				500+?	SHALLOW MARINE - TIDAL FLAT	SHALLOW MARINE - TIDAL FLAT			
						500+?		SHALLOW MARINE - TIDAL FLAT			
UPPER	LOWER MIDDLE	DERİK (Ed)				500+?	SHALLOW MARINE - TIDAL FLAT	SHALLOW MARINE - TIDAL FLAT			
						500+?		SHALLOW MARINE - TIDAL FLAT			
UPPER	LOWER MIDDLE	DERİK (Ed)				500+?	SHALLOW MARINE - TIDAL FLAT	SHALLOW MARINE - TIDAL FLAT			
						500+?		SHALLOW MARINE - TIDAL FLAT			
UPPER	LOWER MIDDLE	DERİK (Ed)				500+?	SHALLOW MARINE - TIDAL FLAT	SHALLOW MARINE - TIDAL FLAT			
						500+?		SHALLOW MARINE - TIDAL FLAT			
UPPER	LOWER MIDDLE	DERİK (Ed)				500+?	SHALLOW MARINE - TIDAL FLAT	SHALLOW MARINE - TIDAL FLAT			
						500+?		SHALLOW MARINE - TIDAL FLAT			
UPPER	LOWER MIDDLE	DERİK (Ed)				500+?	SHALLOW MARINE - TIDAL FLAT	SHALLOW MARINE - TIDAL FLAT			
						500+?		SHALLOW MARINE - TIDAL FLAT			
UPPER	LOWER MIDDLE	DERİK (Ed)				500+?	SHALLOW MARINE - TIDAL FLAT	SHALLOW MARINE - TIDAL FLAT			
						500+?		SHALLOW MARINE - TIDAL FLAT			
UPPER	LOWER MIDDLE	DERİK (Ed)				500+?	SHALLOW MARINE - TIDAL FLAT	SHALLOW MARINE - TIDAL FLAT			
						500+?		SHALLOW MARINE - TIDAL FLAT			
UPPER	LOWER MIDDLE	DERİK (Ed)				500+?	SHALLOW MARINE - TIDAL FLAT	SHALLOW MARINE - TIDAL FLAT			
						500+?		SHALLOW MARINE - TIDAL FLAT			
UPPER	LOWER MIDDLE	DERİK (Ed)				500+?	SHALLOW MARINE - TIDAL FLAT	SHALLOW MARINE - TIDAL FLAT			
						500+?		SHALLOW MARINE - TIDAL FLAT			
UPPER	LOWER MIDDLE	DERİK (Ed)				500+?	SHALLOW MARINE - TIDAL FLAT	SHALLOW MARINE - TIDAL FLAT			
						500+?		SHALLOW MARINE - TIDAL FLAT			
UPPER	LOWER MIDDLE	DERİK (Ed)				500+?	SHALLOW MARINE - TIDAL FLAT	SHALLOW MARINE - TIDAL FLAT			
						500+?		SHALLOW MARINE - TIDAL FLAT			
UPPER	LOWER MIDDLE	DERİK (Ed)				500+?	SHALLOW MARINE - TIDAL FLAT	SHALLOW MARINE - TIDAL FLAT			
						500+?		SHALLOW MARINE - TIDAL FLAT			
UPPER	LOWER MIDDLE	DERİK (Ed)				500+?	SHALLOW MARINE - TIDAL FLAT	SHALLOW MARINE - TIDAL FLAT			
						500+?		SHALLOW MARINE - TIDAL FLAT			
UPPER	LOWER MIDDLE	DERİK (Ed)				500+?	SHALLOW MARINE - TIDAL FLAT	SHALLOW MARINE - TIDAL FLAT			
						500+?		SHALLOW MARINE - TIDAL FLAT			
UPPER	LOWER MIDDLE	DERİK (Ed)				500+?	SHALLOW MARINE - TIDAL FLAT	SHALLOW MARINE - TIDAL FLAT			
						500+?		SHALLOW MARINE - TIDAL FLAT			
UPPER	LOWER MIDDLE	DERİK (Ed)				500+?	SHALLOW MARINE - TIDAL FLAT	SHALLOW MARINE - TIDAL FLAT			
						500+?		SHALLOW MARINE - TIDAL FLAT			
UPPER	LOWER MIDDLE	DERİK (Ed)				500+?	SHALLOW MARINE - TIDAL FLAT	SHALLOW MARINE - TIDAL FLAT			
						500+?		SHALLOW MARINE - TIDAL FLAT			
UPPER	LOWER MIDDLE	DERİK (Ed)				500+?	SHALLOW MARINE - TIDAL FLAT	SHALLOW MARINE - TIDAL FLAT			
						500+?		SHALLOW MARINE - TIDAL FLAT			
UPPER	LOWER MIDDLE	DERİK (Ed)				500+?	SHALLOW MARINE - TIDAL FLAT	SHALLOW MARINE - TIDAL FLAT			
						500+?		SHALLOW MARINE - TIDAL FLAT			
UPPER	LOWER MIDDLE	DERİK (Ed)				500+?	SHALLOW MARINE - TIDAL FLAT	SHALLOW MARINE - TIDAL FLAT			
						500+?		SHALLOW MARINE - TIDAL FLAT			
UPPER	LOWER MIDDLE	DERİK (Ed)				500+?	SHALLOW MARINE - TIDAL FLAT	SHALLOW MARINE - TIDAL FLAT			
						500+?		SHALLOW MARINE - TIDAL FLAT			
UPPER	LOWER MIDDLE	DERİK (Ed)				500+?	SHALLOW MARINE - TIDAL FLAT	SHALLOW MARINE - TIDAL FLAT			
						500+?		SHALLOW MARINE - TIDAL FLAT			
UPPER	LOWER MIDDLE	DERİK (Ed)				500+?	SHALLOW MARINE - TIDAL FLAT	SHALLOW MARINE - TIDAL FLAT			
						500+?		SHALLOW MARINE - TIDAL FLAT			
UPPER	LOWER MIDDLE	DERİK (Ed)				500+?	SHALLOW MARINE - TIDAL FLAT	SHALLOW MARINE - TIDAL FLAT			
						500+?		SHALLOW MARINE - TIDAL FLAT			
UPPER	LOWER MIDDLE	DERİK (Ed)				500+?	SHALLOW MARINE - TIDAL FLAT	SHALLOW MARINE - TIDAL FLAT			
						500+?		SHALLOW MARINE - TIDAL FLAT			
UPPER	LOWER MIDDLE	DERİK (Ed)				500+?	SHALLOW MARINE - TIDAL FLAT	SHALLOW MARINE - TIDAL FLAT			
						500+?		SHALLOW MARINE - TIDAL FLAT			
UPPER	LOWER MIDDLE	DERİK (Ed)				500+?	SHALLOW MARINE - TIDAL FLAT	SHALLOW MARINE - TIDAL FLAT			
						500+?		SHALLOW MARINE - TIDAL FLAT			
UPPER	LOWER MIDDLE	DERİK (Ed)				500+?	SHALLOW MARINE - TIDAL FLAT	SHALLOW MARINE - TIDAL FLAT			
						500+?		SHALLOW MARINE - TIDAL FLAT			
UPPER	LOWER MIDDLE	DERİK (Ed)				500+?	SHALLOW MARINE - TIDAL FLAT	SHALLOW MARINE - TIDAL FLAT			
						500+?		SHALLOW MARINE - TIDAL FLAT			
UPPER	LOWER MIDDLE	DERİK (Ed)				500+?	SHALLOW MARINE - TIDAL FLAT	SHALLOW MARINE - TIDAL FLAT			
						500+?		SHALLOW MARINE - TIDAL FLAT			
UPPER	LOWER MIDDLE	DERİK (Ed)				500+?	SHALLOW MARINE - TIDAL FLAT	SHALLOW MARINE - TIDAL FLAT			
						500+?		SHALLOW MARINE - TIDAL FLAT			
UPPER	LOWER MIDDLE	DERİK (Ed)				500+?	SHALLOW MARINE - TIDAL FLAT	SHALLOW MARINE - TIDAL FLAT			
						500+?		SHALLOW MARINE - TIDAL FLAT			
UPPER	LOWER MIDDLE	DERİK (Ed)				500+?	SHALLOW MARINE - TIDAL FLAT	SHALLOW MARINE - TIDAL FLAT			
						500+?		SHALLOW MARINE - TIDAL FLAT			
UPPER	LOWER MIDDLE	DERİK (Ed)				500+?	SHALLOW MARINE - TIDAL FLAT	SHALLOW MARINE - TIDAL FLAT			
						500+?		SHALLOW MARINE - TIDAL FLAT			
UPPER	LOWER MIDDLE	DERİK (Ed)				500+?	SHALLOW MARINE - TIDAL FLAT	SHALLOW MARINE - TIDAL FLAT			
						500+?		SHALLOW MARINE - TIDAL FLAT			
UPPER	LOWER MIDDLE	DERİK (Ed)				500+?	SHALLOW MARINE - TIDAL FLAT	SHALLOW MARINE - TIDAL FLAT			
						500+?		SHALLOW MARINE - TIDAL FLAT			
UPPER	LOWER MIDDLE	DERİK (Ed)									

Figure 1.2. Generalized stratigraphic section of the southeast Turkey. Taken from Dinçer et al. (1991).




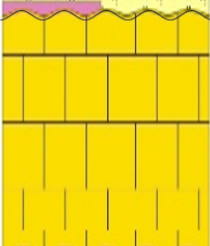
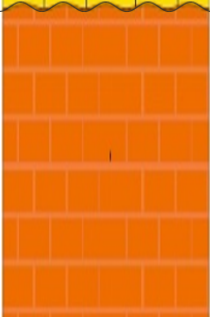
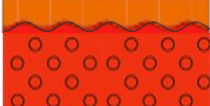
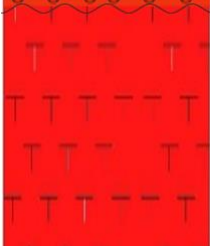
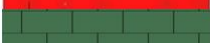

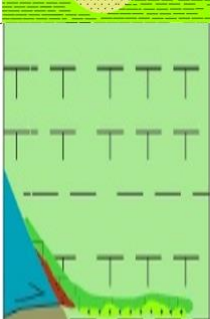


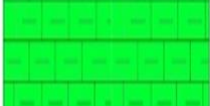
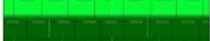


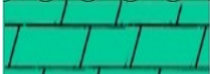
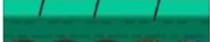

Legend	Formation Appellations	Age	Lithology
	Loose deposits	Quaternary	Soils, Alluvium & Debris
	Lahti formation	Late Miocene	Lacustrine
	Şelmo Formation	Early-late Miocene	Fluvial
	Fırat Formation	Early Miocene	Reefoidal limestone
	Hoya Formation	Late Mid-Eocene-Oligocene	Limestone
	Gercüş Formation	Early Mid Eocene	Alluvial-Fluvial coarse clastics
	Germav Formation	Paleocene-Late Early Eocene	Marl
	Besni Formation	Middle-Late Maastrichtian	Limestone
	Terbüzek Formation	Late Campanian- Early Maastrichtian	Fluvial and sub-marine fan sandstones
	Upper Kastel Formation	L. Campanian	Flysch
	Koçali-Karadut Formation	Triassic- Early Cretaceous	Allochthons
	Lower Kastel Formation	Late Campanian	Shale-Marl
	Sayındere Formation	Campanian	Argillaceous limestone
	Karaboğaz Formation	Campanian	Cherty limestone
	Karababa Formation	Turonian-Santonian	Shallow marine limestone
	Derdere Formation	Cenomanian	Fossiliferous limestone
	Sabunsuyu Formation	Albian	Dolomitic limestone
	Areban Formation	Aptian	Shallow Marine clastics
	Sosink-Sadan-Koruk-Zabuk- Telbesmi Formations	Paleozoic-Neoproterozoic	Sandstone-shale & volcanoclastics

Figure 1.3. Generalized tectono-stratigraphic section of the Adıyaman Region.

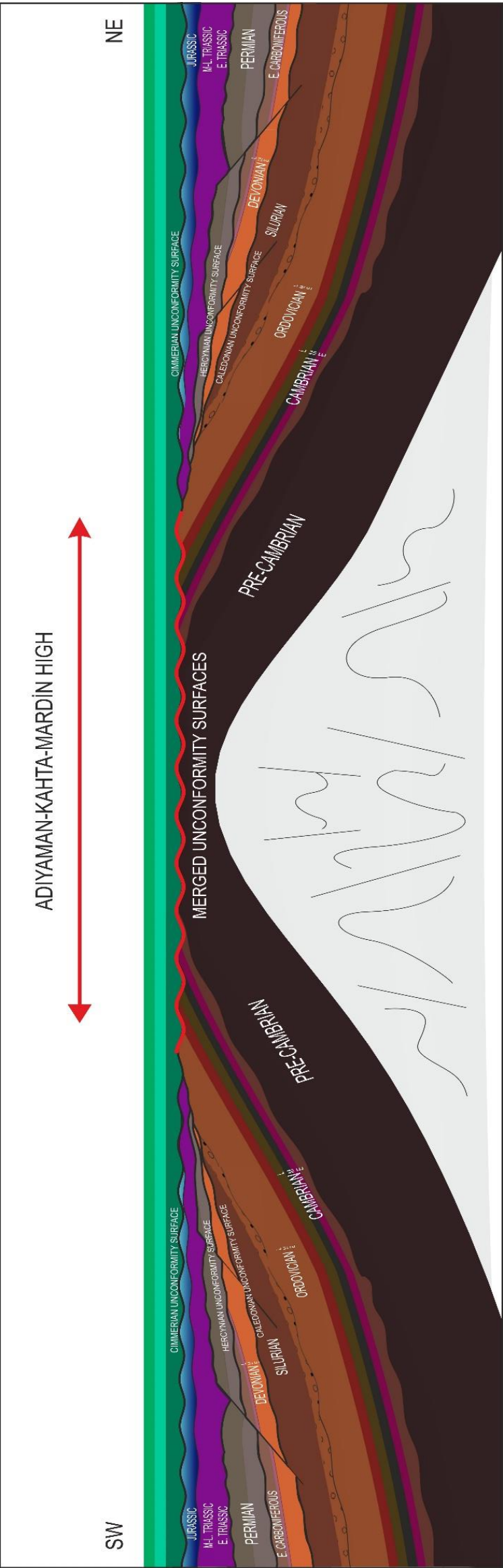


Figure 1.4. A sketch cross-section illustrating stratigraphy and boundary relationships among several rock units in the Adiyaman-Mardin-Kahta paleo-high, which controlled hiatus and erosion events in the study area at the center of the SE Turkey.

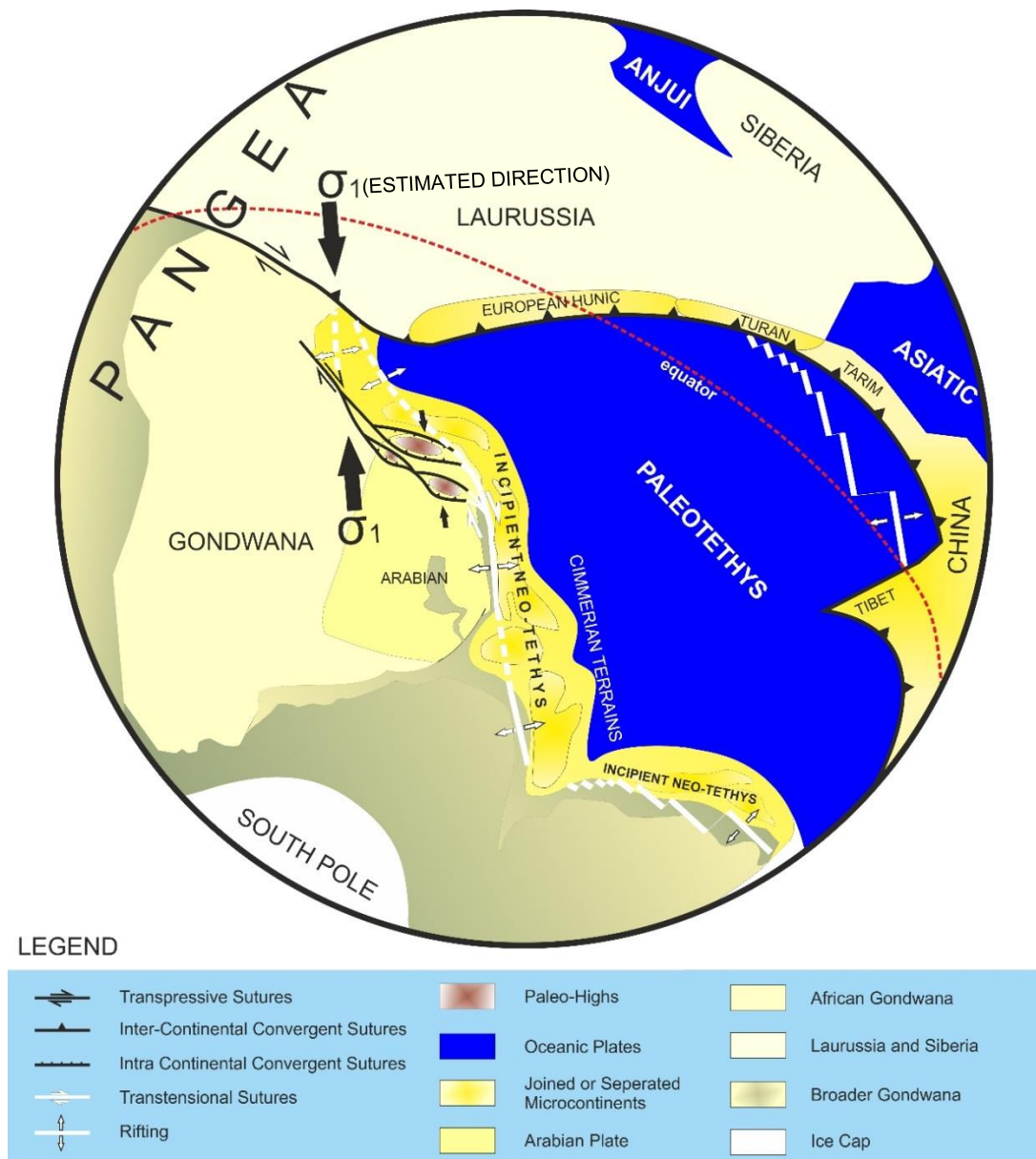


Figure 1.5. Late Early Permian palinspatic reconstruction map modified from Stampfli and Borel (2002). The modifications include the illustrations for the incipient faults of Neo-Tethys rifts as accommodative structures to lengthening related to progressive shortening caused by the collision between Gondwana and Laurussia and for *the formation of sporadic uplifts located at the Northern Arabian Plate. The uplifts and the rifts are considered coeval and genetically related. It is notable that the incipient rifting faults strike sub-parallel to the compression direction. Detailed explanation is in text.

As a consequence of both tectonic depression and a long-term sea-level rise occurred in the Jurassic and Early Cretaceous periods (Haq, 2017), specifically during the Aptian and Campanian, the passive Arabian margin were completely submerged and constituted the basement for the deposition of the Cretaceous platform carbonates as known as the Mardin Group (Görür et al., 1991). The Mardin Group consists of four formations named as Areban Formation, Sabunsuyu Formation, Derdere Formation and Karababa Formation. Derdere and Karababa formations comprise organic-rich intervals whose presence is prerequisite for the petroleum system in the study area.

- **Aptian Areban Formation**

Aptian shallow-marine, coastal or continental clastics of the Areban Formation were transgressively deposited over upper Cambrian clastics of the Sosink Formation in the studied Adıyaman region. Depending upon the number and thickness of the preserved pre-Aptian successions around the regional highs (e.g., the Mardin-Kahta High), the Areban Formation also overlies the Paleozoic, Triassic and Jurassic units in the southeast Turkey (Aksu, R., Dilci, G.M., 2013; *unpublished report in the TPAO archive*). Areban Formation is defined either as fluvial coarse clastics filling the basement lows in the Derik county of Mardin or as shallow-marine sandstone-shale alternations at the wells in the east of the city of Kahramanmaraş (Gül et al., 2014).

- **Albian Sabunsuyu Formation**

During a long period of tectonic quiescence that prevailed from Aptian to Campanian stages, an uninterrupted carbonate sequence was deposited at the northeastern passive margin of the Arabian Plate surrounded by the Neo-Tethys Ocean. The Sabunsuyu Formation is the earliest of the Cretaceous carbonates and defined as deposits of shallow-marine, submarine slope or ebb-tidal environments throughout the shallow platform of the Arabian Plates' northern margin (Alsharhan and Nairn, 1997). The Sabunsuyu Formation is sub-divided into four members; they

are described as bioclastic packstone, lime-mudstone, bioclastic grainstone and dolomitized cherty wackestone (Cater and Gillicrist, 1994).

- **Cenomanian Derdere Formation**

The Derdere Formation was deposited in shelf and intra-shelf basins along the passive margin of the Arabian Plate (Horstink, 1971; Uygur and Aydemir, 1988; Çelikdemir et al., 1991; Ziegler, 2001). During the early Mid Cretaceous relative sea-level changes cause shallowing-upward depositional cycles (Görür et al., 1987) which paves the way for subaerial exposures and unconformity surfaces within the Mardin Group. The Derdere Formation unconformably overlies the Sabunsuyu Formation as indicated by erosion and karstification features at the cores taken from the top of the Sabunsuyu Formation (Wagner and Pehlivanlı, 1985; Çelikdemir et al., 1991; Mülayim, 2013). The Derdere Formation is composed of three sub-units: dolomites, dolomitic limestone and Bioclastic limestone from bottom to top (Mülayim, 2015).

- **Turonian-Santonian Karababa Formation**

The Karababa Formation is mainly consists of carbonates. It unconformably overlies the Derdere Formation and is unconformably overlain by Karaboğaz Formation (Mülayim, 2015). The formation is subdivided into three members as Karababa A, B and C from its lowest to its upmost, respectively. The lowermost member, the Karababa-A is a very fine-grained, organic-rich pelagic limy mudstone (Alsharhan and Nairn, 1997, Mülayim, 2015). It is a good seal for the underlying Derdere Formation and a good source rock for the entire petroleum system of the region. The Karababa-B member is described by a gradual grain size coarsening with respect to the Karababa-A. The uppermost member, the Karababa-C is a partly dolomitized bioclastic limestone.

- **Campanian Karaboğaz Formation**

Karaboğaz Formation unconformably overlies the Karababa Formation. The unconformity is associated with erosion. It consists of heavily chertified limestone. Chertification is associated with burial compaction (Alsharhan and Nairn, 1997). The formation is considered to have developed during a transgression (Cater and Gillcrist, 1994).

- **Campanian Sayındere Formation**

The Sayındere Formation conformably rest on the Karaboğazı Formation. The formation consists mainly of a thin- to intermediate-bedded argillaceous limestone (Figure 1.6). The Sayındere Formation was deposited over a block-faulted basement (e.g., Robertson et al., 2016) with undulated geometry which controls its thickness and local depositional facies. The thickness of the Sayındere Formation ranges from 100 m to 250 m. The formation is subdivided as lower, middle and upper members (Özkaya et al., 2019). The lower member of the Sayındere Formation comprises organic-rich carbonate mudstones and bioclastic limestones at basement lows and highs with varying thicknesses of 10 to 25 m. The middle member consists of clayey bioclastic limestone, which is about 25 to 50 m thick and the upper member comprises pelagic biomicrites which ranging in thickness from 50 to 180 m (Özkaya et al., 2019). Until the discovery of the Şambayat NFR Oilfield in 2008, the Sayındere Formation had long been considered as a cap rock in the regional petroleum system. The discovery of the Şambayat NFR, however, proved that it is a fracture prone unit, and it provides a considerable amount of accommodation space and connectivity for the reservoir fluids.

The Sayındere Formation, as the uppermost carbonate member of the Cretaceous carbonate sequence, could reside within the petroleum column when basins are faulted or fractured. Its more brittle and weaker response to compressive stresses – in comparison with its overlying and underlying units, respectively- causes it to be the uppermost provider of accommodation space in the petroleum column and causes its fabric to be severely fractured (see Section 9.2. for more detail). Because of its fracture proneness and relatively low primary porosity, for this

research, I choose the Sayındere Formation as the focused sedimentary unit to investigate separate contribution of the faults and fractures to the reservoir properties in a petroleum system.

Within the petroleum system of the Adıyaman region, particularly from Cenomanian to Campanian stages, the successive carbonate sequences (Derdere, Karababa, Karaboğaz and Sayındere formations) contain organic carbon-rich intervals. Since the oldest petroleum source rocks preserved in the Adıyaman surroundings are only the aforementioned intervals, the petroleum system in the region is directly dependent on their presence.



Figure 1.6. An outcrop view of thin and intermediate layers of argillaceous limestones of the Sayındere Formation from the northern flank of the Gemrik Anticline, south Adıyaman, southeast Turkey.

In the study area, covering both Şambayat oilfield and the Gemrik Anticline where the Sayındere Formation is either buried or crops out, Cretaceous source rocks were deposited uninterruptedly as evidenced by successions intercepted at the

exploration and production wells drilled in the region besides the outcrop observations.

The Sayındere Formation constitutes the youngest member of the Cretaceous platform carbonate succession whose deposition was ceased by the influx of detrital clays to its depositional environment. The source of the detrital clays is the exposed sections of the ophiolites drifted onto the Arabian passive, hyperextended plate margin during the demise process of the Neo-Tethys.

- **Campanian Kastel or Bozova Formation**

The Kastel or Bozova Formation conformably overlies the Sayındere Formation and commences with a progradational sequence. The late Campanian–Maastrichtian clastic units are respectively denoted as Kastel or Bozova formations at proximal or distal locations with respect to closeness of their depositional area from the approximately ESE–WNW-trending obduction front between ophiolitic units and hyperextended crust of the Arabian Plate (Figure 1.7). The Kastel Formation can be examined as lower and upper members. The Lower member of the Kastel Formation is represented by a chronostratigraphic interval that was overlain by advancements’ detachments surface of the oceanic allochthones.

The detachment surface corresponding the boundary between the Lower and Upper Kastel formations reside at approximately above the first 200 meters of the sediments deposited over the Sayındere Formation (Figure 1.3 and 1.8). These lithological units also form a more or less impermeable cover as cap rocks of the regional petroleum system with their relatively ductile rheology as will be discussed in the Chapter 9.

- **Maastrichtian Terbüzek Formation**

Terbüzek Formation is composed of a fluvio-deltaic conglomerate, pebblestone, sandstone and mudstone alternation that was deposited over the exposed stratum of the obducted oceanic crust over the Arabian Plate and throughout the obduction front within the Arabian foreland basin. Terbüzek Formation unconformably overlies the Kastel Formation with its cutting and filling downwardly scraping channels.

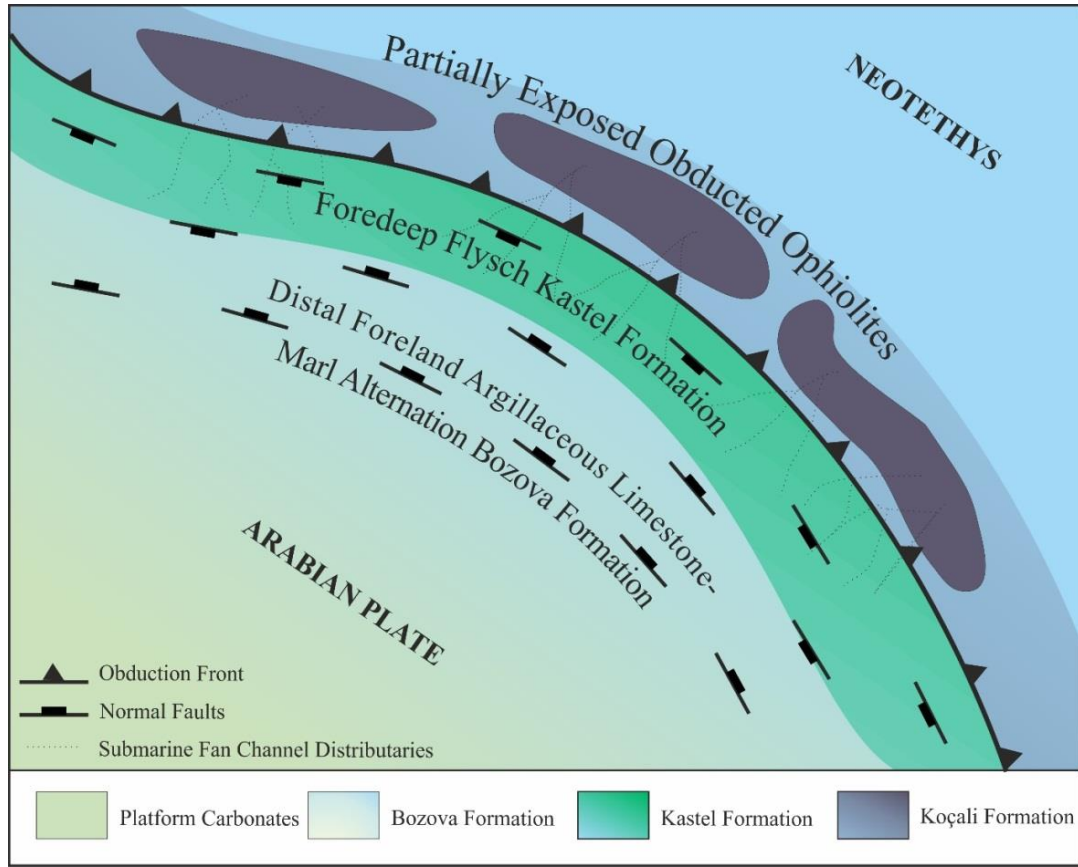


Figure 1.7. Southward advancement of the intra-oceanic Neo-Tethys subduction front over the submerged hyperextension of the Arabian continental plate in the Campanian-Maastrichtian stage has resulted in obduction and sub-aerial exposure of ophiolitic nappes of Koçali Formation. This phenomenon corresponds to the cessation of the deposition of Cretaceous platform carbonates. The normal faults, which had been developed before obduction in the foreland, controlled the thickness of the Sayındere, Kastel and Bozova formations.

The thickness of the formation ranges from 80 m to 400 m. The sub-aerial exposure of the ophiolitic units that create the source for the detrital materials of the Terbüzek Formation are triggered by both the thickening of the collision front via imbricated thrust sheet formation and the accompanying major eustatic sea-level fall 73 MA (Haq, 2014).

The fluvial dominated deltaic, marine extension of the Terbüzek Formation are observed within amalgamated distributary channels and delta lobes of fine

pebblestone and coarse sandstone fining-upward sequence deposits. At some rare localities away from “*cut and fill*” channels and delta lobes, the transition between Kastel Formation and Terbüzek Formation could become conformable.

- **Maastrichtian Besni Formation**

Besni Formation is a bioclastic limestone that conformably overlies the Terbüzek Formation. The sedimentary sequence that comprises the Terbüzek Formation ends with a transgression corresponding to the Maastrichtian maximum flooding surface maximum flooding surface MFS K180 as defined by Sharland et al. (2004) and recalibrated by Gradstein et al. (2004).

A subsequent regression gave rise for the deposition of the bioclastic limestones of Besni Formation. The Besni Formation generally resides on mudstones or marine shales of the uppermost part of the Terbüzek Formation with a carbonate mudstone facies.

- **Paleocene-Late Early Eocene Germav Formation**

Germav Formation is marl, argillaceous limestone and mudstone alternation that conformably overlies the Besni Formation. The stage of the deposition of the Germav Formation corresponds to a prolonged time interval of regional tectonic quiescence. Therefore, temporal influx of coarse-grained, detrital materials to the southern Neo-Tethys is extremely limited. Absence of intra-formational accommodation space within Germav Formation makes it a perfect cap rock for the petroleum system. Regional field observations also confirm that at the localities where the Germav Formation is fully preserved, it is very unlikely to see oil seepages at the surface.

- **Early-Mid Eocene Gercüş Formation**

Gercüş Formation consists of alluvial and fluvial deposits of conglomerates, pebblestone and sandstone alternations. It is a syn-tectonic sedimentary unit deposited in the northernmost Arabian foreland along the imbricated reverse fault zone between Arabian and Anatolian Plates. This reverse faulting regime is

associated with the collision between thickened hyperextension Arabian Plate and the Anatolian Plate, and thus the Middle Alpine Orogeny occurred in the Mid-Eocene. The Gercüş Formation resides on the uplifted and eroded parts of different pre-Mid-Eocene formations unconformably depending upon the severity of the local erosion. In most cases, the Gercüş Formation unconformably overlies scraped and thinned section of the Germav Formation.

- **Late Mid-Eocene–Oligocene Hoya Formation**

Hoya Formation is a reefoidal, bioclastic and muddy limestone alternation. Hoya Formation transgressively overlies pre-Mid-Eocene units ranging from allochthones to upper parts of the Germav Formation either together with or without the Gercüş Formation beneath it. The formation is the earliest sedimentary units which postdates Middle Alpine Orogeny. A fully preserved section of the Hoya Formation could be as thick as 500 m. The formation can be investigated in three horizontal subdivisions as lower, middle and upper parts. The lower part of the formation is reefoidal limestone which is rich in nummulites and reef building organism (e.g. corals). The middle part mostly consists of fossiliferous carbonate mudstone with secondary chertified inclusions. The upper part is a bioclastic limestone.

- **Early Miocene Fırat Formation**

Fırat Formation is a reefal limestone whose main reef building components are mostly echinids, bivalves and foraminiferas. The formation is the latest carbonate units deposited over the demising Neo-Tethys Ocean. As the continued convergence caused the uplift of the northern Arabian Plate since Mid-Eocene, the ocean was completely demised after the deposition of the Fırat Formation and its time equivalents. Talus facies of the Fırat Formation is named as the Cingife Member and it is composed of well-sorted carbonate grains that were deposited over energetic submarine slopes of the reef buildups.

- **Early Late Miocene Şelmo Formation**

Şelmo Formation is the first continental deposits after the closure of the Neo-Tethys Ocean. The formation consists of fluvial conglomerates and coarse

sediments. Since the development of the Şelmo Formation is coeval with the initiation of the Mid-Miocene strike-slip faults, the Şelmo Formation exhibits thicker deposits at the pull-apart basins and escaping blocks between conjugate strike-slip faults and non-deposition over the push-up structures throughout the study area.

- **Late Miocene Lahti Formation**

Lahti Formation consists of the lacustrine varves and fluvial, fine-grained sandstone and millstone alternations. The Formation was deposited within the depression domains on the northernmost part of the Arabian Plate. It is only deformed by contemporaneously active faults and it mostly blankets the older faults and makes the detection of them impossible by field surveys.

1.4. Regional Tectonics

The study area of this research located at northeastern margin of the Gondwana, which is the present days' northern margin of the Arabian Plate, underwent reverse, normal and strike-slip faulting alternately in its geological history.

The most prominent global tectonic events affected the region were the Caledonian Orogeny, the Hercynian Orogeny, opening of Neo-Tethys, Early Alpine (Cimmerian) Orogeny, Middle Alpine (Eocene) and Late Alpine (Himalayan) Orogeny. The Hercynian Orogeny, which is the result of the collision of Gondwana and Laurussia in Middle Carboniferous to form the supercontinent of Pangaea (Stocklin and Setudehnia 1972; Berberian and King, 1981), created transpressional strike-slip faults and reverse faults along (coupled) Gondwana (Figure 1.5) and caused laterally 100s of kilometers extensive blocks (e.g., Mardin-Kahta and Siirt paleo-highs in present-day SE Anatolia) to uplift (Wender et al., 1998; Al-Husseini, 2004; Ruban et al., 2007).

Progressive compression triggered the formation of a mid-ocean ridge and thus opening of the Neo-Tethys during Mid Permian–Triassic period (Stampfli and Borel, 2002) in a semi-perpendicular direction to the collisional front between Gondwana and Laurussia and sub-parallel to the maximum principal stress axis of its age (Figure 1.5). Therefore, beginning with the Mid-Permian, the northern margin of the

Pangean-Gondwana turned into a subsiding passive margin over which some emerged lands are located (Figure 1.5). Pre-Cambrian and Paleozoic basement units were eroded whereas Triassic and Jurassic sequences were partly eroded or not deposited due to multiple separate and merged unconformity surfaces associated with major orogenic events, glaciation periods and/or sea-level falls particularly over the aforementioned emerged lands in the study area. The Mardin-Kahta High, which is the most prominent one of these reliefs, constitutes structural basement of the study area of this research and shows tectonic activity contemporaneous with Caledonian, Hercynian and Cimmerian orogenic phases.

Early Cretaceous unconformity surface, which lay beneath Aptian continental sequence called Areban Formation, overlays entire pre-Aptian units and cuts or merges with older unconformity surfaces.

1.5. Methodology

Since most of the natural fractures are products of poly-axial natural stresses, which exceed brittle failure strengths of rocks at depths, and the focused mechanical stratigraphic unit of this research is the Sayindere Formation, the following workflow was adopted.

The fracture attributes such as frequency, spacing, aperture and filling material within the Sayindere Formation were investigated, quantified and mapped at the localities where the formation is outcropped.

To perform a deductive approach, to see what kind of a poly-axial stress field could induce a brittle deformation on the Sayindere Formation; strength parameters of the Sayindere Formation such as uniaxial compressive strength, tensile strength and poly-axial compressive strength were tested, calibrated and documented within this research. Besides, the in-situ stress magnitudes and their extrapolated gradient curves versus depth were measured from varying depths of different wells within this research since the natural stresses pave the way for break-down of the Sayindere Formation.

After the strength and stress measurements were made, it was preliminarily interpreted that the failure conditions of the Sayindere Formation were not reached

under the influence of far-field stress. This has led the direction of this research to investigate local stress increases around the stress accumulating faults. In this context, I adopted the slip-tendency and stress perturbation concepts into this research to determine and anticipate orientation interval of mechanically active faults under constructed poly-axial stress conditions as well as how the stress field (e.g., stress magnitudes and orientations) changes around those faults.

At last, I integrated mechanical stratigraphy concept, and investigated the varying heights of reservoir fluids in the petroleum system of the study area. Brittle-ductile or stronger-weaker behaviors of naturally fractured reservoirs and supposedly cover rocks were investigated. Migration mechanism of the hydrocarbon through cover rocks into their intra-formational clastic channels were evaluated by studying their capacity to withstand fractures that act as conduits for the reservoir fluids.

(1) Map Revision, Georeferenced Data Collection and Fracture Analysis

The regional geological and structural map with a developed geometrical accuracy is revised to put forward true geometrical and tectonic models of major structures in the study area, as the first step of this research. While mapping in the field, georeferenced fracture and subsidiary slip surface data (e.g., aperture, spacing, dip, azimuth, density, anisotropic fracture porosity and the descriptions of the filling materials like asphaltite, calcite or quartzite) was collected to later value them for interpretation, classification and comparison purposes. The fracture data was collected by utilizing geo-referencing Strike and Dip® freeware installed on smart phone device equipped with GPS functionality and accelerometer sensor and geologist compass. Dips® software of Rocscience Inc. was used to interpret the data by drawing plots, and Petrel® software of Schlumberger to make interpretations and integrations of data from different sources.

Characteristics of fracture zones were investigated by considering their locations around faults and folds by sampling fractures at certain structural stations. Outcrop data were collected at the northern periphery of Bozova right-lateral strike-slip fault, which demarcates southern border of Gemrik and Karababa highs and Kuyulu depression area, where the fault damage zone structures are well exposed within

outcrops of the Sayindere Formation. Determination of outcrop data collection sites, the structural stations, has been done by classifying the locations according to their structural positions with respect to the fault segments of varying geometries causing contractional, extensional or pure shear stress states or with respect to the folds.

The subsurface fracture and fault data has been derived from the seismic surveys and wells operated by Turkish Petroleum at the northern proximity of Samsat dextral strike-slip fault where Şambayat fractured reservoir oilfield has been exploited for years.

(2) Determination of Strength of the Sayindere Formation and Comparison of Its Strength with Its Underlying Units

To put forward distinctive properties of the Sayindere Formation, which is the only proven fractured reservoir host rock of the region, sub-cored cylindrical samples were taken from the cores of the wells penetrated the Sayindere Formation buried at Şambayat oilfield and then rock deformation tests (e.g., uniaxial and triaxial compression and shear wave velocity tests) on those samples were performed. This step was considered as required for the anticipation of the conditions of the incipience of individual fractures.

Besides, some empirical equations that give approximate unconfined compressional strength of the rocks, which derived based on sonic wave slowness (Δt) log readings, were used within this research to make comparison between the strengths of the Sayindere Formation and some other brittle units underlying it.

(3) In-Situ Stress Measurements

In order to identify the natural stress conditions under which the Sayindere Formation had been deformed during oil expulsion period that most probably coincide with neo-tectonic faulting regime stage, an in-situ stress and hydrostatic pressure profile were constructed via measurements using borehole breakout geometries, leak-off test and drilling stem test data collected from different depths at the wells drilled in the region. And then, those measurements are combined to

generate gradients for each principal natural stresses and this is done by extrapolating stress magnitudes for every depth in the region.

(4) Failure Criterion under Natural, Poly-Axial or True Tri-Axial Stress Conditions

Due to unavailability of relevant equipment to simulate true triaxial conditions in which all the principal stresses are in different magnitudes ($\sigma_1 > \sigma_2 > \sigma_3$), the laboratory experiments were conducted under untrue triaxial stress conditions ($\sigma_1 > \sigma_2 = \sigma_3 = P_c$). Singh et al (2011) proposed a modified Mohr-Coulomb Failure Criterion that takes into account the significance of differing magnitudes of intermediate principal stress, σ_2 . In this study, the aforementioned criterion was used in order to estimate extreme or intermediate failure conditions that may occur under natural, decoupling stress environments.

(5) Stress Perturbation Analysis

Since the measured in-situ stresses seem mostly at sub-critical levels to form incipient fractures within the Sayindere intact rock unit, local stress perturbations (e.g., magnifications and drops) are also needed to be investigated in the region. In order to understand how the natural stress conditions for the failure of the Sayindere rock unit is reached, the results of analogue models of De Joussineau *et al.* (2003) was incorporated as will be discussed in Chapter 4. Since the natural remote stress magnitudes, which was measured as a part of the methodology of this research, have found not sufficient to create an incipient fracture on an intact portion of the Sayindere Formation (whose intact strength parameters were defined as another part of our methodology), it is straightforward to think that the natural stresses intensify at places where fracture swarms are present. The stress intensification and decoupling phenomena can be defined by local direction and magnitude measurements of natural stresses around stress accumulating faults especially. The stress perturbation analysis was therefore incorporated to explain localization and existence of fracture swarm sweet spots by comparing fracture data acquired from

the field and the wells. Drilling induced fracture and borehole breakout orientations are also used to detect local stress orientation changes.

(6) Slip Tendency Analysis

The orientations of the optimally oriented and tent-to-slip faults and fractures are determined by orientation and relative magnitudes of natural principal stresses. Accordingly, in order to determine orientation interval of mechanically and hydraulically active existing faults and fault damage zones, slip tendency analyses, based upon contemporary stress field data, were implemented to the delineated fault and fracture population of the Şambayat oilfield for the first time in the region. This was done by using the Mohr Plotter® software, designed by Richard W. Allmendinger © 2014–2015 based on certain structural geology algorithms as indicated in Allmendinger *et al.* (2012).

(7) Seismic Delineation of Hydraulically Active Faults, Subsidiary Faults and Fracture Swarm Sweet Spots

By implementing an enhanced edge detection workflow, including use of dip guided structural smoothing, variance and ant-tracking seismic volume attributes in Petrel® software, almost entire population of existing discontinuities within the Şambayat NFR seismic survey converted into depth domain, was delineated. Based on the slip-tendency analyses with a decent awareness on the spatial stress field perturbations, discontinuities were classified and color coded into 5 distinct categories from red to blue based on their percentile slip tendency intervals. Then, location of wells was compared with respect to tent-to-slip faults and production performances of each well to evaluate possible correlation between those faults and hydraulically active fractures penetrated in the wells.

(8) Mechanical Stratigraphy and Trapping

In order to explain hydrostatic balance between oil and water and accordingly the changing height of the oil column in potentially fractured reservoirs in the study area, fracture proneness and fracture durableness qualities of different lithological

units, especially supposedly cover rocks of the Sayindere Formation, namely the Kastel and Bozova formations, were discussed and compared.

The Reservoir fluids within initially porous and permeable rocks are trapped within structural highs in courtesy of impermeable overlying layers with sufficient sealing capacity if the structures have four-way closure geometry. In some instances reservoir properties e.g. porosity and permeability of reservoir rocks deteriorates laterally and the fluids are confined within such stratigraphic traps. In the fractures reservoirs within initially non-porous and non-permeable rock unit, walls and lengths of the fractures traps the reservoir fluids. The aperture and length of the fractures can be determined by vertically changing mechanical properties of each member of a regional stratigraphic section.

Besides the previous works, backgrounds and highlighted methodological steps touched upon for the whole research in this introductory chapter, there will be literature summary and methodologies addressed with specific explanation in relevant chapters. In this thesis, because of the confidentiality requirements originated from the terms of the Turkish petroleum law, the georeferenced positions of the seismic sections and exact names of the drilled wells, whose data were shared by the Turkish Petroleum to support this research, were not intentionally disclosed.

This thesis is composed of 8 Chapters including;

- (1) Introduction,
- (2) Geological Structures and Petroleum System of the Study Area
- (3) Analyses and Interpretation of Fractures,
- (4) Sayindere Rock Unit's Strength and Poly-Axial Stress Conditions Required for Its Failure,
- (5) In-Situ Stress Estimations and Measurements,
- (6) Slip Tendency Analyses,
- (7) Slip Tendency Analysis: Delineation and Filtering of Conductive Faults on 3D Seismic Survey
- (8) Discussion and Conclusion

CHAPTER 2

GEOLOGICAL STRUCTURES AND PETROLEUM SYSTEM OF THE STUDY AREA

The field survey of this research has been performed in the south of the Adıyaman province, along the southwestern cost of the Atatürk Dam (Figure 1.1). In this area geological and structural map has been revised and elaborated with more frequent geological, structural and kinematic data collections. Previously unmapped members of some geological formations and facies changes have also been included in the revised map. The geometrical and geographic accuracy of the major faults, (e.g., Bozova Fault), and their subsidiary structures are achieved by detailed evaluation and interpretation of structural data collection at several structural stations.

Since the study area of this research is too close to the center of the Mardin-Kahta High, most of the elements of the regional stratigraphy pertaining to pre-Aptian sequences are missing both in the wells and outcrops. Starting with the Aptian stage (125.0 ± 1.0 Ma to 113.0 ± 1.0 Ma; Late Cretaceous), a relatively tectonically quiescent period has allowed deposition of the latest Cretaceous to Middle Eocene successions uninterruptedly. On other hand, Middle Alpine (Middle Eocene) and Late Alpine (Miocene to present) orogenic events and consequent deformational phases (e.g., folding, reverse and strike-slip faulting) caused localized erosion of these successions in greater parts of the study area and whole SE Anatolia.

In terms of the regional petroleum system, mostly preserved latest Early and Late Cretaceous carbonate sequences include high organic carbon potential. For example, lower sequences of the Cenomanian Derdere Formation and Turonian–Santonian Karababa Formation form the well-documented Cretaceous carbonates with source rock properties. Nevertheless, Silurian Dadaş Formation (Figure 1.2) is the only preserved and the most prominent pre-Aptian source rock

unit which is absent in the study area since it is located outside a circular erosional area at the center of the Mardin-Kahta high at present-day SE Turkey (Figure 1.4). Paleozoic petroleum system therefore most likely lacks a preserved source rock element in narrower geographical extent around the study area (in the Adıyaman province). On the other hand, above the pre-Aptian unconformity, Cretaceous and Paleogene successions include each elements of a fully-fledged petroleum system that can be penetrated in all wells drilled in the Adıyaman province. From Aptian to Campanian, a tectonically quiescent period prevailed on the passive margin continental shelf environment of the Arabian Plate that also includes present-day Southeast Turkey.

Although the closure of the southern branch of the Neo-Tethys began in the late Jurassic (Brew, 2001), consequent distant subduction of the oceanic continuation of the Arabian Plate did not immediately induce compressional tectonics on its northern margin where the Cretaceous platform carbonates were deposited. In the late Campanian–Maastrichtian, along with a southward advancement of the subduction front, the oceanic crust was drifted onto the carbonate platform (Figure 1.7). Submerged portion of the Arabian Plates' hyperextension over which the Cretaceous carbonate platform deposited was thicker and more resistive against convergence than the oceanic plate. The exposed reliefs of the ophiolites formed the source area for interfacial, syn-obductional, shaly clastic sediments with sandstone and pebblestone intercalations of the Lower Kastel Formation; these clastic constituents were used as detachment surface for surpassing ophiolites during obduction.

The sub-aerial exposure of the ophiolites is also responsible for the cessation of the deposition platform carbonates by becoming an emerged source for clastic materials. The last products of the Cretaceous platform carbonates were therefore represented by the Campanian argillaceous limestones of the Sayındere Formation. These limestones has formed the focus of fracture analyses in the extent of this research because of its fracturing prone nature and its proven capacity to form naturally fractured reservoirs (NFRs). The Sayındere Formation is buried at about 1800–2200 m depths within the only proven fractured reservoir of the Adıyaman

province, known as Şambayat oilfield whereas it is exposed on the Gemrik and Karababa anticlines demarcated by the Bozova Fault (Figure 1.1c).

Because of the existence of proven and productive fractured reservoir within the Sayındere Formation at the Şambayat oilfield, the Adıyaman Province is considered as a novel area to study effects of faults on occurrence, distribution and extent of fracture corridors. More, the relation of this oilfield with its delimiting regional structures has not yet well documented and well understood as well. This necessitates more satisfactory explanations concerning preferred/potential locations of open fractures and their productive fracture porosities within the oilfield. Isolated contribution of fractures on reservoir qualities could be sufficiently and measurably observed within the Sayındere Formation since it has primarily negligible porosity and permeability.

Northern Passive margin of the Arabian Plate was experiencing an extensional regime from the Permo–Triassic opening of the Neo-Tethys to the onset of its closure in late Campanian–Maastrichtian (Şengör & Yılmaz, 1981; Kazmin, 2002; Barrier et al., 2014; Fontaine et al., 1989). As a result of this extension, the northern Arabian Platform was faulted by mostly north-dipping normal faults that accompanied the deposition of platform carbonates in a thickness zoned fashion; the basement geometry has controlled the thickness of the deposited carbonates in a way that asymmetric grabens has served as depocenters with thicker depositional products whereas horst shoulders as erosional surfaces or thinner deposition areas (Ala and Moss, 1979; Guiraud and Bosworth, 1999).

During the closure, foredeep and forebulge structures formed at the northern edge of the Arabian Plate were subjected to southward displacement as the obduction front moves southward. This also resulted in reactivation of pre-existing faults since they were influenced tensile and compressive forces cyclically as the aforementioned flexural structures displaced through their hosting domains. Therefore depositional and erosional processes were influenced by both fault reactivations and forebulge and foredeep displacement. Deposition of the Sayındere Formation was therefore controlled by these phenomena.

The Sayındere Formation was the last depositional unit on this undulated and faulted basement geometry before a tectonic quiescence period and subsequent compression tectonics began. Along with the onset of sub-aerial exposure of ophiolites and contribution of a major eustatic sea-level fall at 73 Ma (Haq, 2014) during Late Campanian–Early Maastrichtian time interval, significant amount of sediments was shredded from exposed ophiolites, fluxed into the down-flexed fore-deep in front of the advancing nappes that flattened the foreland. This event has increased the amount of clay minerals, such as chlorite, deposited in the basin, which has eventually suffocated and impeded the deposition of platform carbonates and whose latest member, the Sayındere Formation.

Influx of detrital materials from the exposed reliefs also resulted in deposition of sandstone and pebblestone intercalations within the overlying Lower Kastel Formation (Figure 2.1). The regional progradational sequence along with a subsequent period of aggradation represented by sandstone or pebblestone deposits (Figure 2.1) at the lower part of the Kastel Formation provide additional accommodation pore volume for the reservoir fluids including hydrocarbons in the presence of proper structures, such as faults and fractures, that create conduits for the fluids as will be discussed in the Chapter 9.2.

Continued influx of detrital, clay-rich clastic sediments gave rise the formation of a flysch succession, namely Upper Kastel Formation (Figure 1.3). Intra-oceanic subduction and gravitational pull of the subducting oceanic plate was dominant at the early stages of the closure since the thickness of the subducting oceanic plate was not sufficient to create a notable amount of resistance to the gravity pull of itself. Because of that gravity pull, a North to South extensional regime has prevailed at the Arabian Plate side of the subduction front, and formed WNW–ESE-trending horst-and-graben structures (Figure 1.7). Accordingly, WNW–ESE-oriented major grabens (such as Euphrates Graben) or the major hosts (e.g., Bozova high) were the products of this extensional regime along the northern margin of the Arabian Plate. Along with the onset of obduction and compression associated with the continued convergence, inversion of these normal faults took place in the late Maastrichtian, Mid Eocene, Oligocene and Early Miocene.

As the subduction front translated over Arabian Plate's northerly-dipping margin, and overlapped the zones where crustal thickness of the Arabian Plate is much higher, Arabian Plate became more resistive to convergence and particularly to subduction. Obduction of northerly ophiolites and accompanying compression has therefore commenced by Late Maastrichtian in the study area. There have been, however, several compressional events with intervening tectonic quiescence periods. As the convergence turned into a resistive movement and ultimate collision, the margin has been heavily subjected to a compressional tectonic regime which caused formation of reverse and oblique-slip faults since late Maastrichtian with some intervening quiescence periods.

This research mainly concentrates on Paleogene and Neogene events with a special emphasis on Miocene phases (tectonic events) since lithological unit (a.k.a. the Sayindere Formation) of interest is either younger than or was synchronously deposited with the aforementioned extensional tectonic phases. Based on field investigations, the relations between some major compressional phases and their post-tectonic sedimentary units have been clearly revealed in this study as it is briefly stated below (Figure 2.2 and Table 2.1):

(1) In the Permian–Triassic Boundary, along with the opening of the Neo-Tethys, at the northeastern passive margin of the Pangean-Gondwana, an extensional tectonic regime began prevailing via stair-stepped normal faults (Figure 1.4) mostly dipping towards newly forming Neo-Tethys.

(2) In the early Campanian, the gravity pull originated from the subducting slab of the intra-oceanic subduction within the Neo-Tethys Ocean generated an extensional tectonics over the northern margin of the Arabian Plate. The extensional stress orientation was about NNE to SSW, and consequent horst-and-graben structures lies perpendicular to the extensional stress direction. Accordingly, WNW–ESE-oriented major asymmetric grabens formed.

(3) In the Late Campanian–Maastrichtian, with the complete emplacement of ophiolitic nappes, a tectonic quiescence period began.

(4) In the Mid Eocene, reverse faulting phase prevailed and high-angle imbricated reverse faults at the north of the study area have developed (Figure 2.2).

(5) In Oligo–Miocene, WNW–ESE-oriented relict normal faults located at the study area were reactivated as reverse faults and similarly trending folds have formed; most of these folds are also demarcated by these reverse faults.

(6) In Mid-Miocene, some of the WNW–ESE-oriented reactivated reverse faults have undergone reactivation as oblique strike-slip faults that may indicate a counterclockwise reorientation of the greatest principal stress direction (S_H) or a slight change in tectonic regime by stress permutation of the least horizontal stress (S_h) with vertical stress (S_V) in the smallness order according to theory of faulting of Anderson (1942/1951).

(7) In the Late Miocene to present, WNW–ESE-oriented oblique strike-slip faults continued to work and new conjugate strike-slip faults systems with NE–SW and NW–SE orientations have developed.

Briefly, northern margin of the Arabian tectonic plate was normal faulted during opening and early closure of the Neo-Tethys (Figures 1.5 and 1.7), then reverse faulted (Figure 2.2) on the verge of the full closure. Later on, along with possible reorientation of S_H direction, or tectonic regime change from reverse faulting to strike-slip faulting due to the drop of S_h , those faults were re-activated in oblique strike-slip faulting and some Late Miocene faults and fault systems have formed (Figure 2.2). Because of this sophisticated nature of the northern Arabian Plate, stress field perturbations around the faults are expected to have occurred. During their activity periods, these faults impeded accumulation of stress within locations aligned perpendicular to their surfaces and concentrated the stress tensors at the localities close to its growing tips and walls.

Accordingly the current and former tips and locked portions of the faults are critical to assess stress field perturbations and to estimate associated fracture orientations during structural analyses within the frame of present research. Hydrocarbon potential of those fractures must however be assessed by considering the timing of oil expulsion from the source rocks in the basin and timing of hydraulic activity of themselves as will be addressed in the Discussion Chapter.

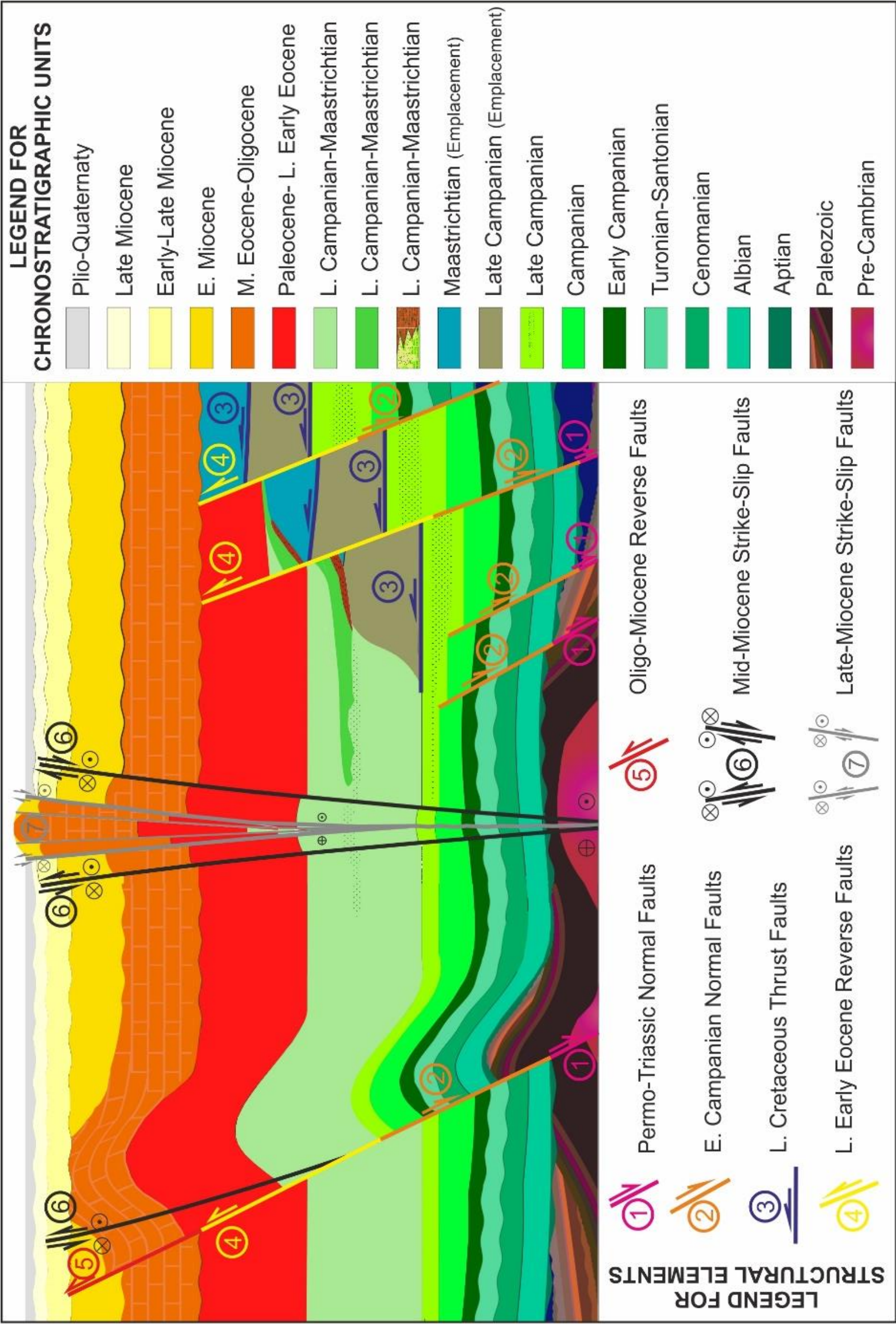


Figure 2-2 Tectonic faulting regime alternations affected the study area were numbered by their chronological orders. Number 1 and 2 represent the normal faulting regimes of Permo-Triassic and Cretaceous. Number 3 represents latest Cretaceous nappe style emplacements of the allochthonous units in the region and they were associated with the closure of the Neo-Tethys. Number 4 faults, with their high-angle geometry, represent Mid Eocene compressional regime which mostly cause reverse reactivation of older normal fault surfaces. Number 5 type faults, which induce reverse reactivation on number 1 and/or 2 type normal faults, represent the diachronism of the compression due to ongoing collision of Arabian and Eurasia plates. Number 6 and 7 represent neo-tectonic, strike-slip faulting regime in the study area.

Table 2.1. Timing and description of events causing compressional tectonic phases prevailed in the northwestern Arabian Plate after the deposition of Campanian Sayındere Formation. Characteristics and the most common appellations of sedimentary units attributable to these tectonic phases are also given.

Compressional Phase	Events	Post-Tectonic Deposits
Late Campanian – Maastrichtian	Imbrication of ophiolitic nappes accompanied by a global eustatic sea-level fall (73 Ma)	Fluvial deposits of the Terbüzek Formation and its temporal equivalent submarine clastics
Mid Eocene	Formation of high-angle imbricated reverse faults	Alluvial & fluvial deposits of the Gercüş Formation
Late Eocene – Oligocene – Miocene	Reverse faulting, inversion of type-1 and/or type-2 normal faults & formation of WNW–ESE-oriented folds	Post-tectonic alluvial-fluvial deposits of the Şelmo Formation
Mid Miocene	Strike-slip reactivation of WNW–ESE-oriented thrusts with some obliquity & right-lateral sense of shear because of prevalence of strike-slip regime by a drop in S_h .	Fluvial (e.g., conglomerates) and locally lacustrine (e.g., varves and chalks) deposits of the Lahti Formation at the depression areas along strike-slip fault strands.
Late Miocene	Formation of youngest conjugate strike-slip faults systems & E–W-oriented thrust faults & thrust related folds	Pliocene-Quaternary continental deposits (e.g. alluvial, fluvial and debris deposits)

2.1. Faults

In order to examine localization and hydraulic activity of minor conductive discontinuities, such as fractures or subsidiary faults, the activity of the major structures responsible for their formation should be investigated. In the northern Arabian Plate, from the Paleozoic to Quaternary, many tectonic faulting phases with their predominant faulting characteristics have been documented. Inherited faults

from preceding tectonic regimes predominate (determine) propagation geometry of the subsequently formed younger faults in the northern Arabian Plate. For instance, the normal-faulted substratum of the Permo–Triassic margin of the Arabian Plate (Figures 1.4 and 1.5) seems to have a major influence on relatively high-angle geometry of the reverse faults that formed succeeding compressive tectonic regimes such as Mid-Eocene (Figure 2.2 and Table 2.1). Ultimately, the steeply-dipping character of the older reverse faults seems to have determined the path where the strike-slip fault strands follow when propagating during the contemporarily prevailing strike-slip faulting regime over the Northern Arabian Plate since Mid-Miocene. Therefore, geological history and tectonic activity of the regional faults and the depositional processes associated with them are critical aspects to study existing conductive fault related- fractures which serves as conduits for reservoir fluids.

2.1.1. Normal Faults

Normal faults are mostly buried or overprinted structures along the northern margin of the Arabian Plate and they are mostly observed at seismic sections (Figure 2.3). Nevertheless, they have a determining role on controlling the geometry and kinematics of the faults of different subsequent tectonic regimes. There are two different types of normal faults are identified and their characteristics will be summarized below.

2.1.1.1. Type-1 Paleozoic Normal Faults

The oldest normal faults in the region are denoted as type 1 (Figure 2.2); they are interpreted as coevals of the late early Permian incipience and Triassic spreading of the Neo-Tethys oceanic rifting. And calculating the subsequent reorientations of the Arabian Plate, those normal faults strike roughly ESE–WNW direction and dip ~ 60-80° NNE or SSW in the present day configuration. Type-1 normal faults are mostly terminated upward by pre-Aptian unconformity surfaces – erosional surfaces of early and late Cimmerian orogenic events – and are overlain by transgressive Aptian sequence of the Araban Formation.

2.1.1.2. Type-2 Early Campanian Normal Faults

In the Early Campanian, during the early closure of the Neo-Tethys, type-1 normal faults sporadically underwent reactivation and paved the way for the formation of type-2 normal faults (Figure 2.2). Type-2 normal faults are terminated upward by upper Kastel Formation that marks temporal tectonic quiescence and cessation of further advancements of the allochthonous units during late Campanian. Type-1 and type-2 normal faults are distinguished by their relationships with different rock units in the stratigraphy. For instance, at some areas, type-2 normal faults form independently in the absence of any type-1 fault, whereas at some other areas type-1 normal faults do not undergo a normal faulting reactivation and terminate against Aptian horizons (Figure 2.2).

Incipience of Bozova Fault as a Normal Fault

The WNW–ESE-trending Bozova Fault extends from Adıyaman Province in the west to Şanlıurfa Province in the east. The fault formed as a syn-sedimentary normal fault in the Early Campanian (Figure 1.1). This inference is evidenced by sporadically missing sequences of the pre-Late Campanian units (e.g., Karababa, Karaboğaz and Sayındere formations) on its footwall (horst shoulder) in the south and thickened and continuous deposition of the same units on its hanging wall in the north. This erosion was facilitated by a major eustatic sea-level fall leading those horst shoulders to form sub-aerial exposures in the Early Campanian (73 Ma) (Haq, 2014). The Bozova Fault underwent inversion with reverse and strike-slip faulting regimes in the later geological epochs and this will be explained in the following sections.

In addition to the aforementioned Paleozoic and Late Campanian normal faults, there are also small-scale local normal faults formed during later stages of compressional tectonics prevail in the studied region.

Dilatational Riedel-type normal faults that demarcates Akçakale Graben, small-scale normal faults at extensional step-overs of major strike-slip faults (Figure

2.4a) and sheared tension joints oriented perpendicular to axis of Besni Anticline (Figure 2.4b) can be given as best examples of this type of normal faults.

2.1.2. Thrust Faults

Thrust faults are the slip surfaces with reverse sense of shear and with a dip angle smaller than 45°; these structures are denoted as Type-3 in this study (Figure 2.2). The oldest traceable thrust faults are associated with tectonic transport of the ophiolitic and oceanic allochthonous units of the Koçali and Karadut formations onto the northern Arabian Plate during the Late Campanian–Maastrichtian. The shaley and marly upper section of the late Campanian lower Kastel Formation was used as a detachment surface along which allochthonous units were tectonically translated and override the northern margin of the Arabian Plate.

Koçali Formation is mainly composed of a *mélange* of tectonically complex ophiolitic units of the Neo-Tethys Ocean (Rigo de Righi and Cortesini, 1964; Robertson et al., 2007) while the Karadut Formation is described as flydsch (Sungurlu, 1974; Perinçek, 1979) and deep-sea carbonate turbidite deposits (Altiner, 1989), which originally formed later than the Koçali Formation. Koçali and Karadut thrust sheets form a thrust duplex and are being drifted onto the northern Arabian Plate together during late Campanian–Maastrichtian. The activity of these thrust faults seem to have terminated since Maastrichtian in the Adıyaman Province. The movement of the thrust duplex might have occurred diachronically because its activity period has varied from place to place within the full Neo-Tethys closure front.

At the localities both thrust sheets were accompanied by generation of thick tectonic units; the overburden force these tectonic units create caused northern extension of the Arabian Plate to make a down-flexed movement. This down-flexed movement has caused targeted traditional petroleum reservoirs in the region (e.g. Derdere, Karababa and Sayındere formations) to be buried deeper as well as the overlying Kastel Formation to deposit thicker.

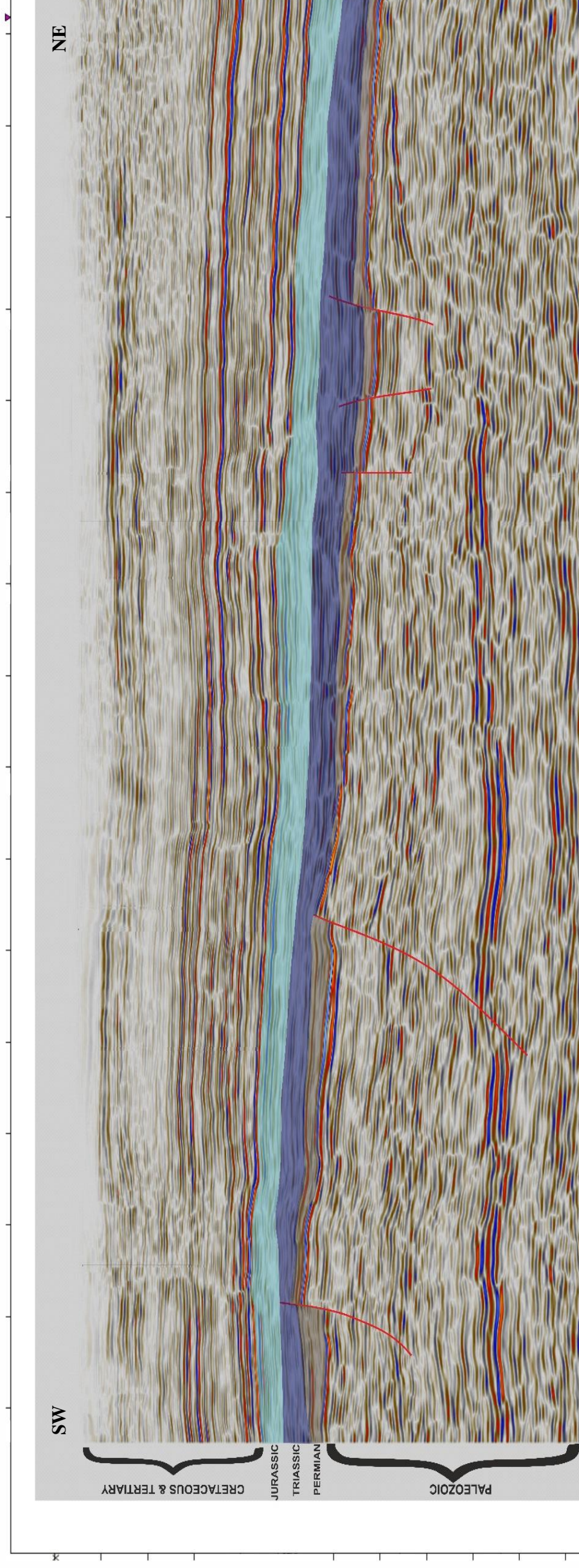


Figure 2.3. A seismic section taken from SE Turkey illustrating the type-1 normal faults affected pre-Jurassic rock units, which are interpreted as associated with the opening of Neo-Tethys, during late Early Permian and Jurassic time interval. Interpretation of the section is done during this study. The seismic section is from the TPAO company database.



Figure 2.4. (a) Dilatational Riedel-type slip surfaces deform Upper Kastel Formation's sandstone-shale alternations at the extensional quadrant of the Bozova Fault near Besni County of Adiyaman Province. (b) A sheared tensional fault formed at the steeply-dipping northern edge of the E–W-elongated Besni Anticline striking perpendicular to the axis of the anticline. It deforms steeply positioned bioclastic limestones of Maastrichtian Besni Formation.

2.1.3. Reverse Faults

Reverse faults are slip surfaces with a reverse sense of shear and with a dip angle greater than 45° ; they are, based on their relative age, denoted as type-4 and type-5, respectively (Figure 2.2). They are interpreted as products of compressional tectonic settings, which have discretely prevailed in the study area from Paleozoic to the present day with some intervening extensional tectonism and/or tectonically quiescent periods. Paleozoic reverse faults are however difficult to detect, delineate or trace since (i) they were deeply buried, located at a time interval where seismic resolution is insufficient and/or (ii) they mostly might have been overprinted by late Paleozoic ‘type-1’ normal faults. Though Paleozoic orogenic processes and their erosional implications are well known as evidenced by missing sequences penetrated along the wells drilled in the study area, the mechanism(s) of paleo-high formation during Paleozoic is still contentious and forms subject of further research. Reverse faults might have developed by reactivation of the pre-existing steeply-dipping older normal faults as it is observed in some oilfields of the Adıyaman (Figure 2.5). At places where the pre-existing normal fault surfaces’ frictional strengths are lower than the brittle failure strength of the intact medium, incipience of new faults are hindered (cf. Kelly et al., 1999). In the case of northern Arabian Plate, there are steeply dipping Late Paleozoic and Early Campanian normal faults (type-1 and type-2) (60° and 85° , respectively) (Figure 2.5). Thus, when mechanical transformation of the tectonic regime from normal faulting to reverse faulting may occur, at the localities where steeply-dipping normal faults exist, the normal faults tend to reactivate first as reverse structures (cf. Williams et al., 1989; Kelly et al., 1999). The reactivation of the Bozova normal fault can be explained in this framework.

2.1.3.1. Reverse Faulting Reactivation of the Bozova Normal Fault

As convergence between Arabia and Eurasia continued, steeply-dipping imbricated reverse faults have developed along the collision front located at the northernmost margin of the Arabian Plate (cf. Fouad, 2010). These reverse faults are considered as the mostly contributing elements of the Middle Alpine mountain building processes. Nevertheless, except the Bozova Fault, the reverse faults did not

become as widespread, dominant and intense in the foreland area where the studied region of this research is located.

The Bozova Fault interpreted as product of reverse faulting reactivation in Mid Eocene Oligocene period demarcates pre-Mid-Eocene units deformed along anticlines (e.g., Gemrik and Karababa anticlines) (Figure 1.1c). The uplifts, demarcated by these reverse faults analogous and genetically related to the Bozova Fault, were partly eroded as evidenced by both missing upper sections of pre-Mid-Eocene units and existence of post-tectonic continental conglomerates of the Gercüş Formation (Figure 1.3), deposited along an arced zone proximal to the collision front.

Either these reverse faults or variably eroded pre-Mid Eocene units are overlain by Mid-Eocene reefal limestones of the Hoya Formation, intermittently along with a basal conglomerate horizon (Table 2.1)

2.1.4. Strike-Slip Faults

In the Mid-Miocene, approximately 13 to 11 Ma ago, along with the formation of North Anatolian and East Anatolian faults, which are responsible for the escape tectonics of Anatolia (Şengör et al., 2005), the strike-slip faulting regime has become prevailing along the northern Arabian foreland portion of the indented convergence zone between African and Eurasian plates since the lateral containment decreased and consequently magnitudes of the E–W acting regional lateral stress (S_h) have dropped below the magnitudes of the vertical stress (S_v).

The Anderson's theory of faulting (Anderson, 1942/1951) expresses that compressive regimes that favor strike-slip faulting require principal stresses to be arranged in a fashion where vertical stress (S_v) exceeds the least horizontal stress (S_h). In a similar way, to be surpassed by the most horizontal stress (S_H) in magnitude, the strike-slip faulting settings ($S_H \geq S_v \geq S_h$) has been predominant in the study area since the Mid-Miocene.

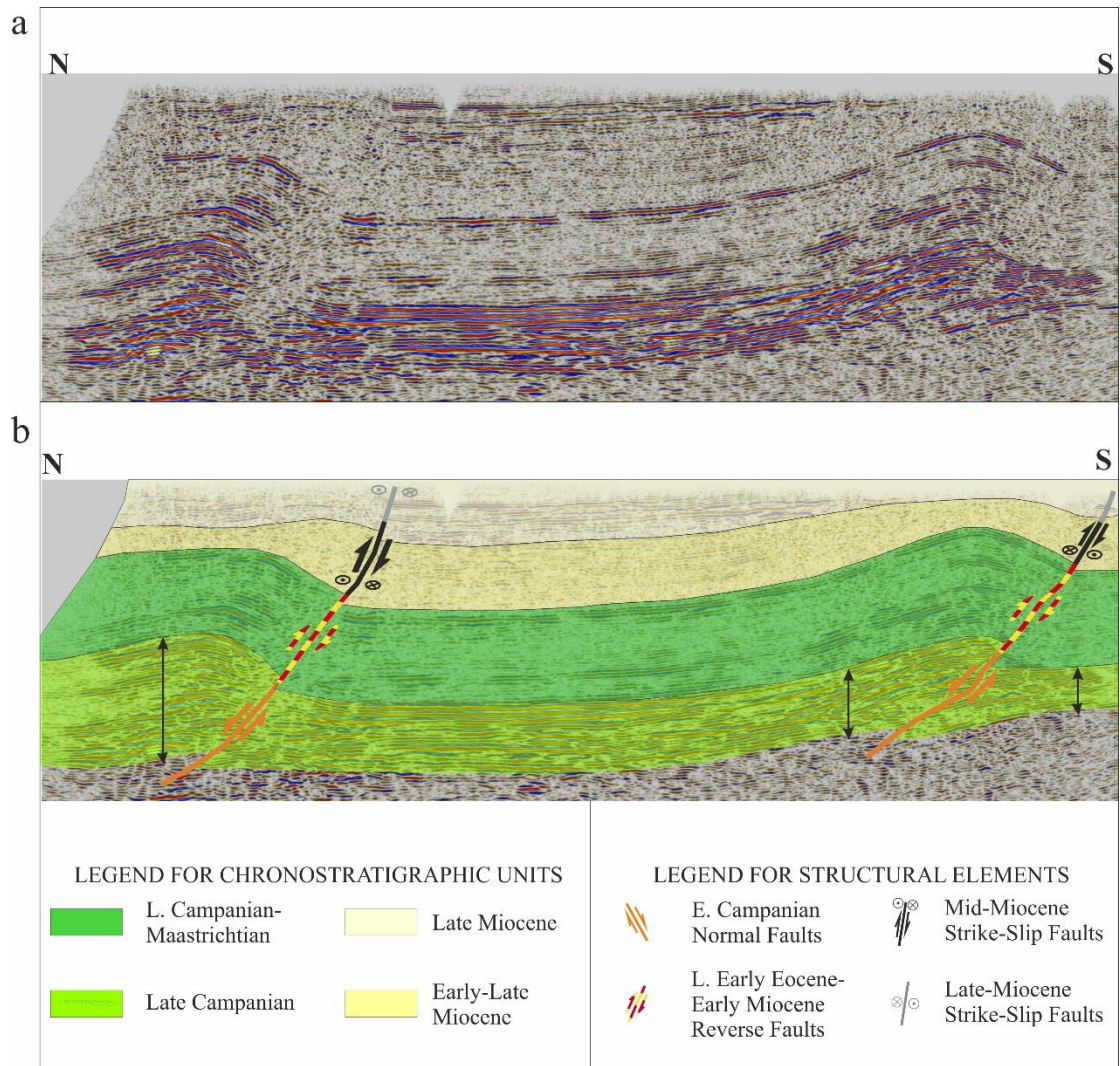


Figure 2.5. A seismic section from Adıyaman Province illustrating reverse faults, which are considered to have used normal fault remnants of earlier extensional tectonic regimes. Perpendicular arrows show normal faulting related thickening in the Late Campanian sedimentary units at the hanging walls of the downward extension of the reverse faults. The aspect ratio of the seismic images is 1:1.

Strike-slip fault activity manifested itself either with the strike-slip reactivation of pre-existing reverse faults (e.g., Bozova Fault) or incipience of new slip surfaces (e.g., Kemerli Fault). The Transfer faults are inferred with their character of juxtaposing growth sedimentary packages and condensed sections, which were deposited over fore-deep and fore-bulge locations on the foreland of the Arabian Plate, respectively. None of them are, however, located either close to subsurface or field survey sites of this research; for this reason these structures will not be elaborated in this study.

The angle between the strikes of the reactivated strike-slip faults and the regional maximum principal stress axis (which is roughly N to S) is larger than 50° and it is not in strong compliance with the anticipated angles (~30°) with respect to the greatest principal stress axis for the Andersonian faults (Anderson, 1942/1951). The reason of reactivation is interpreted as that the frictional strengths of those pre-existing faults were lesser than the initial failure strength of the intact medium.

Still, orientations of segment tying faults bifurcated from general shear zone direction of reactivated right-lateral strike-slip faults or newly formed left-lateral strike-slip faults are in decent compliance with the geometrical rules of the Andersonian strike-slip faults which is anticipated to make 30° from the regional most compressive principal stress direction (SH).

2.1.4.1. Strike-Slip Reactivation of the Bozova Fault

The WNW–ESE-trending right-lateral Bozova Fault extends from (Bozova County) Adıyaman Province in the west to Şanlıurfa Province in the east and forms very good example of a reactivated strike-slip fault in the study area. The fault demarcates Gemrik Anticline, Kuyulu low and Karababa uplift in the Adıyaman Province.

The evidence documented in this thesis suggests that the Bozova Fault is of late Miocene age; it is interpreted as reactivated Early–Mid Miocene high-angle reverse fault, which have reactivated a late Campanian ESE–WNW-trending north-dipping normal fault. Uninterrupted and thickened deposition of the late Cretaceous units on the northern block of the Bozova Fault, and the missing sequences of the pre-Maastrichtian units as a result of horst shoulder erosion over the southern block of the Bozova Fault indicates the syn-sedimentary normal faulting in the late Campanian.

The Bozova Fault zone extends to east-southeast, merges with and overprints Oligocene to Early–Mid-Miocene high-angle reverse faults, which demarcates fault propagation folds of Gemrik Anticline and Karababa High (Figures 1.1, 2.6 and 2.7). On the other hand, Bozova Fault seems to have reactivated as either predominantly

reverse fault or fractures associated with the main fault or with the folds formed leaning against this fault.

The latest (youngest) reactivation of the Bozova Fault deforms Tortonian conglomerates of the Şelmo Formation and is overlain by Pliocene lacustrine sediments of the Lahti Formation along the Bozova strike-slip fault strand. A quasilinear arrangement of exhumed, deformed blocks of steeply-dipping Şelmo Formation within the structures of isolated lenses associated with strike-slip faulting was encountered (Figure 2.8). This phenomenon also helped to distinguish the Bozova Fault's trace along with other indicators, such as polished surfaces and juxtaposed rock units that were not in contact when they first formed (Figures 2.9 and 2.10).

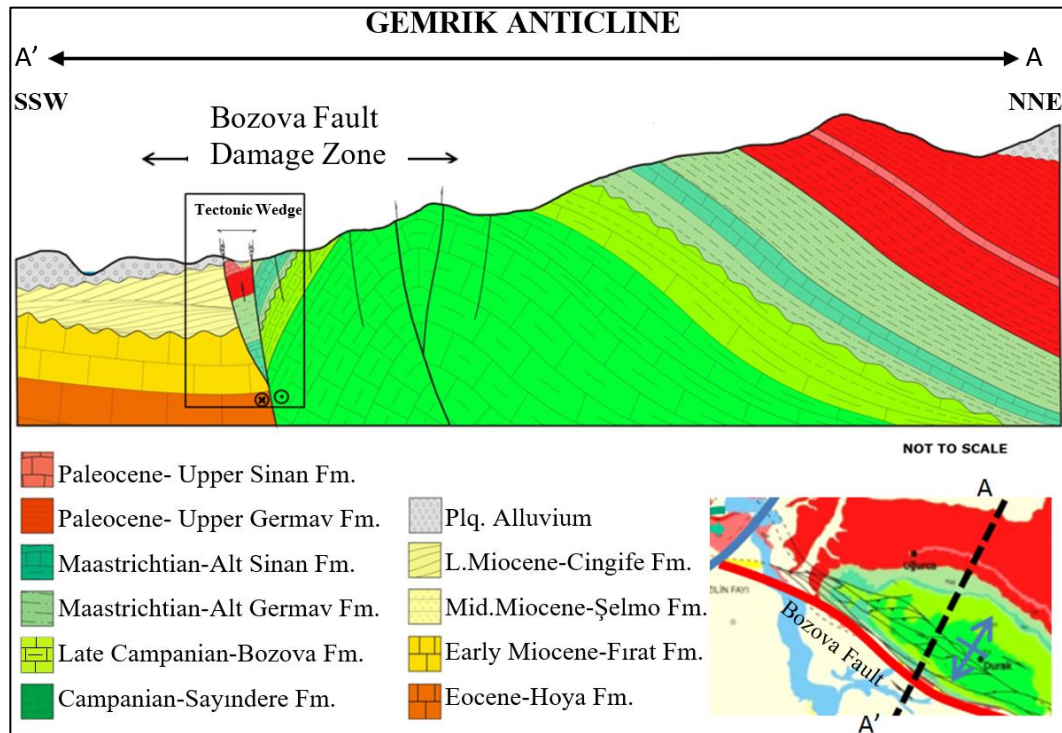


Figure 2.6. Sketch cross section illustrating relationship between the Bozova Fault and the Gemrik Anticline. In the framed area, labelled as 'tectonic wedge', fractured hinge line of the anticline was lately faulted by subsidiary strands of the Bozova Fault. Deformed yellow colored Mid. Miocene units are shown on the top of the wedge structure. See inset map for line of the section.

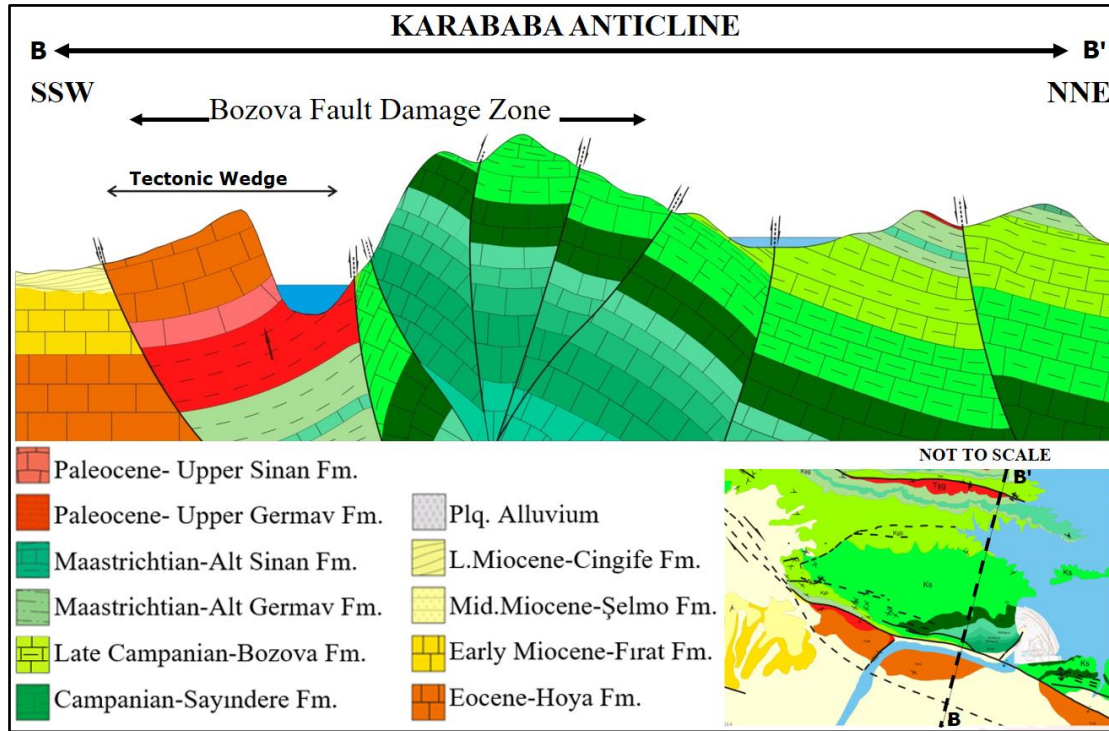


Figure 2.7. Sketch cross section illustrating relationship between the Bozova Fault and the Karababa Anticline. In the area that is labelled as ‘tectonic wedge’, deformed yellow colored Mid. Miocene units are shown on the top of the wedge structure. The transpressional reactivation of the Bozova Fault in this domain seems more dominant since the positive flower structure is more distinctive. See inset map for line of the section.

The positive rake angles measured on the striated slip surfaces proves transpressional character of the strike slip activity of the Bozova Fault (Figure 2.10).

2.1.4.1. Kemerli Strike-Slip Fault

Kemerli Fault (Figure 1.1) with its late Miocene incipience, is an example of the latest left-lateral strike-slip faults formed in the study area. It strikes nearly SW to NE with about 45–50° azimuthal interval. The Kemerli Fault and its damage zone are partly affective in the field survey site. The fault forms an overlapped damage zone with the right-lateral strike-slip Bozova Fault in the western part of the field survey site as will be elaborated in the Chapter 3.

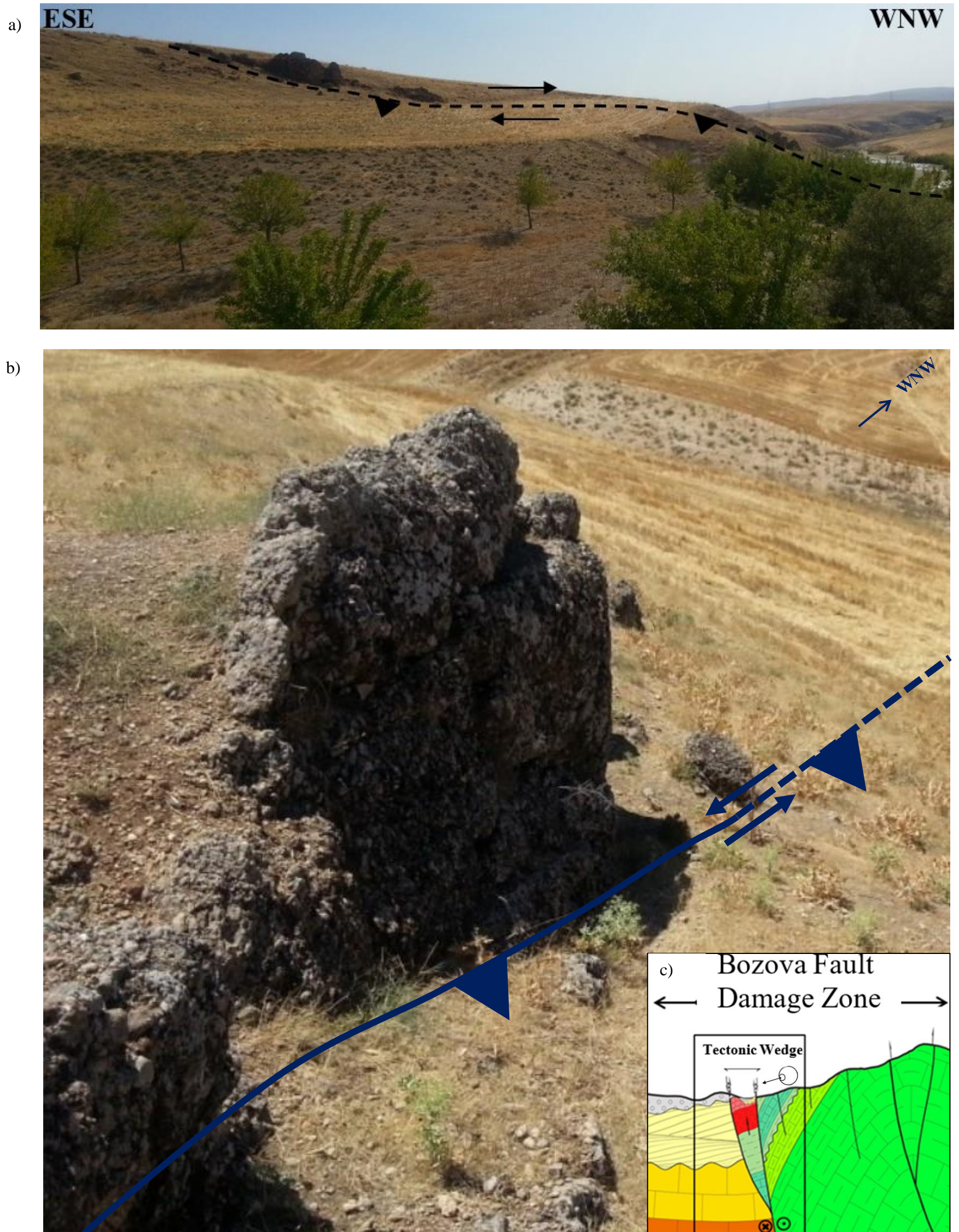
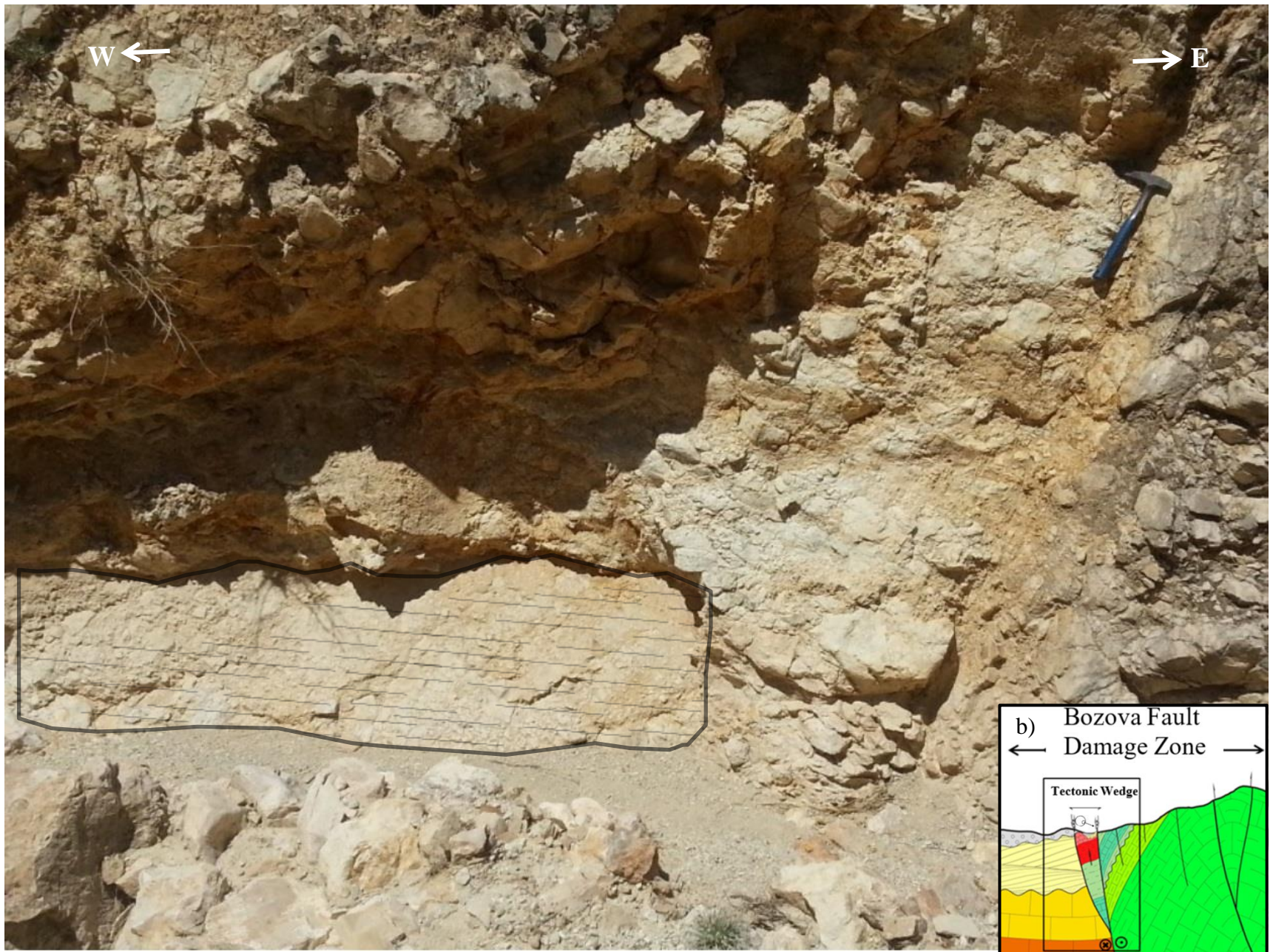


Figure 2.8. (a, b) Quasilinear arrangement of exhumed, deformed blocks of steeply dipping Şelmo Formation within the structures of isolated lenses associated with strike-slip movement of the Bozova Fault. c) Inset cross section cropped from the Figure 2.6. The Observer symbol represents the point of view where the pictures were taken from.

a)



c)



Figure 2.9. (a,c) Brecciated materials and polished subsidiary slip surfaces from the fault damage zone of the Bozova Fault. The lineations represent direction of observed striations. **b)** Inset cross section cropped from the Figure 2.6. The Observer symbol represents the point of view where the pictures were taken from. 30 cm long geologist hammer were placed as scale.



Figure 2.10. A close-up view from a striated slip surface along the trace of the Bozova Fault, proving its transpressional character with positive rake angles between 00° and 45° .

2.2. Folds

In the North Arabian foreland, most of the south-vergent unless symmetric folds have a roughly W–E strike, which is perpendicular to the compression axis since the Mid-Miocene. Symmetric folds mostly form as features of positive flower structures along innate, type-6 and type-7 strike-slip fault strands (Figure 2.2), whose strikes are sub-parallel to general shear zone directions of the strike-slip faults which they owe their formation. Asymmetric folds form as related to, and demarcated by, once reversely functioned faults (e.g., type-4 and type-5 faults; Figure 2.2) even if those faults mostly have undergone strike-slip and oblique reactivation with reverse component lately. Roughly WNW–ESE strike of the regional asymmetric folds is compatible with the compression direction of post Mid-Eocene, pre-Mid Miocene interval. Such asymmetric folds can be classified as moderately or steeply inclined folds according to the geometrical classification of folds proposed by Fleuty (1964).

2.2.1. Asymmetric Folds

The asymmetric folds located in the study area are the ones whose axial surfaces moderately or steeply dip to the NNE and verge to the SSW. They are demarcated by once reversely worked WNW–ESE-striking, steeply NNE-dipping faults.

- **Gemrik and Karababa Asymmetric Folds**

Bozova and Samsat faults, which bounds outcropped and buried data collection sites of this study, have a reverse faulting record in their history and they both demarcate asymmetric folds such as Gemrik, Karababa and Şambayat anticlines (Figures 1.1, 2.5 and 2.6). Gemrik anticline is one of a few gently doubly-plunging culminations on a thoroughgoing folded zone at the hanging wall of the Bozova Fault, which also include depression areas such as Kuyulu low (See Chapter 3). The Karababa High, on the other hand, formed as a doubly-plunging, neat culmination, however, later on deformed and compartmentalized by P-shear bifurcations of the strike-slip Bozova Fault strand (Figure 2.7). Therefore, it is evident that the Karababa asymmetric anticline was lately overprinted and divided by symmetric positive flower structures due to strike-slip reactivation of the Bozova Fault. Such doubly-plunging anticlines are significant targets for hydrocarbon exploration activities since they provide four-way dip closures. These structures are interpreted as fault-propagation folds developed on the hanging walls of E–W-trending blind thrust faults (Şahbaz and Seyitoğlu, 2018).

2.2.2. Symmetric Folds

In the study area, based on their formation mechanisms, there are two types of symmetric folds described: (i) positive flowers formed by strike-slip fault strands, and (ii) upright cylindrical folds formed as a result of ductile response to medium to the pure compression. The symmetric folds within the positive flower structures strike roughly NW–SE or NE–SW within the study area. They form in-between bifurcated and merged splays of right-lateral or left-lateral, innate strike-slip faults in lenticular geometries. They can be lined up as en-échelon arrays throughout the strike-slip fault trajectories. In the Figure 2.2, the symmetric folds within strike slip fault strands located in the study area are

schematized as anticlines formed in-between synthetical and antithetical strike slip fault pairs (e.g., Number 6 and Number 7 faults).

2.3. Fractures and Veins

Causative relations of the collected fracture and subsidiary fault data with the faults, folds and kinematic analyses of the structural data will be presented in the next chapter. Nevertheless, here it is intended to note that the genesis of fractures is defined by conducting a comparative analysis based on their structural domains. For instance, at the sites where gentle anticlines plunge and the inter-limb angle is wide (between 120–180°), the fault-related fractures are readily distinguishable Riedels and antithetic Riedels. In the areas where the fault segments demarcate folds, fault- and fold-related fractures coexist especially within damage zones of the fault segments. At distant-to-fault sites over the folded units, specific fold-related joints predominate the general population of defects.

In order to collect fracture and subsidiary fault data, field studies are performed around the sites where the Campanian argillaceous limestones are exposed. Right-lateral Bozova Fault, which delimits the geographic highs of Gemrik Anticline at the WNW and Karababa Anticline, is traced/mapped during this study (Figure 1.1). In-between both highs (anticlines) in the Kuyulu area (Figure 1.1) anticlines plunge and smooth the curvature, shear fracture corridors are observed. These corridors are composed of interconnected network of systematic fracture sets most of which are filled with asphaltite. Asphaltite in the fractures also has some liquid petroleum component. Light fractions of the initial petroleum input must have lost in some degree overtime and a variety of oxidation, evaporation and biodegradation must have occurred during the exhumation and exposure process. Nevertheless, around the study area where analogous structures are buried and overlain by a thicker column of cap rocks, a lighter petroleum output is expected to be discovered, as it happened in the Şambayat Oilfield. The location of the exhumed fractured reservoir of Kuyulu coincides with the termination of existing fault segments at the east and at the west while maximum horizontal principal stress (SH) direction is aligned from North to South in the region (see Chapter 3). It is therefore straightforward to relate the localization of the systematic and hydraulically active fracture sets with the stress concentration domains expected to occur at the termination of

optimally oriented and critically stressed fault segments. The details of this correlation in the field will be presented and explained in Chapter 3.

2.3.1. Tension Joints/Veins

Tension joints are observed mostly over the antiformal structures in the region. They are generally in the same age interval with the Late Eocene–Early Miocene folding before fast oil expulsion occurred in the region. The tension joints and veins are considered as accommodative to the lengthening of the anticlines. They are aligned parallel to the maximum principal stress direction of its age and it is roughly in N–S direction, specifically in-between 350°N and 015°N narrow interval of azimuths. At least four joints with an average 7% linear fracture thickness are observed in a one meter scanline placed perpendicular to their strike (Figure 2.11a). The tension joints dip almost vertically with $85^{\circ} \pm 5^{\circ}$. Most joints are filled with calcite and contain trace amount of asphaltite. Their average aperture is about 1 cm and aperture of individual tension joints could reach up to 3 cm (Figure 2.11b).

2.3.2. Pressure Solution Seams (PSSs)

Pressure solution seams (PSSs) are contractional structures that form perpendicular to the maximum compressive stress. The suitable stress state for their formation is near the brittle-ductile transition, which is at intermediate effective mean stress levels in the vicinity of a transition between dilatant shear failure and compacting cataclastic flow. In the study area, PSSs are mostly localized over the southern fore-limb of the Gemrik Anticline and sporadically at the compressive damage zones of the Bozova Fault; they occur as thin bands with widths ranging from 0.03mm to 0.2 mm (Figure 2.12a). Since azimuthal orientation of the σ_1 axis of the Late Eocene to Late Miocene was about 020°N and of the Late Miocene to the present day is roughly N–S, PSSs' strikes vary between 070°N and 110° N. The walls of PSSs are made up of recrystallized calcites (Figure 2.12a). At least 24 PSSs with an average 1.2% linear fracture width are observed in a one meter scanline placed perpendicular to their strike (Figure 2.12b). The PSSs can involve slight sense of shear and even strike-slip reactivation through their interfaces between crystalline gouge and one of the hosting walls in courtesy of a rotation of the local maximum compressive stress direction as proposed by Nenna and Aydın (2011).



Figure 2.11. Field views from tension joints taken from the structural station located at the back limb of the Gemrik Anticline where the wall damage zone of the Bozova Fault is distant: (a) A view illustration how joint survey was performed in the field. The extended, foldable wooden ruler, which is one meter long, is placed perpendicular to the strikes of the tension joints and average density is 4 to 5 joints per meter; (b) a close-up view from 3-cm-width calcite filled vein.

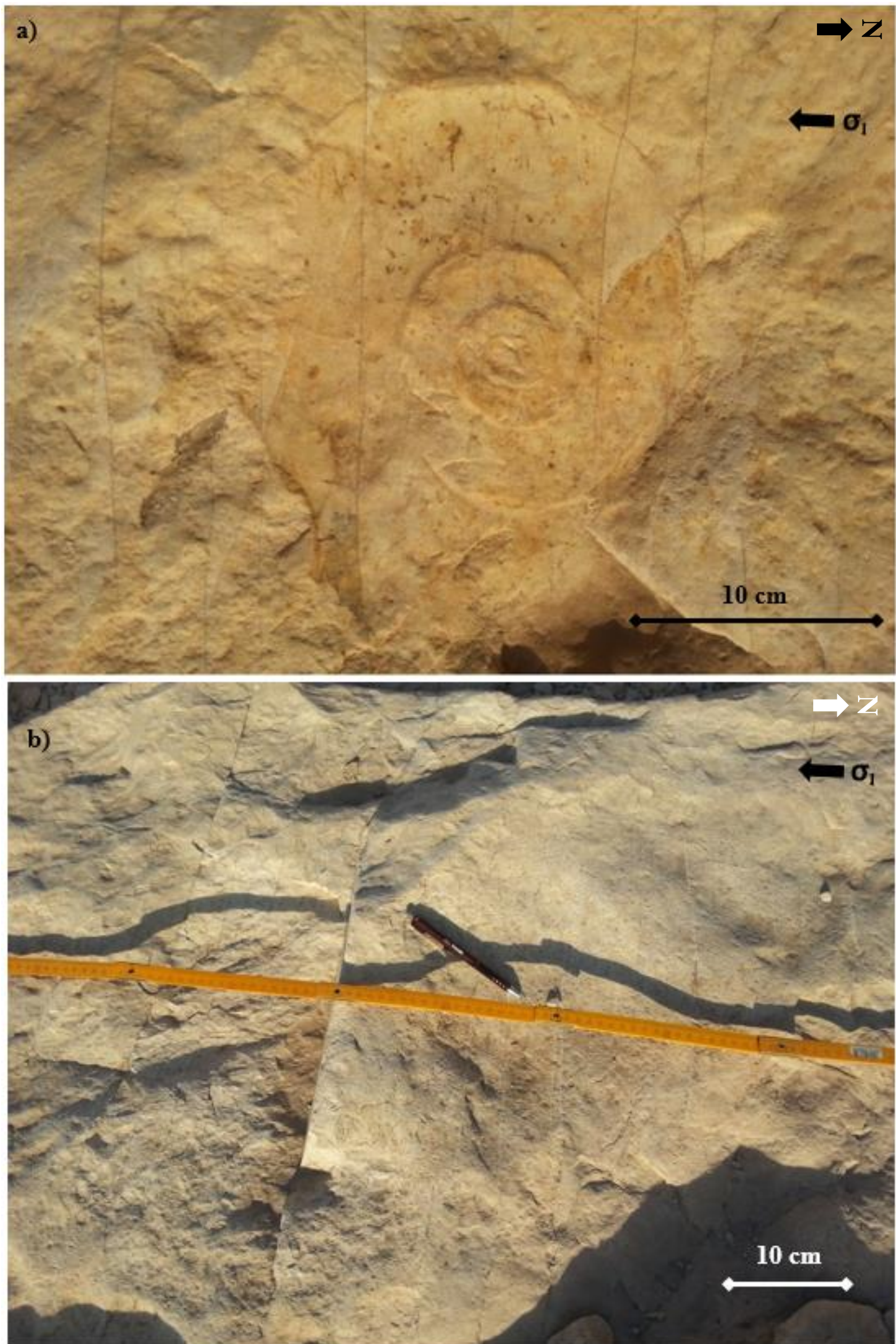


Figure 2.12. (a) A close-up view from a shallower facies of the Sayndere Formation which consists of an Ammonite fossils and undergone compression and anti-crack formation. (b) A view from thin, barely visible and frequent anti-cracks aligned roughly E–W direction, which is perpendicular to the roughly maximum compressive stress direction of the region. The fragment of the foldable wooden ruler is 20 cm long.

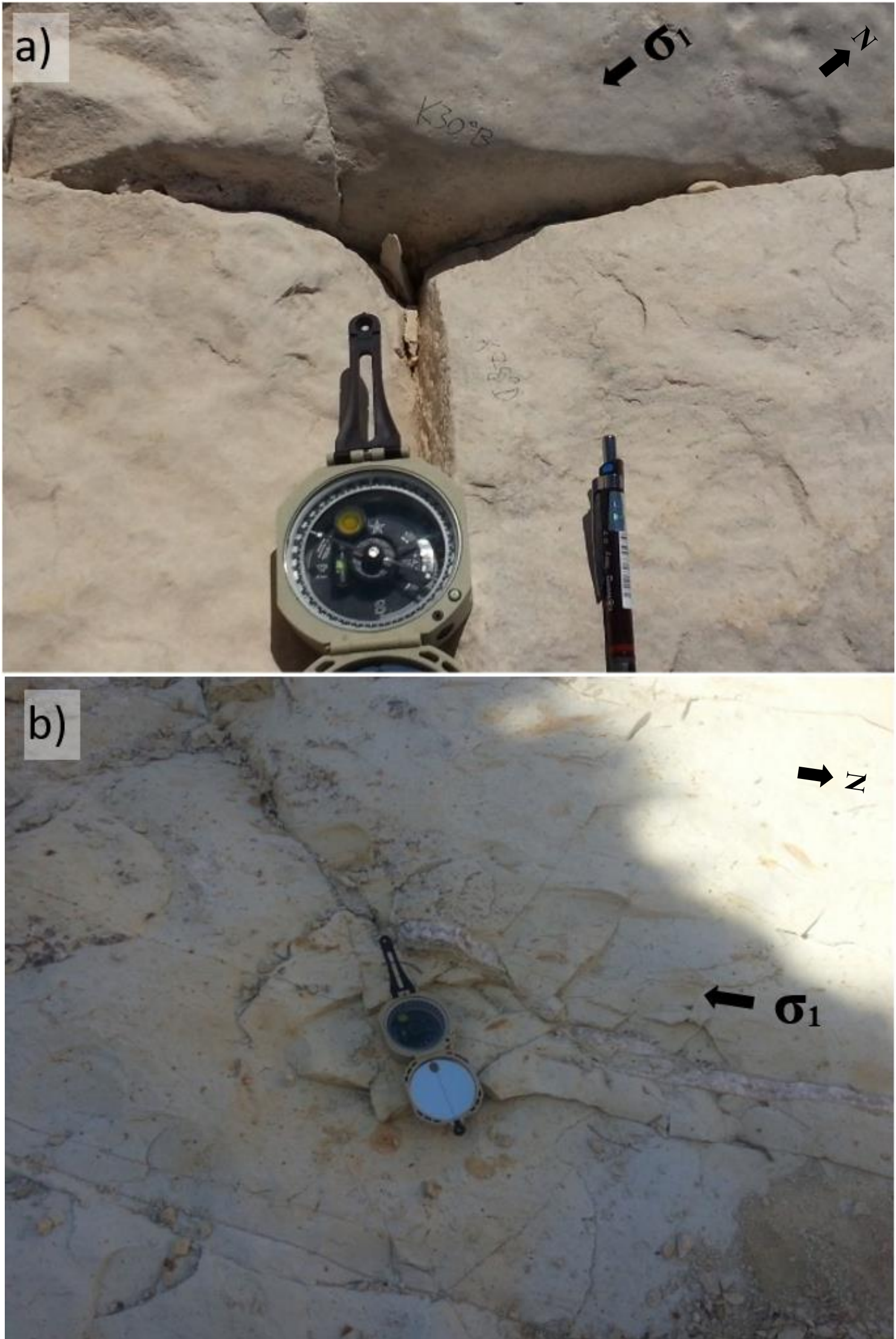


Figure 2.13. (a) A close-up view of an antithetic shear fracture that undergoes slip movement and creates offsets on an anti-crack located on its direction. (b) A set of synthetic shear fractures and slip surfaces that create offsets and terminations on a tension vein located on its direction. The octagonal body of the geologist compass which is used as scale here, is 6 cm long.

The theory for the role of the pressure solution seams in the formation of strike-slip faults and reworked symmetrical folds has been tested in the exploration activities conducted in SE Anatolia. Some petroleum explorers have focused on the possibility of symmetrical fold formation in between reactivated, steeply-dipping pressure solution seams with a strike-slip sense of shear despite their perpendicular orientation with respect to the maximum principal stress direction. E–W-oriented discontinuities are not seemingly optimally oriented to develop under N–S-striking remote maximum compressive stress direction. As it was however mentioned earlier in this Chapter, at the compressional quadrants of the stress accumulating faults, the maximum principal stress direction rotates and makes E–W-oriented surfaces to become locally optimally oriented.

2.3.3. Shear Fractures

Shear fractures and slip surfaces form and develop in both embryonic and progressive stages of the strike-slip faults. They are also arranged in en-echelon arrays exhibiting braided networks of synthetic and antithetic Riedel and P-Shears (Cloos, 1928; Riedel, 1929; Tchalenko, 1968) depicting dilatational and contractional behaviors, respectively. In the study area, shear fractures are mostly oriented 030°N to 060°N and 120°N to 150°N azimuthal intervals near the major strike-slip faults' wall and tip damage zones as will be elaborated in the following chapter. The shear fractures that arrange in 030°N to 060°N interval are antithetical to the right-lateral strike-slip Bozova Fault with their left-lateral sense of shear.

The shear fractures that arrange in 120°N to 150°N interval are synthetic to the right-lateral strike-slip Bozova Fault with their right-lateral sense of shear. They exhibit small slip movement along their lengths by cross-cutting older fractures (e.g., anti-cracks or tension joints; Figure 2.13a) that formed during folding and reverse faulting prevalent, pre Mid-Miocene (Table 2.1). They could also display small slip movement, which can be noticed by the small offsets they created on the older fractures along their lengths (Figure 2.13b).

The Shear fractures observed in the study area could be the products of strike-slip faulting regime of the post Mid-Miocene (See Chapter 3 for detail). About 20 antithetical shear fractures with an average 2% linear fracture width are observed in a one meter scanline placed perpendicular to their strike at the damage zones of the Bozova Fault.

CHAPTER 3

ANALYSES AND INTERPRETATION OF FRACTURES

3.1. Introduction and Background

Rock bodies are deformed as a result of an integrated influence of variably oriented natural stresses acted upon them throughout geological history. This deformation can occur in ductile, transitional or brittle fashion and may localize in narrow or large distances. Brittle deformation localized along oblique- and strike-slip fault strands forms the main scope of investigation in this research. A special emphasis was given to the brittle deformation because it is spatially enhanced and localized as corridors that comprise parallel or en-échelon arrangement of multiple fractures with similar orientation. Fracture corridors play a crucial role in the fluid flow and act as migration pathways characteristically in petroleum, geothermal and epithermal systems; fractures are interpreted to constitute attractive apertures for accommodation and precipitation of liquids of any chemical composition available at the time of opening. Localization and frequency systematics, and geometrical attributes of fractures may be controlled by, and causatively related to, large-scale faults and folds; this also depends on stress system, rheology and lithology as well (cf. Kim et al., 2004). Strike-slip faults, which are the dominant fault type in the study area, form along with a network of conjugate sets of shear and hybrid fractures. In the progressive stages of relative plate movement, those fractures may act as subsidiary faults with synthetic and antithetic senses of shear in addition to their pioneering role in growth of fault strands. Such subsidiary faults can accommodate total displacement between tectonic blocks by distributed slip and create secondary hierarchy local stress fields around them and this will be elaborated in the Discussion Chapter.

According to the Andersonian theory of faulting (1942/1951), obeying the Mohr-Coulomb failure criterion, right- or left-lateral strike-slip faults ideally occur at acute angles of $\pm (45\phi_i/2)$ from the maximum principal stress direction where ϕ_i is the internal friction angle of the rock. Nevertheless, as it was noted in the Chapter 2,

in the absence of optimally oriented faults with high-slip tendency (HST), amount of stress accumulation in a tectonic environment to reactivate non-optimally oriented faults with relatively lower-slip tendency (LST) may be higher than what is needed to form new HST faults; it is interpreted here that this is observed in the present study area. Since the fault-related structures (e.g., Riedel shear bands or p-shear fractures) are associated with secondary hierarchy stress fields and since they form around active or re-activated faults, such subsidiary structures are expected to form around non-optimally oriented faults (e.g., Bozova Fault in the present study area). As explained in the Chapter 1, since there are folds demarcated by those faults (e.g., Gemrik and Karababa anticlines), we expected to see some folding-related structures in the study area as well. Therefore, it is planned to collect outcrop fracture data with awareness on their structural locations, such as their distance to faults, fold hinges, fold limbs or structural domains (within or outside fault damage zones/strands); this will be elaborated later in this chapter. Fault-related structures that are commonly observed around strike-slip faults develop in their embryonic and progressive stages (cf. Klimczak, 2011; Johansen and Fossen, 2008; Katz et al., 2004). They are generally arranged in en-échelon arrays and exhibit braided networks of fractures with synthetic and antithetic senses of shear which are denoted as Riedel shear bands (cf. Closs, 1928; Riedel, 1929; Tchalenko, 1968). The term "Riedel Shears" was denoted by Hills (1963) in reference to a typical fault pattern with a distinctive geometry, which was firstly demonstrated in clay-cake models conducted by Riedel (1929). Riedel shear patterns are composed of synthetic R and antithetic R'-shears, Y-Shears, tensional T fractures and synthetic P-shears (Bartlett et al., 1981) (Figure 3.1)

Y-shears are synthetic fractures that form parallel with the principle shear zone (PSZ). They mostly outdate other shear fractures in process of forming a through-going main fault (cf. Tchalenko, 1968; Bartlett et al., 1981). R-shears are generally the earliest structures to form in sequential development process of architecture of a Riedel shear pattern and constitute the most prominent sets (cf. Morgenstern and Tchalenko, 1967; Tchalenko, 1970; Bartlett et al., 1981). They develop at an acute angle with the PSZ points in the direction of the relative sense of movement on the fault and are equal typically to 1020° . They often form in an en-échelon and

overstepping arrays and evolve as a sequence of linked displacement surfaces. They make clockwise and counterclockwise deviation from directions of PSZ's of right- and left-lateral SS fault strands, respectively (Figure 3.1a, b).

R' shears fractures have a sense of displacement opposite to the bulk movement and mostly develop contemporaneously with R-Shears (cf. Tchalenko, 1968; Moore, 1979). They are oriented at a high angle of approximately 75° from the PSZ direction by exhibiting symmetry with R-shears with respect to σ_1 direction. R' shears fractures preferentially occur at overlap zones between R-shears and generally connect two of them (cf. Riedel, 1929; Tchalenko, 1968).

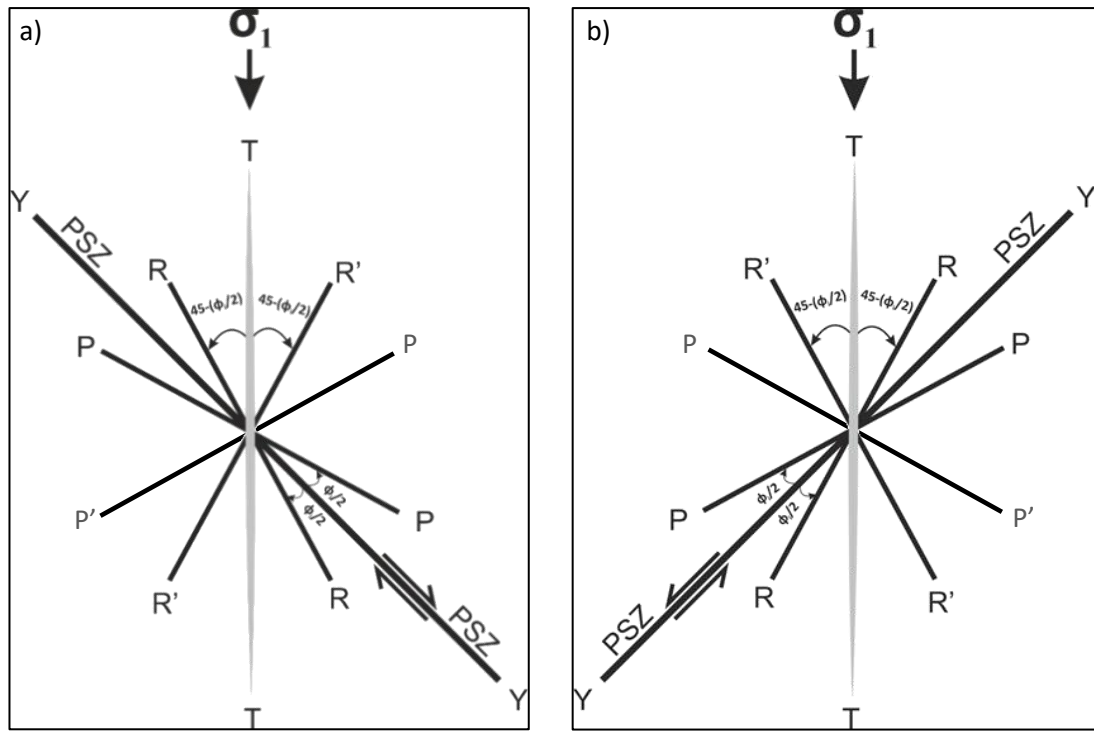


Figure 3.1. Geometrical relations of shear band fractures with principal shear zone (PSZ) and maximum principal stress direction for (a) right-lateral and (b) left lateral strike-slip faults, where ϕ is the internal friction angle of the host rock (Riedel, 1929; Tchalenko, 1968). T refers to tension fractures expected to align parallel with σ_1 direction. Y refers to fractures form parallel with the PSZ. R and R' refer to synthetic and antithetic Riedel fractures where P and P' refer to synthetic and antithetic P-shear fractures, respectively.

R' shears fractures have a sense of displacement opposite to the bulk movement and mostly develop contemporaneously with R-shears (cf. Tchalenko, 1968; Moore, 1979). They are oriented at a high angle of approximately 75° from the PSZ direction by exhibiting symmetry with R-shears with respect to σ_1 direction. R' shear

fractures preferentially occur at overlap zones between R-shears and generally connect two of them (cf. Riedel, 1929; Tchalenko, 1968). P-shears also form in en-échelon arrays in directions with acute deviation from PSZ's by displaying symmetry with R-shears with respect to PSZ's. They are observed less commonly than R or R'-shears since they require more bulk displacement over PSZ to form. Therefore, P-shears mostly outdate and link R-shears (cf. Tchalenko, 1968; Moore and Byerlee, 1992).

Geometrical attributes of each member within Riedel shear patterns is governed and affected by physical rock properties (e.g., ϕ_i), stress field perturbations or block rotations. For example, the change of the amount of ϕ_i during the progressive stages of deformation was manifested by Tchalenko (1968) and the highest value is denoted as ϕ_i' for the peak friction resistance stage, which corresponds to the internal friction angle of an intact rock. The lowest value is denoted as ϕ_r for the residual friction resistance stages and correspond the internal friction angle of a previously fractured and faulted rocks. Since it is expected for ϕ_i to decrease as the deformation of host rock increases, in progressive stages of deformation, secondary, tertiary or more lately developed R and P shears can be expected to form in a direction more parallel to the PSZ. In that case, it would be difficult to distinguish them from Y-shears and through-going development of associated segment of the main fault must almost be completed. As the translation between tectonic blocks continues, deformation bands divide the rock into smaller blocks at overlap zones (e.g., between two R-shears) and those blocks may be subjected to rotation in a “*bookshelf*” fashion under simple shear (Mandl, 1987). Thus, the relative position of R and R' fractures may change due to the rotation of those micro-blocks. Katz et al. (2004) denoted the angle between R and R' bands as β_0 , which should ideally be equal to $90-\phi_i$; these authors also have put forward a relation between varying β values, spacing (s) of R-shears, displacement (d) occurred on the R-band and corresponding rotation ($\beta-\beta_0$) as expressed in the equation below and Figure 3.2.

$$\frac{d}{s} = \frac{\sin(\beta - \beta_0)}{\sin\beta_0 \sin\beta}$$

Equation 1

Nevertheless, they discussed the reason of the varied β values handling two possibilities. One possibility is that structures originally form with different geometries due to variations in the host-rock properties (i.e. ϕ_i) or perturbed stress states during their evolution. Another possibility is that structures might have formed according to the basic Riedel geometry and subsequently changed during progressive deformation because of the rotation (see Discussion Chapter). As also discussed in the Chapter 4.5, stress field perturbations may play a significant role for the localized failure of rocks around faults, thus could create variable orientation of the deformation bands as well. Therefore, in order to anticipate the locations and orientations of the fractures or to classify them with respect to those attributes, it is necessary to take into account the effects of perturbing behavior of each fault within a region of investigation.

De Joussineau et al. (2003), by conducting photoelasticity experiments, investigated stress field perturbations occurred between two en-échelon defects within birefringent plates subjected to biaxial loading and interpreted modified σ_1 trajectories from isoclinic patterns. They concluded that the differential stress field and local maximum principle stress direction may display significant variation according to the compressive or dilatant tendency of volumetric change between the defects (see figures 11, 13, 18 and 19 from the publication of De Joussineau et al., 2003).

This phenomenon is a direct result of the incapability of cohesion-less defect to sustain shear traction. Since such defects behave as free surfaces, stress trajectories tend to be perpendicular or parallel to them (Figure 3.3.) resulting in bunching up and spreading out of the trajectories (see Chapter 4 for details) forming high and low stress concentration domains as well as extensional and compressional domains (Figure 3.4) around the faults.

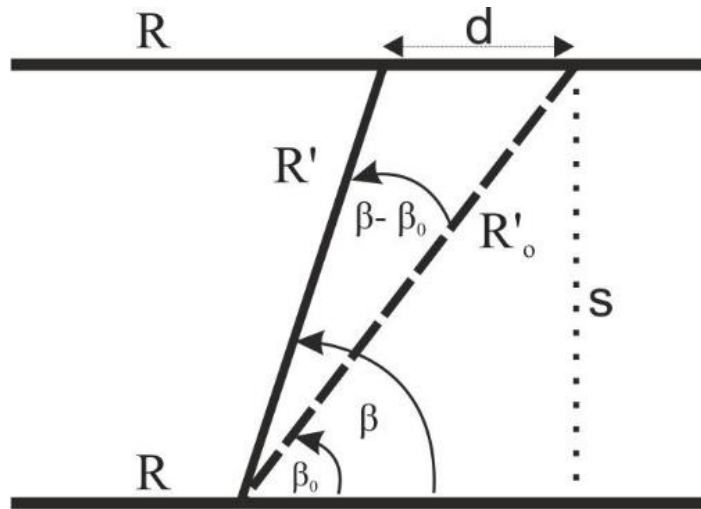


Figure 3.2. “Bookshelf” type rotation (Mandl, 1987) of micro-blocks between R’ bands and explanation of varying angles between synthetic and antithetic Riedel shear bands (R and R’). β_0 and β respectively refer to the angles before and after rotation. Dashed and solid lines represent pre-rotation and post-rotation lineaments of antithetic R’ bands respectively. The figure is from Katz et al. (2004).

Remote stress field in any tectonic regime could therefore be perturbed and deviated locally along pre-existing faults and fractures and this phenomenon can be responsible for variably oriented secondary and tertiary structures in the vicinity of the faults (Simon et al., 1999; Bourne and Willemse, 2001; Mandl, 2005). Since the tectonic activity may travel along faults, any specific domain in-between fault segments could experience compression and dilation periodically in evolutionary history of a fault. Therefore, in between two R-Shear fractures, inter-linking fractures may form in different orientations, and for such phenomena, the rotation explanation may not always be as suitable as the stress perturbation explanation. For example, Georg Mandl (2005) suggested that, within smaller shear lenses along simple shear faults, the maximum principal compressive stress (σ_1) direction becomes reoriented and secondary, even tertiary synthetic and antithetic faults and fractures form at angles in accordance with this new orientation of σ_{1r} (Figure 3.3). Thus, fractures collected from outcrop are classified by taking into account the parameters mentioned above.

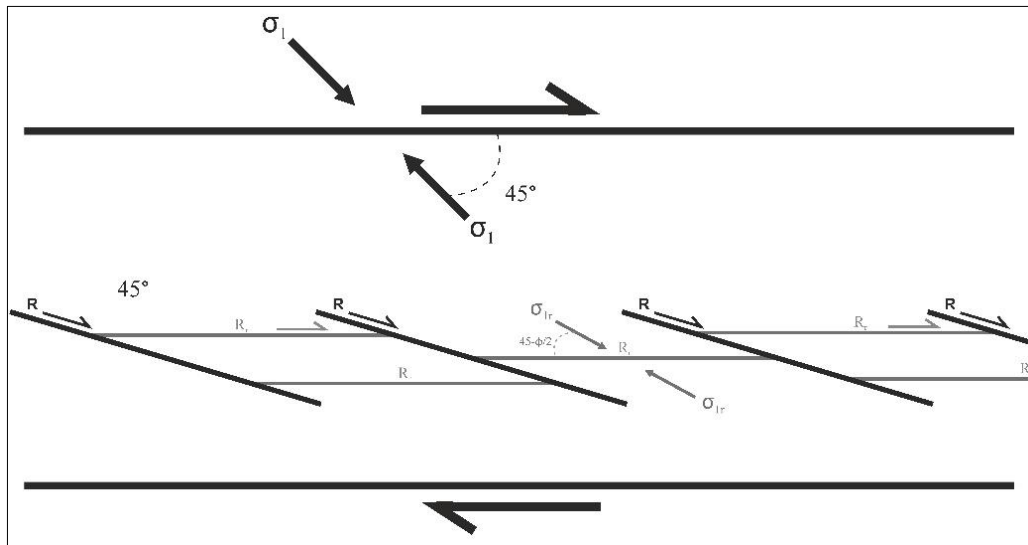


Figure 3.3. Schematic sketch of primary Riedel shear fractures (R, lighter black lines) which may develop within jogs between two simple shear faults (Y shear) and inter-linking synthetic, secondary R-shear fractures (Rr) considered as products of reoriented maximum principal stress direction (σ_{1r}) locally within the jog between parallel Riedels. Figure is based on and modified from figure 8.7 of the book of “Rock Joints: The Mechanical Genesis” of G. Mandl (2005), Springer, p. 190).

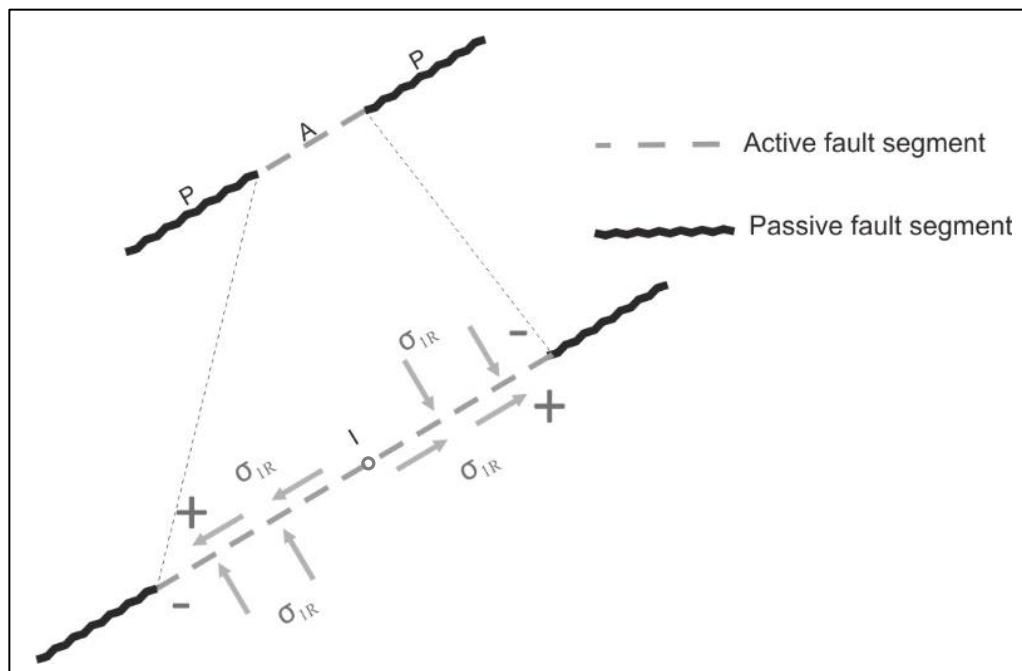


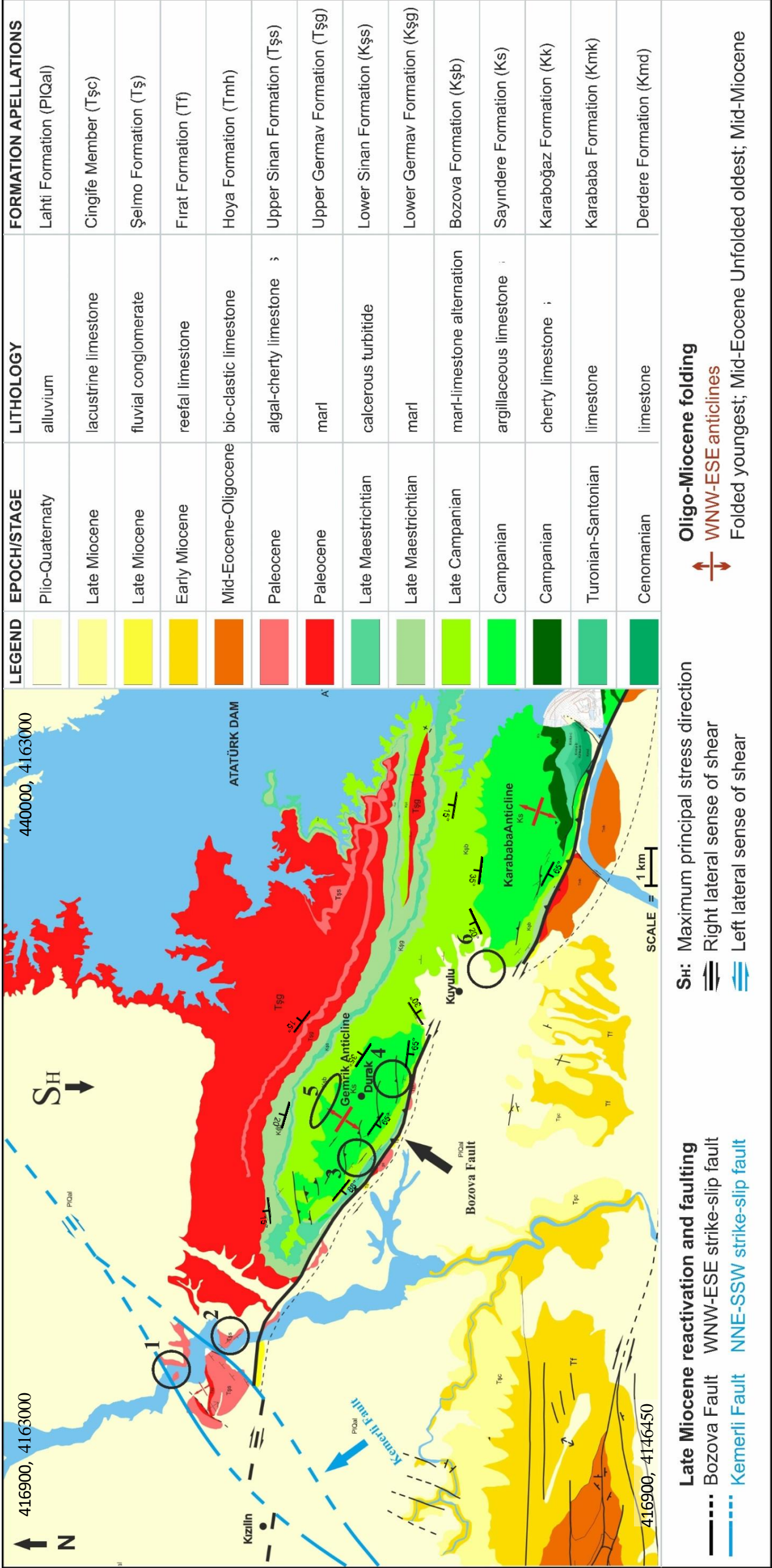
Figure 3.4. Perturbation of σ_1 trajectories around an active segment (A) of a fault limited by fault tips or passive segments (P). Changes of the trajectories are discrete and either parallel or perpendicular to fault surface at each of four quadrants divided by an isotropic central point (I) on the fault A. Figure is based on and modified from figure 7.9B of the book of “Rock Joints. The Mechanical Genesis” of G. Mandl (2005), Springer, p. 177).

3.2. Methodology

Fracture characteristics of various types of damage zones are investigated by considering their locations around faults and by sampling fractures at certain structural stations. Specific lithological units are chosen as host rocks to collect fracture data; this is the Sayındere Formation deposited on the northernmost Arabian Plate during Campanian and early Maastrichtian. The Sayındere Formation with originally negligible porosity is chosen to test isolated effects of the fractures on reservoir qualities. This research is therefore particularly focused on the Sayındere Formation which crops out either in folded areas or in areas proximal to dextral strike-slip faults within the studied region. By focusing on geometrical accuracy, structural and geological features are mapped elaborately (Figures 1.1c and 3.5). Then, data collection sites (structural stations) within various types of damage zones are defined by their structural positions with respect to the bending, overlapping or stepping sites of the geometrically accurate main or subsidiary fault lineaments. Those structural stations are described by the closest influential structures, such as (i) domains damaged by multiple faults, (ii) affected by both faulting and folding, (iii) distant or close to faults or (iv) domains within tip, linking or wall-damage zones along fault strands. Each structural station is georeferenced along with photographs. Geometrical and physical attributes of each fracture sets are also collected and recorded: such as dip, azimuth, linear fracture density, aperture and filling material.

3.3. Fracture Data Collected at Structural Stations

Sayındere Formation and overlying Bozova Formation with rather similar mechanical properties outcrop at the sites 25 km SE of Şambayat oilfield where Gemrik anticline and its delimiting faults (e.g., Bozova and Kemerli faults) are located (Figures 1.1b and 3.5). To examine individual contribution(s) of each structural element to the fracture and subsidiary fault architectures, outcrop collection sites are sub-divided and classified with respect to their proximity to, and deflections of, major structures. Fracture data is collected from 6 structural stations.



Station 1 is located within a zone deformed by predominantly a left-lateral strike-slip fault. Station 2 is located close to the intersection of two conjugate strike-slip faults (Kemerli and Bozova faults) and at a plunged edge of the long axis of a fold (Gemrik anticline). At that place the effect of folding is expected to be minimum; thus, both conjugate faults passing closely by this area are expected to be responsible from the formation of most all elements of the local fracture architecture. Station 3 is located close to the wall of a right-lateral strike-slip fault (Bozova Fault) and also at the steeper-dipping edge of the short axis of a fold (Gemrik anticline). It is expected to observe both fold- and fault-related structures around here. Station 4 comprises locations away from the faults and smoothly dipping edge of the short axis of a fold. Station 5 is located close to a right-lateral strike-slip fault, which locally makes counterclockwise rotation enhancing compression. Station 6 is located in extensional isolated lenses between terminated tips of right-lateral strike-slip faults.

3.3.1. Station 1: Wall Damage Zone of Left-Lateral Strike-slip Kemerli Fault

The most closely-spaced fractures in the structural architecture of the Station 1 (Figure 3.5.) are systematical antithetic, R' shear fractures that are truncated by relatively more sporadic Riedel and P-shear fractures (Figure 3.6).

Average preferred strike orientation of R' shears are 317° whereas the average dip angles of their planes are 83.6° . Bedding planes are dipping 19° to the NW at this station (Figure 3.6b). The bedding strike and dips are considered as aligned in accordance with the geometry of the push-up structures (e.g., Yarım Tepe) formed along the Kemerli strike-slip fault strand. Therefore, the reorientation of the bedding planes in this vicinity is interpreted to postdate the fracturing and faulting. Therefore, we implemented bedding unfolding to the fracture data in this location to acquire pre-folding orientations of the fractures. The most prominent observation in the location 1 is the angular variation interval of R' fractures. As they form as linking structures between synthetic R- and P-shear fractures, probably as their precursors, after the stage which the synthetic fractures get into a through-going character and allow progressive displacement over their complete trajectory, R' shear fractures are

subjected to “bookshelf” type rotation (Figure 3.2) as suggested by Mandl (1987) and deviated about $\pm 12^\circ$ from their theoretical orientation (Figure 3.1b) within jogs in between P and R-shears faults (Figure 3.6d).

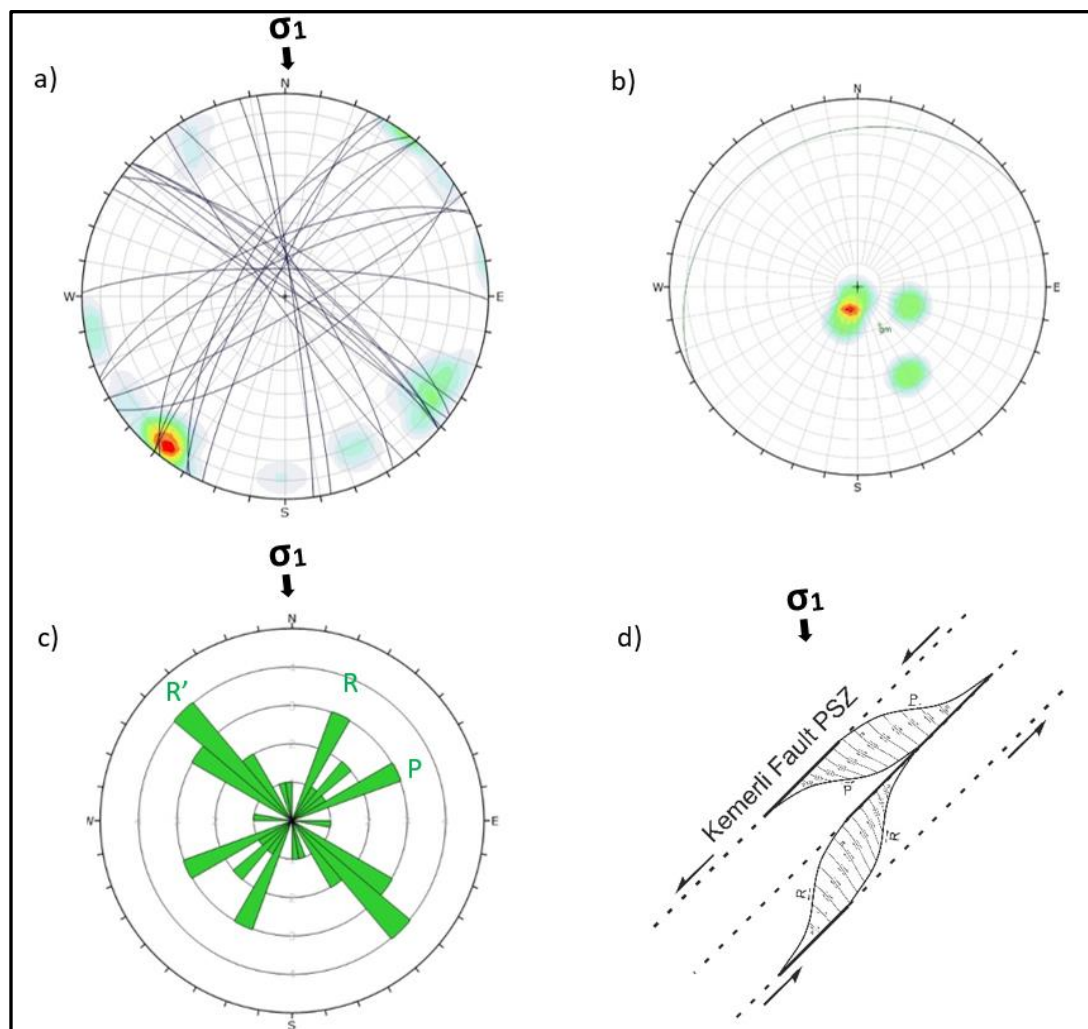


Figure 3.6. (a) In a stereographic plot with lower hemisphere and equal area projection, semi-circular representation of fractures located in the wall damage zone of the left-lateral strike-slip Kemerli Fault. (b) Poles to bedding planes and their mean circle measured in the locality. (c) Rose diagram representing preferred strike orientations of fracture sets pertaining to the locality. (d) Simplified sketch representing local fracture types and their relations with each other and also with the PSZ of the Kemerli Fault.

3.3.2. Station 2: Triangular Area Close to Bozova and Kemerli Faults' Intersection

This structural domain specifically presents the most diverse fracture network in the study area. Besides fractures that are directly associated with Bozova and Kemerli faults, data is collected from fractures that can be associated with localized

secondary hierarchy stress fields. Since this particular area is interpreted as being located in the plunging north westernmost edge of the long axis of the Gemrik anticline, the bedding strikes and dip values are in accordance with the spherical geometry of this fold. And, since the formation of the Gemrik anticline pre-dates the strike-slip faulting in the region, it is not required to unfold the fault-related fracture data with respect to bedding to classify fractures by their orientations. R- and P-shear local fracture sets which deviate from the PSZ's of both Kemerli and Bozova faults are collected (Figure 3.7d, e). Besides, a tension fracture set, which clearly displays a disassociation with the closest faults, is also observed (Figure 3.7f). Those fractures are interpreted as outcomes of local stress perturbation occurred at the vicinities of the wall damage zone of the left-lateral Kemerli Fault as experimentally studied by Joussineau et al. (2003).

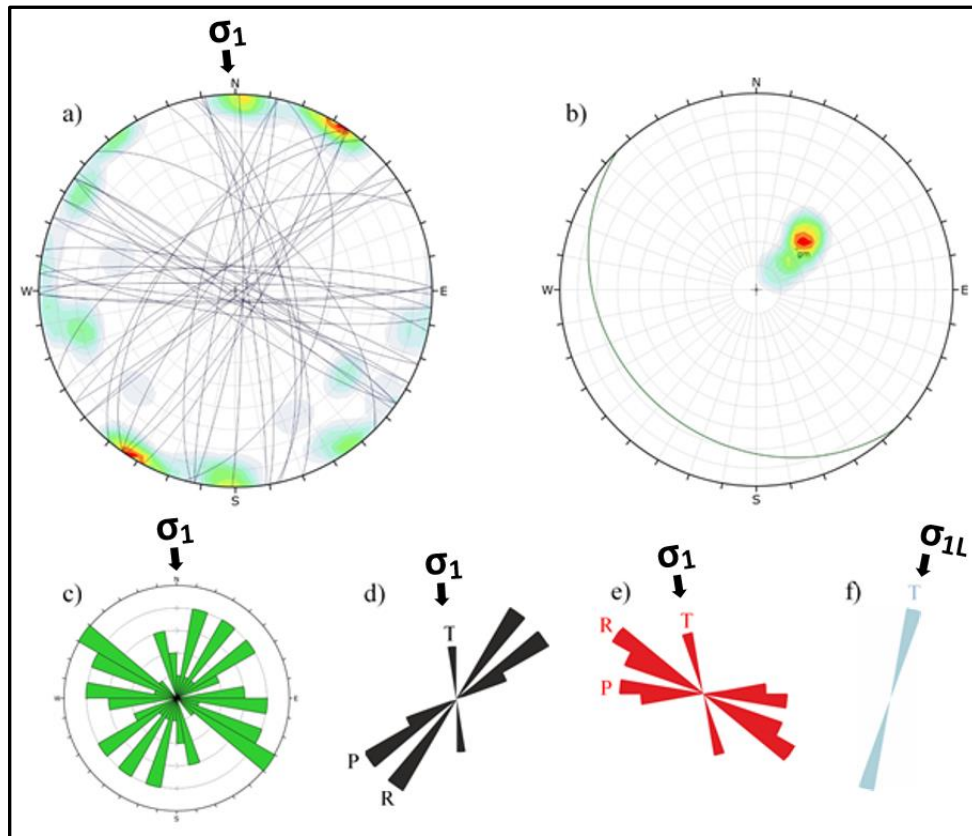


Figure 3.7. (a) Stereographic semi-circular representation of fractures located in overlapping damage zones of the left-lateral Kemerli Fault and right-lateral Bozova Fault. (b) Poles to bedding planes and their mean circle measured in the Station 2. Rose diagrams representing preferred strike orientations of: (c) all fracture sets, (d) the fracture sets associated with the Kemerli Fault, (e) the fracture sets associated with the Bozova Fault and (f) a fracture set that is considered as the product of the perturbed (bended), local σ_{1L} trajectory along the wall of the Kemerli Fault.

The stress trajectories near the fault walls show a tendency to bend in such a way that they become parallel or sub-parallel to the fault surfaces (see Chapter 4 for more detail). Nevertheless, if the magnitude of such deviated stresses could reach to a critical level (e.g., rock strength), perturbation related fracture may form.

Therefore, perturbed tension fracture set associated with Bozova Fault are not particularly observed whereas they are associated with the Kemerli Fault in the station 2. Moreover, considering the stress state and the direction of the most principal stress, denoted as S_H or σ_1 in the present text, the right-lateral Bozova Fault displays a geometry that is expected to show relatively less slip tendency in this location. This geometrical feature leads one to think that a more cohesive and thus resistant segment of the Bozova Fault is located here. Local stress trajectories around this area are therefore expected to show small or negligible deviation triggered by the Bozova Fault plane from its far-field orientation. This may also explain the absence of a deviated set of tension fractures associated with the Bozova Fault.

3.3.3. Station 3: Precursory Fractures to Folding and the Fractures Associated with the Strike-slip Activation of the Bozova Fault Plane

One of the two systematical fracture sets located at the station 3 are genetically related to the originally 024°N oriented compression responsible for the onset of the formation of the Gemrik Anticline that predates the strike-slip faulting and postdates the sedimentation of the Paleocene and older lithological units exposed in around the study area (Figure 3.8e). It is an orthogonal set of two mutually intercepting arrays of 015°N oriented tension joints (TJs) and 126°N oriented pressure solution seams (PSSs) whose bedding reconstructed strikes are 24°N and 120°N, respectively, that formed parallel and sub-perpendicular respectively to the maximum principle stress direction of their age (024°N). As the long axis of the Gemrik Anticline is parallel to the average orientations of PSSs, the PSZ of the reactivated local (at the station 3) segment of the Bozova Fault is oriented sub-parallel to both aforementioned structures with its 124°N orientation. Nevertheless, the orientation PSZ of the local strike-slip fault segment is parallel with the strikes of beds and local PSSs. Also, the Bozova segments seem to trail folded, and reoriented direction of the PSSs which

they acquired during the anticline formation. Therefore it may be inferred that the Bozova Faults' location and geometry is directly related to the weakness zones of the PSSs as suggested in an earlier study of Nenna and Aydın (2011) where they discussed the role of PSSs in the formation of reverse and strike-slip faults.

On the other hand, there are one more contemporaneous fracture sets consisting of three different arrays of shear fractures in the station 3. By their orientation, sense of movement and cross-cutting relationships with the initial aforementioned orthogonal fracture set, they are considered as associated with the activation of the right-lateral Bozova Fault, which postdates formation of the TJs and PSSs (Figure 3.8).

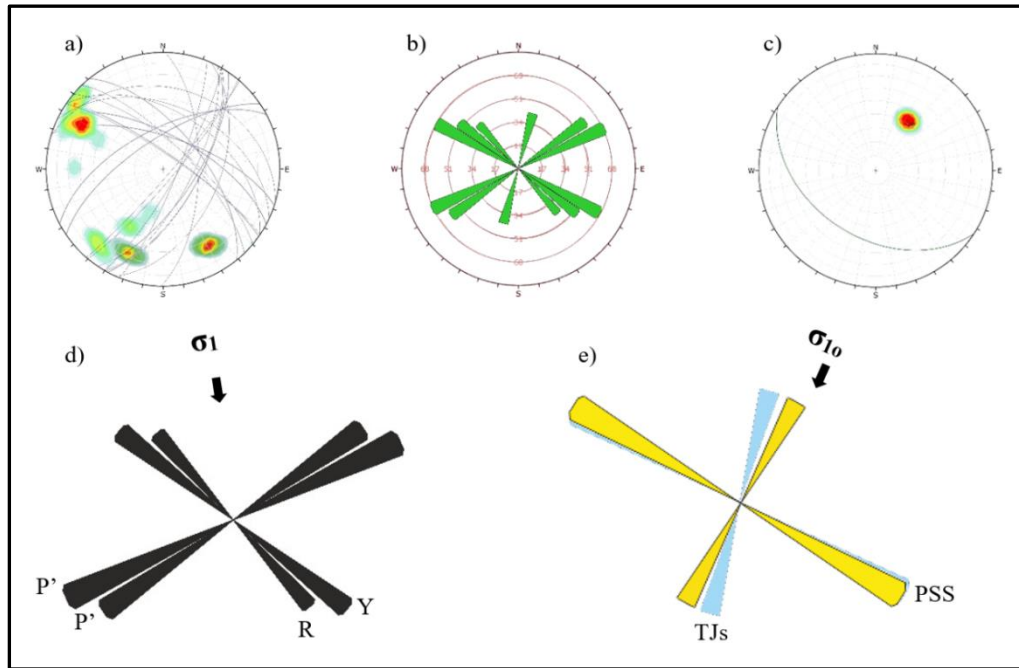


Figure 3.8. (a) Stereographic semi-circular representation of fractures located in the wall damage zone of the right-lateral SS Bozova Fault at the steeper fore limb of the Gemrik anticline. (b) Rose diagram representing preferred strike orientations of all fracture sets located at the station-3. (c) Stereographic projection of bedding planes' mean circle and contour of poles to bedding planes in the Station 3. (d) Rose diagram illustrating shear fracture arrays related to the Bozova Fault and their relative orientation with respect to the contemporaneous σ_1 direction of 350° . (e) Rose diagram showing original (yellow peaks) and folded (blue peaks) orientations of the orthogonal fracture sets of TJs and PSSs that formed prior to the formation of the Gemrik anticline.

These shear fracture arrays are classified as Y-shears, Riedel (R) shears and P'-shears by their average orientations of 304°N , 320°N and 240°N , respectively .

These shear fractures are all considered as related and contemporaneous with strike-slip reactivation of the Bozova Fault and products of the same stress conditions. Strike-slip reactivation of the PSSs suggests a counterclockwise remote stress rotation of 034°N corresponding to a σ_1 orientation of 350°N (Figure 3.8 d) at the time of formation of strike-slip fault and fracture assemblages located in the station 3 (Figure 3.8.).

For the station 3, linear healed fracture thickness (LHFT) and linear density (LD) values are also measured for each set of fractures (Figure 3.9). By a vectorial sum of the normal vectors to the fracture surfaces, which weighted by their LHFTs, the best azimuthal directional drilling trajectory is also calculated (Figure 26f) to cut and produce from as many fractures and as much fracture porosity as possible for the future exploration activities on analogous domains, except for the fractures being filled by hydrocarbon instead of being healed by calcite. The total linear fracture thickness (TLFT) calculated for the domain of the station 3 is %7.7 in the optimal directional drilling azimuth of 87.1°N (Figure 3.9f).

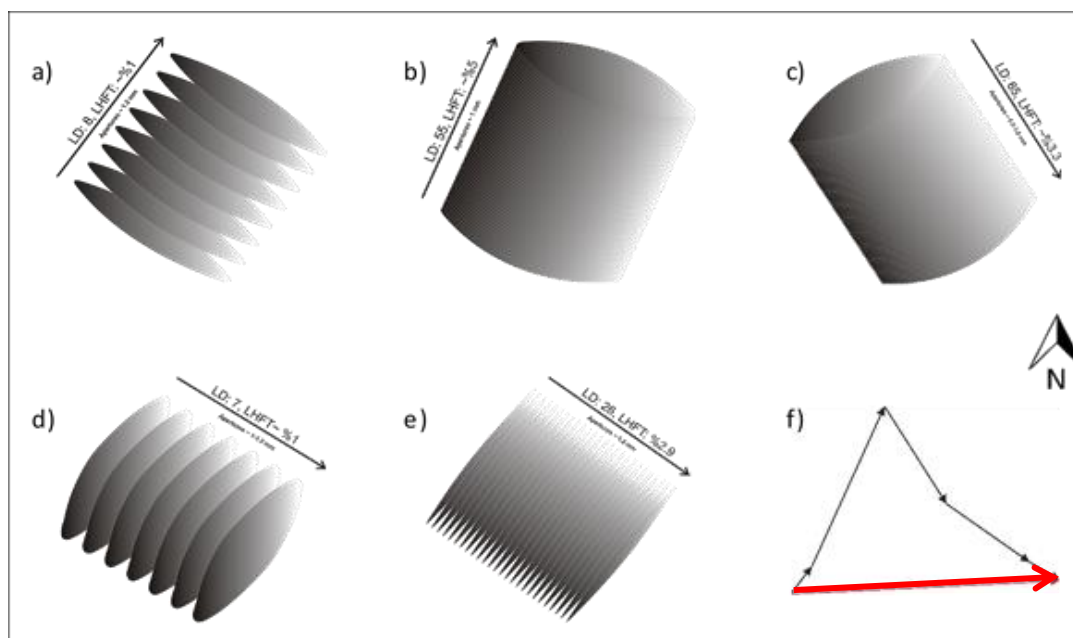


Figure 3.9. (a–e) Disc shape representations of orientation, density and thickness values of the elements of different fracture sets in one meter scanlines located in the station-3. **(f)** Calculation of the resultant vector (red arrow) representing best directional drilling trajectory to cut maximum number of fractures and maximum amount of total linear fracture thickness (TLFT). The black arrows represents the normal vector to fracture planes weighted by LHFT percentages of each set of fractures which are %1.0, %5.0, % 3.3, %1, and %2.9, respectively.

3.3.4. Station 4: Fractures Formed Around P-Shear Segment of the Bozova Fault

After a preliminary evaluation of whole fracture data collected from the P-shear domain of the Bozova Fault where the orientation of the main fault zone bends 017°N counterclockwise, syn- or pre-folding fractures are unfolded with respect to the bedding orientation to reconstruct their original position at the time of their formation. The strike-slip faulting related fractures were remained unchanged before analyses and classification efforts, since they postdate the folding. The rose diagram of fracture strikes with their original orientations is shown in the Figure 3.10. The most closely spaced fractures in the structural architecture of the Station 4 (Figure 3.10.) are systematical PSSs and tension fractures (TJs) that are accompanied by relatively rarer antithetic P' & R shear fractures, and older PSSs-TJs orthogonal couples (Figure 3.10.).

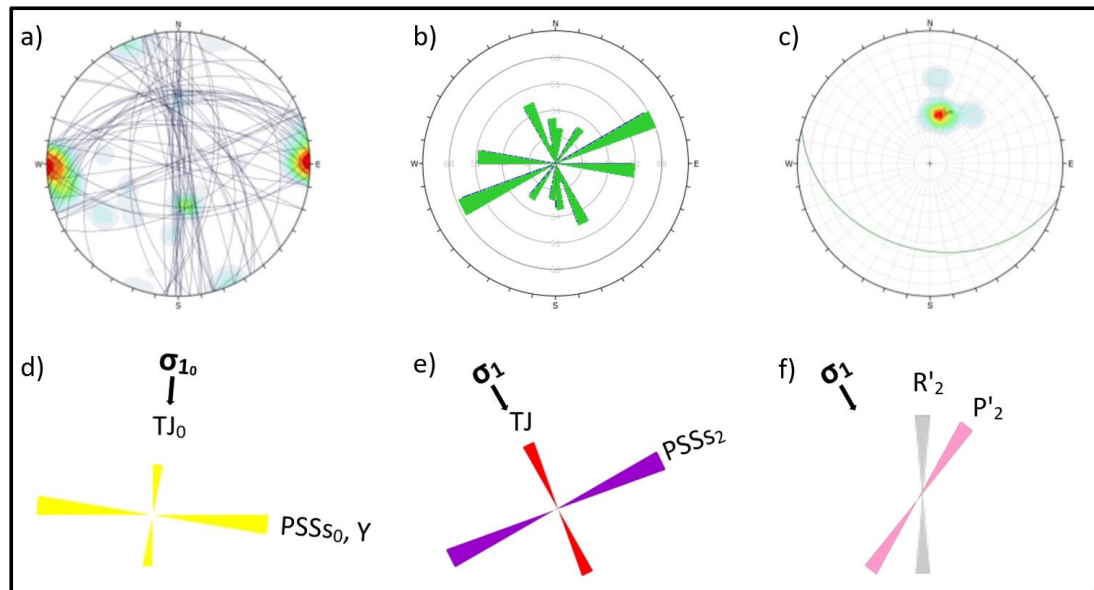


Figure 3.10. (a) Stereographic semi-circular representation of fractures located in the compressional quadrant damage zone of the right-lateral Bozova Fault at the steeper fore limb of the Gemrik Anticline (Station 4). (b) Rose diagram representing preferred strike orientations of all fracture sets located at the station 4. (c) Stereographic projection of bedding planes' mean circle and contour of poles to bedding planes in the Station 4. (d) Rose diagrams illustrating: (d) orthogonal fracture sets of TJs and PSSs that formed prior to the formation of the Gemrik anticline, (e) orthogonal fracture sets of TJs and PSSs that formed at the compressional quadrant of lately SS reactivated Bozova Fault and (f) antithetic R' and P' shear fractures related to strike-slip reactivation of the Bozova Fault.

Some of the Y-shear fractures seem to have innately formed as PSSs of older regime of pre-folding with its 005°N oriented σ_1 . Though they are considered as P-shear with respect to the PSZ of the main fault, for this locality they act as Y-shear fractures with 030°N counterclockwise rotated σ_1 direction of the succeeding regime of the strike-slip faulting.

There are two differing ages for sets of tension joints that are in the strikes of 185°N and 156°N; the former is considered as the product of pre-folding compression and the latter is the product of the reoriented σ_1 axis during the strike-slip reactivation of the Bozova Fault. Average preferred strike orientation of R' shears are 170°N whereas the average dip angles of their planes are ~90°. Bedding planes' average dipping is 35° to the SSW at this vicinity (Figure 27c). For the station 4, linear healed fracture thickness (LHFT) and linear density (LD) values are also measured for each set of fractures (Figured 3.11.).

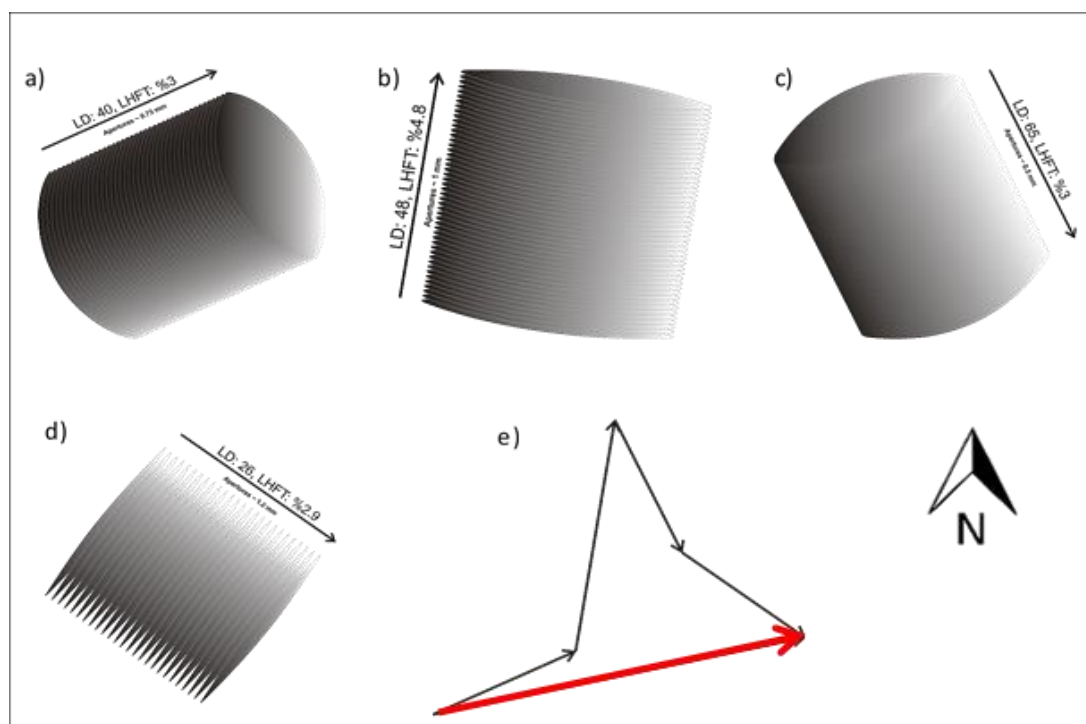


Figure 3.11. (a–d) Disc shape representations of orientation, density and thickness values of the elements of different fracture sets in one meter scanlines located in the station-4. (e) Calculation of the resultant vector (red arrow) representing best directional drilling trajectory to cut maximum number of fractures and maximum amount of total linear fracture thickness (TLFT). The black arrows represents the normal vectors to fracture planes weighted by LHFT percentages of each set of fractures which are %3.0,%4.8, %3.0 and %2.9, respectively.

By a vectorial sum of the normal vectors to the fracture surfaces, which weighted by their LHFTs, the best azimuthal directional drilling trajectory is calculated (Figure 3.11.) to cut and produce from as many fractures and as much fracture porosity as possible for the future activities on analogous domains except for the fractures being filled by hydrocarbon instead of being healed by calcite. The total linear fracture thickness (TLFT) calculated for the domain of the station 4 is %7.2 in the optimal directional drilling azimuth of 77.3°N.

3.3.5. Station 5: Fractures Formed at Outer Damage Zone of the Bozova Fault and Hinge Zone to Back Limb of the Gemrik Anticline

Station 5 is located between the hinge and two way plunging northeastern backlimb of the Gemrik Anticline as can be deduced from the main circle of the bedding planes' orientation at this station (Figure 3.12.).

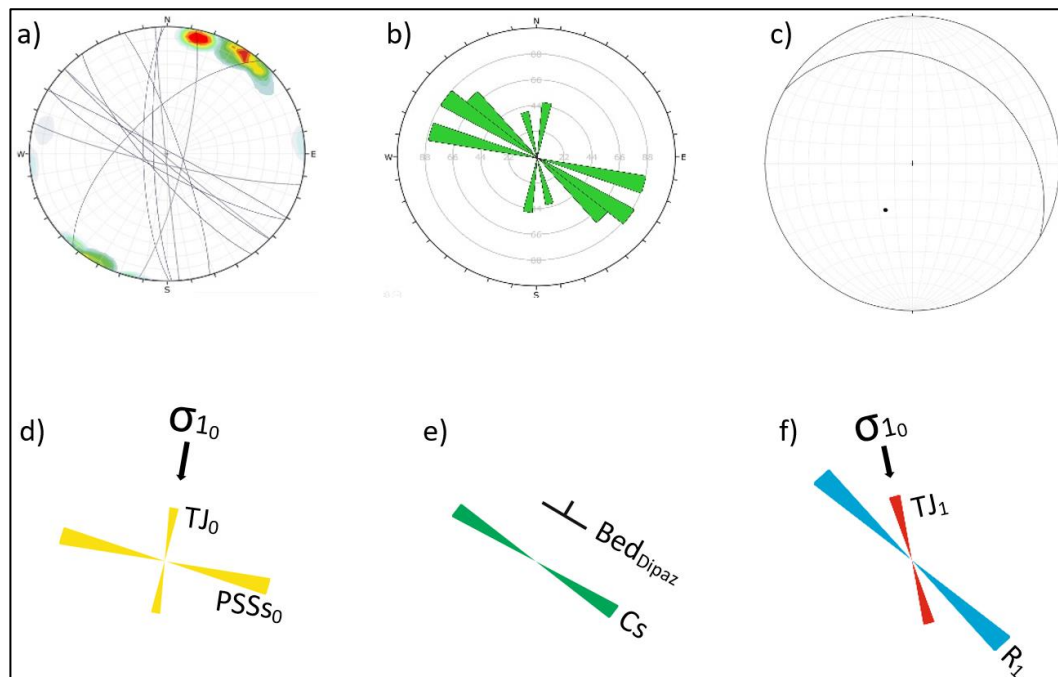


Figure 3.12. (a) The mean circles of the systematical fracture sets located at the station 5. (b) Rose diagram representing preferred strike orientations of all fracture sets located at the station 5. (c) Stereographic projection of bedding planes' mean circle and the pole to bedding planes in the station 5. Rose diagrams of: (d) orthogonal fracture sets of TJs and PSSs that formed prior to the formation of the Gemrik anticline, (e) preferred strike orientation of the fold related extensional outer arc cleavages parallel to the strikes of the bedding planes at the longitudinally plunging hinge zone of the Gemrik Anticline, and (f) R-shear fractures and TJs formed during strike-slip activity of the Bozova Fault at its outer damage zone.

This locality is about 2.5 km away from the PSZ of the Bozova Fault (Figure 3.5). Therefore, predominantly fold-related structures (Figure 3.12d) and precursory to folding structures (Figure 3.12e) are observed around here. Outer arc-related extensional structures (e.g., cleavages) are also observed at this domain (Figure 3.12e); this interpretation is based on the proximity of the station 6 to the hinge zone of the Gemrik Anticline. A few shear fractures and tensional structures (Figure 3.12f) are also observed; they are attributed to a subsequent stress field because this domain is located at an adequate position for the stress field acting on it to be perturbed by the Bozova Fault remotely.

For the station 5, linear healed fracture thickness (LHFT) and linear density (LD) values (Figure 3.13) are measured for each set of fractures observed (Figure 3.12). By a vectorial sum of the normal vectors to the fracture surfaces, which weighted by their LHFTs, the best azimuthal directional drilling trajectory are calculated to cut and produce from as many fractures and as much fracture porosity as possible for the future exploration activities on analogous domains except for the fractures being filled by hydrocarbon instead of being healed by calcite. The total linear fracture thickness (TLFT) calculated for the domain of the station 5 is %11.3 in the optimal directional drilling azimuth of 72.2°N (Figure 3.13f).

3.3.6. Station 6: Kuyulu Low as an Exhumed Fractured Reservoir Formed at the Extensional Step-over of the Bozova Fault

At the station 6, the Bozova Faults' segments terminate and show an extensional step-over; it is here termed as Kuyulu low at the vicinity of Kuyulu town. There, asphaltite filled, interconnected fracture sets are discovered and denoted as “exhumed fractured reservoir” (Figures 3.5 and 3.14).

The station 6 is near Kuyulu town and is located over a geographical low where Karababa and Gemrik anticlines plunge and curvature on the long axis of the fold system almost zeroes. The Bozova Fault makes an extensional step-over (Figure 3.5) in between its two segments demarcating Gemrik anticline and the Karababa high around the station 6.

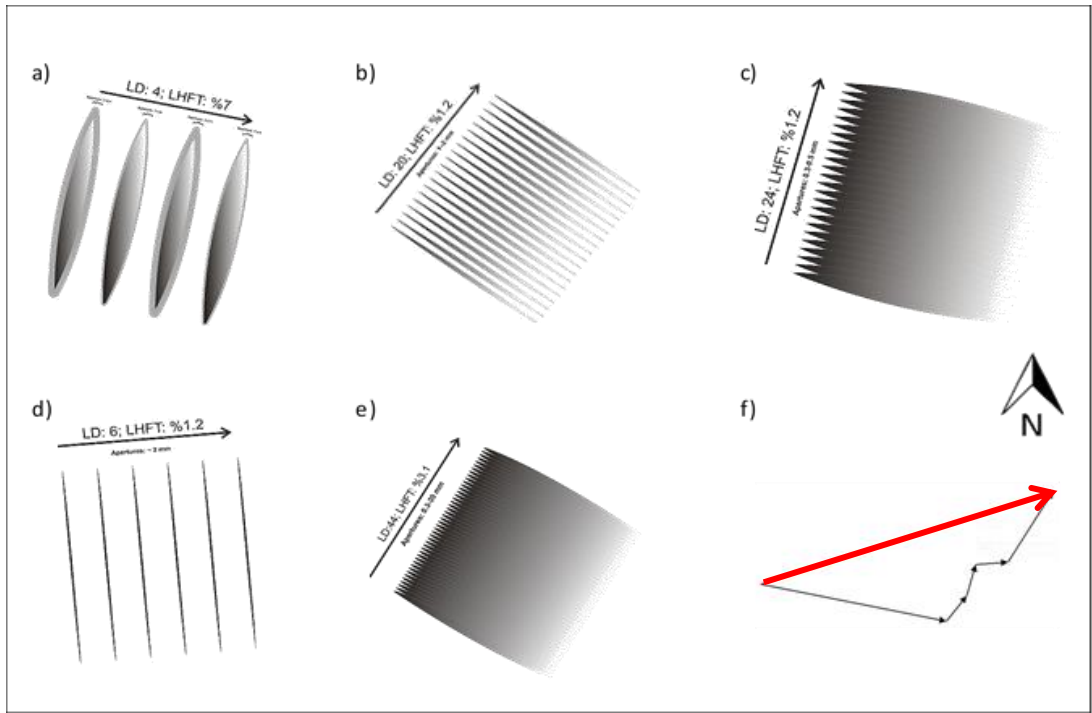


Figure 3.13. (a–e) Disc shape representations of orientation, density and thickness values of the elements of different fracture sets in one meter scanlines located in the station 5. **(f)** Calculation of the resultant vector (red arrow) representing best directional drilling trajectory to cut maximum number of fractures and maximum amount of total linear fracture thickness (TLFT). The black arrows represents the normal vectors to fracture planes weighted by LHFT percentages of each set of fractures which are %7.0, %1.2, %1.2, %1.2 and %3.1, respectively.

At this locality fold-related structures do not exist because of diminished influence of the folding as it seen from the low bedding angles (Figure 3.15c). Almost all structural elements of the fracture sets located at this domain are filled with asphaltite or heavy liquid petroleum. This indicates locally persisted hydrocarbon expulsion beneath the topographical lows as well as proper timing and hydraulic activity period of the fractures formed at the station 6 in terms of hydrocarbon trapping.

Since the folding is dated back to the pre-Mid Miocene while strike-slip reactivation of the Bozova Fault is dated post-Mid-Miocene, it is evident that the timing of the regional hydrocarbon expulsion rate maxima (see Discussion Chapter) overlaps the timing of the fracture formations during the strike-slip faulting while postdates the formation of the folding. This phenomenon may explain the calcite

filling of the fold-related fractures and hydrocarbon filling of the solely strike-slip fault-related ones as will be discussed in the Discussion Chapter. Dip-parallel vectors of the fractures located in the station 6 indicate that the fracture configuration supports the vertical migration of the fluids since most of the systematic fracture sets are vertical or steeply dipping (Figure 3.15a, b).

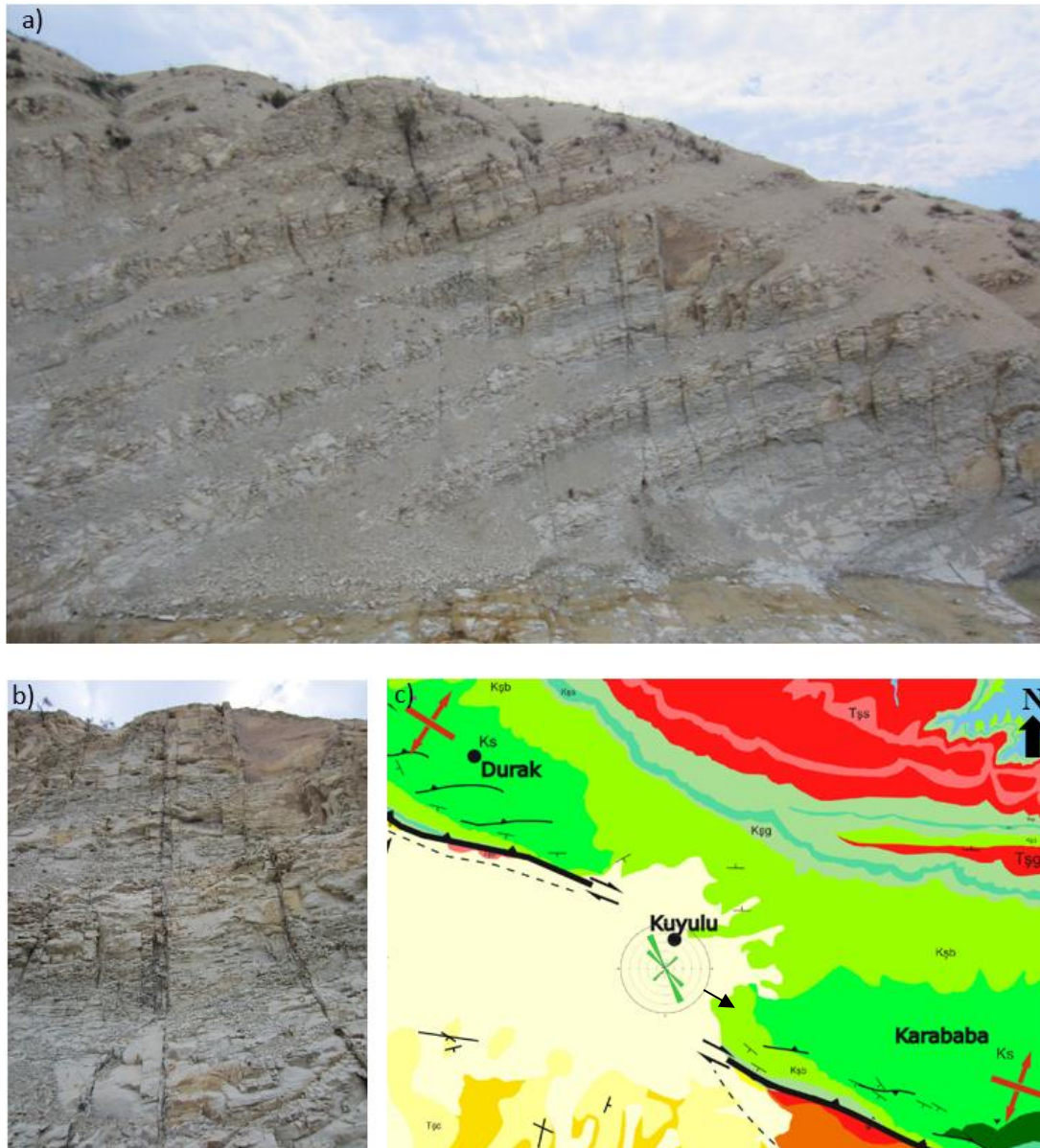


Figure 3.14. (a, b) Field views from outcropped asphaltite-filled fractures within Campanian argillaceous limestones; apertures ranges from 0.5 to 30 mm. (c) Geo-located rose diagram for the preferred orientations of the asphaltite-filled fractures collected at the extensional step-over domain of the right- lateral strike-slip Bozova Fault.

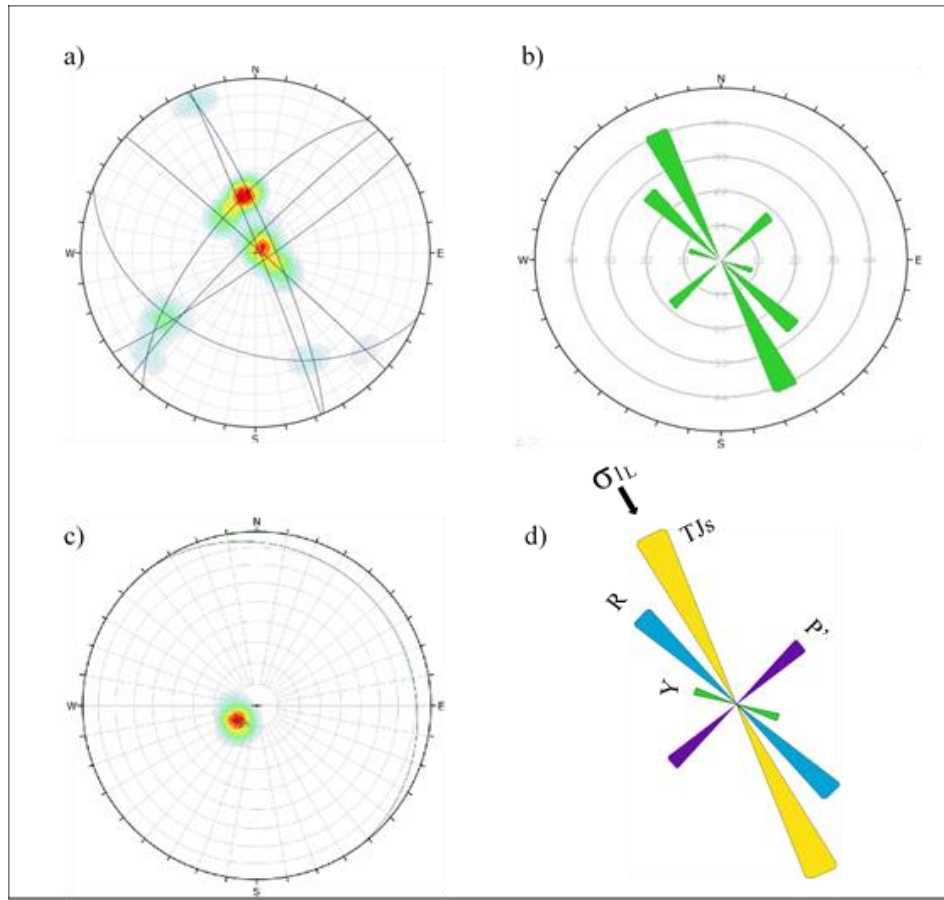


Figure 3.15. (a) The mean circles of the systematical fracture sets located at the station 6. The contours represent vertical fluid flow direction since they are drawn from the projections of the dip parallel vectors of the fractures. (b) Rose diagram representing preferred strike orientations of all fracture sets located at the station 6. (c) Countour diagram of bedding planes' mean circle and the pole to bedding planes in the station 6. (d) Rose diagram illustrating preferred orientations of the tension joints (yellow rose peak), Riedel shear (blue rose peak), P'-shear (purple rose peak) and Y shear (Green rose peak) fractures within the station 6. All of the fractures here are associated with the stress field that developed during the strike-slip reactivation of the Bozova Fault.

The domain includes Riedel shear and tension fractures (Figure 3.15d) that stimulate coalescence of main step-over segments of the Bozova Fault. The P'-shear fractures are not thoroughgoing, and mostly truncated by the R-Shears. The curved coalescence of the Bozova Fault gives the domain an extensional pull-apart character. The extension seems to have distributed among minor structures since they constitute a significant amount of accommodation space (Figure 3.16) for circulating reservoir fluids.

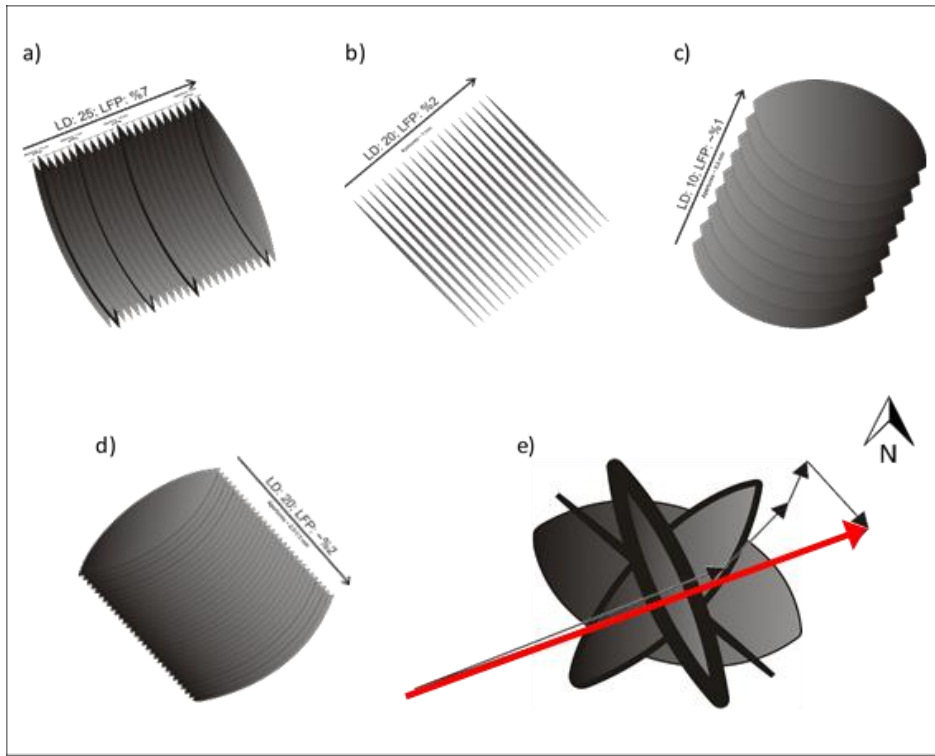


Figure 3.16. (a–d) Disc shape representations of orientation, density and thickness values of the elements of different fracture sets in one meter scanlines located in the station 6. **(e)** The intercepting discs with varying thicknesses indicate total anisotropic, oil filled fracture porosity (total linear fracture porosity) values originated from different set of fractures. Calculation of the resultant vector (red arrow) representing best directional drilling trajectory to cut maximum number of fractures and maximum amount of TLFPs. The black arrows represent the normal vectors to fracture planes weighted by LFP percentages of each set of oily fractures which are %7.0, %2, %1.0 and %2.0, respectively.

For the station 6, linear fracture porosity (LFP) and linear density (LD) values for each set of fractures are measured (Figure 3.16). By a vectorial sum of the normal vectors to the fracture surfaces, which weighted by their LFPs, the best azimuthal directional drilling trajectory (Figure 3.16e) are calculated to cut and produce from as many fractures and as much fracture porosity as possible for the future exploration activities on analogous, oil bearing fracture domains. The total linear fracture porosity (TLFP) calculated for the domain of the station-6 is %10.1 in the optimal directional drilling azimuth of 068°N (Figure 3.16e).

CHAPTER 4

SAYINDERE ROCK UNIT'S STRENGTH AND POLY-AXIAL STRESS CONDITIONS REQUIRED FOR ITS FAILURE

In this research, a special emphasis is given to the effects of natural stresses on brittle behavior of the Sayindere Formation, since it is the only regionally acknowledged fractured reservoir host rock of the SE Turkey. The Sayindere Formation is an initially non-porous, Campanian argillaceous limestone is exposed or buried in various locations proximal to right-lateral strike-slip faults within the studied region.

Since the matrix porosity have a negligible contribution to its overall porosity, the Sayindere Formation has a great fitness for the investigations on solely contribution of fractures to reservoir qualities. Therefore, mechanical response of the Sayindere Formation to natural stresses at the localities, either where it crops out or where it is buried, is investigated.

The Sayindere Formation has sufficient carbonate input to demonstrate brittleness, to bear up fractures with its ability not to collapse. On the other hand, the Sayindere Formation has sufficient clay compound to show smaller brittle failure strength under natural stresses in comparison with other limestone units with negligible clay content (e.g., Derdere, Karababa and Besni formations). Because of its distinctive proneness for fracturing, the Sayindere Formation has drawn attention as an exceptional candidate host rock to be a naturally fractured reservoir. It has therefore become more important to know its mechanical strength and elastic properties in order to estimate where it can be fractured; this is done by considering measured magnitudes of the in-situ natural stresses acting in the studied area.

4.1. Methodology

Mechanical genesis of fracturing and rheological attributes of the reservoir analogue of the Sayındere Formation were experimentally investigated by using uniaxial and triaxial compression tests and dynamic deformability tests in order to determine intrinsic mechanical parameters of the rock; the parameters include internal friction angle (ϕ), cohesion (C), uniaxial compressive strength (UCS), Mohr-Coulomb failure envelope and elastic properties.

In order to estimate the response of the rocks to the tectonic stresses, mechanical material properties of these rocks have to be given to include in the formulations to calculate stress distribution around dislocations (e.g., faults, subsidiary faults and fractures).

In order to determine Poisson ratio, elasticity modulus, shear wave modulus, p-wave modulus and bulk modulus, ultrasonic velocity (UV) tests on cylindrical rock specimens with diameters of 1.5 inch and aspect ratios of 1 using P&S wave generating equipment are conducted.

In order to determine cohesion, internal friction angle, Mohr-Coulomb failure envelope and uniaxial compressive strength (UCS) of the rock, uniaxial and tri-axial compression experiments on cylindrical rock specimens with diameters of 1.5 inch and aspect ratios of 2 using pressure vessels are conducted in the rock mechanics laboratory of the Research and Development Center of Turkish Petroleum with the permission of the institution. The specimens were sub-cored from the cores of the wells drilled in Şambayat oilfield at the depths of around 1500 meters within the horizon of the Sayındere argillaceous limestone.

The samples were taken from macroscopically undisturbed spots, such as intact rock in-between two fractures and the spots missing out drilling induced fractures. After this careful sampling, the specimens are assumed to be mostly intact, homogeneous and isotropic. The smaller-scale discontinuities that are not visible to naked eyes were neglected in the process of choosing sampling intervals within the cores. There might have still been some pre-existing microscopic dislocations or

slight differences in terms of composition. Thus, mechanical strength between the specimens, despite of these slight occurrences, can be considered as negligible.

4.2. Determination of Strength & Frictional Parameters of the Sayındere Formation

Uniaxial compressive strength (UCS) of the Sayındere Formation was determined through a series of experimental procedures. Twelve cylindrical samples with a diameter of 1.5" and about 1:2 aspect ratios in 3 sample sets were prepared. One of these sets is composed of 6 samples; half number of them was taken bed parallel while the remaining half, bed perpendicular. All samples were subjected to axial compression at unconfined condition. Other 2 sample sets are totally composed of 6 samples taken both directions, subjected to three-axial compression tests with different confining pressures ranges from 170 MPa to 390 MPa (Figures 4.1 and 4.2).

The Sayındere Formation demonstrates anisotropy in terms of UCS. The bed-parallel samples showed significantly greater strength than those bed-perpendicular samples. While the average UCS of bed-parallel samples was measured as 183 MPa, it is 130 MPa for bed-perpendicular samples (Figures 4.1 and 4.2).

Using the experimental data inventory, Mohr-Coulomb failure envelopes for bed-parallel and bed-perpendicular samples were plotted. The coefficient of internal friction values are derived from both faulting angles and slope of the Mohr-Coulomb failure envelopes and determined as about 0.73 ($\tan 36^\circ$) and 0.58 ($\tan 30^\circ$) for bed perpendicular and bed parallel specimens respectively (Figures 4.1 and 4.2).

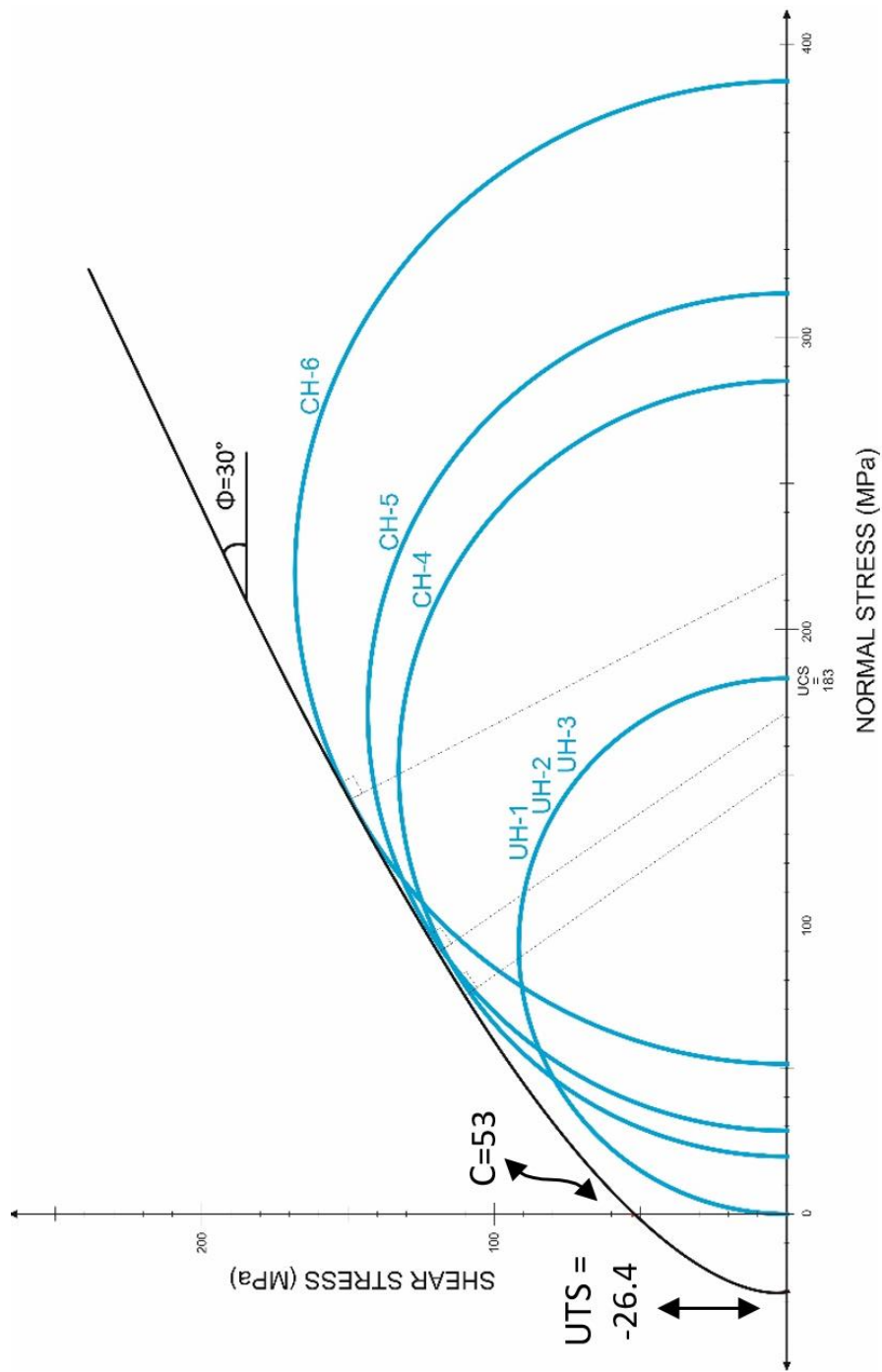


Figure 4.1. Mohr circles drawn for 6 compressive tests for strengths of bedding-parallel samples. While the three of them were subjected to unconfined compression (UH-1, 2, 3), the other three (CH-4, 5, 6) of the six samples were subjected to compression with three different confining pressures. The average 183 MPa of the unconfined compressive tests' UCS findings are in accordance with Mohr-Coulomb failure envelope constructed for the triaxial test's mohr circles.

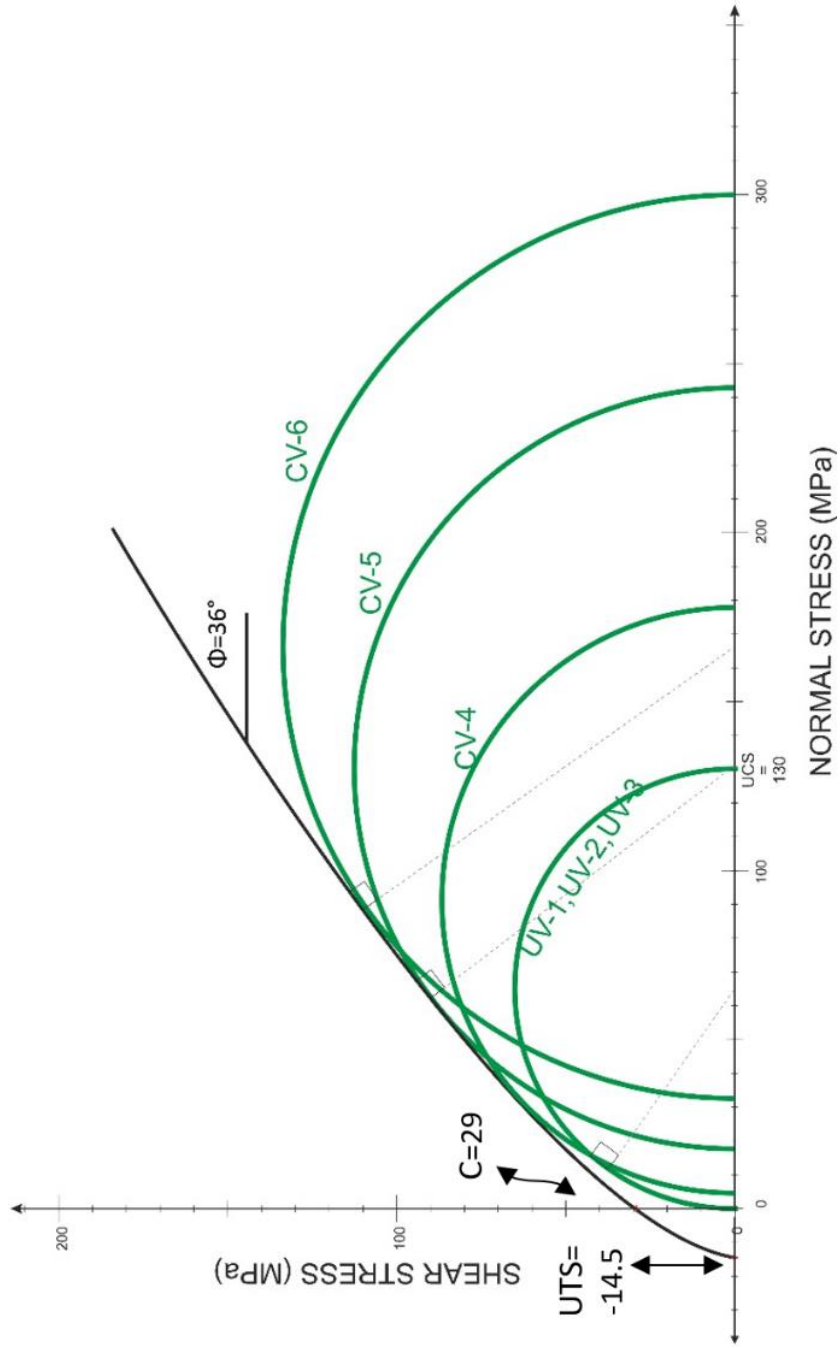


Figure 4.2. Mohr circles drawn for 6 compressive tests for strengths of vertically (perpendicular to bedding) taken samples. While the three of the samples were subjected to compressive stress with unconfined condition (UV-1, 2, 3), the other three (CV-4, 5, 6) of the six samples were subjected to triaxial compression tests with three different confining pressures. The average 130 MPa of the unconfined compressive tests' UCS findings are in an accordance with mohr-coulomb failure envelope constructed for the triaxial test's mohr circles.

Since the cohesion (C) of the rocks is not a directly measurable parameter, we derived C using its relation with the UCS and coefficient of internal friction expressed below;

$$UCS = 2C [(\mu_i^2 + 1)^{1/2} + \mu_i] \quad \text{Equation 1}$$

Thus, cohesion values of bed perpendicular and bedding parallel specimens are determined as 29 MPa and 53 MPa, respectively. Unconfined tensile strength, denoted by UTS of the unit, can be determined by using Griffith failure criterion modified by Murrell (1963) in the equation below:

$$\tau^2 = 4\sigma_n UTS^2 + 4\sigma_n UTS \quad \text{Equation 2}$$

When τ is denoted for shear stress and σ_n is denoted for normal stress. When the normal stress is taken zero, then the UTS becomes equal to the half of the shear stress, $2UTS = \tau$ (Figure 4.3).

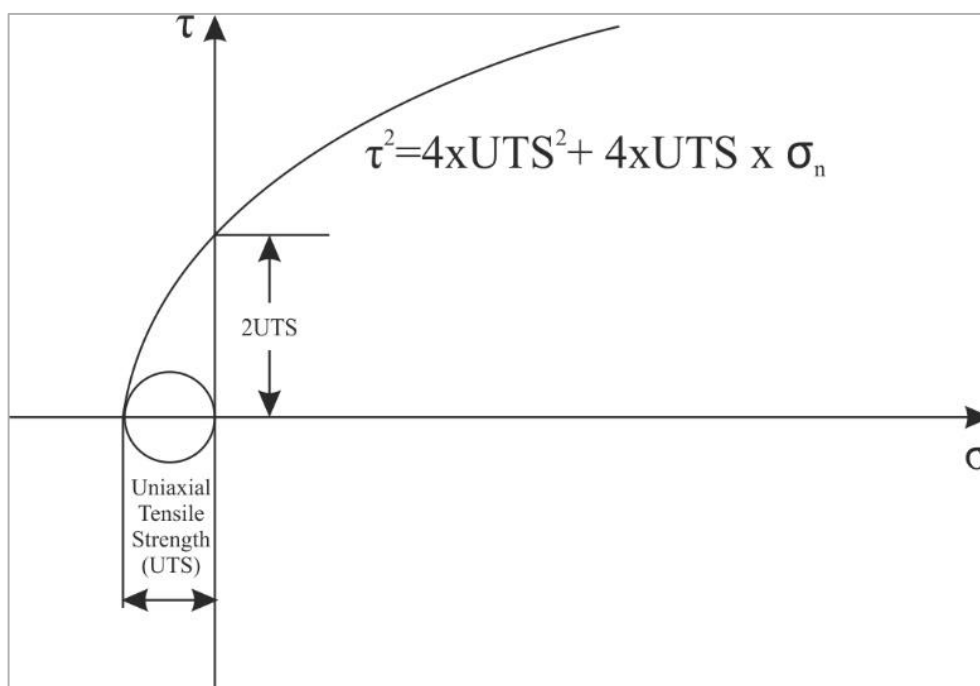


Figure 4.3. Griffith failure criterion of brittle fracture in tensile domain expressed as the equation of a Mohr envelope, modified by Murrell (1963).

Therefore, in bedding-parallel direction, UTS is estimated to be around –26.5 MPa which is half of the cohesion of theoretically intact rock (53 MPa). In bed-perpendicular directions, UTS of the rock unit was found as –14.5 MPa which is half of the derived value of cohesion (29 MPa). These strength findings are particularly important to facilitate in-situ stress measurements from wellbore breakouts by constraining both SH magnitudes as it is discussed in Chapter 5.

4.3. Determination of Elastic Parameters of the Sayindere Formation

Cylindrical samples with a diameter of 1.5" and 1:1 aspect ratio are prepared; and their density, shear and p-wave velocities are measured through velocity tests. These parameters are used in the empirical equations, which relate them with elastic properties.

During the ultrasonic velocity tests, the specimens are subjected to P and S waves, and transmission velocities of those waves are measured, using transducers placed at the tops and bottoms of the specimens. The signals reaching the transducers were amplified and monitored using an oscilloscope. Following these procedures, the transmission time intervals (Ts and Tp) and accordingly the velocities of the waves (Vs and Vp) are measured (Table 4.1).

P and S wave velocities are utilized to calculate Bulk Modulus (K), Shear Modulus (G), Poisson ratio (ν), Young Modulus (E), and P-wave Modulus (Table 4.2) using the equations given below;

$$E = \rho V_s^2 (3V_p^2 - 4V_s^2) / (V_p^2 - V_s^2), \quad \text{Equation 3}$$

$$K = \rho V_p^2 - (4/3) \rho V_s^2 \quad (\text{Pa}) \quad \text{Equation 4}$$

$$G = \rho V_s^2 \quad (\text{Pa}) \quad \text{Equation 5}$$

$$\nu = (V_p^2 - 2V_s^2) / 2(V_p^2 - V_s^2) \quad \text{Equation 6}$$

Where; ρ refers to density (kg/m³), V_p and V_s refer to P and S-wave velocities (m/s) respectively.

Table 4.1. Sayindere Formation rock specimens' dimensions, densities and seismic wave velocities that were derived from ultrasonic velocity measurements.

Specimen # / Depth (m)	Direction	h (cm)	h (inch)	ρ (g/cm ³)	T _s (μs)	V _s (m/s)	T _p (μs)	V _p (m/s)	Well
H _{1,1} / 1489	Horizontal	3.78	1.49	2.68	12	3150	7.5	5040	S ₃ -6
H _{1,2} / 1489	Horizontal	3.42	1.35	2.68	14	2443	7.2	4750	S ₃ -6
H _{2,1} / 1492	Horizontal	3.18	1.25	2.67	11.2	2839	6.3	5048	S ₃ -6
H _{2,2} / 1492	Horizontal	3.61	1.42	2.67	11.3	3195	6.2	5832	S ₃ -6
V _{2,1} / 1490	Vertical	2.65	1.05	2.68	7.6	3487	4.4	6023	S ₃ -6
V _{2,2} / 1490	Vertical	3.92	1.54	2.68	11.8	3322	7	5600	S ₃ -6
V _{3,1} / 1490	Vertical	3.56	1.40	2.68	10.8	3296	6.4	5562	S ₃ -6
V _{3,2} / 1490	Vertical	4.39	1.73	2.68	14.9	2946	8.5	5165	S ₃ -6

Table 4.2. Elastic properties of Sayindere argillaceous limestone specimens derived from ultrasonic velocity measurements.

Specimen # / Depth (m)	P-wave Modulus	-G- Shear Modulus (GPa)	-V- Poisson Ratio	-E- Modulus of Elasticity (GPa)	-K - Bulk Modulus (GPa)
H _{1.1} / 1489	68025485	26.57	0.18	62.68	0.033
H _{1.2} / 1489	60422375	15.98	0.32	42.20	0.039
H _{2.1} / 1492	67808411	21.45	0.27	54.42	0.039
H _{2.2} / 1492	90227402	27.16	0.28	69.79	0.054
V _{2.1} / 1490	97039715	32.53	0.25	81.18	0.054
V _{2.2} / 1490	83888000	29.52	0.23	72.53	0.045
V _{3.1} / 1490	82784319	29.07	0.23	71.48	0.044
V _{3.2} / 1490	71388254	23.22	0.26	58.48	0.040

4.4. Poly-Axial Failure Criterion and Stress Conditions Required to Yield the Sayindere Formation

Magnitudes of in-situ stresses are delimited by the frictional strength of the optimally oriented surfaces. In the absence of such surfaces, the natural stresses accumulate up to the host rocks' failure whose failure conditions are determined by the poly-axial failure criterion. In certain stress intensification domains (e.g., vicinities of compressional quadrants or locked portions of faults components of in-situ natural stresses) shows a significant increase up to a level at which the host rock's failure criterion is reached. Therefore it must be anticipated that the in-situ stress magnitudes and directions are modified and re-directed near faults. On the other hand, far-field stresses, which represent means of the stress magnitudes and directions for broader areas including away-from-fault locations, can provide us a strong reference point to use in both failure criterion and stress perturbation analyses. As explained in the Chapter 5, three principal stresses are therefore determined for varying depths in a region of interest to construct a mechanical earth model and then to use for the analyses mentioned above. As explained in the Chapter 5, vertical stress magnitudes increase linearly with depth, following the relation given by equation 9. Nevertheless, maximum (S_H) and minimum (S_h) horizontal stresses decouple for many reason; e.g., directional tectonic confinement, tectonic escape mechanism, azimuthal mechanical anisotropy, stress field perturbations around faults, etc. Once the principal stresses are measured for certain depths they could be extrapolated to estimate poly-axial stress conditions at other depth intervals of interest. Measuring in-situ stresses (S_H , S_h and S_v) in a decent level of confidence is the first step to speculate if there may be fracture formations within a particular tectonic unit. Nevertheless, some mechanical qualities of the rock unit of interest must be available to speculate further. The unconfined compressive strength (UCS), cohesion (C), coefficient of internal friction (μ_i), elastic moduli and Poisson's ratio (ν) of the Sayindere Formation are therefore determined by conducting confined and unconfined compressive tests and by measuring seismic wave velocities as explained in the preceding sections of this chapter.

As will be discussed in the Chapter 6, conditions of reactivation of pre-existing surfaces are defined by optimally oriented planes with negligible cohesion and their coefficient of static friction (μ_s) or static (sliding) friction angle (ϕ_s). When it comes to the formation of new fractures, a significant amount of cohesion, unconfined compressive strength (UCS) and coefficient of internal friction (μ_i) or internal friction angle (ϕ_i) of the rock unit “*need to be reached*” to failure conditions. If we reckon the instantaneous values of in-situ stress measurements (Chapter 5) at certain depths of the wells in Şambayat Oilfield as (stationary) far field principal stresses, though they can activate some pre-existing surfaces, they are apparently not sufficient to form new fractures on a rock unit with 183 MPa unconfined compressive strength, 53 MPa of cohesion, 0.58 of coefficient of internal friction and 30° of internal friction angle as it is determined by conducting compressive tests on core specimens of the Sayındere Formation (Figures 4.1). Accordingly, a significant build-up of S_H , a significant drop of S_h or a moderate divergence of both magnitudes is necessary to generate new fractures within theoretically intact sub-domains. When we show principal stress magnitudes that are necessary for failure as three-dimensional Mohr diagrams (Mohr-Coulomb and Griffith criterion, using average strength parameters for bed-parallel and bed- perpendicular samples for simplification, $C_{o(av)} = 41$ MPa, $UTS_{(Av)} = -20,5$ and $\phi_{i(Av)} = 33^\circ$ and using average static friction angle value for optimally oriented faults from 1500 m to 2500 m burial depths for simplification, $\phi_s = 27^\circ$), it is seen that the far field stress state for the depths mentioned above is sufficient to reactivate fault surfaces that are most optimally oriented, in their presence, nevertheless some degree of amplification of S_H , decrease of S_h or increase of P_p or combination of those deviations are necessary for failure of an intact rock medium (Figure 4.4). Since the significant P_p increase is considered as an extreme case, by keeping it constant, two cases are possible as explained as follows (Figure 4.4a, b);

- 1st case: P_p and S_h are kept stationary while S_H is increased up to failure,
- 2nd case: P_p is kept stationary while S_h and S_H are moderately decreased and increased respectively up to failure.

To be more specific about the magnitudes, we can use modified Mohr-Coulomb poly-axial failure criteria proposed by Singh et al. (2011) that takes into account non-linearity of Mohr-Coulomb failure envelope at high pressures and importance of relative magnitude of intermediate principal stress, σ_2 as shown below;

$$\sigma_1 - \sigma_3 = \text{UCS} + \frac{2\sin\phi_i}{1-\sin\phi_i} \left(\frac{\sigma_2 + \sigma_3}{2} \right) - \frac{1}{\text{UCS}} \frac{\sin\phi_i}{1-\sin\phi_i} \left(\frac{\sigma_2^2 + \sigma_3^2}{2} \right) \quad \text{Equation 7}$$

Where ϕ_i is the internal friction angle and the expression is applicable for the stress range; $0 \leq \sigma_3 \leq \sigma_2 \leq \text{UCS}$. Three principal stresses for different depths are calculated (such as, 1500 m, 1810 m, 1880 m, 2200 m and 2500 m), by using our mechanical earth model. It is therefore shown that, to create new fractures within intact mediums of the Sayindere Formation, poly-axial stresses and required S_H' need to increase while S_h' is to decrease according to the modified Mohr-Coulomb poly-axial criteria (Equation 7) proposed by Singh et al. (2011) (see Table 4.3 for more information).

Table 4.3. Critical principal stress magnitudes that must be realized due to perturbation of stress field near fault tips to form new fractures and subsidiary faults within a theoretically intact and cohesive blocks of the Sayindere argillaceous limestone. The units for the numerical values listed in the depth column are in meters whereas others are MPa.

Depth	P_P	S_V	S_h	S_H	Required S_h - S_H couple for failure					S_V'	S_h'	S_H'
1500	15	38	34	79	0-155	15-188	20-199	25-210	34-229	23	19	64
1810	18.5	46	39	88	0-155	15-189	20-200	25-211	39-240	27	20	70
1880	19.5	48	40	90	0-155	15-189	20-201	25-212	40-243	29	21	71
2200	23	56	45	99	0-155	15-190	20-201	25-212	45-255	33	22	76
2500	26	64	50	108	0-155	15-190	20-202	25-213	50-266	38	24	82

The stress magnitudes required to form new faults and fractures within the Sayindere Formation based on its strength parameters presented in the Figures 4.1 and 4.2 is expected to realize in the areas where optimally oriented faults terminates. It is observed that there is such a geometrical association between fault terminations and asphaltite-filled, exhumed fracture corridors in the field around Kuyulu site as explained in the Chapter 3. Though the magnitudes of the in-situ stresses are delimited by the frictional strength coefficient of the optimally oriented faults in

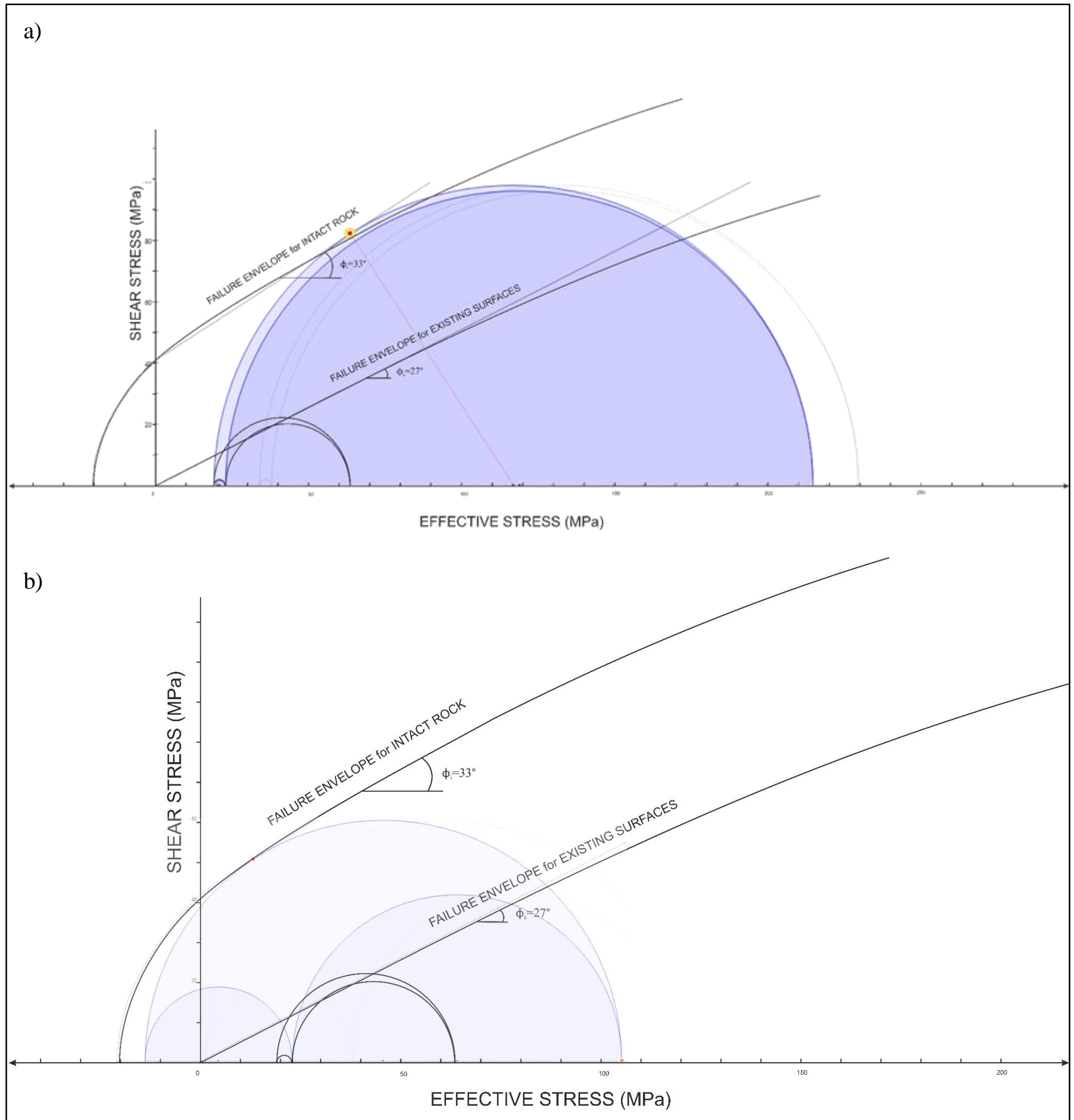


Figure 4.4. In 3-dimensional Mohr diagrams, remote effective principal stresses (black semi-circles) that are derived from MEM for the studied region for 1500 m burial depth and theoretical local stress states (purple semi-circles) that were denoted as 1st and 2nd cases are shown along with failure envelopes of pre-existing cohesionless surfaces and of intact rock medium. In both cases, far field stress state is sufficient to reactivate cohesionless, optimally oriented faults but not sufficient to create a new faults or fractures. **(a)** the 1st case that is corresponding to a theoretical local stress state whose amplified S_H component (purple semi circles) is demonstrated. It is deduced that about 2-fold increase (from 79 MPa to 230 MPa) is required to create new faults and fractures. **(b)** The 2nd case that is corresponding to a theoretical local stress state whose moderately decreased S_H and moderately increased S_H components is demonstrated. It is seen that only a 50% increase in the S_H (from 79 MPa to 120 MPa) can be sufficient to create new faults and fractures when accompanied by a decrease in S_H .

their presence, stress perturbations and concentrations around fault tips and in areas with non-optimally oriented faults (e.g. locked segments), such high magnitudes can be reached. Therefore slip tendency analysis were carried out to be used as the filtering criteria to specify the optimally oriented faults' dip and azimuth intervals for certain poly-axial stress conditions. The natural stresses are calculated for the target units' burial depth intervals (1500–2500 m) within the Şambayat oilfield (see Chapters 6 and 7 for details).

4.5. Stress Perturbation Analyses & Estimating the Scale of Magnitude Buildups

In a compressively stressed elastic medium with defects (e.g., open holes, voids, joints, faults, etc.) differential stress tend to amplify in the compressional quadrants of the longitudinal axes of defects. As it can be inferred from Table 4.3, to form a primary fracture within the Sayindere argillaceous limestone, S_H magnitude must show 1-fold increase if the S_h decreases for about %50, or S_H must increase 1.5-fold if the magnitude of s_h remains stable. As the changes of stress field along faults were investigated and numerically described by de Joussineau et al. (2003) it can be adapted that it is possible for the S_H to increase more than 1.66-fold and for the S_h to decrease more than %50 with respect to their far field magnitudes especially at the vicinities of compressional quadrants of the fault tips, when the far field stress ratio σ_3/σ_1 is set to 0.7 (Figure 4.5). De Joussineau et al. (2003) performed photoelastic experiments on birefringent polymethylmethacrylate (PMMA) plates that present fringes named isoclinics when subjected to mechanical stresses. They implemented biaxial compression and interpreted birefringent patterns as contours and trajectories of principle stresses. Those patterns are indications of photoelastic behavior of originally isotropic, birefringent materials which then gain anisotropy through elastic deformation induced by loading analogously to the natural rocks. De Joussineau et al. (2003) observed and interpreted perturbed stress field by utilizing isoclinics appear in the PMMA sample when subjected to biaxial loading with varying principle stress (σ_3/σ_1) ratios (e.g., 0.0, 0.2, 0.4, 0.6 and 0.7), and illustrated varying intensity and direction of local σ_1 values (σ_{1L}) around either a single defect or around a compressive jog formed by two en-échelon defects. From their results it is inferred that maximum principal stress value could locally increase far beyond the

sufficient values for local brittle failure of the Sayındere Formation when far field stresses applied in the measured magnitudes as will be shown in the Chapter 5. Changes of stress field along faults were also mathematically described and modelled by Hirano and Yamashita (2011) in terms of Coulomb failure function (CFF) which is defined as;

$$\text{CFF} = \tau + \mu_i \sigma_n, \quad \text{Equation 8}$$

Where τ is the shear stress, μ_i is the coefficient of internal friction and σ_n is the normal stress acting on a hypothetical fault plane. As inferred from their results, it is possible for the CFF to go up to 6 times higher than its remote magnitude specifically around the tips of the fault planes which corresponds to the drop of the principal stress ratio (S_h/S_H) down to 0.1. This solution also indicates that the magnitude of S_H could amplify 5 times around fault tips when S_h is assumed to remain constant. Therefore secondary hierarchy stress fields around faults are proved to be sufficient to form fracture corridors as they move both direction of the faults as they propagate.

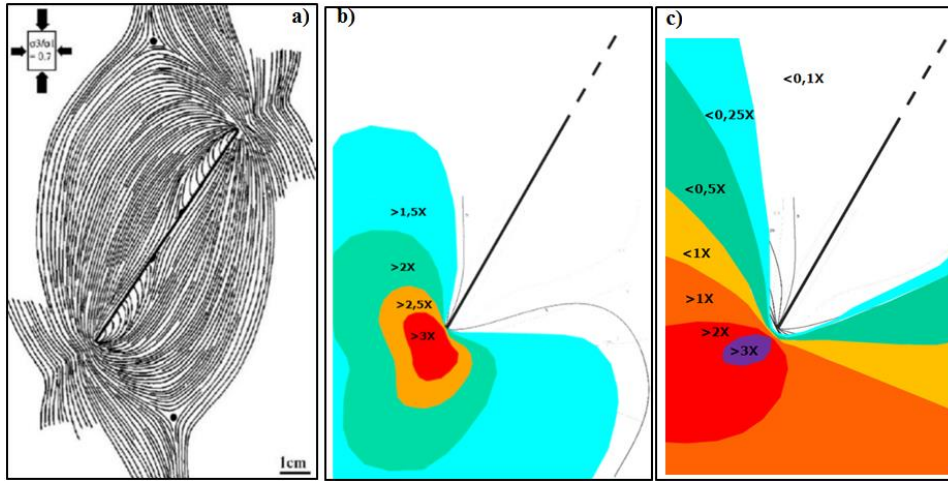


Figure 4.5. (a) Local maximum principal stress (σ_{1L}) trajectories form around a single, cohesion-less defect. Density distribution of trajectories indicates magnitude buildups where the trajectories are closely spaced and magnitude drops where they are sparsely spaced. Fault sub-parallel alignment of σ_{1L} trajectories near compressive quadrants is notable. (b) Modified contours for amplifications of maximum principal stress magnitudes around the leading fault tip of a fault derived from photoelastic and numerical experiments conducted by Joussineau et al. (2003) under biaxial loading when σ_3/σ_1 stress ratio is 0.7. X's represent remote stress and the numbers represent factors. (c) Contours of amplification and drops of remote minimum horizontal stress around the leading fault tip. X's represent remote stress and the numbers represent factors more than 2 fold increase of σ_1 and more than %50 drop in σ_3 magnitudes are notable.

CHAPTER 5

IN-SITU STRESS ESTIMATIONS AND MEASUREMENTS

5.1. In-Situ Stress Estimations

According to Anderson's theory of faulting (Anderson, 1942/1951) compressive regimes that favor reverse faulting necessitate principal stresses to be arranged in a style in which both the most and the least horizontal stresses (S_H and S_h , respectively) to exceed the vertical stress (S_V) in magnitude ($S_H \geq S_h \geq S_V$). This process has prevailed during periods when the Arabian Plate preserved its mechanical integrity sufficiently enough to impede crustal fragments' horizontal movement parallel to collision front. Lateral confinement of the colliding plates formed boundary conditions in a fashion that are in favor of strengthening of minimum horizontal stress, which enabled reverse faulting regime ($S_H \geq S_h \geq S_V$) prior to the Mid-Miocene. These boundary conditions were existing in the Adıyaman region until fragmentation, and escape mechanism have started to prevail through the formation of a fully-fledged conjugate fault network. In other words, as extent of compressive intra-plate deformation progressively increased and squeezed, the northern margin of the Arabian Plate was subjected to some degree of fragmentation; the boundary conditions of northern Arabian Plate was then gradually transformed into a new configuration in which the magnitude of the least horizontal stress has decreased significantly and caused strike-slip faulting regime to prevail ($S_H \geq S_V \geq S_h$). According to some (Amadei and Stephansson, 1997; Brown and Hoek, 1978; Herget, 1974; Zang et al., 2012), magnitudes of vertical stresses can be estimated by overburden weight and they increase linearly with depth (Brown and Hoek, 1978). Within Şambayat Oilfield, today's depth of the targeted Sayındere Formation is mainly around 1500 meters. For this depth, current vertical stress (S_V) is calculated, by using equation below, to be around 39 MPa:

$$S_V = \rho * g * h$$

Equation 9

Where ρ is average density of the overlying sediments, which is around 2.6 g/cm^3 , g is the gravitational constant of 9.8 m/s^2 and h is the burial depth of today. The Sayindere Formation horizon is considered to have been uplifting since the onset of reverse faulting regime and the horizon was at about 2500 m at the time of onset of the strike-slip regime in early Miocene (average thickness of post-Campanian to pre-Miocene units; see Figure 1.2 for details). At the time of the burial, maxima for the Sayindere Formation under the strike-slip regime, the vertical stress was about 64 MPa. Horizontal principal stresses are however expected to demonstrate a great decoupling due to additional contribution of tectonic compression in N–S direction. Whereas one portion of the horizontal stresses is originated from vertical stress and is proportional to the depth; the other portion of them is exerted by tectonic stresses and shows no significant change with depth (Taherynia et al., 2016). In order to estimate the proportion of the sum of the horizontal stresses with vertical stress in different tectonic regimes, an empirical value called lateral stress coefficient (K) was proposed as shown below:

$$K = 0.5 (S_H + S_h) / S_v \quad \text{Equation 10}$$

Domain of variation of K values (Figure 5.1) in reverse faulting regimes is between 1.0 and 3.12 ($1 < K < 3.12$) where it is close to 1.0 in the strike-slip faulting regimes (Jamison and Cook, 1978).

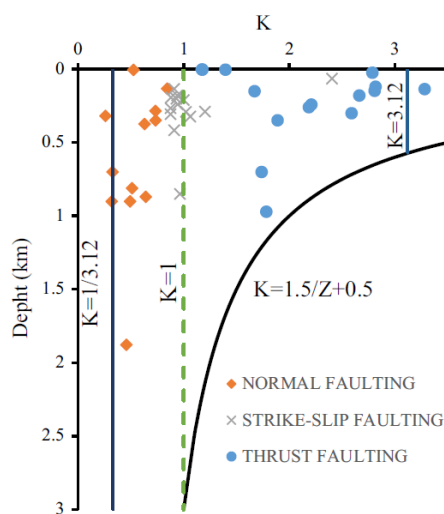


Figure 5.1. Domain of variation for K values in different tectonic regimes. Taken from Taherynia et al. (2016); data is from Jamison and Cook (1978).

Provided that the study area has been experiencing a strike-slip faulting with reverse component since Early Miocene, it is straightforward to assume K value to be above 1.0, since the values of K below 1.0 correspond to normal faulting. Neo-tectonic regime of the study area has also repeatedly proved to be as strike-slip faulting regime by earthquakes and fault plane solutions derived from seismic radiations. In this study, the most recent moderately violent earthquakes (5.6 Mw and 5.2 Mw) and their aftershocks along with their rupture depths are considered as a constrain parameters for prediction of lateral stress coefficient K .

5.1.1. Local Earthquakes as Natural Confirmations of Strike-slip Faulting

In March 2, 2017 and April 24, 2018 moderately violent earthquakes (5.6 and 5.2 Mw, respectively) ruptured at about 13.5 km and 10.0 km depths in Samsat County of Adıyaman Province (Figure 5.2.).

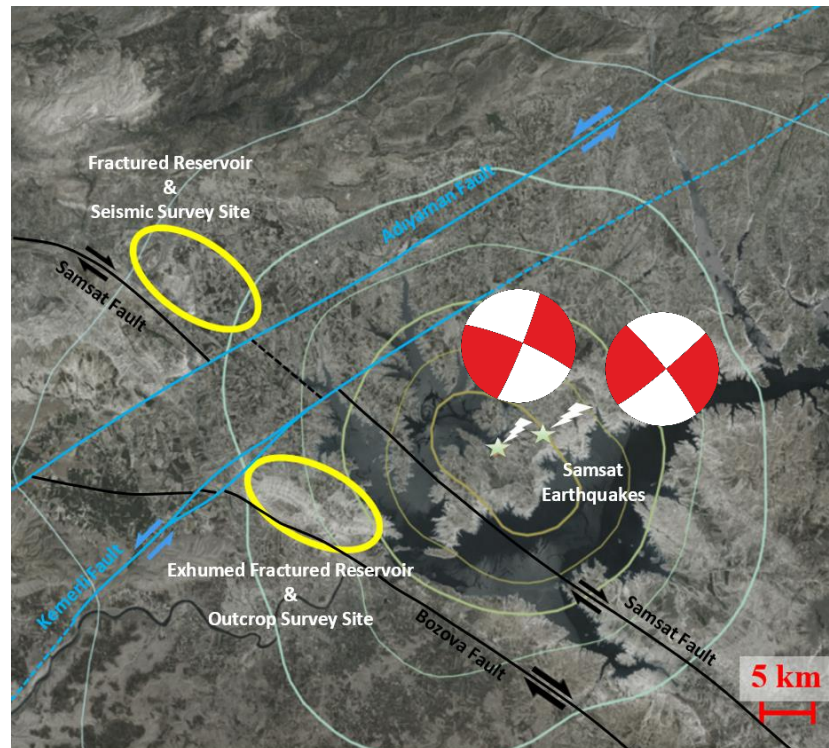


Figure 5.2. Star signs indicate epicenters of the most recent moderately violent earthquakes; beach ball representation of fault plane solution of the earthquake indicates a strike-slip faulting. Yellow ellipses shows Şambayat Oilfield and outcrop data collection site for fractures of the Sayındere Formation. Blue and black lines represents left lateral and right lateral strike slip fault respectively. Earthquake data compiled from USGS and Kandilli Observatory and Earthquake Research Institute.

The earthquakes occurred on a right-lateral strike-slip fault; more, epicenters are too close to both outcrop (15 km) and seismic survey (30 km) sites of this study. Aftershocks aligned at WNW and ESE extension of one of the orthogonal nodal plane pairs address the fact that right-lateral slip occurred on those planes. The main values of strikes, dips and rake angles measured on the slip planes of primary earthquake and aftershocks are about 322° , 51° and -172° respectively (data compiled from USGS, AFAD and Kandilli Observatory). Those measurements imply that almost pure strike-slip faulting is prevailing in a specific interval of 7 to 10 km and an oblique strike-slip regime with normal dip-slip component at locations deeper than 10 km. This data is utilized to better approximate the actualized value of K for the studied area by providing a confidence factor to fix it around 1.0 for specific earthquake hypocenters' depth interval of 7 km.

5.1.2. Upper and Lower Bound Estimations for Lateral Stress Coefficient, K

The value of K is so strongly dependent on depth that in some circumstances as of the studied area of this research, the faulting regime changes along with depth. In order to define the variation of K with depth, Brown and Hoek (1978) suggested lower and upper bounds of K values for increasing depths:

$$[(0.1/z) + 0.3] \leq K \leq [(1.5/z) + 0.5] \text{ where } z = \text{depth from ground surface (km)}$$

McCutchen (1982) and then Sheorey (1994) have proposed a spherical shell model for Earth's crust and claimed that the crust is a homogeneous and elastically isotropic shell, which lies onto a thermo-elastic mantle and deformed by gravity. They algebraically expressed the change of the lateral stress coefficient with depth as $K = a/z + b$. Many researchers have however determined two delimiting expressions (lower and upper) to narrow down the estimation of K value. Zang et al. (2012) used biaxial stress model (based on Poisson ratio) to determine lower bound; they have also proposed, by adapting lithological factors, an upper bound expression for sedimentary rocks and hard rocks as follows;

$$K \leq 3/4z + 4/5, \text{ for sedimentary successions}$$

$$K \leq 6/5z + 4/5, \text{ for hard rocks}$$

As it will be shown later in this chapter (see section on ‘in-situ stress measurements’), measured poly-axial stress condition of the present region gives a compatible upper bound curve with the one that is adapted for mixed rock types and basins. This can be explained by the fact that the rock units beneath the region of this research are composed partly of hard rocks (e.g., meta-sediments, meta-volcanic and obducted ophiolites along with sedimentary successions at shallower depths). Nevertheless, as earthquake focal mechanisms (see above section) proved that, earthquakes in Adiyaman region as most of the northern Arabian foreland occur in strike-slip setting, which necessitates the lateral stress coefficient (K) to be around 1.0 at earthquake hypocenters.

It is therefore straightforward to constrain estimations of lateral stress coefficient, K, with such direct proofs. Using in-situ stress measurements and earthquake data (Figure 5.2), the upper bound expression is adopted as shown below;

$$K \leq 1/z + \frac{9}{10} \quad \text{Equation 11}$$

Nevertheless, based on field observations on surfaced contemporarily active reverse faults deforming young units in the study area, which are more compatible with expectation that K should be higher than 1.0 at shallower depths to allow reverse faulting. Lower bound expression of Brown and Hoek (1978) is also used. Accordingly, the bounds used in this study for K are calculated as shown below:

$$[(0.1/z) + 0.3] \leq K \leq 1/z + 9/10 \quad \text{Equation 12}$$

On the other hand, K bound values converge to a unity at depths. For example, the upper bound of K is expected to be around 1.5 at 1500 m and to decrease at further depths. Since 5.5 magnitude of the Samsat earthquake (in March 2017) ruptured at 7 km depth; it is compatible with almost pure strike-slip faulting as demonstrated by focal mechanism (fault plane solution). It is therefore suggested that actualized K values are not expected to be lower than 1.0 at depths shallower than 7 km. Thus, within the depth interval of 1.5–2.5 km’s where the Sayindere Formation horizon is located or has ever located since the onset time of primary oil expulsion in the region, the tectonic coefficient K is expected to show a slight

variation between far above 1.0 and just below 1.5. Actualized tectonic coefficient K is finally measured as to be around 1.37 ± 0.13 according to the upper bound expression (Equations 11 and 12). The measured (actualized) K values exactly coincide with upper bound estimation curve. Accordingly, it can therefore be inferred that tectonic faulting regime must be varied from 1.5 km to 2.5 km as strike-slip regime with a slight reverse component and a purer strike-slip regime, respectively. Thus, ratio between in-situ vertical and sum of horizontal stresses at 1.5 to 2.5 km depth interval would be as follows;

$$3 S_V \cong (S_H + S_h) \text{ when } z = 1500 \text{ m}$$

$$2.5 S_V \cong (S_H + S_h) \text{ when } z = 2500 \text{ m}$$

With measured S_V values for the Sayındere Formation burial intervals, sum of lateral stress magnitudes corresponding to known vertical stresses would be estimated as shown below;

$$z = 1500 \text{ m}; S_V \cong 38 \text{ MPa}; S_H + S_h \cong 113 \text{ MPa}$$

$$z = 2500 \text{ m}; S_V \cong 64 \text{ MPa}; S_H + S_h \cong 158 \text{ MPa}$$

5.1.3. Estimations of Tectonic Stress Ratio (S_h/S_H)

To implement a poly-axial failure criterion, or to construct a mechanical earth model, it is not sufficient to only calculate, by utilizing the K values, the sum of the horizontal stress magnitudes. It is also necessary to put forward how horizontal stresses decouple in an oblique and strike-slip faulting regime. Based on the database of Quantitative World Stress Map (Zang et al., 2012) compiled from in-situ stress measurements within regions where reverse and strike-slip faulting are dominant tectonic regimes, the main values of S_h/S_H “tectonic stress ratios” are found to be 0.57 and 0.53, respectively. In the study area of this research, the strike-slip regime is expected to prevail at the depths greater than 1000 m. Therefore, within exhumation history of the Şambayat oilfield, an oblique-slip faulting regime with minor thrust component can be considered to have been prevailing from the times when Sayındere Formation was located approximately at a depth of 2500 m bsl (also the oil expulsion time in the region) to the times when the same unit was elevated to

about 1500 m bsl. Tectonic stress ratio for the region of this research is therefore expected to be about 0.53 since the strike-slip faulting is the pertaining tectonic regime in the area. With respect to the vertical profiles of principal stresses, measured and presented here, it is shown that the tectonic stress ratio tends to increase with depth. Even though the estimated value of 0.53 is reached at the depths below 6000 m, this value goes down to 0.4's at the shallower depths within the studied area. Nevertheless, this value is considered to have been higher during earlier times in the geological history. It could be deduced that the hanging wall of the Samsat Fault, where the Şambayat oilfield is located, has undergone an elevation through a dextral radial translation. The tectonic block comprising Şambayat oilfield was later unloaded primarily through erosion since then. When a reverse faulting is considered to have been prevailing as a consequence of pure continental collision between nearly intact Arabian Plate and Eurasian Plate, the Arabian Plate was having negligible intracontinental weakness zones or fragmentation. Lack of sufficiently populated weakness zones within northern Arabian margin at the early stages of convergent movement back to Maastrichtian is considered to impose a sufficient lateral strength to impede escape tectonics and caused proportionally high least horizontal stress magnitudes (S_h) surpassing S_v magnitudes. This phenomenon is considered as responsible for a pure reverse faulting during pre-Miocene times in the studied region. On the progressive stages of deformation of the Arabian Plate, the plate have scarred with increasing number of faults and fractures, which lead to a collapse in its lateral strength (confinement). The least horizontal stress magnitudes (S_h) have decreased with the decrease of lateral strength of the continent and became lower than S_v magnitudes after the continent had a sufficient amount of plastic deformation and fragmentation. Since late Miocene, the tectonic regime of the study area has been oblique-slip faulting with both reverse and sinistral components even though its character changes with the depth. Though its obliquity changes with depth, strike-slip faulting regime is predominant for wider range of depths in the region as seen from earthquake focal mechanisms as of today (this will be explained later in this chapter). Accordingly, the tectonic stress ratio is expected to be around 0.53 for the widest range of depths within the present study area.

5.2. In-Situ Stress Measurements

5.2.1. Determination of the Least Principal Stress (σ_3) from Leak-off Tests

As a drilling operation, leak-off tests (LOT) are carried out either (i) to determine equivalent mud weight in order to maintain well stability by not fracturing the formation while drilling or (ii) to determine minimum principal stress that is used as an input to construct mechanical earth models (MEM's). As it is explained later in this chapter, in order to determine shear and normal stresses on arbitrarily oriented natural faults, it is required to know each of the three principal stresses. Thus, tendency of slip and hydraulic activity of any fault in a given geomechanical environment can be speculated.

To perform a successful leak-off test, the casing is cemented in a given depth and the well is drilled about 5 m. This open section of the borehole is pressurized up to the initiation of a hydraulic fracture. Theoretically, the magnitude of this pressure is reckoned as the least principal stress. In a standard procedure that must be followed during the leak-off tests, pressure vs volume charts are constructed while a constant flow rate is maintained. The point where the curve deviates from linearity at the first pressurization phase is denoted as leak-off point (LOP) and this corresponds to the formation of extra accommodation space on the wellbore wall by the opening of the hydraulic fracture (Figure 5.3). The pressure magnitudes changing during the tests are measured at the surface; therefore, to determine the least principal stress at the depth of the test, the pressure formed due to the column of the wellbore fluid must be added to the pressure measured at the leak-off point. If the pressurization is stopped before reaching LOP, then the test is called as formation integrity test (FIT). FIT's are performed mostly to determine the safe interval of mud pressure during drilling and not to proceed to the LOP due to the well stability concerns. The FIT magnitudes cannot be used as a parameter to determine least principal stress. Nevertheless, they can give an idea about its lower limits. If the pressurization is stopped before reaching LOP, then the test is called as formation integrity test (FIT). FIT's are performed mostly to determine the safe interval of mud pressure during drilling and not to proceed to the LOP due to the well stability concerns. The FIT magnitudes cannot be used as a parameter to determine least principal stress.

Nevertheless, they can give an idea about its lower limits. If the pressurization is kept increasing after the LOP is reached, the test is called as extended leak-off test (XLOT). During XLOT's, right after a peak strength of the formation against pressurization is reached (the formation breakdown pressure: FBP), the hydraulic fractures starts to propagate away from the wellbore wall. And due to the addition of more accommodation space that is composed of wider and deeper fracture apertures, the pressure drops down and gets stabilized in a magnitude at which the fractures propagate at a constant rate (fracture propagation pressure: FPP). FPP is more or less equal to the LOP and it is a more distinctive tool to determine σ_3 in comparison with LOP. It can only be acquired with further pressurization tests (XLOT), and this is mostly avoided because of the well stability concerns especially in fractured reservoir oilfields (such as the Şambayat oilfield). Therefore, only LOT's were performed in the Şambayat area and we could only use LOP data to constrain and determine σ_3 . During the XLO Tests' FPP stage, the pressure measurement was performed right after ceasing flow into the well; the instantaneous shut-in pressure (ISIP) can be obtained during this time. It also corresponds to LOP and FPP and is a more reliable σ_3 indicator since it eliminates additional pressure effect associated with friction (cf. Haimson and Fairhurst, 1967).

If there are concerns about significant friction losses due to the viscosity of the selected circulation fluid, fracture closure pressure (FCP) can also be used to determine σ_3 . This is done by observing pressure decrease versus time of \sqrt{t} charts that is used to detect the deflection of the curves from linearity (Nolte and Economides, 1989).

LOT's performed in the wells drilled in Adıyaman province, the broader area comprising also the Şambayat Oilfield, showed that the σ_3 's measured at depths of 1760 m, 2020 m 2140 m and 2700 m are much lower than the calculated S_v 's from the measured S_v gradient (Figure 5.4). The σ_3 from the LOTs is therefore associated with the minimum horizontal stress (S_h) in the study area. According to Andersonian theory of faulting, if S_h is the least principal stress (as it is found so in the study area), the strike-slip faulting must be the prevailing tectonic regime in a given area.

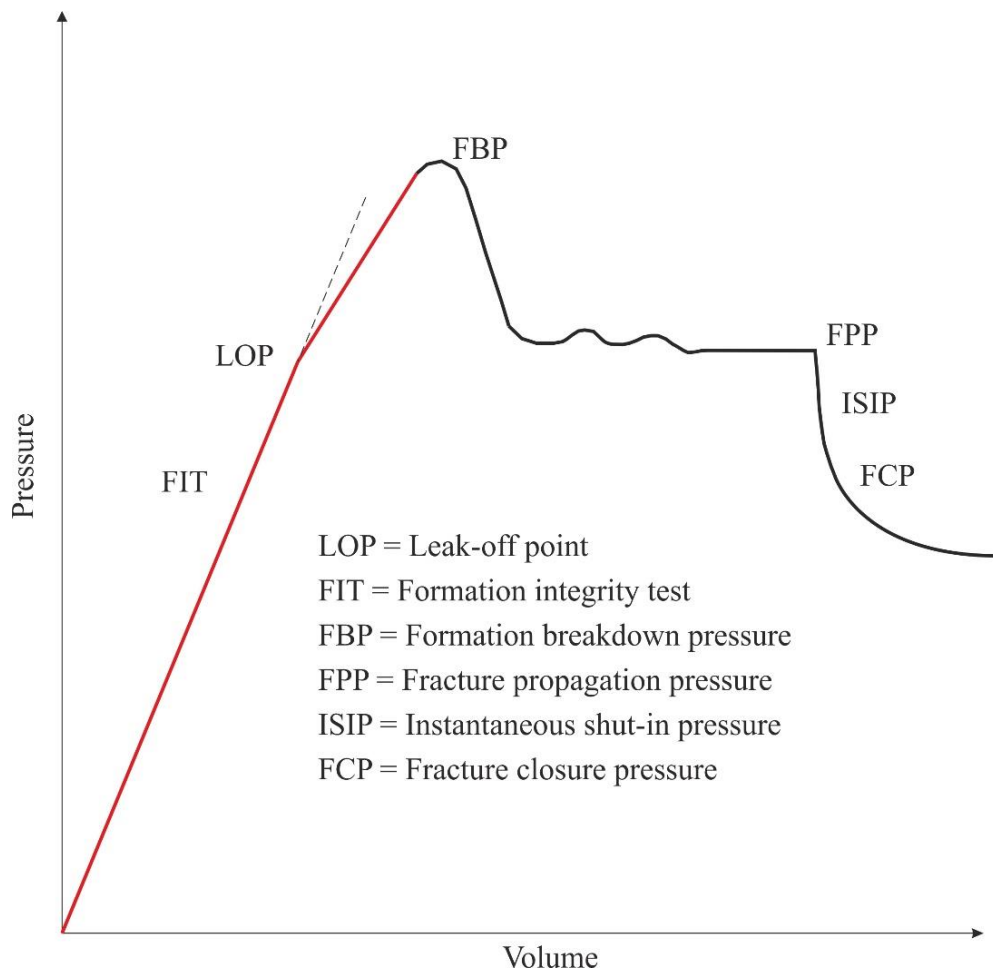


Figure 5.3. Schematized stages of a fully-fledged XLOT, the extended leak-off test (red and black line combined). Modified after Zoback (2007). The red line represents the Leak-off test stages that are also used in this study.

5.2.2. Constraining S_H from Borehole Breakouts

Borehole breakouts are products of a compressive failure process which takes place when the circumferential “*Hoop*” stress around the wellbore exceeds the strength of the rock. This leads to a compressive failure of the rock surrounding the wellbore (Bell and Gough, 1979; Zoback et al., 1985; Bell, 1989). Since such a free artificial surface cannot withstand shear traction, stress trajectories show a tendency to bend in such a fashion as to be aligned perpendicular and parallel to the wellbore wall as shown in the figure below (Figure 5.4).

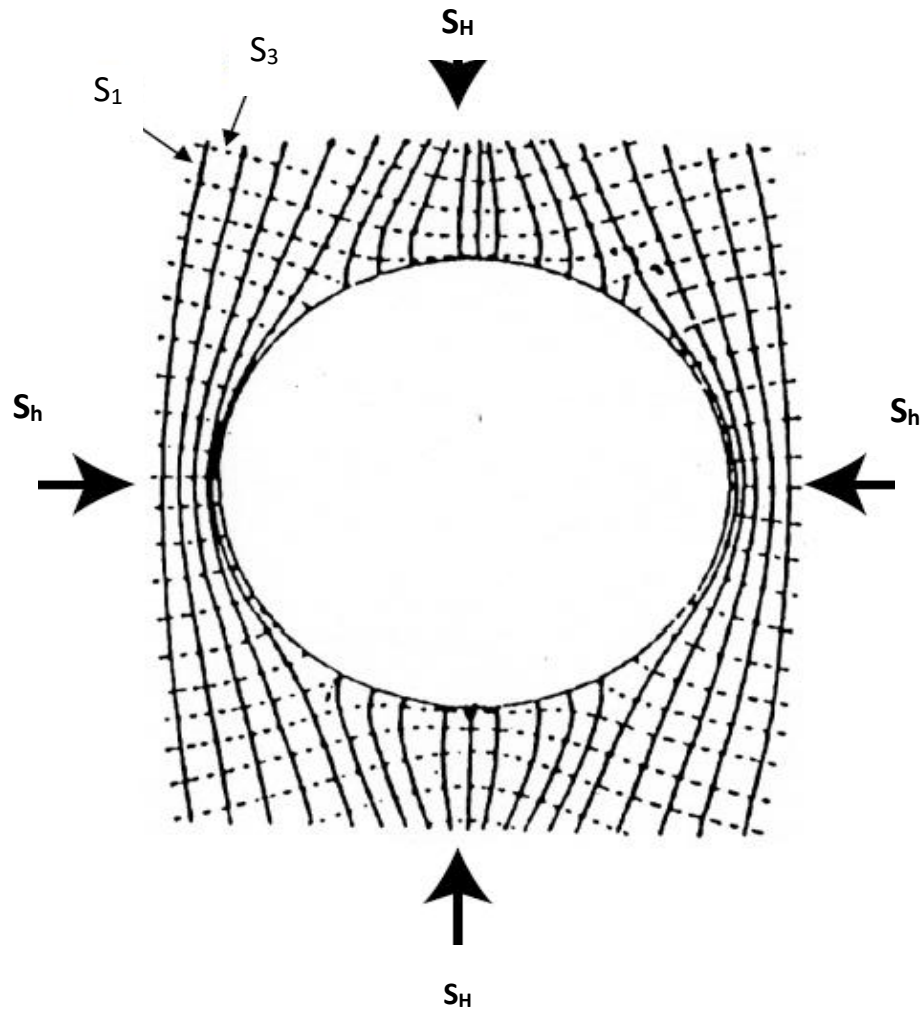


Figure 5.4. Trajectories of principal stress around a cylindrical opening in a bi-axial stress field based on Kirsch equations (Kirsch, 1898). The trajectories are inclined to be parallel or perpendicular to the free surface of the wellbore wall. At the azimuth of S_h stresses are more compressive since the trajectories of S_H converge and accumulate whereas at the azimuth of S_H stresses are less compressive since the trajectories diverge and aligned in a sparsely populated fashion. The figure is taken from Zoback (2007).

When drilling equipment and any other material removed from the well, far field stress can no longer be counteracted and intensifies at the azimuth of S_h while weakens at the azimuth of the S_H . Kirsch (1898) mathematically defined how elastic stress field perturbed and principal stresses change around such cylindrical openings (e.g., wellbore walls under one directional compression in a cylindrical coordinate system) by the following equations;

$$\sigma_{rr} = \frac{(S_H + S_h - 2P_o)}{2} \times \left(1 - \frac{R^2}{r^2}\right) + \frac{(S_H - S_h)}{2} \times \left(1 - \frac{4R^2}{r^2} + \frac{3R^4}{r^4}\right) \times \cos 2\theta + \frac{P_o R^2}{r^2}$$

Equation 13

$$\sigma_{\theta\theta} = \frac{(S_H + S_h - 2P_o)}{2} \times \left(1 - \frac{R^2}{r^2}\right) - \frac{(S_H - S_h)}{2} \times \left(1 + \frac{3R^4}{r^4}\right) \times \cos 2\theta + \frac{P_o R^2}{r^2} - \sigma^{\Delta T}$$

Equation 14

$$\tau_{r\theta} = \frac{(S_H - S_h)}{2} \times \left(1 + \frac{2R^2}{r^2} + \frac{3R^4}{r^4}\right) \times \sin 2\theta$$

Equation 15

where r is the radius of the wellbore, R , distance from the wellbore center, θ , angle measured from the azimuth of S_H , ΔP , pressure difference between circulation fluid (e.g., mud) and reservoir pressure (e.g., hydrostatic) and $\sigma_{\Delta T}$, thermal stress exerted from thermal cooling caused by mud whose temperature is generally lower than the formation, which can be ignored at depths shallower than 2000 m in moderately heated basins. According to the equations above, stress concentration around a wellbore shows a strong variation as a function of distance and position around the wellbore. The Kirsch equations could be simplified in order to calculate stresses right at the wellbore by substituting $r = R$;

$$\sigma_{\theta\theta} = S_H + S_h - 2(S_H - S_h) \times \cos 2\theta - 2P_o - \Delta P - \sigma^{\Delta T} \quad \text{Equation 16}$$

$$\sigma_{rr} = \Delta P \quad \text{Equation 17}$$

$$\sigma_{zz} = S_v - S_v(S_H - S_h) \times \cos 2\theta - P_o - \sigma^{\Delta T} \quad \text{Equation 18}$$

As the position e.g. " θ angle" from the azimuth of S_H changes, the magnitude of circumferential hoop stress varies in a sinusoidal fashion and amplifies the far field stress significantly at the azimuth of S_h . Nevertheless at certain positions around the well, the hoop stress reaches the magnitude of unconfined compressive strength (UCS) of the rock and causes initial breakout formation contorting circular cross sectional geometry of the wellbore wall.

The breakouts have a finite width (width of break-out = WBO) and it depends on rock strength for a given polyaxial stress state (Zoback et al., 1985). This width does not change over time in the progressive stages of the deformation even if the

breakout deepens (Mastin, 1984; Zoback et al., 1985). Therefore, when the breakout with a certain width (WBO) occurred at a certain depth and unconfined compressive strength (UCS) of the material (e.g., rock) is known, one can determine particular relative magnitudes of horizontal stresses. The mathematical relation between s_h , S_H and WBO with a known UCS is expressed below;

$$S_H = \frac{(UCS + \Delta P + 2P_p)}{(1 - 2 \cos(\pi - WBO))} - S_h \frac{(1 + 2 \cos(\pi - WBO))}{(1 - 2 \cos(\pi - WBO))} \quad \text{Equation 19 (Barton *et al.*, 1988)}$$

As firstly addressed by Hubbert and Willis (1957), considering the coexistence of the drilling induced tensile wellbore wall fractures (DITF's) along with the borehole breakouts, one can constrain the ratio of S_h/S_H , since DITF's are induced when the hoop stress ($\sigma_{\theta\theta}$) equals to or lower than zero in the direction of S_H , where it is expected to reach its minimum as shown in the expression below;

$$-UTS = \sigma_{\theta\theta}^{\min} = 3S_h - S_H - 2P_p - \Delta P - \sigma^{\Delta T} \quad \text{Equation 20}$$

Since, the S_3 values derived from four LOTs show a significant disassociation with the S_V gradient, it is calculated from the density logs for the studied region. S_h gradient is later generated out of them (Figure 5.14). Additionally, using the corresponding S_h magnitudes for the specific depths, S_H values are delimited and calculated from 3 wells drilled in Şambayat oilfield (Well-1, Well-2 and Well-3) at which borehole breakouts and some DITF's are observed. This is important because the knowledge about the both phenomena could help us to constrain S_h and S_H values as discussed earlier in this chapter. It is now possible to calculate the third stress component (S_H) of the mechanical earth model mainly using geometries of borehole breakouts occurred at different depths from Well-1, Well-2 and Well-3, respectively.

Well-1 is a vertically drilled well in which the Sayındere Formation is intercepted at depth interval of 1828–2016 m. Based upon available drilling data, circulating mud density used during both drilling and log taking processes were 69,5 lb/ft³, which is slightly greater than the hydrostatic pressure throughout the well trajectory (Table 4). Pore pressure (P_p) at the depth of initial breakout formation is 20 MPa and this corresponds to 10,628 MPa/km hydrostatic gradient, which is

compatible with drilling stem tests (DST) results acquired for different depths in the well 1. Relatively high Pp gradient in well-1 is attributed, according to the well's available production data, to relatively high percentage of water (>%55) in this particular compartment of oily reservoir.

The density difference of reservoir and circulation fluids creates 1,17 MPa radial stress ($\Delta P = \sigma_{rr}$) at 1882 m where the electrical image tool catches dark borehole breakout bars with a breakout width (WBO) of 25° (Table 5.1, Figure 5.6). SV, for this depth, is calculated using Equation 9 as 47,95 MPa where 2.6 g/cm³ is taken as average density of overlying units and 9.8 m/s² as the gravitational constant.

Radial position of initial breakout formation defined by (i) the angle of WBO, (ii) difference of counteracting fluid pressures acting upon wellbore wall, (iii) ΔP and (iv) unconfined compressive strength (UCS) of the Sayındere limestone (which is 183 MPa) are used as variables to constrain SH (Equation 19). On the other hand, -26.4 MPa of unconfined tensile strength (UTS) of bed parallel samples of the Sayındere limestone are used as a specific value for the minus minimum hoop stress ($-\sigma_{\theta\theta}^{\min}$) to allow formation of drilling induced tensile fractures (DITF).

In the Well-1, no DITF's is observed, and this observation complies with implementation of the Griffith tensile failure criterion calculated from three effective stresses $\sigma_{\theta\theta}$, σ_{rr} and σ_{zz} around vertical wellbore wall at the azimuth of Sh (Figure 5.7), since the $\sigma_{\theta\theta}^{\min}$ must be $\leq -26,4$ to satisfy the conditions allowing the DITF's to form.

From the S_h gradient (Figure 5.14) S_h is determined as 40.3 MPa and from the Equation 19 S_H is derived as 90.9 MPa for the depth of breakout formation, 1882 m. Accordingly, at 1882 m in the Well-1, poly-axial stress magnitudes, tectonic stress ratio and lateral stress coefficient are expressed below (Table 5.1);

According to Anderson's faulting theory, such a polyaxial stress condition coincides with a domain of strike-slip faulting regime as shown in a stress polygon below (Figure 5.5);

Table 5.1. Previously known elastic parameters, experimentally derived strength parameters, imposed pressure conditions, measured geometrical values and measured poly axial stress magnitudes that created conditions for formation of borehole breakout at the depth of 1882 m. on the wellbore wall of the Well-1 drilled in Şambayat Oilfield.

S_H (MPa)	90,90	ρ_{Mud} (lb/ft ³)	69,5
S_h (MPa)	40,31	P_{grad} (psi/ft)	0,48
S_V (MPa)	47,95	ρ_(w+oil) (g/cm ³)	1,08
P_P (MPa)	20	P_{Mud} (psi)	2979,88
ΔP (MPa)	0,53	ρ_{Mud} (g/cm ³)	1,113283
Breakout half width °	12,5	P_{Mud} (MPa)	20,53
S_{ΔT} (Thermal Stresses)	0,00	S_h/S_H	0,44
Young Modulus (MPa)	57500	K	1,37
ν (Poisson Ratio)	0,25	Measured BO width °	25
Depth (m)	1882	UCS (MPa)	183,00
Depth (ft.)	6174,54	UTS (MPa)	-26,4

$$S_h = 40.3 < S_v = 47.95 < S_H = 90.90$$

$$S_h/S_H = 0.44$$

$$K = 1.37$$

As the three principal stresses; $\sigma_{\theta\theta}$, σ_{rr} and σ_{zz} defined in cylindrical coordinate system acting on the wellbore wall of Well-1 at azimuths of SH and Sh are shown as three-dimensional Mohr diagrams (Mohr-Coulomb and Griffith criterion, $C_0 = 52.8$ MPa, $UTS = -26.4$ and $\phi_i = 30^\circ$), it is seen that the compressive failure envelope is reached. So the formation of the borehole breakout is expected.

Because the tensile failure envelope is not reached, the formation of DITF's is not expected (Figure 5.7) and this is compatible with observations from electrical image logs (Figure 5.6b).

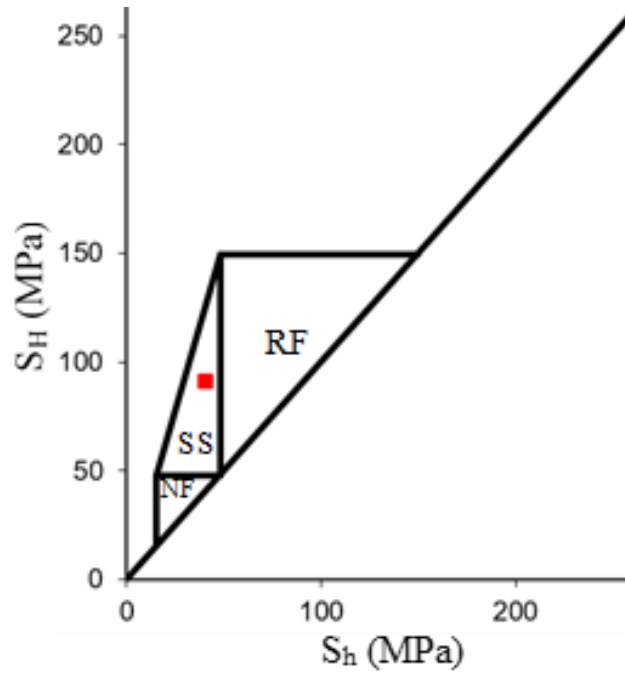


Figure 5.5. Tectonic faulting regimes polygons, customized by the stress magnitudes, are calculated and measured for Well-1. It is shown that the red square plotted by using measured S_H - S_h magnitudes from Well-1 at 1882 m falls into the strike-slip faulting domain. NF– normal faulting, RF– reverse faulting, and SS– strike-slip faulting.

The Well-2 is also a vertically drilled well in which the Sayındere Formation is intercepted at the depth interval of 1512–1886 m. Circulating mud density used during drilling and log taking processes were 67.5 lb/ft³ and, respectively. Pore pressure at the depth of initial breakout formation was calculated as 1836 m from the results of a DST conducted at a closest depth interval. At the depth of 1786 m, a borehole breakout bar with a width (WBO) of 25.8° is caught (Figure 5.9) and 0.56 MPa radial stress ($\Delta P = \sigma_{rr}$) is measured.

SV, for this depth, is calculated as 45.5 MPa. Based on the S_h gradient, S_h is 38.75 MPa as derived from LOT's s (Figure 5.14). S_H , then found as 89.73 MPa from the Equation 19. Such a polyaxial stress condition coincides with a domain of strike-slip faulting as shown in a stress polygon (Figure 5.8).

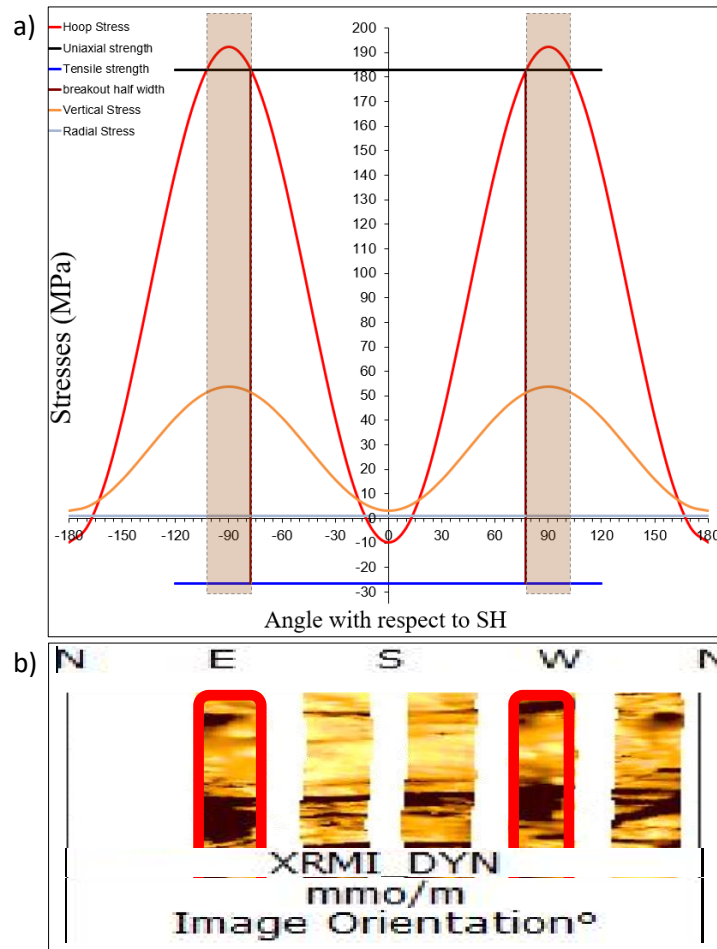


Figure 5.6. (a) Circumferential, $\sigma_{\theta\theta}$, (red curve), vertical, σ_{zz} (orange curve) and radial, σ_{rr} (grey line) stresses acting on the wellbore wall of the Well-1 in a cylindrical coordinate system plotted using optimal S_H - S_h combination. UCS (black) and initial breakout formation angular position (maroon) intersect with the $\sigma_{\theta\theta}$ curve at the state of failure in the Well-1 at 1882 m. UTS of the rock unit is indicated as blue line. **(b)** Image log of the wellbore wall around 1882 m. where a part of a series of breakouts in a wider depth interval is observed.

Thus, in the Well-2, at 1786 m poly-axial stress magnitudes (MPa), tectonic stress ratio and lateral stress coefficient are as shown in Table 5.2 and as expressed below;

$$\begin{aligned}
 S_h &= 38.75 < S_v = 45.5 < S_H = 89.73 \\
 S_h/S_H &= 0.43 \\
 K &= 1.4
 \end{aligned}$$

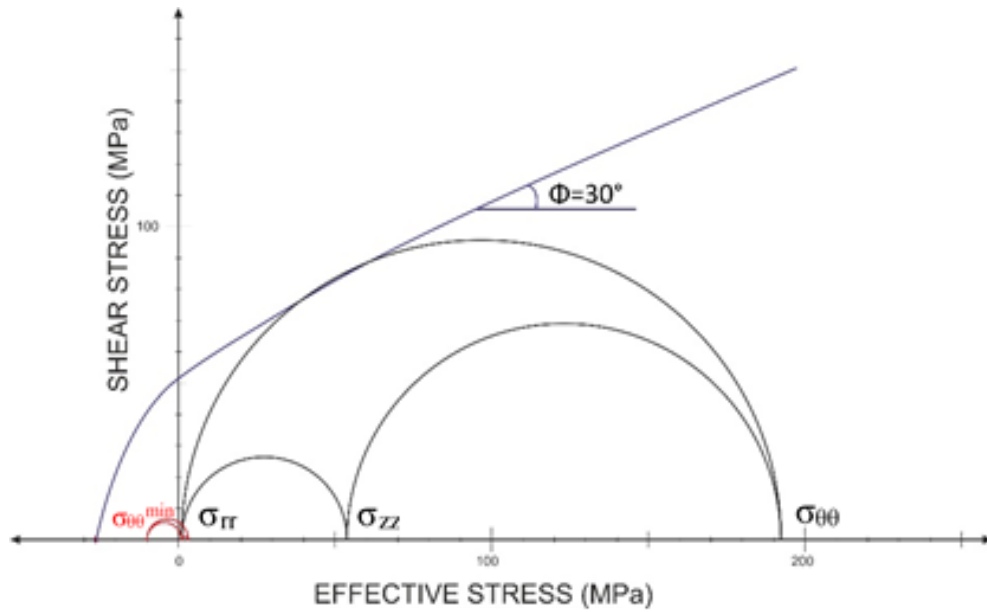


Figure 5.7. Three effective principal stresses, $\sigma_{\theta\theta}$, σ_{rr} and σ_{zz} at the wellbore of Well-1 shown as three dimensional Mohr diagrams at the azimuths of S_H (Black Mohr Circles) and S_h (Red Mohr circles). Strength of the rock which is shown by purple failure envelope is exceeded in compressive domain but not exceeded in the tensile domain.

Table 5.2. Previously known elastic parameters, experimentally derived strength parameters, imposed pressure conditions, measured geometrical values and measured polyaxial stress magnitudes that created conditions for the formation of borehole breakout at the depth of 1786 m on the wellbore wall of the Well-2 drilled in Şambayat Oilfield.

S_H (MPa)	89.73	ρ_{Mud} (lb/ft³)	67.5
S_h (MPa)	38.75	P_{grad} (psi/ft)	0.47
S_v (MPa)	45.5	$\rho_{(w+oil)}$ (g/cm³)	1.049
P_P (MPa)	18.36	P_{Mud} (psi)	2746.50
ΔP (MPa)	0.56	ρ_{Mud} (g/cm³)	1.081
Breakout half width °	12.9	P_{Mud} (MPa)	18.92
S_{AT} (Thermal Stresses)	0.00	S_h/S_H	0.43
Young Modulus (MPa)	57500.00	K	1.41
ν (Poisson Ratio)	0.25	Measured BO width °	25.8
Depth (m)	1786.00	UCS (MPa)	183.0
Depth (ft.)	5859.58	UTS (MPa)	-26.4

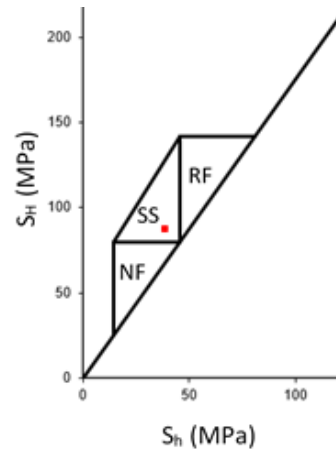


Figure 5.8. Tectonic faulting regimes polygon customized by the stress magnitudes calculated and measured for Well-2 and it is shown that the red square plotted using measured S_H - S_h magnitudes from Well-2 at 1786 m falls into the strike-slip faulting domain of tectonic faulting regimes.

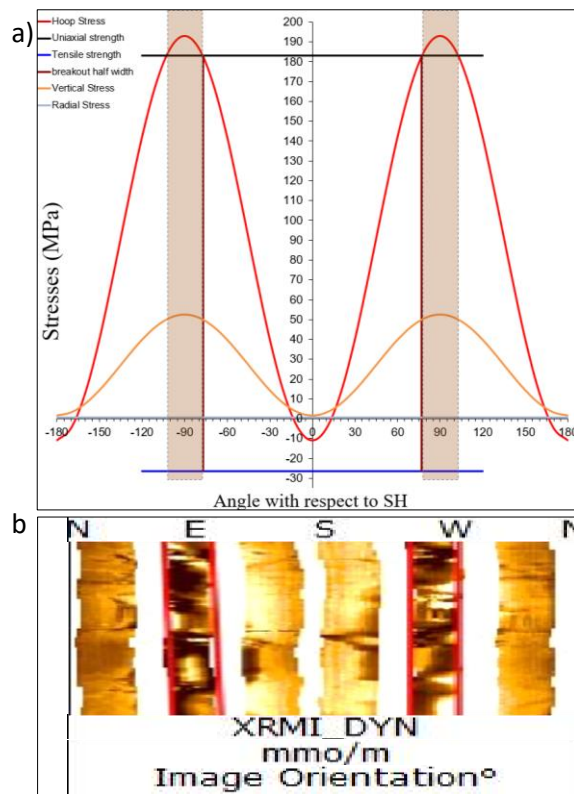


Figure 5.9. (a) Circumferential, $\sigma_{\theta\theta}$, (red curve), vertical, σ_{zz} (orange curve) and radial, σ_{rr} (grey line) stresses acting on the wellbore wall of the Well-2 in a cylindrical coordinate system plotted using optimal S_H - S_h combination. UCS (black) and initial breakout formation angular position (maroon) intersect with the $\sigma_{\theta\theta}$ curve at the state of failure in the Well-2 at 1786 m. UTS of the rock unit is indicated as blue line. (b) Image log of the wellbore wall of Well-2 at the same depth where a part of a series of breakouts in a wider depth interval is observed.

Similarly to the Well-1, the three principal stresses; $\sigma_{\theta\theta}$, σ_{rr} and σ_{zz} acting on the wellbore wall at the azimuths of S_H and S_h in the Well-2 are shown as a three-dimensional Mohr diagram, and from the implementation of both criterion it could be inferred that the formation of a borehole breakout is expected, but the drilling induced tensile fractures (DITF's) are not expected (Figure 5.10). These criterion verify observations from electrical image logs (Figure 5.9b).

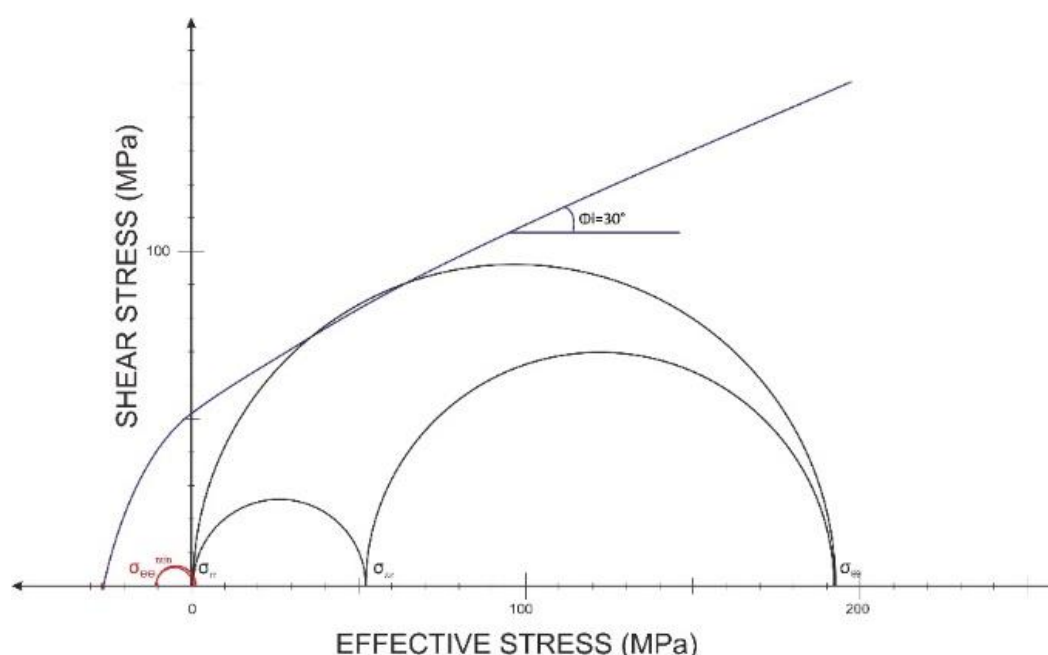


Figure 5.10. Three effective principal stresses, $\sigma_{\theta\theta}$, σ_{rr} and σ_{zz} at the wellbore of Well-2 shown as three dimensional Mohr diagrams at the azimuths of S_H (Black Mohr Circles) and S_h (Red Mohr circles). Strength of the rock which is shown by purple failure envelope is exceeded in compressive domain but not exceeded in the tensile domain.

Lastly, the Well-3, as a vertically drilled well in the Şambayat Oilfield intercepted the Sayındere Formation at the depth interval of 1527–1831 m. Circulating mud density used during drilling and log taking processes were 65 lb/ft³ and This is lower than the average density of the formation fluid of 66.8 lb/ft³ at any depth throughout the well trajectory. DST results show that the P_p at the depth of initial breakout formation is 19 MPa and this corresponds to 10.48 MPa/km hydrostatic gradient compatible with DST results acquired for different depths in the Well-3. This density difference creates –0.5 MPa radial stress (σ_{rr}) at 1813 m where a 17.28° wide borehole breakout bar is detected (Figure 5.12). S_v , for this depth, is 46.20 MPa. Based on the gradient derived from LOT's (Figure 5.14), S_h is found as

39.1 MPa for this depth and the corresponding S_H is calculated as 88 MPa from Equation 19. Such a stress state indicates a strike-slip faulting in a stress polygon (Figure 5.11). Thus, in the Well-3, at 1813 m, poly-axial stress magnitudes (MPa), tectonic stress ratio and lateral stress coefficient are expressed below (Table 5.3);

$$S_h = 39.1 < S_v = 46.20 < S_H = 88$$

$$S_h/S_H = 0.565 / K = 1.558$$

Table 5.3. Previously known elastic parameters, experimentally derived strength parameters, imposed pressure conditions, measured geometrical values and measured polyaxial stress magnitudes that created conditions for formation of borehole breakout at the depth of 1813. on the wellbore wall of the Well-3 drilled in Şambayat Oilfield.

S_H (MPa)	88.00	ρ_{Mud} (lb/ft³)	65
S_h (MPa)	39.1	P_{grad} (psi/ft)	0.45
S_v (MPa)	46.20	$\rho_{(w+oil)}$ (g/cm³)	1.07
P_P (MPa)	19.00	P_{Mud} (psi)	2684.76
ΔP (MPa)	-0.5	ρ_{Mud} (g/cm³)	1.041266
Breakout Half width °	8.64	P_{Mud} (MPa)	18.51
$S_{\Delta T}$ (Thermal Stresses)	0.00	S_h/S_H	0.565
Young Modulus (MPa)	57500.00	K	1.558
ν (Poisson Ratio)	0.25	Measured BO width ° :	17.28
Depth (m)	1813.00	UCS (MPa)	114.00
Depth (ft.)	5948.16	UTS (MPa)	11.40

Similarly to the Well-1 and Well-2, the likelihood of compressive and tensile failure around wellbore walls for the stress conditions prevailing along the Well-3 are analyzed by showing $\sigma_{\theta\theta}$, σ_{rr} and σ_{zz} values at the azimuths of S_H and S_h in the Well-3 as three-dimensional Mohr diagrams (Figure 5.13). The implementation of both criterion showed that, in accordance with the image log observations, the formation of a borehole breakout is expected, but the drilling induced tensile fractures (DITF's) are not (Figure 5.13).

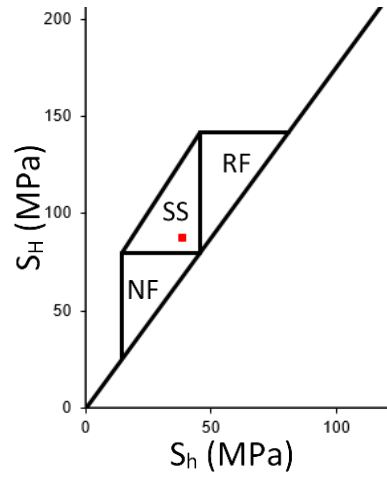


Figure 5.11. Tectonic faulting regimes polygon customized by the stress magnitudes calculated and measured for Well-3 and it is shown that the red square plotted using measured S_H - S_h magnitudes from Well-3 at 1813 m falls into the Strike-slip faulting domain of tectonic faulting regimes.

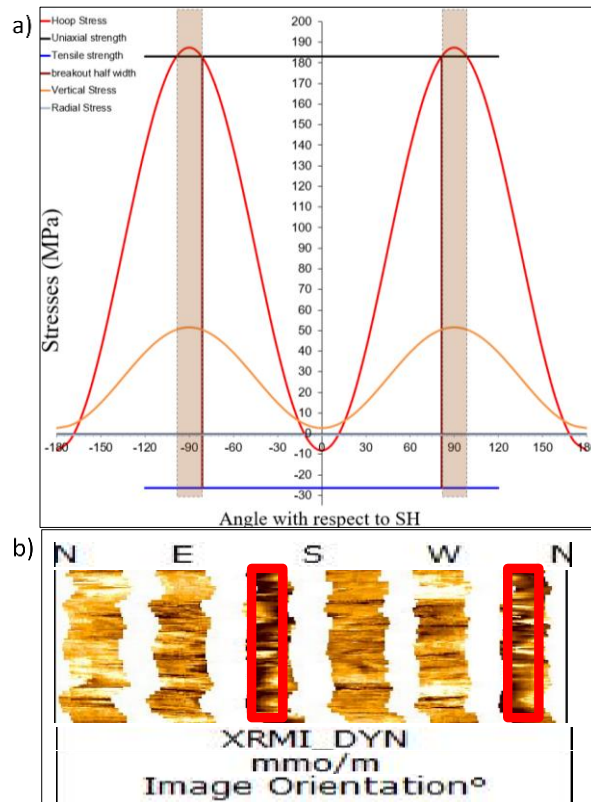


Figure 5.12. (a) Circumferential, $\sigma_{\theta\theta}$, (red curve), vertical, σ_{zz} (orange curve) and radial, σ_{rr} (grey line) stresses acting on the wellbore wall of the Well-3 in a cylindrical coordinate system plotted using optimal S_H - S_h combination. UCS (black) and initial breakout formation angular position (maroon) intersect with the $\sigma_{\theta\theta}$ curve at the state of failure in the Well-3 at 1813 m. UTS of the rock unit is indicated as blue line. (b) Image log of the wellbore wall of Well-3 at the same depth where a part of a series of breakouts in a wider depth interval is observed.

5.3. Extrapolated Vertical Profiles of Coefficient of Friction, Principal Stresses and Hydrostatic Pressure

The three natural effective principal stresses acting upon any buried rock medium in the Earth's crust throughout all the depths of interest for the Adıyaman province has been approximated by in-situ stress estimations, measurements and extrapolations in the context of this research.

The poly-axial natural stresses have been used:

- (i) To make comparison with the strength parameters of the Sayındere Formation,
- (ii) To make slip tendency analyses and then
- (iii) To determine critically stressed, optimally oriented, tectonically, mechanically and hydraulically active faults and the fractures associated with them.

At the four wells located in the Adıyaman province, within or around the study area, proper leak-off tests were conducted and recorded as pressure versus volume charts to determine minimum principal stress (S_h) at those specific depths. These tests were performed at burial depths of 1761 m, 2021 m, 2234 m, and 2703 m and provided with different values of minimum principal stress (S_h). By using these values, S_h gradient and an extrapolated S_h vertical profile throughout the depth interval of interest of this research are generated (Figure 5.14).

Besides, by using corresponding S_h values as input parameters, maximum principal stress (S_H) values for three different depths of 1786 m, 1810 m and 1882 m are measured by using borehole breakout geometries and pressure parameters measured at the wells while drilling.

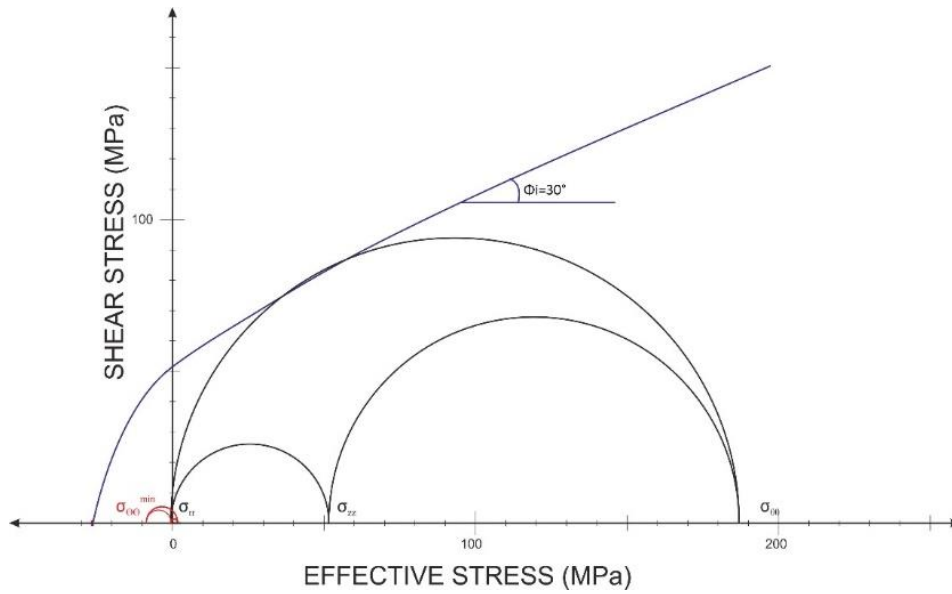


Figure 5.13. Three effective principal stresses, $\sigma_{\theta\theta}$, σ_{rr} and σ_{zz} at the wellbore of Well-3 shown as three dimensional Mohr diagrams at the azimuths of S_H (Black Mohr Circles) and S_h (Red Mohr circles). Strength of the rock which is shown by purple failure envelope is exceeded in compressive domain but not exceeded in the tensile domain.

Using these S_H and S_h measurements along with the lateral stress coefficient (K) approximations acquired from the earthquake data (Figures 5.2 and 5.15), an S_H gradient and an extrapolated S_H vertical profile throughout the depth interval of interest of this research are produced (Figure 5.14). Additionally, from the drilling stem tests, hydrostatic pressure data from many different wells drilled in and around the study area are gathered; then a hydrostatic pressure gradient for the depth of interest is generated.

By incorporation of the hydrostatic pressure values, vertical profiles of maximum, minimum and intermediate effective stresses are produced (Figure 5.14) to later use as input parameters for slip tendency analyses that will be elaborated in the-following-Chapter.

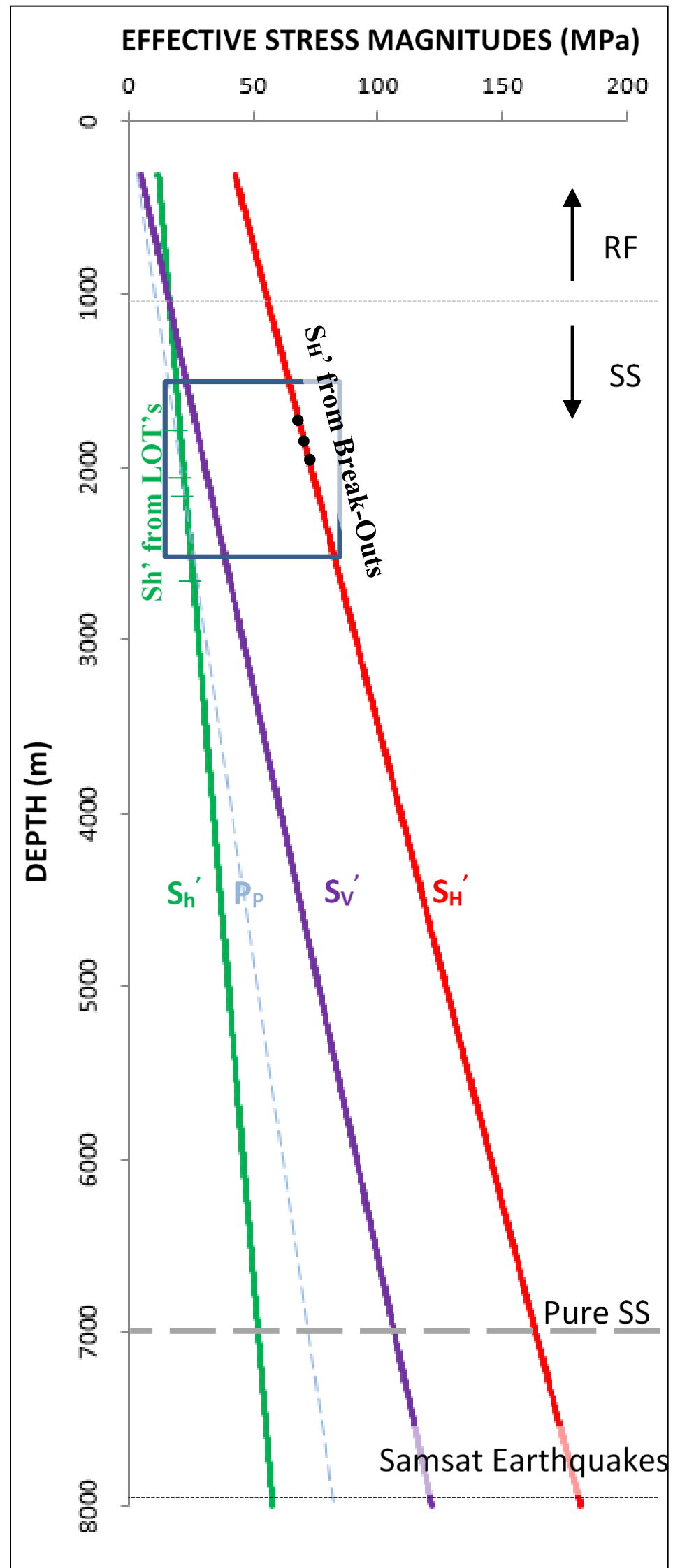


Figure 5.14. Change of in-situ effective stress magnitudes by depth over Adiyaman Province. Blue square delimits the depth and stress magnitude intervals that the Sayindere Formation in the Şambayat Oilfield has ever experienced since the time when regional oil expulsion began. Light dashed grey line shows the boundary between SS and RF regimes. Heavy dashed grey line shows the stress conditions for a pure SS regime in which zero pitch angle is expected. Black dashed line shows the stress condition thought to be responsible for the March 2017, Samsat, Adiyaman Earthquake. Depths of Leak-off tests (LOT's) constraining S_h values are shown with green horizontal lines. S_H measurements from breakouts are show by black dots.

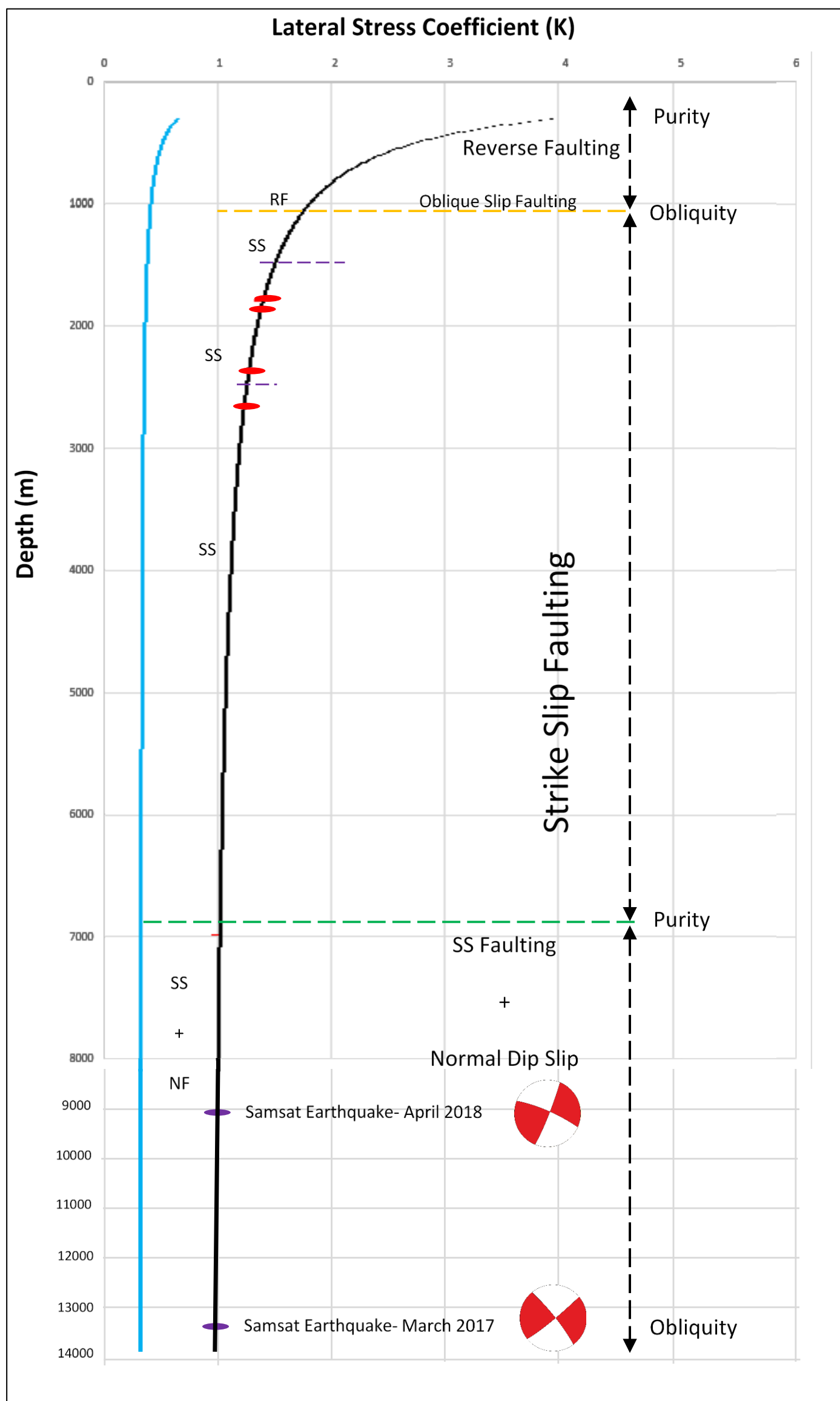


Figure 5.15. K values derived from in situ stress measurements (red ellipses) within Şambayat Oilfield. Upper (black) and lower bound (blue) curves derived using corresponding expressions for bounds of K elaborated in the text and inverse solution of an earthquake focal mechanism (purple ellipse). All the K's follow closely the upper bound we derived, just as the derived K for the Samsat earthquakes occurred at 9000 m and 13500 m. Green dashed line indicates pure SS where orange dashed line separates SS and RF. Purple dashed lines represent the depths at which Saymdere Formation has ever located since the beginning of oil expulsion which has seemingly undergone oblique SS faulting mostly.

CHAPTER 6

SLIP-TENDENCY ANALYSES

Pre-existing faults, fractures and imperfections with varying orientations exist naturally in any tectonic environment. The orientation and stress difference ratio of the principle stresses determine which set of faults are in optimal orientation (i) to show slip tendency, (ii) to accumulate stress and thus (iii) to perturb the stress field. The slip tendency (TS) on a pre-existing plane of weakness is defined by Morris et al. (1996) as the ratio of the shear (τ) to the normal stress (σ_n) acting on those surfaces, as also being equal to the coefficient of friction for a fault in a particular orientation;

$$T_s = \mu = \tau / \sigma_n \quad \text{Equation 21}$$

The coefficient of static friction (μ_s) is the slope of the failure criterion whose general values is limited by the experiments of Byerlee (1978) in the range of 0.6–0.85. Relative magnitude and permutations of intermediate stress in a true tri-axial stress environment (e.g., $\sigma_1 > \sigma_2 > \sigma_3$) manifests special limitations for T_{smax} and thus coefficient of static friction (μ_s) for pre-existing fractures subjected to those special poly-axial stress field. Stress field formed under these circumstances is described by stress difference (R) and stress division ratios (k) as expressed below;

$$R = (\sigma_1 - \sigma_2) / (\sigma_1 - \sigma_3) \quad \text{Equation 22}$$

$$k = (\sigma_1 / \sigma_2) / (\sigma_2 / \sigma_3) \quad \text{Equation 23}$$

As well as one would have an in-situ measurements of principal stress magnitudes along with pore pressure knowledge at any particular depth on earth, T_{smax} , which is the greatest realizable ratio of τ_{max} / σ_n for that particular poly-axial stress condition, can be calculated. Then, a normalized slip tendency (T_s') any fault with any particular orientation would be defined as a percentage of the T_{smax} can also be calculated as shown below;

$$T_s' = T_s / T_{smax} \quad \text{Equation 24}$$

In order to derive T_{smax} , the maximum shearing stress (τ_{max}) and normal stress (σ_n) must be calculated as a function of principal stresses and direction cosines by the expressions derived by Bott (1959) below;

$$T_{max}^2 = m^2 (\sigma_y - \sigma_x)^2 + n^2 (\sigma_z - \sigma_x)^2 - \{m^2 (\sigma_y - \sigma_x) + n^2 (\sigma_z - \sigma_x)\}^2 \quad \text{Equation 25}$$

$$\sigma_n = l^2 \sigma_x + m^2 \sigma_y + n^2 \sigma_z \quad \text{Equation 26}$$

Where σ_z is vertical and σ_v and σ_x are horizontal principal stresses, when the Cartesian coordinate axes, x, y and z in which the surfaces are defined, are taken parallel to the axis of S_H , S_h , and S_v , respectively. Relatedly; l, m and n are the direction cosines for the angles (α , β , γ) of normal to arbitrary planes with respect to the principal stress axes S_H , S_h , and S_v , respectively (Figure 6.1).

Direction cosines are interrelated each other through the equation below;

$$l^2 + m^2 + n^2 = 1 \quad \text{Equation 27}$$

The pitch angle (Ω) of the τ_{max} was given by the expression derived by Bott (1959) below;

$$\tan \Omega = n/lm \{m^2 - (1-n^2) \times [(\sigma_z - \sigma_x) / (\sigma_y - \sigma_x)]\} \quad \text{Equation 28}$$

Plunge (P) and trend (T) of the τ_{max} with respect to a horizontal plane and the maximum principal stress direction are related with the strike and dip of planes of any arbitrary orientation through the expressions below;

$$\text{Trend} = \text{Strike} + \cos^{-1} \{(\cos \Omega) / \cos P\} \quad \text{Equation 29}$$

$$\text{Plunge} = \sin^{-1} \{(\sin \text{dip}) \times (\sin P)\} \quad \text{Equation 30}$$

Accordingly, τ_{max} and its corresponding pitch angle Ω would realize in a variety of strike and dip combination of arbitrary planes.

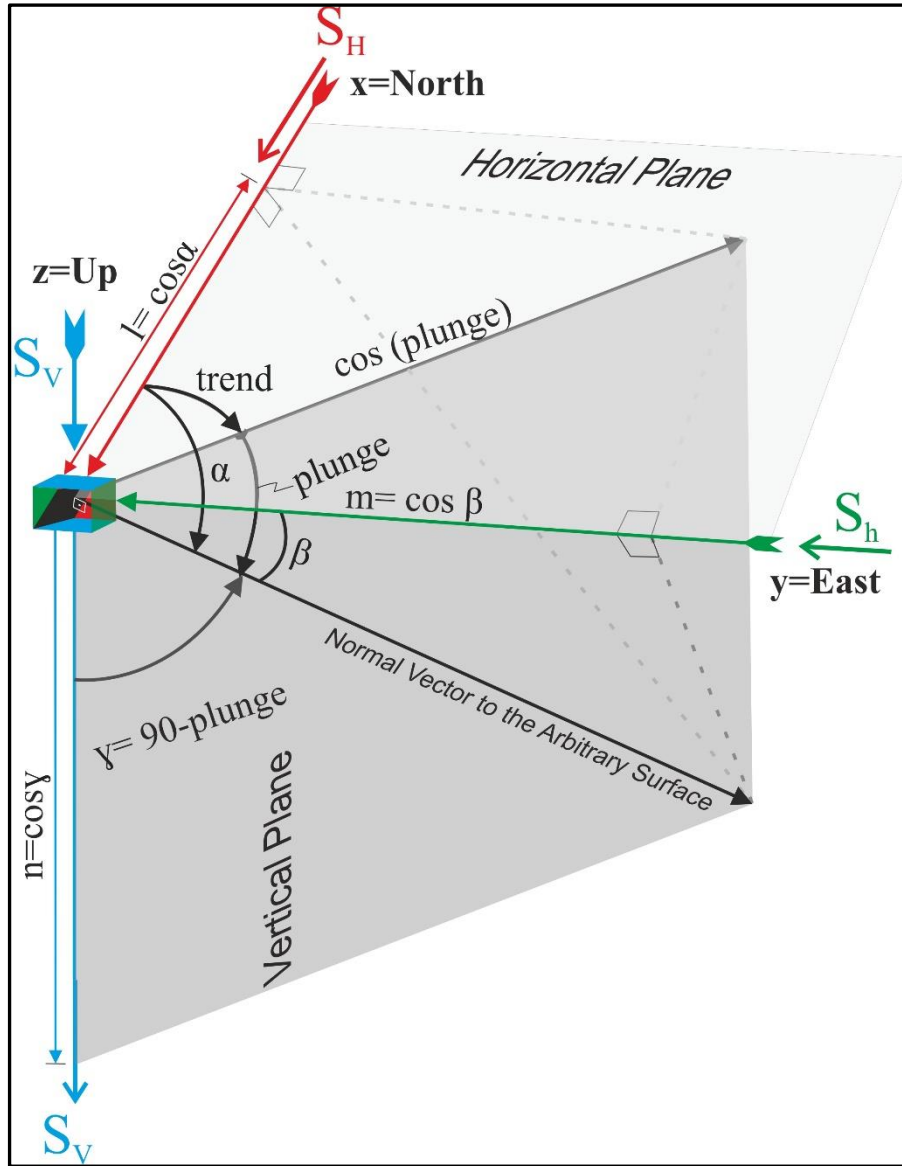


Figure 6.1. Geometrical relation between direction cosines and the angles that the principal stresses make with the normal vector to any arbitrary surface (modified from Allmendinger et al., 2012). In the case of this study, the directions of maximum and minimum horizontal principal stresses correspond to North and East, respectively.

The slip has higher tendency to occur in a narrower range of strike and dip depending upon the stress field characteristics, which are defined by: (i) firstly the permutation of magnitudal superiority of horizontal and vertical stresses according to Andersonian theory of faulting and (ii) secondly the ratios of R (stress difference ratio) and k (stress division ratio) in terms of their obliquities. According to

Andersonian theory of faulting, tectonic regimes are classified with reference to vertical principal stress ($S_V = \sigma_v$).

When;

- (i) $S_V = \sigma_1$: Normal faulting occurs through ideal fault surfaces striking parallel to S_H direction and deviating $\approx 30^\circ$ ($45 - \phi_i/2$) from S_V direction
- (ii) $S_V = \sigma_2$: Strike-slip faulting occurs through ideal fault surfaces dipping parallel to S_V direction and deviating $\approx 30^\circ$ from S_H direction
- (iii) $S_V = \sigma_3$: Reverse faulting occurs with ideal fault surfaces striking parallel to S_h direction and deviating $\approx 30^\circ$ from S_H direction.

The relative magnitudes of principal stresses changes in a continuous fashion and these three end-member Andersonian tectonic regimes vary transitionally due to replacement of S_H or S_h with S_V within $\sigma_1 > \sigma_2 > \sigma_3$ arrangement. Within these end-members, value of stress difference ratio (Equation 22) becomes equal to 0.5 and pitch of the maximum shear stress becomes perfectly parallel or perpendicular to the strikes of the slip surfaces (e.g., $\pm 90^\circ$ for normal faulting and reverse faulting, whereas 00° for strike-slip faulting). Besides, in such “*no-obliquity*” conditions, ratio of shear to normal stress reaches its highest value on the most optimally oriented faults pertaining to the stress field. As the ratio of stress difference, converges to 1.0, obliquity on slip surfaces reaches its maxima and pitch angle becomes 45° . R value ranges from 0.5 to 1.0 within strike-slip regime and $R = 0.5$ and $R = 1.0$ correspond to the stress states in which the pitch angle equals 0.0° and 45° , respectively. Within reverse faulting regime the stress states in which $R = 0.5$ and $R = 1.0$ corresponds to the situations in which the pitch angle equals to 45° and 90° , respectively. Therefore, for each stress state, the surfaces oriented in a certain range of strike and dip configuration that ensure highest slip tendency satisfying the special pitch angles are denoted and maximum shear stresses are calculated only for those stress states as optimally oriented surfaces (Figure 6.2). Accordingly, the slip preferentially occurs on optimally oriented surfaces that favor highest shear to normal stress ratios rather than other surfaces in case of their pre-existence in the environment (Figure 6.2). For example, based on our in-situ stress measurements, a dextral radial regime is expected at 1060 m in which $\sigma_1 = 66.9 \text{ MPa} > \sigma_2 = \sigma_3 = 27 \text{ MPa}$; and 10.9 MPa of

hydrostatic pressure is calculated by using the equations derived for extrapolation. Using those magnitudes, the highest allowable coefficient of static friction for pre-existing surfaces, μ_s , are calculated for this stress regime as 0.667, which corresponds to 33.7° of static friction angle, ϕ_s . As the highest μ_s value is taken as T_{Smax} (as suggested by Morris *et al.*, 1996), the planes which have static friction angle range of 31° to 35° show over %85 normalized slip tendency, T_s' for this depth. α and β angles of the slip surfaces with respect to the least and the most principle compressive stress directions respectively is related with the static friction angle, ϕ_s by the expressions below;

$$\beta = 45 - \phi_s/2 \quad \text{Equation 31}$$

$$\alpha = 45 + \phi_s/2 \quad \text{Equation 32}$$

Accordingly, optimally oriented slip surfaces, with higher than %85 of normalized slip tendency located at 1060 m in the Şambayat Oilfield, are the ones oriented from 33.3° to 34.5° with respect to the σ_1 direction (the maximum horizontal principal stress, S_H) aligned at N to S in region of study. For the depth intervals where data is available to perform quality check, this extrapolation has higher confidence. As explained in the previous chapter, this extrapolation relies on in-situ stress measurements within 1.5–2.5 km interval and a focal mechanism solution of an earthquake ruptured at about 7 km. The quasilinear tectonic coefficient upper and lower bound curves and $K=1$ line, constructed (Figure 5.15) for study area of this research, provide a quite narrow interval for extrapolation of the stress state within depths of 1.5–2.5 km. These depths correspond to horizon(s) where the Sayındere Formation has ever been located after the first oil expulsion is considered to have occurred in the Şambayat Oilfield. Therefore, optimally oriented faults for any depth in-between 1.5 km and 2.5 km can be calculated in a higher confidence. Besides, normalized slip tendency values of many surfaces in a dataset with multiple combinations of strikes and dips are plotted on stereonet with their color coded poles normal to each surfaces (Figures 6.3 and 6.4). For example, when (i) measurements of in-situ σ_1 , σ_2 and σ_3 magnitudes from Well #1 at 1810 m, and from well #2 at 1880 m (red ellipses in Figure 5.15), and (ii) extrapolated estimations based on the expression for changes of K (Equation 11) at 1500 m, 2000

m and 2500 meters along with contours of R and k values on $\ln(\sigma_1/\sigma_2)$ vs. $\ln(\sigma_2/\sigma_3)$ graphs are all considered, and if the slip tendency plots of each measurement and extrapolation are superimposed (Figure 6.4), one can see how the preferred orientation of high-slip tendency planes and domains of faulting regime change from reverse to strike-slip faulting with increasing depth (Figure 6.4).

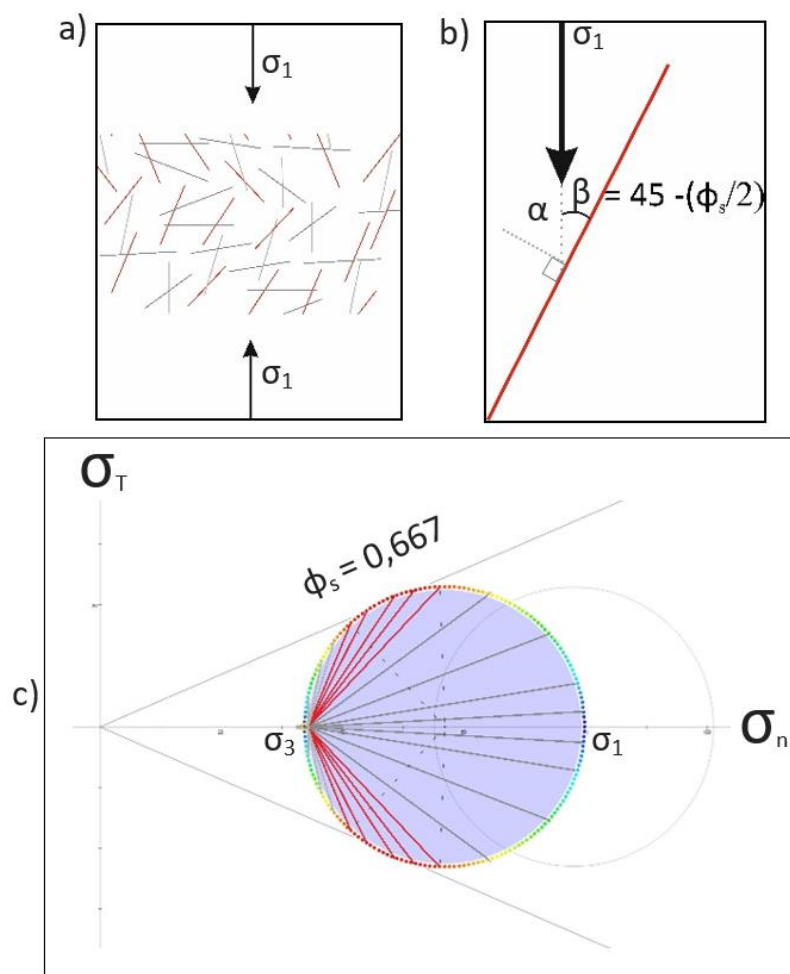


Figure 6.2. (a) Arbitrary distribution of pre-existing faults and fractures under compression; red colored ones are at optimal direction whereas grey ones are not. (b) The relationship between static friction and the angle of "expected to reactivate" faults. (c) Orientation interval of optimally oriented, high-slip tendency faults with respect to maximum principal stress direction and the static coefficient of friction for the most optimally oriented surface.

Naturally, faults and fractures are usually observed at many orientations while some are critically-stressed, mechanically active and optimally oriented for neo-tectonic regime, while some are passive and form remnants of older tectonic

regimes. According to critically-stressed fault hypothesis introduced by Barton et al. (1995), mechanically active faults are also hydraulically active and whereas mechanically passive faults are hydraulically passive and expected to be closed and healed. Slip tendency analysis (introduced by Morris *et al.*, 1996) enables us to classify natural faults and fractures with respect to their tendency of mechanical activity for any specific stress state in comparison with all differently oriented fault and fracture population available in a tectonic environment of interest. Using slip tendency analysis software, one can calculate normalized slip tendency as a percentage of the highest slip tendency value allowable for a certain poly-axial stress state.

When software is run to calculate normalized slip tendency for all planes with $360 \times 90 = 32400$ different integer strike and dip combinations and then plot their poles on stereonets with lower hemisphere equal area projection by slip tendency values, one can acquire plots as shown below (Figure 6.4):

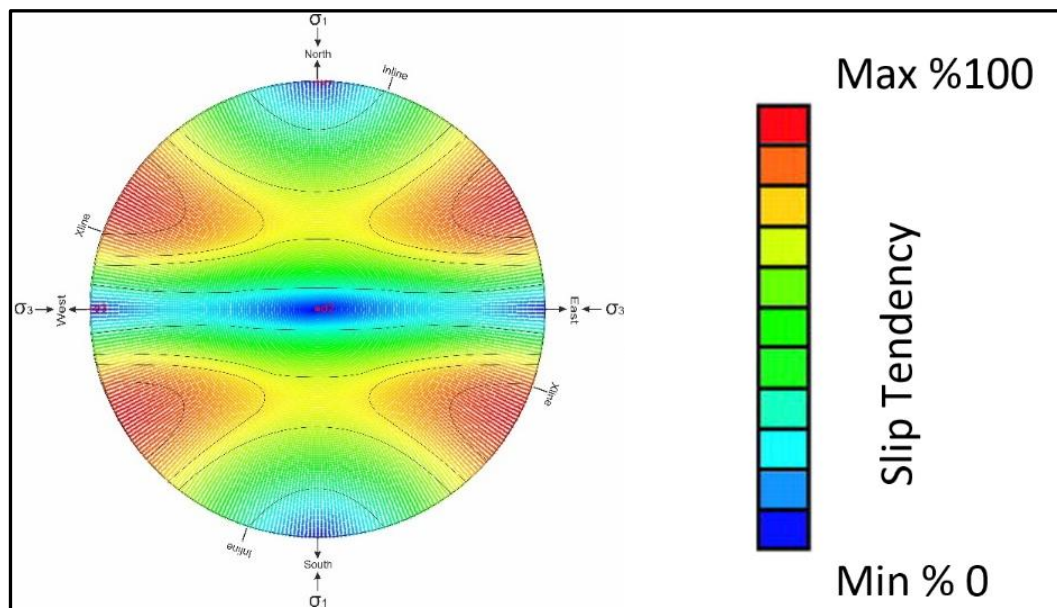


Figure 6.3. Pole demonstration of planes' every ($360 \times 90 = 32400$) possible integer strike and dip combination. The poles are colored by their calculated normalized slip tendency as a percentage of maximum slip tendency allowable for this particular poly-axial stress condition. Planes with red color coded poles shows over %90 slip tendency where dark blue colored ones shows below %10 slip tendency. This plot was generated based on in-situ stress measurements for 1600 m in Şambayat Oilfield.

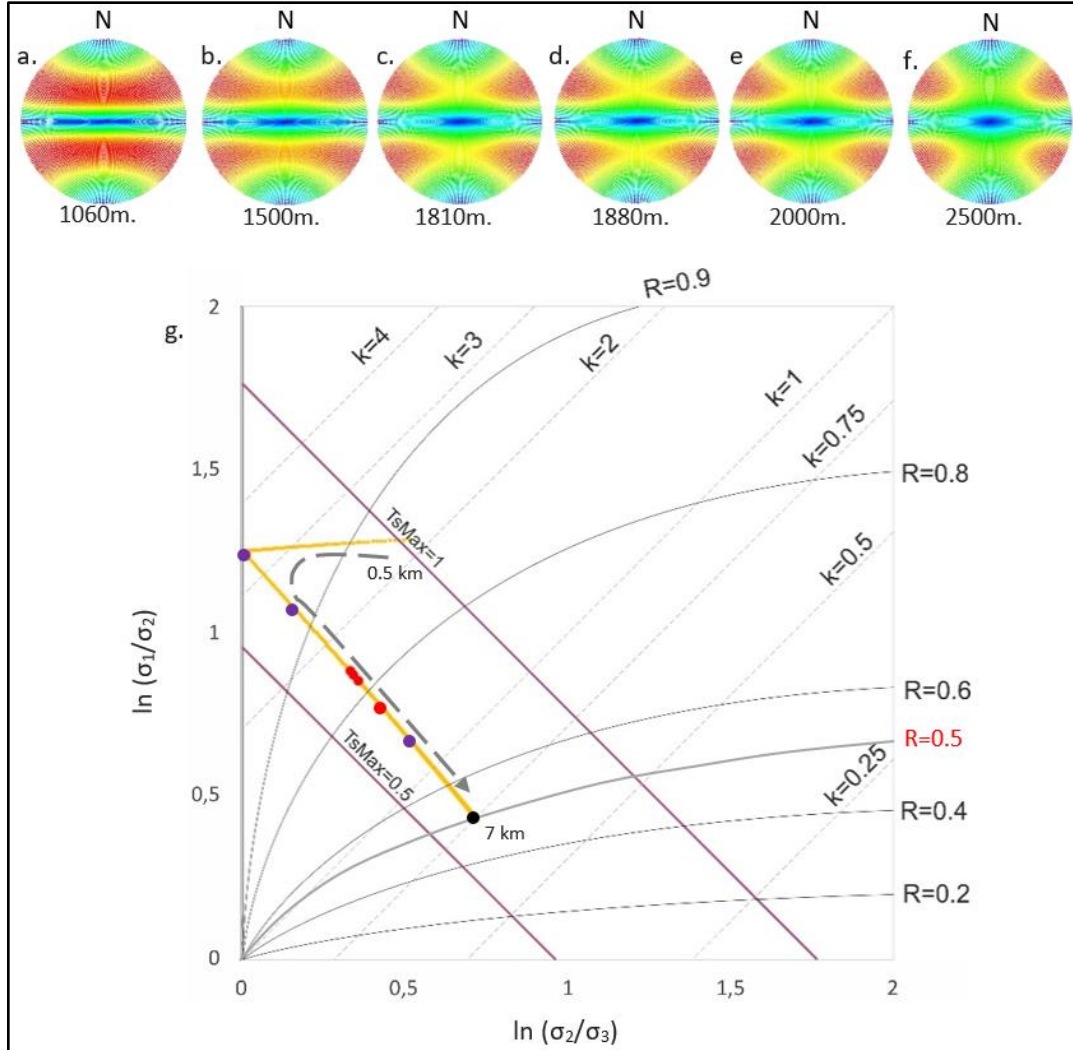


Figure 6.4. (a–f) Slip tendency plots of lower hemisphere, equal area projection of poles to slip planes for various depths were created according to changing poly-axial stress states. (g) The stress conditions of selected depths at which slip tendencies were analyzed (a–f) and the stress states of a local earthquake (black dot) and extrapolated intervals (yellow line) are superimposed on \ln/\ln graph of σ_1/σ_2 vs σ_2/σ_3 (g) with contours of R (grey lines), T_{Smax} (purple lines) and k (dashed lines). Red dots (c, d, e) are direct in-situ stress measurements from the wells while the purple dots (a, b, f) were derived from the equation for change of tectonic coefficient with depth. Dashed grey curve with arrow expresses increase in depth while vicinity of its inflection point (at 1.06 km) corresponds to the transpressional regime (45° pitch angle), its beginning (at 0.5 km) corresponds to RF regime with SS component and its' ending (at 7 km) corresponds to strike-slip faulting regime.

CHAPTER 7

SLIP TENDENCY ANALYSIS: DELINEATION AND FILTERING OF CONDUCTIVE FAULTS ON 3D SEISMIC SURVEY

For accurate and detailed characterization of naturally fractured and faulted reservoirs, a decent quality 3D seismic survey is a prerequisite in order to detect subtle faults and fracture swarm sweet spots that are barely over the detection limits of the seismic resolution. For conditioning the seismic survey before the implementation of edge detection processes, the signal to noise ratio should be increased by data processing. The processed Şambayat 3D seismic survey, which constitute subsurface data source of this research with the permission of TPAO, covers the Şambayat naturally fractured reservoir oilfield and allows applying seismic attributes to sufficiently delineate small faults and sweet spots.

Natural fractures and faults may act either as conduits or as barriers for the fluid flow. The hydraulic activity of any arbitrary discontinuity buried in a tectonic environment can be determined by their orientation interval with respect to the prevalent stress field. According to '*critically stressed faults concept*' (proposed by Zoback et al., 1995), hydraulic activity of any planar discontinuity is directly proportional to its mechanical properties and tectonic activity in a given region. Zoback et al. (1995) identified fracture geometry and reservoir attributes by using borehole televiewer images and high resolution temperature logs in boreholes from Cajon Pass, Long Valley and Yucca Mountain areas (Figure 7.1). They then stated that the faults, which are ought to be critically stressed because of their orientation according to the Coulomb frictional-failure criterion, and whose ratios of resolved shear to normal tractions are between 0.6 and 1.0 in accordance with the Byerlee's law (Byerlee, 1978), also show hydraulic activity (Figure 7.1).

To classify faults and fractures with respect to their tectonic, mechanic or hydraulic activity, Morris *et al.* (1996) introduced '*slip tendency*' concept by denoting the ratio of shear to normal stress acting on planar surfaces as the '*slip*

tendency' (Equation 21). Using a slip tendency analysis software (i.e. Mohr Plotter®) designed by Allmendinger (2015), *normalized slip tendency* (Equation 24) as a percentage of the highest slip tendency value allowable for a certain poly-axial stress state can be calculated for any arbitrary plane and can be shown in slip tendency stereonet polar plots (Figures 6.3 and 6.4).

As will be demonstrated in this chapter, the slip tendency polar plots, which is derived for certain depth intervals, can be used as filtering tool to classify entire population of main or subsidiary fault segments and fracture swarm sweet spots.

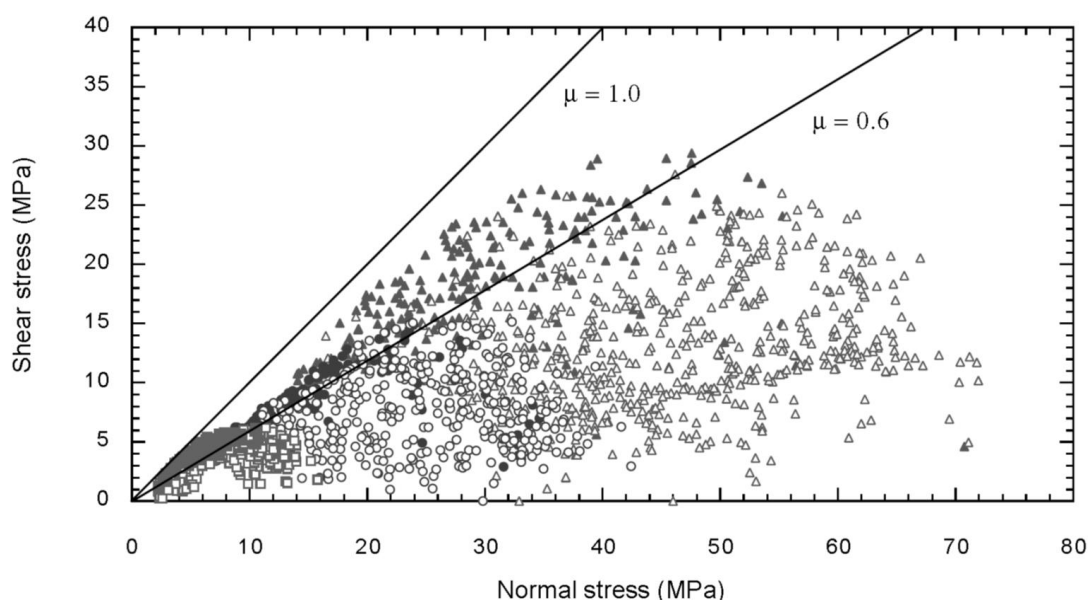


Figure 7.1. A shear stress to normal stress binary plot illustrating fractures whose geometry and hydraulic connectivity properties are identified with borehole imaging techniques in Cajon Pass (triangles), Long Valley (circles), and Nevada Test Site (squares) boreholes. Filled symbols, mostly in 0.6 to 1.0 static friction coefficient interval, are interpreted as hydraulically conductive fractures and faults, while the open symbols with the aforementioned interval are non-conductive fractures and faults. From Townend and Zoback (2000) based on original data of Zoback et al. (1995).

In order to delineate the entire population of those discontinuities from the re-processed Şambayat PSTM 3D seismic data; 3D curvature, Structural Smoothing, Variance and Ant Tracking cubes are respectively derived by using seismic volume attributes built in the Petrel® software in depth domain as part of an advanced edge

detection workflow (Figure 7.2). In the workflow, the outcome of each volume attribute process was used as input for the subsequent process at the sequence specified above. For example, the input for the Ant-tracking calculation is the conditioned variance volume, the input for the variance calculation is the conditioned structural smoothing volume, the input for the structural smoothing volume calculation is the conditioned frequency filter volume etc.

As the entire population of discontinuities are detected by multiply re-iterated ant-tracking calculations, filtering and color-coding are applied over the ant-tracking cube by using the slip tendency plots (Figures 6.3, 6.4 and 7.2a) generated from the vertical profile of the principal stresses for the Şambayat region for all of the specific depth intervals of interest (see Chapter 5), i.e. the average burial depth of the Sayındere Formation, which is at 1600 m at the Şambayat NFR oilfield (Figure 6.3).

At the depth of 1600 m, measurements indicate that $\sigma_1 = \text{N}10^\circ\text{W} - \text{N}10^\circ\text{E} = 82.2$ MPa; $\sigma_2 = \text{vertical} = 40.8$ MPa; and $\sigma_3 = \text{N}10^\circ\text{E} - \text{S}10^\circ\text{E} = 35.7$ MPa. Hydrostatic pressure at this depth will be about 16.5 MPa (extrapolated from the well test results). Accordingly, effective principal stresses would be: $\sigma_1 = \text{N}10^\circ\text{W} - \text{N}10^\circ\text{E} = 65.7$ MPa; $\sigma_2 = \text{vertical} = 24.3$ MPa; and $\sigma_3 = \text{E}10^\circ\text{N} - \text{S}10^\circ\text{E} = 19.26$ MPa (see the Chapter 5 for measurements and extrapolations). After the delineation of existing fault segments with a variety of slip tendency proportions, five distinct categories with 5 different color codes are defined and each will be explained below;

- *Blue color-coded discontinuities:* They comprise vertical faults with minimum 80° dip angle; faults are aligned in east–west direction perpendicular to the maximum compressive stress axis (S_H), which is roughly oriented north to south in the studied region. Those E–W-striking vertical faults can be associated with processed and propagated pressure solution seams. The blue color-coded faults are expected to act as barriers to the fluid flow with exceptional cases of induced activity.

- *Green color-coded discontinuities:* They are east–west-striking sub-vertical faults with dip angles varying between 60° and 80° ; they are possibly associated with reverse faults, and are considered as reactivated pressure solution seams that are

supposed to be the product of an earlier tectonic faulting regime. The green colored faults have normalized slip tendency values ranging from %20 to %40 and they are not expected to accumulate stress for the contemporarily prevailing stress field in the existence of warmer color-coded faults in the environment. Nevertheless, local stress perturbation (e.g., local rotations in the maximum principal stress, S_H) can cause them to accumulate stress (see Discussion Chapter).

- *Yellow colored discontinuities:* They mostly strike nearly perpendicular to the contemporary S_H axis and dip between 25° and 42° against north or south. They are sparse elements of the whole population observed in the entire seismic coverage area of the Şambayat oilfield. These faults have normalized slip tendency values ranging from %40 to %60.

- *Orange colored discontinuities:* These faults comprise sub-vertical surfaces that make about $45\text{--}52^\circ$ or $75\text{--}80^\circ$ from the S_H axis. They have normalized slip tendency values ranging from %60 to %80. It is very likely that these faults have a proclivity to accumulate stress along with the high-slip tendency (HST) faults with slight perturbations on the stress field. They can be associated with R-shear or P-shear subsidiary faults bifurcated from the red color-coded principal shear zone of the Samsat Fault as can be observed in the left lower corner of the Figure 7.2c.

- *Red colored discontinuities:* They are vertical faults that make 52° to 75° azimuthal deviation from the S_H axis. These faults have the highest normalized slip tendency values among existing fault population in the Şambayat NFR oilfield and these values range from %80 to %100. They most likely accumulate stress and their subsidiary elements (e.g., small faults or fracture swarms) are expected to be hydraulically and mechanically active. The secondary hierarchy asperities along their trajectory (e.g., P-shear or R-shear bifurcations and tertiary hierarchy structures related to them) are all expected to show hydraulic activity. Their spatial extent is therefore crucial for the naturally fractured reservoir (NFR) explorations. The extent of the damage zones related with the high-slip tendency faults will be discussed in the next chapter.

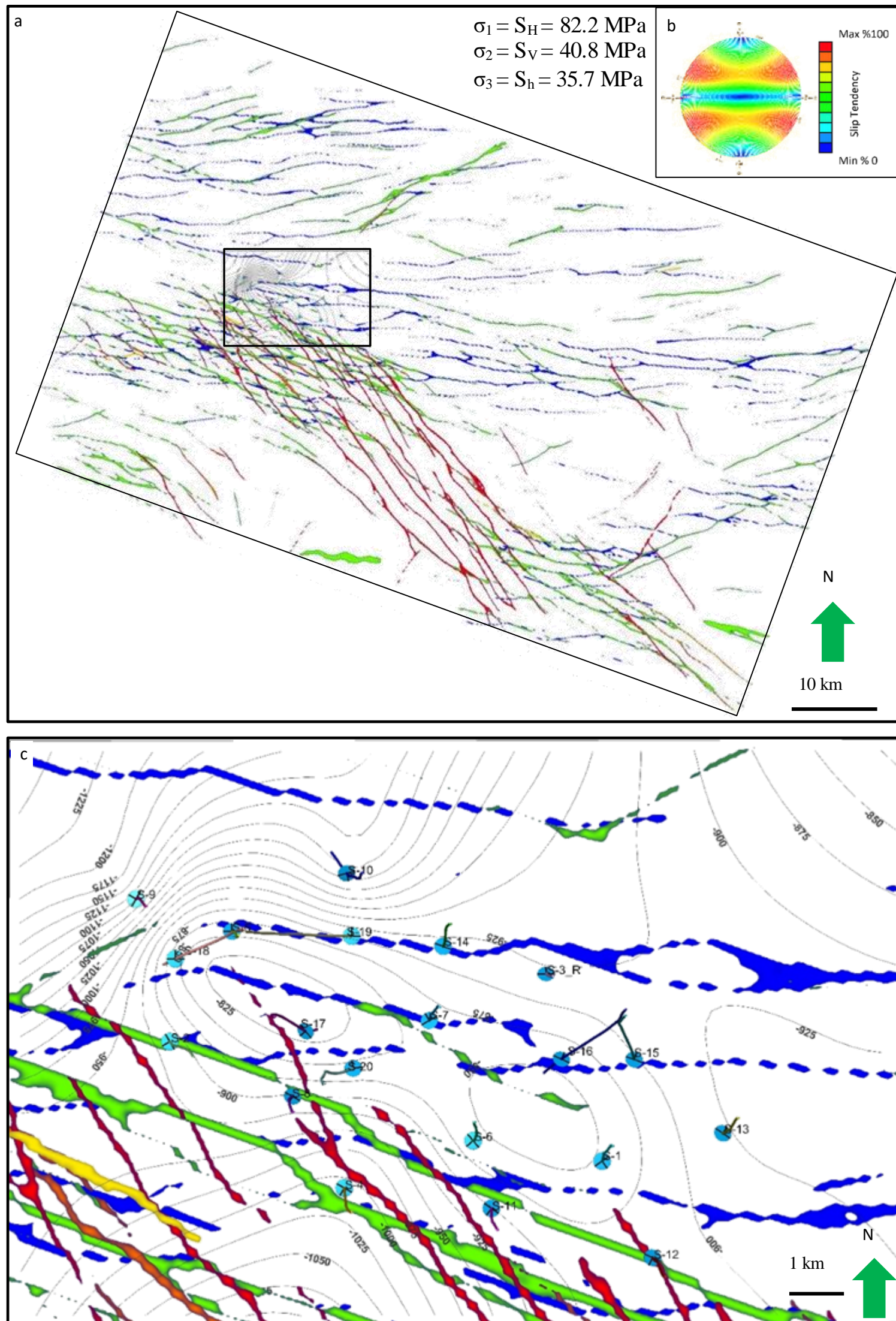


Figure 7.2. (a) A cropped ant-tracking depth slice of the -1100 m corresponding to an average regional burial depth of 1600 m of the Sayındere Formation from the Şambayat 3D seismic coverage area. The smallest rectangle demarcates the Şambayat **naturally fractured reservoir (NFR)** oilfield (Şambayat anticline), which is located near the tip of the red colored fault populations of the highest slip tendency. (b) The stereonet polar plot showing slip tendency fraction of accordingly color coded fault segments on the depth slice. (c) A closer view to the Şambayat NFR oilfield and its production wells. The contours show elevation of the Sayındere Formation tops from the wells drilled into the Şambayat antiformal structure. Most of the wells are at the overlapped area of tip damage zone of Samsat faults, **high-slip tendency (HST)** segments and the highs of the Şambayat structure.

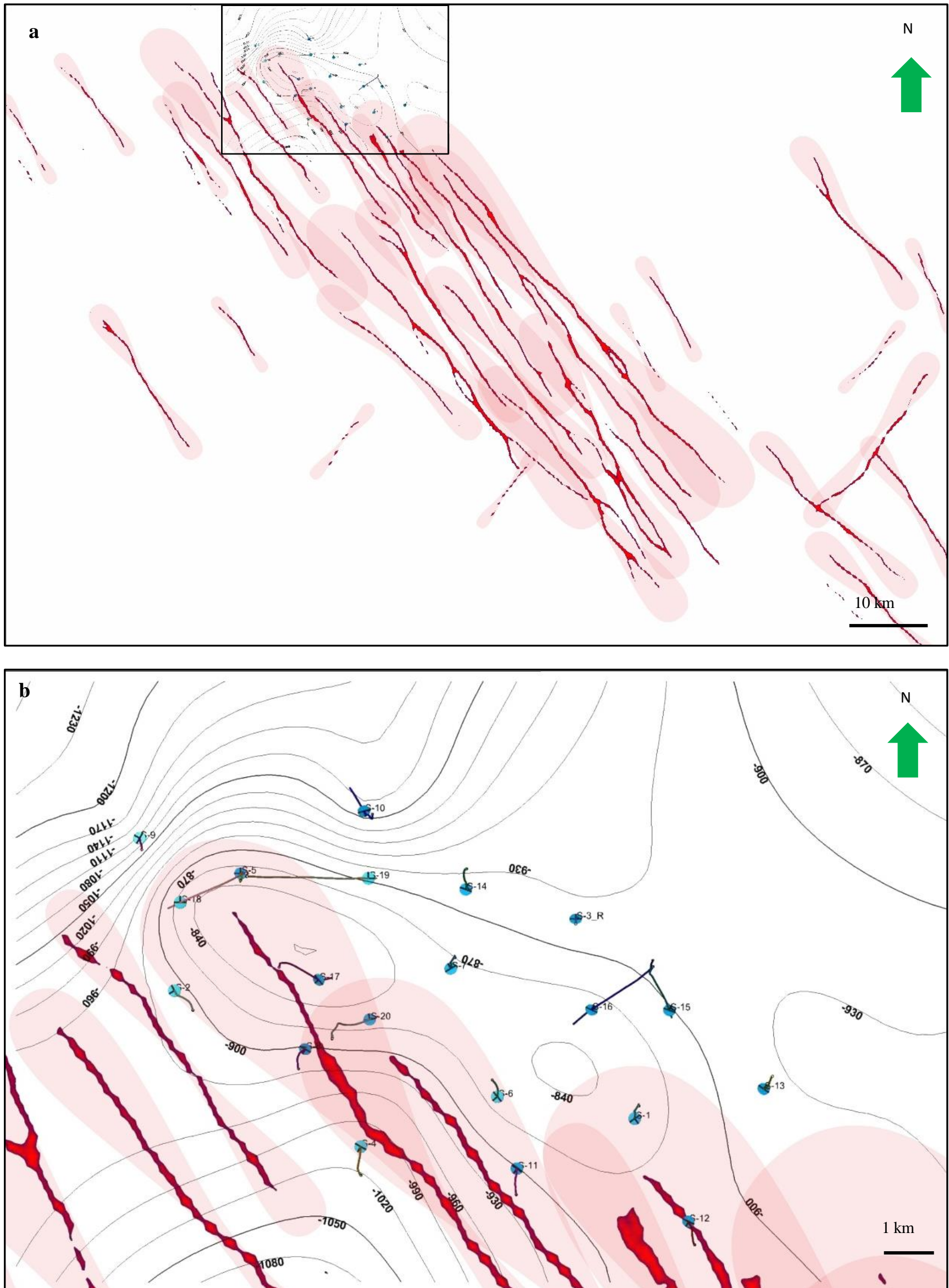


Figure 7.3. Maps showing highest-slip tendency, red color-coded principal shear zone segments of the Samsat Fault and envisaged damage zone extents for each one of those segments based on bilaterally growing fault models of Faulkner et al. (2011). **(a)** The broader view shows the Şambayat NFR oilfield, the smaller square is located at the tip zone of the active segments of the Samsat strike-slip fault zone. **(b)** The closer view shows that most of the exploration and development wells are coincided with the fault damage zones and the structural high.

Several high-slip tendency (HST) fault segments, whose lengths range from 6 to 40 km from the outcome of the advanced edge enhancement workflow incorporating multiply re-iterated ant-tracking processes, are observed. The Şambayat NFR oilfield and, its exploration and production wells are located either

- (i) At the tip zone of those HTS fault population,
- (ii) Within domains where multiple tip damage zones overlap (Figures 7.2 and 7.3).
- (iii) Within damage zones of the mechanical activity induced fault segments (See Discussion and Conclusion).

The width of the damage zones of individual fault segment is expected to be wider at its propagation tip since this domain, as a product of the latest and longest form of the main fault, is subjected to the highest stress accumulation (cf. Faulkner *et al.*, 2011). Therefore, the widths of the tip damage zones are expected to be associated with the displacement, length of the faults as well as the earthquake rupture velocity (cf. Wilson *et al.*, 2003; Engvik *et al.*, 2005; Rice *et al.*, 2005; Faulkner *et al.*, 2010). The extents of the damage zone of individual fault segments can be envisaged as it is demonstrated in the Figure 7.3.

This page intentionally left blank

CHAPTER 8

DISCUSSION AND CONCLUSION

In this chapter, I will discuss if this research could shed light upon any of the regional or conceptual problems that are mentioned in the “Purpose and scope” section of the introduction Chapter.

In the section 8.1, conceptual and regional problems that are related to the role of faults and stress field perturbations around faults on the formation and localization of fracture networks are addressed. Regionally poorly studied concepts of hydraulic and mechanical activity of faults and related fractures are also discussed in this section

In the section 8.2, it is indicated that the regional problems that are associated with the lack of previous works on strength parameters of the host rock and mechanical genesis of fracturing were tried to be resolved within this study. The local approaches to the regional problem of “the water-flooding” were also investigated in this section.

In the section 8.3, relative timing of fracturing and oil expulsion and its relation with the type of filling material is addresses.

In the section 8.4, kinematic interpretations for the localization of oil filled fractures are addressed.

In the section 8.5, the compilations of regional and conceptual conclusions that were come up with within this research are presented. The respective steps of a sufficient workflow to investigate NFR’s are also summarized in this section.

8.1. Combination of Slip Tendency and Stress Perturbation Analyses

Since the stress tensors have a tendency to bend to be parallel to the surfaces with negligible cohesion, which cannot withstand shear traction, the local orientation and magnitudes of the stress components tend to change in areas where many faults

and asperities exist. Such stress perturbations in any tectonic environment create secondary or tertiary hierarchy local stress fields. The main faults, which create primary stress perturbation, is expected to have the prime potential to accumulate the greatest stress and thus to pave the way for the formation of the most far-reaching fracture sets and subsidiary faults in broad deformation bands owing to their wide process zone as expected to be proportional to their length (Faulkner *et al.*, 2011). On the other hand, the strain energy is expected to disseminate in smaller portions among secondary and tertiary hierarchy faults. Therefore, those subsidiary faults cause the formation of relatively restricted, narrower deformation bands with smaller and not far-reaching elements. Nevertheless, relict and quite thorough-going faults (e.g., the products of earlier faulting regimes) may be subjected to reactivation because of changes in local orientation and magnitude of the stress field. Such faults may therefore gain potential as much as the contemporarily active faults to form extensive fractures and faults as they could accumulate sufficient stress either.

In such cases, a simple implementation of slip-tendency analysis to all existing fault population at all scales (as proposed by Morris *et al.*, 1996) may lead us to underestimate the number of locations where fracture swarm sweet spots might exist. For instance, the intensity distribution of fractures (whose openness and hydraulic activity are interpreted from the image logs and drilling stem test data acquired from the Sayındere Formation) penetrated in the Sambayat NFR oilfield wells (Özkaya *et al.*, 2013) indicate that some supposedly inactive relict faults, which are considered so based on measured remote stress magnitudes and orientations, might have been induced mechanical and hydraulic activity by the nearby faults via stress field perturbation (Figure 8.1). The orientation of the maximum principal stress – acquired from the drilling induced fractures in the wells (e.g., the Well S-10) bored in the northeastern contractional quadrant of the contemporarily active Samsat strike-slip fault strands– is about N30°–40°W (Figure 8.2). The relict faults coinciding this domain seem to induce mechanical and hydraulic activity since the wells drilled close to them has resulted in production from both fracture and matrix porosity as interpreted from DST tests (Figure 8.3).

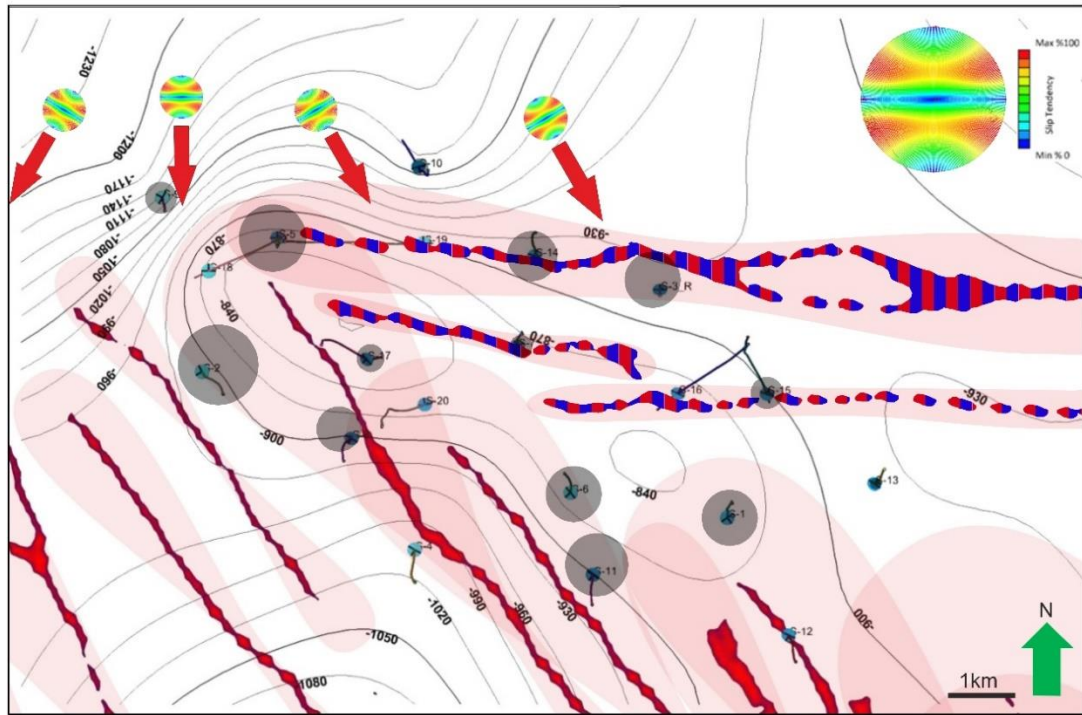


Figure 8.1. Dually color-coded (red and blue) faults are considered to show induced mechanical and hydraulic activity; these are in fact inactive relict faults, as depicted in the Figure 7.2 as blue color-coded, and are subjected to reactivation. This inference is based on a perturbation unaware slip-tendency analysis conducted with remote stress orientation and magnitude values. The transparent, grey bubbles indicate open fracture intensity within the penetrated zone of the Sayındere Formation at the production wells. Red arrows indicate local orientation of the maximum principal stress SHL derived from the image logs taken in the wells located at the northeastern tip of the temporarily active (red) segments of the Samsat strike-slip fault strand. The transparent pink areas indicate process zones of deformation for individual fault segments which are delineated from the Şambayat 3D seismic data.

Figure 8.3 illustrates pressure derivative logarithmic curves plotted with respect to the elapsed time derived from the drilling stem tests' second buildup phases. Stem tests are conducted at the wells drilled close to the dually colored faults (as shown in Figure 8.1). This diagram (Figure 8.3) indicates the presence of dual porosity in the Şambayat NFR oil field and provides evidence for the existence of hydraulically active fractures. These fractures are presumably related to the faults that are considered to show induced hydraulic activity due to activity of nearby high-slip tendency (HST) faults (Figure 8.1).

On the other hand, the formation of these fractures may be explained by the fact that the orientation of principal stresses and their magnitudes might have been subject to sporadic changes around HST faults either. Available data sources (e.g.,

extended leak off tests conducted in a number of wells or image logs obtained to define drilling induced borehole failures), however, are not frequently distributed in the study area in order to generate a high resolution picture of the local variations in stress magnitudes. For this reason, in-situ stress magnitude measurements are not possible. Nevertheless, the orientation variation(s) observed at the wellbore electrical image logs can be measured as exemplified in the Figure 8.2.

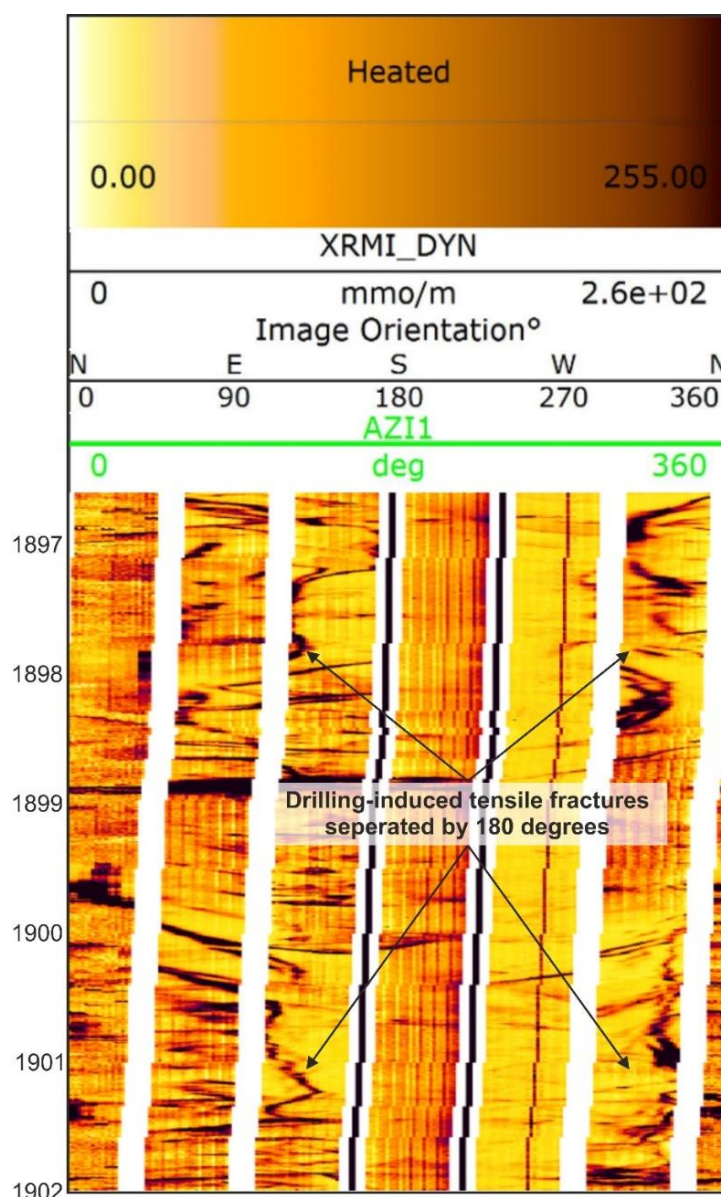


Figure 8.2. Image log showing drilling-induced fractures. Log belongs to Well-10, which is located at the north of the northwestern end of the hydraulically active and HST segments of the Samsat strike-slip fault strand. The fault strand perturbs the stress field and induce slip tendency to the relict faults (Figure 8.1) on the northern edge of the Şambayat NFR oilfield where S-3, S-5, S-7, S-10, S14, S-15, S-16 and S-19 wells are located.

Slip-tendency analyses are therefore reiterated for domains at which stress orientations are perturbed; it is assumed, as mentioned earlier in the text, that the magnitudes remain constant due to lack of high resolution in-situ stress magnitude data.

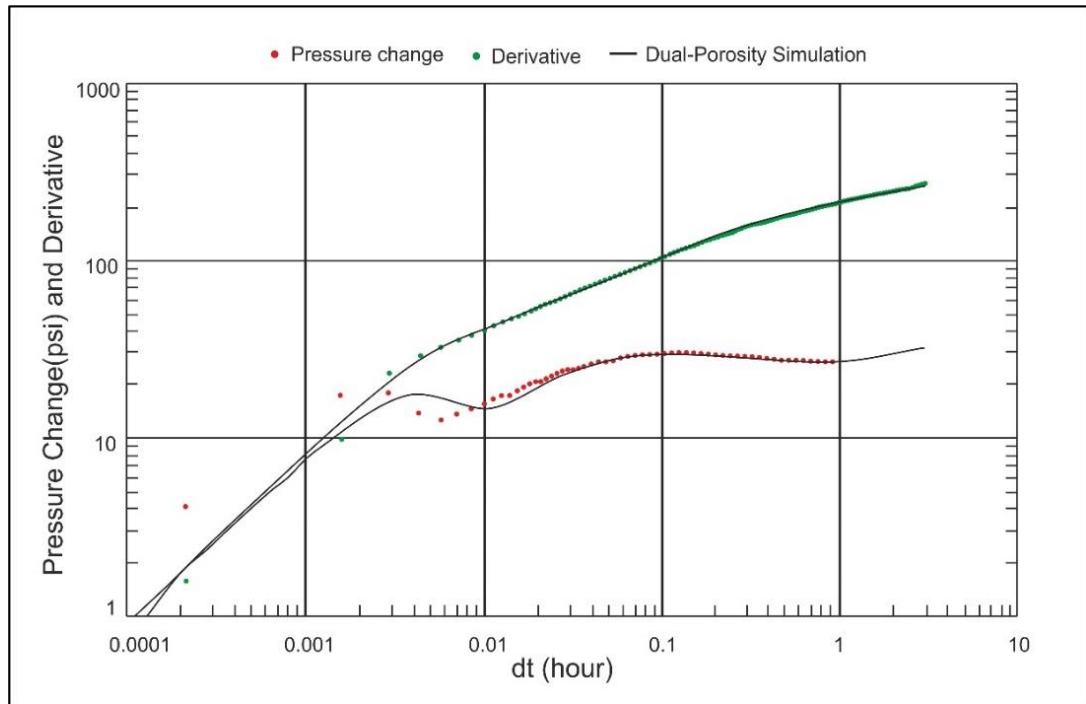


Figure 8.3. Log-log plot illustrating pressure change and derivative values with respect to elapsed time during the 2nd buildup phase of a drilling stem test conducted in Sayindere Formation at well S-14. The fluctuating response of the pressure derivative indicates dual (matrix and fracture) porosity.

As also mentioned earlier in the text, extended leak-off test (XLOT) charts, borehole breakout analyses, hydrostatic pressure gradient derived from drilling stem tests and rock density logs for derivation of the vertical stress must be available for as many wells as possible in order to define a fully-fledged depiction of the stress field with changing magnitudes throughout entire study area. Also, to ensure the validation of the stress measurements, sonic dipole dispersion analysis, whose theory is based on acoustoelastic effects of anisotropic loadings in rocks, can be incorporated to the workflow as a quality check parameter for the measurement of the maximum principal stress (Sinha *et al.*, 2008). Shear wave splitting processes of borehole sonic data are however not available for quality check purposes in this research.

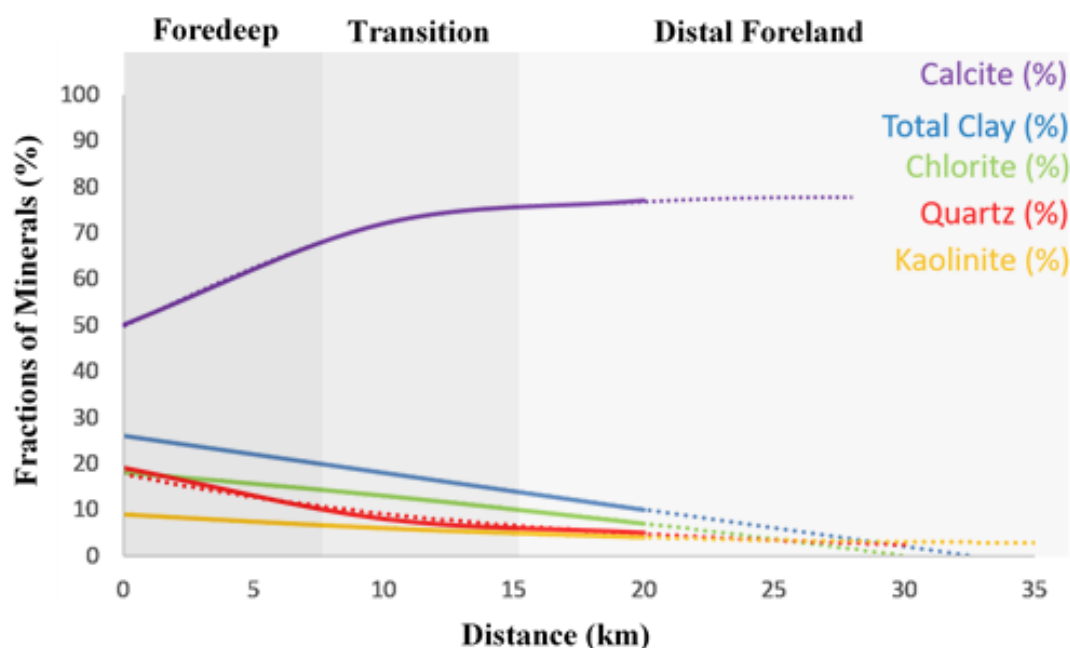


Figure 8.4. Binary plot showing gradients of mineral compositions from foredeep to distal foreland sediments of the syn-obduction upper Campanian Upper Kastel Formation and its contemporaneous distal counterpart, the Bozova Formation. X-Ray diffraction analysis are applied to the samples cored from Kastel-Bozova depth intervals in the wells drilled in foredeep, transition and distal foreland regions.

8.2. Mechanical Stratigraphy

There are two more problems to be addressed in this chapter: (1) underestimated height of the fluid column and its relation with the mechanical stratigraphy and fracture proneness of the overlying units of the Sayindere Formation and (2) what the Sayindere Formation owes its ability to preferentially become more fractured than other stiff units existing in the study area. The Sayindere Formation is overlain, depending upon the distance of the locality from the obduction front of allochthones drifted onto Arabian carbonate platform during late Campanian–early Maastrichtian time interval, by either: (i) marl-shale and sandstone alternation of flysch-like deposits of the Kastel Formation (Figure 8.6a) or (ii) argillaceous limestone-marl alternation of distal deposits of the Bozova Formation (Figure 8.6b). The allochthons caused a down-flexed movement on the underlying crust of the northern margin of the Arabian microcontinent during the Campanian; consequently the fore-deep was terminated southward, whereas depositional environments in distant regions have become shallower. The Bozova Formation is the chronostratigraphic, distal counterpart of the proximal the Kastel

Formation, which was deposited within the fore-deep environment. Mainly, they are coeval and separated from each other by a transition zone over an arc that lies parallel nearly east–west-trending termination line of the allochthones.

Bozova Formation is more of a chemical sedimentary unit in comparison with the clastic sedimentary Kastel Formation; it is evident by significantly higher percentage of calcite and lower percentage of total clay and quartz components (Figure 8.4). Relatively loose, granular aggregate constituents of the Kastel Formation can be considered as an elasto-plastic material and are expected to demonstrate a non-brittle granular flow instead of brittle fracturing. Additionally, based on field observations, the Kastel Formation does not frequently withstand far-reaching penetrative fractures for significant lengths since they collapse. Whereas most cracks and long fractures maintain their integrity and continuity within the Bozova Formation (Figure 3.14). The fluid column may therefore reach the interior of the Bozova Formation by forming an interconnected fracture network with the fractures within the underlying Sayındere Formation. In the existence of intercalating turbiditic sands and/or amalgamated distributary channels, which can provide additional accommodation volume to the fluids owing to their high porosity and permeability, the fluid column is plausibly connected with them; oil column might have therefore been drifted upward away from traditionally oil producing primarily porous Cretaceous platform carbonates (Figure 8.5). Thus, one can infer that decreasing clay and increasing calcite contents favors the fracture proneness of the sedimentary rocks. In other words, due to their higher calcite component, predominantly chemical depositional units, in courtesy of their higher cohesion, can withstand fractures better than relatively loose granular aggregates. When chemical sediments of limestones and argillaceous limestones are compared with respect to their fracture intensity and fracture porosity, the argillaceous limestones show a higher fracture proneness as it is observed in outcrops and production wells. It is also shown that either intensity or total porosity of fractures as well as their total contribution to the oil production are higher for the chemical sediments with significant clay content (e.g., Sayındere and Bozova formations) in comparison to limestones with negligible clay fraction (e.g., Derdere and Karababa formations).

According to field observations in different rock units of the Cretaceous succession, it can be deduced, based on their response to natural tri-axial compression, that the best naturally fractured reservoir (NFR) candidate rock unit must be stiff and cohesive enough to show brittle response and thus to accommodate fractures, but it must be the weakest among those cohesive rocks to preferentially get fractured first.

Earlier in the text, the brittle Sayındere Formation is compared with its overlying relatively ductile Kastel Formation. It is also important to understand why Sayındere Formation is preferentially get fractured more severely than its underlying brittle limestone units. In order to compare their strengths, some physical properties (e.g., sonic wave velocity and interval travel time) of those Cretaceous limestone units (e.g., Sayındere, Karaboğaz, Karababa and Derdere formations) are compared, since those properties are related with their uniaxial compressive strengths through empirical equations below:

$$\text{UCS (Mpa)} = \left(\frac{7682}{\Delta t} \right)^2 / 145 \quad \text{Equation 25 (Militzer, 1973)}$$

$$\text{UCS (Mpa)} = 10^{(2.44 + \frac{109.14}{t})} / 145 \quad \text{Equation 26 (Golubev and Rabinovich, 1976)}$$

Where Δt is the sonic log reading in $\mu\text{s}/\text{ft}$ and t is the interval transit time in seconds. According to these equations, the sonic log reading, Δt value, is inversely proportional with the uniaxial compression strength of the rocks. With is average 58 $\mu\text{s}/\text{ft}$ of Δt reading from the sonic logs and 145 MPa empirical UCS value, as calculated from the equation 26, the Sayındere Formation is expected to show the lowest brittle strength among all the Cretaceous limestone units, such as Karaboğaz, Karababa and Derdere formations with their average Δt readings of 55, 53 and 50 $\mu\text{s}/\text{ft}$ and of empirical UCS values of 183, 217 and 289 MPa, respectively. It is therefore reasonable for the Sayındere Formation, with its slighter compressive strength, to preferentially be more fractured than other limestones in the study area.

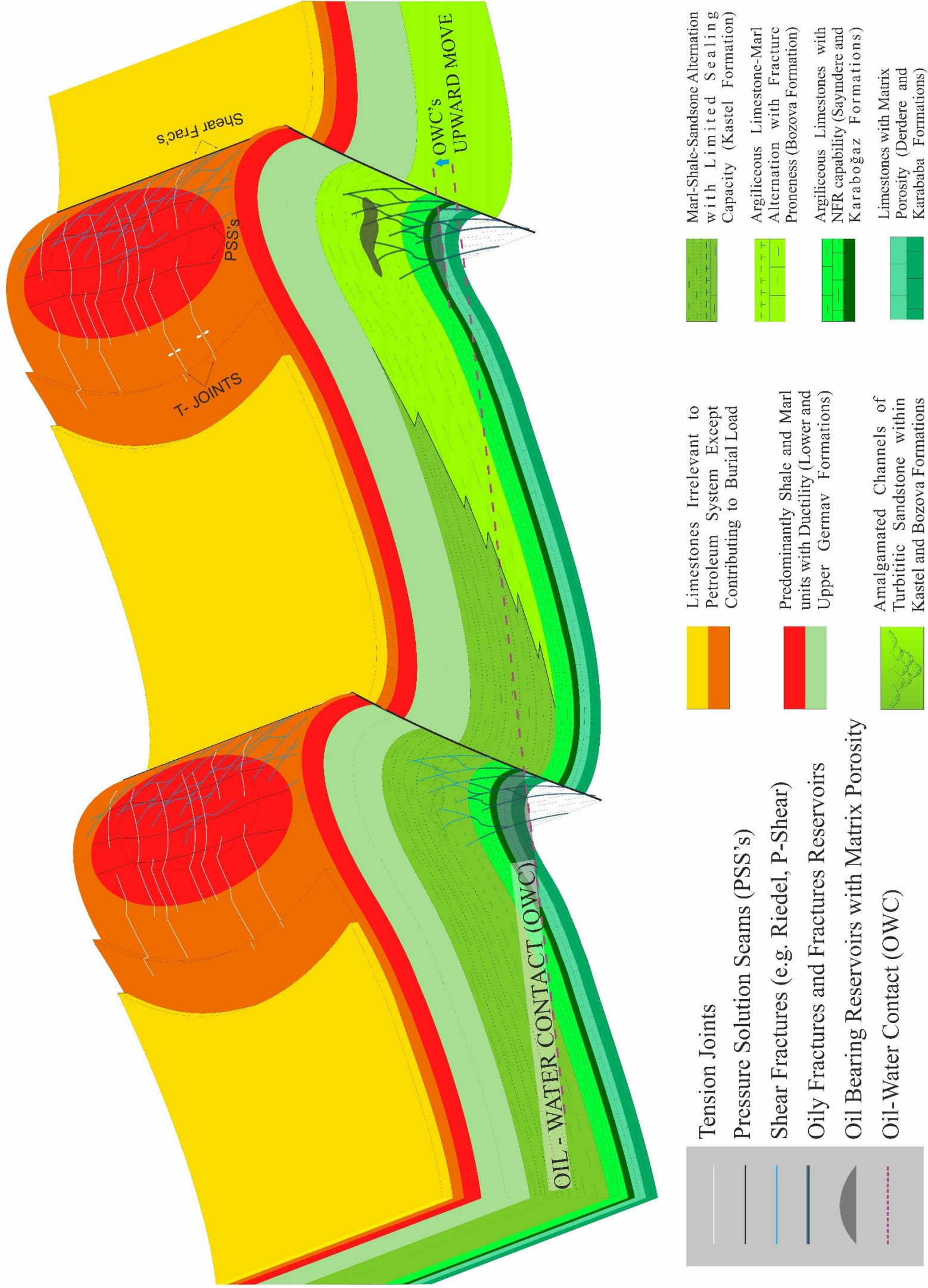


Figure 8.5. Conceptual model for changing heights of the oil column related to facies and mechanical stratigraphy of the supposedly cover rocks deposited over different oilfields.

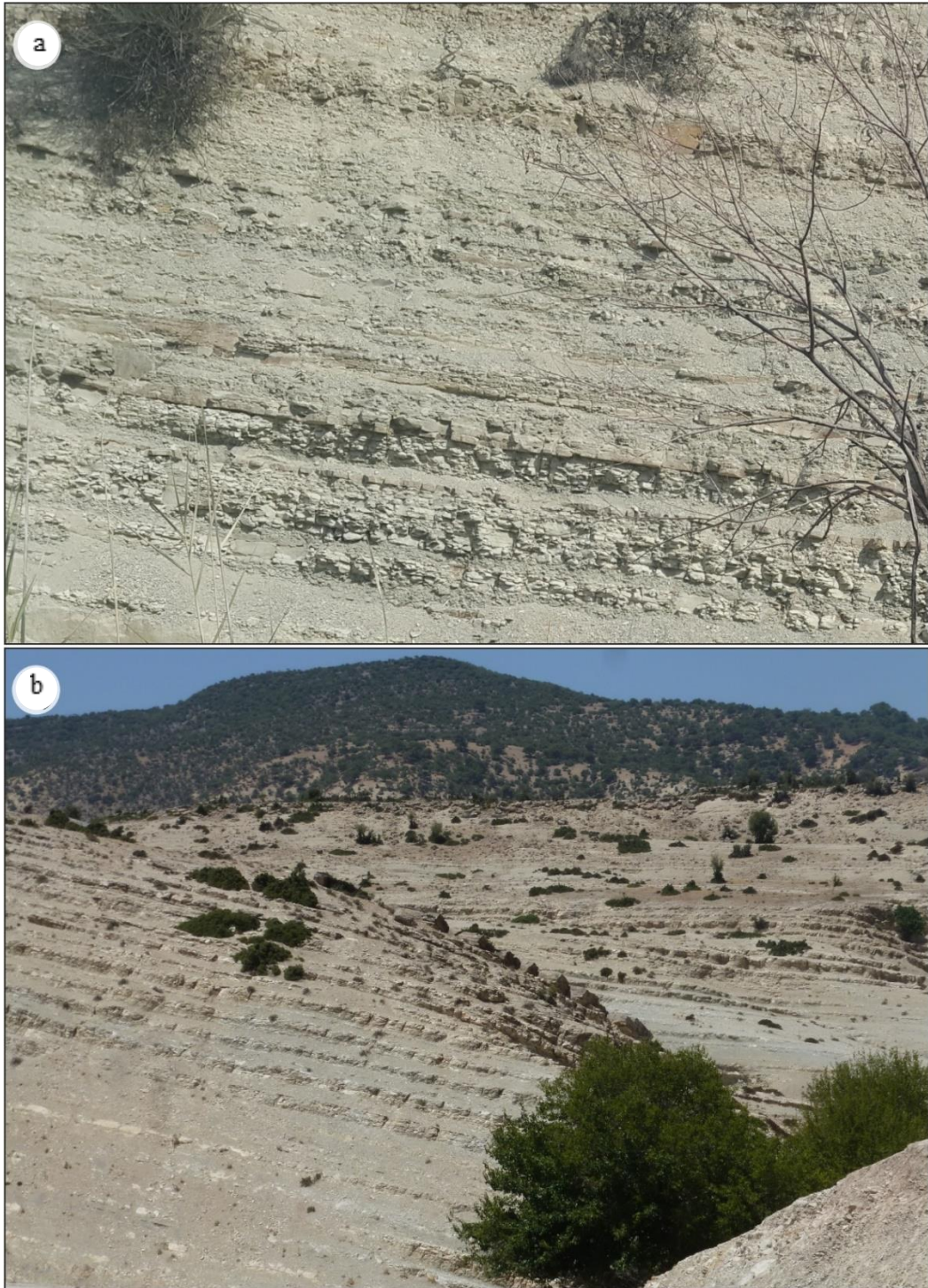


Figure 8.6. Field views from (a) the Kastel Formation outcrop from a proximal location to the allochthons' final advancement line – the unit comprises marl, shale and sandstone alternation (near Besni County of Adiyaman province of SE Turkey) and (b) the Bozova Formation outcrop from a distal location with respect to the final advancement line of the allochthons – the formation consists of argillaceous limestone-marl alternations (near Kuyulu town of southern Adiyaman province at the northern gentle wing of the Karababa anticline).

8.3. Incorporation of Oil Expulsion Timing Into Fracture Oiliness Predictions

Based upon basin analysis studies conducted for the region, the diagrams of geological time against hydrocarbon generation and expulsion rates of regional source rocks (Figure 8.7) suggest that: (i) at present day, oil generation and expulsion is still ongoing at a moderate rate, (ii) late Miocene–Pliocene period was the time of highest oil expulsion rate in the region and (iii) the expulsion rate was however negligible during Eocene to Miocene time interval (Figure 8.7).

Therefore, the faults and fractures, whose activity periods ended earlier than Miocene, are expected to be filled by other circulating minerals (such as calcite) as observed during field studies (see Chapter 3) whereas structures younger than middle Miocene or the ones that are contemporarily active are expected to be filled by oil if other circumstances (e.g., structural position, seal and trap availability) are also in favor of this incidence.

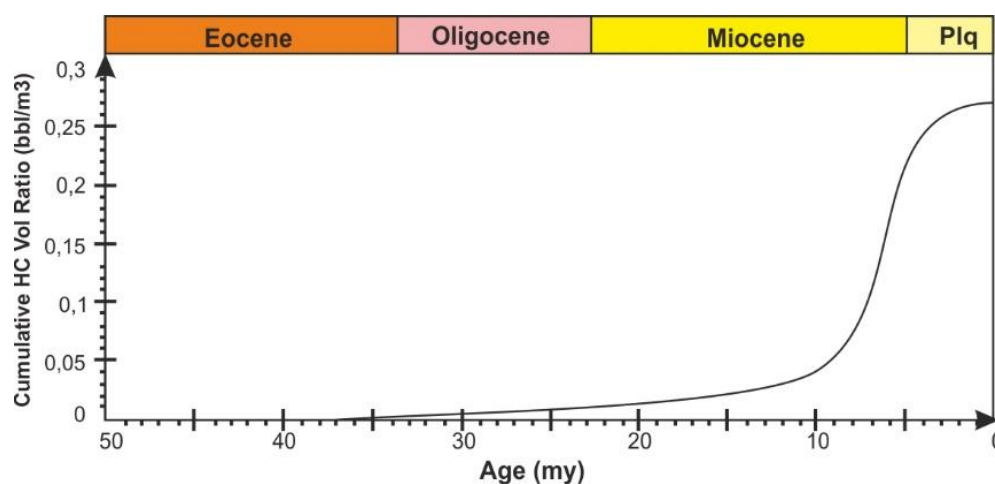


Figure 8.7. A binary plot illustrating oil generation and expulsion rates versus time for Adiyaman province foreland basins in general, including the Şambayat NFR oilfield.

8.4. Localization Mechanism and Orientation of the Oil Filled Fractures

Observations on the filling materials of any kinds of fractures around faults or folds show that the fractures located within highs (e.g., anticlines that have raised up and eroded enough to possibly pave the way for the cessation of the oil generation

due to loss of heat and overburden pressure) include calcite rather than oil derivatives within their walls. On the other hand, fractures located within lows (e.g., extensional step-overs, the Kuyulu low) become oily probably due to: (i) local maturation of the locally sufficiently buried source rocks and consequent uninterrupted oil generation, and/or (ii) courtesy of hydraulic activity and/or (iii) down-dip penetrating fashion of the strike-slip fault-related dilatational Riedel shear fractures.

As it is shown in Figure 3.15a, fractures in the Riedel shear domain of the Kuyulu low (station 6) favor the vertical migration of the fluids. Nevertheless, information (production data, electrical image log interpretations and locations of the wells producing from the fractures) from buried oilfields in the Adıyaman region suggest that fold-related tension joints and/or fault-related shear fractures at the buried highs can still become oily because oil generation might have not been interrupted in courtesy of sufficient burial load of the preserved thickness of the overlying units.

Field observations also show that deviations from the principal shear directions of the main strike-slip faults affect the preferred orientations of the fractures around them. This results in formation of Riedel shear, P-shear domains with predominantly Riedel and P-shear type of fractures, respectively. This would be the case for the basins whose organic-rich deposit barely reached maturity in the recent geological past.

8.5. Conclusive Remarks

From the field observations on the Cretaceous successions in terms of whose each members' response to natural tri-axial compression, it can be deduced that the best NFR candidate rock unit must be strong and cohesive enough to be brittle and thus to accommodate fractures, but must be the weakest among those cohesive rocks to preferentially get fractured first. To explore NFR intervals in undocumented regions in this respect, conducting triaxial and uniaxial strength tests over the NFR candidate rock units and/or determining their compressive strength by using its empirical relations with other physical properties can be important steps as parts of a

fully-fledged NFR exploration workflow. As this research numerically, experimentally and qualitatively proved, in the Northern margin of the Arabian microplate, among the lithological elements of the Cretaceous petroleum system, the Sayındere formation is separated from its overlying shaley units with its brittleness and from its underlying units with its weakness to be the best candidate to form a Naturally Fractured Reservoir.

The measured and extrapolated far field stresses are found insufficient to initiate fractures in the Sayındere formation regarding its measured tri-axial compressive strength. Nevertheless, based on our stress perturbation analysis, amplified natural stresses which could reach at levels beyond critical to fracture Sayındere formation can occur in the stress concentration areas where the optimally oriented faults alter the stress field. Therefore determination of the active, stress accumulating optimally oriented faults is a must to explore NFR's. However, as it was analyzed from the production data of the wells drilled in the Şambayat NFR oilfield, some supposedly relict and inactive faults and fractures that had formed in an earlier tectonic faulting regime can lately induce activity in courtesy of neighboring faults and the local stress field perturbed by them. Therefore, a stress perturbation analysis based on densely spaced magnitude and vectorial in-situ stress measurement data is another necessity to locate fracture swarm sweet spots and NFR's.

Even in most cases, the shear fractures provide only permeability of the reservoir rocks, the Riedel shear fractures, which may have both slip and extension tendency, can contribute bulk porosity on a level with %10 total linear fracture porosity as evidenced by the oil filled fracture thickness measurements conducted within this research. In the pull apart or extensional step-over domains such as Kuyulu area, the total volumetric opening can be distributed among Riedel and tension fractures, and thus the fracture porosity could reach such significant amounts. Therefore, as the NFR's with negligibly porous matrices cannot support lateral flow of the fluids, low areas with vertical fractures can be prospective for petroleum explorations.

REFERENCES

- Ala, Mamun & Moss, B. (2007). Comparative petroleum geology of SE Turkey and NE Syria. *Journal of Petroleum Geology*. 1.3-27. 10.1111/j.1747-5457.1979.tb00626.x.
- Al-Husseini, Moujahed. (2004). Pre-Unayzah unconformity, Saudi Arabia. *GeoArabia*.
- Allmendinger, Richard & Cardozo, Nestor & Fisher, Donald. (2012). Structural geology algorithms: Vectors and tensors. *Structural Geology Algorithms: Vectors and Tensors*. 10.1017/CBO9780511920202.
- Alsharhan, Abdulrahman & Nairn, A.E.M.. (1997). *Sedimentary Basins and Petroleum Geology of the Middle East*. Elsevier Science.
- Altiner, demir. (1989). An Example for the Tectonic Evolution of the Arabian Platform Margin (SE Anatolia) during Mesozoic and some Criticisms of the Previously Suggested Models. 10.1007/978-94-009-2253-2_7.
- Amadei, Bernard & Stephansson, Ove. (1997). *Rock Stress and Its Measurement*. 10.1007/978-94-011-5346-1_8.
- Anderson, E.. (1951). *The Dynamics of Faulting and Dyke Formation With Application to Britain*. Oliver and Boyd, London, ed. 2. 206.
- Aydemir, Attila. (2011). Comparison of Mississippian Barnett Shale, Northern-Central Texas, USA and Silurian Dadas Formation in Southeast Turkey. *Journal of Petroleum Science and Engineering*. 80. 81–93. 10.1016/j.petrol.2011.10.009.
- Aydin, Atilla. (2000). Fractures, faults, and hydrocarbon entrapment, migration and flow. *Marine and Petroleum Geology*. 17. 797-814. 10.1016/S0264-8172(00)00020-9.
- Barrier, Eric & Machhour, Louai & Blaizot, Marc. (2014). Petroleum Systems of Syria. *AAPG Memoir 106. Petroleum systems of the Tethyan region*. 335-378. 10.1036/13431862M1063612.

Bartlett, W.L. & Friedman, M. & Logan, J.M.. (1981). Experimental folding and faulting of rocks under confining pressure Part IX. Wrench faults in limestone layers. *Tectonophysics*. 79. 255-277. 10.1016/0040-1951(81)90116-5.

Barton, Colleen & Zoback, Mark & Moos, Daniel. (1995). Fluid flow along active faults in crystalline rocks. *Geology*. 23. 10.1130/0091-7613(1995)023<0683:FFAPAF>2.3.CO;2.

Barton, Colleen & Zoback, Mark & Burns, Kerry. (1988). In-situ stress orientation and magnitude at the Fenton Geothermal Site, New Mexico, determined from wellbore breakouts. *Geophysical Research Letters*-15. 467-470. 10.1029/GL015i005p00467.

Bell, J.. (1990). Investigating stress regimes in sedimentary basins using information from oil industry wireline logs and drilling records. Geological Society, London, Special Publications. 48. 305-325. 10.1144/GSL.SP.1990.048.01.26.

Bell, J.S. & Gough, D.I.. (1979). Northeast-southwest compressive stress in Alberta evidence from oil wells. *Earth and Planetary Science Letters*. 45. 475-482. 10.1016/0012-821X(79)90146-8.

Berberian, M., King, G.G.P., 1981, Towards a paleogeography and tectonic evolution of Iran: *Canadian Journal of Earth Sciences*, 18, 210–265.

Berra, Fabrizio & Angiolini, Lucia. (2014). The Evolution of the Tethys Region throughout the Phanerozoic: A Brief Tectonic Reconstruction. 10.1306/13431840M1063606.

Beydoun, Ziad. (1998). Arabian plate oil and gas: Why so rich and so prolific?. *Episodes*. 21. 74-81. 10.18814/epiiugs/1998/v21i2/001.

Bott, M.H.P.. (1959). The mechanism of oblique slip faulting. *Geological Magazine*. 96. 109-117.

Bourne, Stephen & Willemse, Emanuel. (2001). Elastic stress control on the pattern of tensile fracturing around a small fault network at Nash Point, UK. *Journal of Structural Geology*. 23. 1753-1770. 10.1016/S0191-8141(01)00027-X.

Brew, G.E. (2001): Tectonic evolution of Syria interpreted from integrated geophysical and geological analysis.– PhD Thesis, Cornell University, Ithaca, New York, 323 p.

Brown, E. T. and Hoek, E. 1978. Trends in relationships between measured rock insitu stresses and depth. Int. J. Rock Mech. Min. Sci. & Geomech. Abstr. Vol. 15, pp. 211-215.

Byerlee, J.. (1978). Friction of Rocks. Pure and Applied Geophysics PAGEOPH. 116. 615-626. 10.1007/BF00876528..

Cater, J. M. L. and Gillcrist, J. R. 1994. Karstic Reservoirs of the Mid-Cretaceous Mardin Group, SE Turkey: Tectonic and Eustatic Controls on their Genesis, Distribution and Preservation. Journal of Petroleum Geology, 17(3): p. 253-278.

Cloos, H.. (2019). Experimente zur inneren Tektonik. Centralbl. Mineral. Pal.. 609-621.

Cobb, R.E. (1957). Columnar section Bedinan Kanisorik Paleozoic. TPAO Arama Grubu, Rapor No.576.

Davis, George & Reynolds, Stephen. (1997). Structural Geology of Rocks and Regions. Journal of Structural Geology. 19. 10.1016/S0191-8141(97)85684-2.

Dercourt, J. & Zonenshain, L.P. & Ricou, L.-E & Kazmin, V.G. & Le Pichon, Xavier & Knipper, A.L. & Grandjacquet, C. & Sbertshikov, I.M. & Geyssant, J. & Lepvrier, Claude & Pechersky, Diamar & Boulin, J. & Sibuet, Jean-Claude & Savostin, L.A. & Sorokhtin, O. & Westphal, M. & Bazhenov, Mikhail & Lauer, J.P. & Biju-Duval, B.. (1986). Geological evolution of the Tethys belt from the Atlantic to the Pamirs since the LIAS. Tectonophysics. 123. 241-315. 10.1016/0040-1951(86)90199-X.

de jousineau, Ghislain & Petit, Jean & Gauthier, Bertrand. (2003). Photoelastic and numerical investigation of stress distributions around fault models under biaxial compressive loading conditions. Tectonophysics. 363. 19-43. 10.1016/S0040-1951(02)00648-0..

De Swaan, Abraham. (1976). Theory of Waterflooding in Fractured Reservoirs. Society of Petroleum Engineers Journal. 18. 10.2118/5892-PA.

Engvik, Ane & Bertram, Andreas & Kalthoff, Jörg & Stöckhert, Bernhard & Austrheim, Håkon & Elvevold, Synnøve. (2005). Magma-driven hydraulic fracturing and infiltration of fluids into the damaged host rock, an example from Dronning Maud Land, Antarctica. Journal of Structural Geology. 27. 839-854. 10.1016/j.jsg.2005.01.009.

Fairchild, Ian. (2009). Balmy Shores and Icy Wastes: The Paradox of Carbonates Associated with Glacial Deposits in Neoproterozoic Times. 10.1002/9781444304534.ch1.

Faulkner, Daniel & Jackson, Christopher & Lunn, Rebecca & Schlische, Roy & Shipton, Zoe & Wibberley, Christopher & Withjack, Martha. (2010). A review of recent developments concerning the structure, mechanics and fluid flow properties of fault zones. Journal of Structural Geology. 32. 1557-1575. 10.1016/j.jsg.2010.06.009.

Faulkner, Daniel & Mitchell, Thomas & Jensen, Erik & Cembrano, Jose. (2011). Scaling of fault damage zones with displacement and the implications for fault growth processes. J. Geophys. Res. 116. 10.1029/2010JB007788.

Fleuty, M.J.. (1964). The Description of Folds. Proceedings of The Geologists Association - PROC GEOL ASSOC. 75. 461-492. 10.1016/S0016-7878(64)80023-7.

Fontaine, J. & Monod, O.. (1989). Hezan Units: a fragment of the south neo-Tethyan passive Continental margin in SE Turkey. Journal of Petroleum Geology. 12. 29 - 50. 10.1111/j.1747-5457.1989.tb00219.x.

Fouad, S.F.A. (2010). Tectonic and Structural Evolution of the Mesopotamia Foredeep, Iraq. Iraqi Bulletin of Geology and Mining, 6 (2), 41-53.

Golubev, A.A. & Rabinovich, G.Y.. (1976). Resultaty primeneia apparatury akusticeskogo karotasa dlja predeleina proconstych svoistv gornych porod na mestorosdeniaach tverdyh isjopaemyh. Prikl. Geofiz. Moskva. 73. 109-116.

- Gorur, N. & Celikdemir, E. & Dulger, S.. (1991). Carbonate platforms developed on passive continental margins: Cretaceous Mardin carbonates in SE Anatolia as an example. *Bulletin - Technical University of Istanbul*. 44. 301-324.
- Gradstein, Felix & Ogg, James & Smith, A.G.. (2005). A geologic Time Scale 2004. A Geologic Time Scale 2004. i-viii. 10.1017/CBO9780511536045.
- Grotzinger, John & Knoll, Andrew. (1996). Anomalous Carbonate Precipitates: Is the Precambrian the Key to the Permian?. *Palaaios*. 10. 578-96. 10.2307/3515096.
- Guiraud, René & Bosworth, William. (1999). Phanerozoic geodynamic evolution of northeastern Africa and northwestern Arabian platform. *Tectonophysics*. 315. 73-104. 10.1016/S0040-1951(99)00293-0.
- Gül, M.A., Kirici, S., Türesin, F.M., Arıkan, G.Ç., Güzel, A., Altınsoy, B., Geniş, A.E., and Güray, A., 2014. Lithostratigraphy and facies characteristics of the Mesozoic units in Mardin, Mazıdağı and Derik Regions. 67th Geological Congress of Turkey.
- Haimson, Bezalel & Fairhurst, Charles. (1967). Initiation and Extension of Hydraulic Fractures in Rocks. *SPE Journal*. 7. 310-318. 10.2118/1710-PA.
- Haq, Bilal. (2013). Cretaceous Eustasy Revisited. *Global and Planetary Change*. 113. 10.1016/j.gloplacha.2013.12.007.
- Haq, Bilal. (2017). Jurassic Sea-Level Variations: A Reappraisal. *GSA Today*. 28. 10.1130/GSATG359A.1.
- Haq, Bilal & Schutter, Stephen. (2008). A Chronology of Paleozoic Sea-Level Changes. *Science (New York, N.Y.)*. 322. 64-8. 10.1126/science.1161648.
- Herget G (1974) Ground stress conditions in Canada. *Rock Mech* 6:53–74
- Higgins, J.A. & Schrag, D.P., 2003. Aftermath of a snowball Earth. *Geophysics, Geochemistry, Geosystems* 4, 10.1029/2002GC000403.
- Hills, E.. (1964). *Geology*. (Book Reviews: Elements of Structural Geology). *Science*. 143. 945-946.

Hirano, Shiro & Yamashita, Teruo. (2011). Analysis of the static stress field around faults lying along and intersecting a bimaterial interface. *Geophysical Journal International*. 187. 1460 - 1478. 10.1111/j.1365-246X.2011.05202.x.

Hubbert, M.K. & Willis, D.G.W.. (1972). Mechanics of hydraulic fracturing [J. Mem. - Am. Assoc. Pet. Geol.; (United States)]. 18.

Jamison, Dennis & Cook, Neville. (1978). Analysis of measured values for the state of stress in the earth's crust. 10.2172/932965.

Johansen, T. & Fossen, Haakon. (2008). Internal geometry of fault damage zones in interbedded siliciclastic sediments. *Geological Society, London, Special Publications*. 299. 35-56. 10.1144/SP299.3.

Katz, Yoram & Weinberger, Ram & Aydin, Atilla. (2004). Geometry and kinematic evolution of Riedel shear structures, Capitol Reef National Park, Utah. *Journal of Structural Geology*. 26. 491-501. 10.1016/j.jsg.2003.08.003.

Kazmin, V.. (2002). The late Paleozoic to Cainozoic intraplate deformation in North Arabia: a response to plate boundary-forces. *Stephan Mueller Special Publication Series*. 2. 10.5194/smsps-2-123-2002.

Kelly, P.G. & Peacock, David & Sanderson, David & McGurk, A.C.. (1999). Selective reverse-reactivation of normal faults, and deformation around reverse-reactivated faults in the Mesozoic of the Somerset coast. *Journal of Structural Geology*. 21. 493-509. 10.1016/S0191-8141(99)00041-3.

Kennedy, Martin & Christie-Blick, Nicholas & Sohl, Linda. (2001). Are Proterozoic Cap Carbonates and Isotopic Excursions a Record of Gas Hydrate Destabilization Following Earth's Coldest Intervals. *Geology*. 29. 443-446. 10.1130/0091-7613(2001)029<0443:APCCAI>2.0.CO;2.

Ketin, İ., 1964, Güneydoğu Anadolu Paleozoyik teşekküllerinin jeolojik etüdü hakkında rapor (I.Kısım: Derik-Bedinan, Penbeğli-Tut ve Hazro bölgesi): TPAO Arama Grubu, Rapor no. 287, 36 s., Ankara.

Kim, Young-Seog & Peacock, David & Sanderson, David. (2004). Fault damage zones. *Journal of Structural Geology*. 26. 503-517. 10.1016/j.jsg.2003.08.002.

Kirsch, Ernst. (1898). Die Theorie der Elastizität und die Bedürfnisse der Festigkeitslehre. *Z VDI. Zeitschrift des Vereines Deutscher Ingenieure*. 42. 797-807.

Klimczak C (2011) Processes of progressive deformation with applications to jointing faulting and fluid flow. Dissertation, University of Nevada, Reno

Knoll, Andrew & Christie-Blick, Nicholas & Walter, Malcolm & Narbonne, Guy. (2006). The Ediacaran Period: A New Addition to the Geologic Time Scale. *Lethaia*. 39. 10.1080/00241160500409223.

Li, Kewen & Horne, Roland. (2003). A Decline Curve Analysis Model Based on Fluid Flow Mechanisms. *SPE Reservoir Evaluation & Engineering*. 8. 10.2118/83470-MS.

Mandl, G.. (1987). Discontinuous fault zones. *Journal of Structural Geology* - 9. 105-110. 10.1016/0191-8141(87)90047-2.

Mandl, G.. (2005). Rock joints: The mechanical genesis. 10.1007/b137623.

Mastin, L. G., An analysis of stress-induced elongation of boreholes at depth, M.S. thesis, Stanford Univ., Stanford, Calif., 1984

McCutchen, W.R.. (1982). Some elements of a theory for In-situ stress. *International Journal of Rock Mechanics and Mining Sciences & Geomechanics Abstracts*. 19. 201-203. 10.1016/0148-9062(82)90890-7.

Militzer, H. & Stoll, R.. (1973). Einige Beitrageder geophysics zur primadatenerfassung im Bergbau. *Lipzig*. 3. 21-25.

Moore, J.. (1979). Tectonics of the Najd Transcurrent Fault System, Saudi Arabia. *Journal of The Geological Society* 136. 441-452. 10.1144/gsjgs.136.4.0441.

Moore, Diane & Byerlee, J.. (1992). Relationships between sliding behavior and internal geometry of laboratory fault zones and some creeping and locked strike-slip faults of California. *Tectonophysics*. 211. 305-316. 10.1016/0040-1951(92)90067-G.

Morgenstern, N.R. & Tchalenko, John. (1967). Microstructural observations on shear zones from slips in natural clays. Proc. Geotechnical Conf. (Oslo). 1. 147-152.

Morris, Alan & Ferrill, David & Henderson, D. (1996). Slip-tendency analysis and fault reactivation. *Geology*. 24. 10.1130/0091-7613(1996)024<0275:STAAFR>2.3.CO;2.

Murrell, S.A.F.. (1963). A criterion for brittle fracture of rocks and concrete under triaxial stress and the effect of pore pressure on the criterion. *Rock Mechanics*. 563-577.

Nelson, Ronald. (2001). *Geologic Analysis of Naturally Fractured Reservoirs*. Gulf Professional.

Nenna, Filippo & Aydin, Atilla. (2011). The formation and growth of pressure solution seams in clastic rocks: A field and analytical study. *Journal of Structural Geology* 33. 633-643. 10.1016/j.jsg.2011.01.014.

Niven, E.B. and Deutsch, C.V. 2009. A sensitivity analysis for equivalent permeability tensors calculated from 2D discrete fracture networks. In *Centre for Computational Geostatistics: Report 11*

Nolte, K.G. and Economides, M.J. 1989. Fracturing Diagnosis Using Pressure Analysis. In *Reservoir Stimulation*, ed. M.J.Economides and K.G.Nolte, Chap. 7, Englewood Cliffs, NJ.: Prentice Hall, Inc.

Ozkaya, Sait & Dölek, Tacettin & Yapan, Kadri & Durukan, B.. (2019). Controls on fracture flow potential in a tight carbonate reservoir: Sayindere Formation (Campanian), West Adiyaman basin, SE Turkey. *Journal of Petroleum Geology*. 42. 10.1111/jpg.12730.

Perinçek, D., 1979, The geology of Hazro-Korudağ-Çüngüş-Maden-Ergani-Hazer-Elazığ-Malatya area: Ankara, Turkey, Türkiye Jeoloji Kurumu Yayını, 34 p.

Rice, James & Sammis, Charles & Parsons, Robert. (2005). Off-Fault Secondary Failure Induced by a Dynamic Slip Pulse. *Bulletin of the Seismological Society of America*. 95. 109-134. 10.1785/0120030166.

Ridgwell, Andy & Kennedy, Martin & Caldeira, Ken. (2003). Carbonate Deposition, Climate Stability, and Neoproterozoic Ice Ages. *Science* (New York, N.Y.). 302. 859-62. 10.1126/science.1088342.

Riedel, W.. (1929). Zur Mechanik geologischer Brucherscheinungen. *Zur Mechanik Geologischer Brucherscheinungen*. 354–368. 354-368.

Righi, M. & Cortesini, A.. (1964). Gravity tectonics in foothills structure belt of southeast Turkey. *American Association of Petroleum Geologists Bulletin*. 48. 1911-1937.

Robertson, A.H.F. & Parlak, Osman & Rizaoglu, Tamer & Ünlügenç, Ü & İnan, N. & Taşlı, K. & Ustaömer, Timur. (2007). Tectonic evolution of the South Tethyan ocean: Evidence from the Eastern Taurus Mountains (Elazığ region, SE Turkey). 10.1144/GSL.SP.2007.272.01.14

Rolland, Yann & Marc, Sosson & Adamia, Shota & Sadradze, Nino. (2011). Prolonged Variscan to Alpine history of an active Eurasian margin (Georgia, Armenia) revealed by $^{40}\text{Ar}/^{39}\text{Ar}$ dating. *Gondwana Research - GONDWANA RES.* 20. 798-815. 10.1016/j.gr.2011.05.007

Roxar. 2009. Naturally fractured reservoirs: An introduction to their appraisal and management [online]. Available from <http://www.roxar.com/category.php?categoryID=2141> Cited April 22 2009

Ruban, Dmitry & Al-Husseini, Moujahed & Iwasaki, Yumiko. (2007). Review of Middle East Paleozoic Plate tectonics. *GeoArabia*. 12. 35-56

Schmidt, G. C. 1965. Proposed Rock Unit Nomenclature, Petroleum District V, S.E. Turkey (autochthonous terrain). Chart 1. Revised Edition. Stratigraphie Committee, Turkish Association of Petroleum Geologists, Ankara (unpublished).

Senalp, Muhittin & Bahtiyar, İsmail & Isikalp, Umut & Kaya, Mahir & Uz, Elif. (2018). Sequence Stratigraphy and Sedimentology of the Paleozoic Successions on the Arabian Platform and their Impact to Hydrocarbon Explorations in Southeast Turkey.

Şengör, A.. (1990). A new model for the late Paleozoic-Mesozoic tectonic evolution of Iran and implications on Oman. *The Geology and Tectonics of the Oman Region*.

Sengor, Ali Mehmet Celal & Tuysuz, Okan & İmren, Caner & Sakıncı, Mehmet & Eyidoğan, Haluk & Görür, Naci & Le Pichon, Xavier & Rangin, Claude. (2004). The North Anatolian Fault: A new look. *Annual Review of Earth and Planetary Sciences*. 33. 37-112. 10.1146/annurev.earth.32.101802.120415.

Sharland, Peter & Casey, D.M. & Davies, Roger & Simmons, Mike & Sutcliffe, Owen. (2004). Arabian Plate Sequence Stratigraphy – revisions to SP2. *Georabia - Manama*. 9. 199-214.

Sheorey, P R, 1994. A theory for in situ stresses in isotropic and transversely isotropic rock, in *International Journal of Rock Mechanics, Mining Science and Geomechanics*, Abstr., 31, pp 23-34.

Simón, J.L. & Arlegui, L. & Liesa, Carlos & Maestro, Adolfo. (1999). Stress perturbations registered by jointing near strike-slip, normal, and reverse faults: Examples from the Ebro Basin, Spain. *Journal of Geophysical Research*. 104. 15141-15153. 10.1029/1998JB900070.

Singh, Mahendra & Raj, Anil & Singh, Bhawani. (2011). Modified Mohr–Coulomb criterion for non-linear triaxial and polyaxial strength of intact rocks. *International Journal of Rock Mechanics and Mining Sciences* - 48. 546-555. 10.1016/j.ijrmms.2011.02.004.

Sinha, B. K., Wang, J., Kisra, S., Li, J., Pistre, V., Bratton, T. & Sanders, M. 2008. Estimation of formation stresses using borehole sonic data. In: *Transactions, 49th SPWLA Annual Symposium*. Edinburgh, May.

Stampfli, Gérard & Borel, G.D.. (2002). A plate tectonic model for the Paleozoic and Mesozoic constrained by dynamic plate boundaries and restored synthetic oceanic isochrons. *Earth and Planetary Science Letters*. 196. 17-33. 10.1016/S0012-821X(01)00588-X.

Stampfli, Gérard & Kozur, Heinz. (2006). Europe From the Variscan to the Alpine Cycles. 10.1144/GSL.MEM.2006.032.01.04.

Stocklin L. and Setudehnia, A.O., 1972. Lexique Stratigraphique internationale de l' Iran; 3, 9b, 311.

Sungurlu, O., 1974, VI. Bölge Kuzey sahalarının jeolojisi (Geology of the northern part of Petroleum district-VI), in Okay, H., and Dileköz, E., eds., 2nd Petroleum Congress of Turkey, Proceedings: Ankara, Turkey, Association of Petroleum Geologists, p. 85-107.

Şahbaz, N., Seyitoğlu, G., 2017. Gaziantep Kuzeydoğusunun Neotektoniği: Bozova ve Halfeti Doğrultu Atımlı Fayları ve Bunların Kır Bindirmeler ile İlişkileri, Türkiye.Maden Tetkik ve Arama Dergisi 10–20. <https://doi.org/10.19076/mta.350433>

Tchalenko, J.S., 1968. The evolution of kink-bands and the development of compression textures in sheared clays. Tectonophysics 6, 159–174.

Tchalenko J S 1970. Similarities between shear zones of different magnitudes; Geol. Soc. Amer. Bull. 81 1625–1640.

Taherynia, M.H., Aghda, S.M.F. & Fahimifar, A. 2016. In-Situ Stress State and Tectonic Regime in Different Depths of Earth Crust. Geotech Geol Eng, 34, 679-687.

Townend, J., Zoback, M.D., 2000. How faulting keeps the crust strong. Geology 28(5), 399-402.

Turkmen, Melike & Gozel, Mustafa. (2014). Fracture Characterization of a Carbonate Reservoir by DFN Modeling: A Case Study. Proceedings - SPE Annual Technical Conference and Exhibition. 3. 1648-1669. 10.2118/170699-MS.

Vail, P.K & Mitchum, R.M & Todd, R.G & Widmier, J.M & Thompson, S & Bubb, J.N & Hatfield, W.G. (1977). Seismic stratigraphy and global changes in sea level, Parts 1 and 2.

Waldren, D. & Corrigan, A.. (1985). An Engineering and Geological Review of the Problems Encountered in Simulating Naturally Fractured Reservoirs. 10.2118/13717-MS.

Wender, L.E. & Bryant, J.W. & Dickens, M.F. & Neville, Allen & Al-Moqbel, A.M.. (1998). Palaeozoic (Pre-Khuff) hydrocarbon geology of the Ghawar area, eastern Saudi Arabia. *GeoArabia*. 3. 273-302.

Williams, G. & Powell, C. & Cooper, Mark. (1989). Geometry and Kinematics of Inversion Tectonics. Geological Society, London, Special Publications. 44. 3-15. 10.1144/GSL.SP.1989.044.01.02.

Wilson, Jennifer & Chester, Judith & Chester, F.M. (2003). Microfracture analysis of fault growth and wear processes, Punchbowl Fault, San Andreas System, California. *Journal of Structural Geology*. 25. 1855-1873. 10.1016/S0191-8141(03)00036-1.

Yuan, Haijun & Johns, Russell & Egwuenu, A.M. & Dindoruk, Birol. (2004). Improved MMP Correlations for CO₂ Floods Using Analytical Gas Flooding Theory. 10.2523/89359-MS.

Zang, Arno & Stephansson, Ove & Heidbach, Oliver & Janouschkowetz, Silke. (2012). World Stress Map Database as a Resource for Rock Mechanics and Rock Engineering. *Geotechnical and Geological Engineering*. 30. 10.1007/s10706-012-9505-6.

Zoback, Mark. (2007). Reservoir Geomechanics. 10.1017/CBO9780511586477.

Zoback, Mark & Moos, Daniel & Mastin, Larry & Anderson, Roger. (1985). Well Bore Breakouts and in Situ Stress. *Journal of Geophysical Research*. 90. 5523-5530. 10.1029/JB090iB07p05523.

PERSONAL INFORMATION

Surname, Name : DİLCİ, Göktürk Mehmet
Nationality : Turkish (TC)
Date and Place of Birth : 15 June 1983, Adana:
Phone : +90 312 207 23 33
E-mail : gdilci@tp.gov.tr

EDUCATION

Degree	Institution	Year of Graduation
MS	Texas A&M Geology & Geophysics	2010
BS	Ankara University Geological	2006

WORK EXPERIENCE

Year	Place	Enrollment
2010-Present	Turkish Petroleum Corporation	Project Manager Exploration Geologist

FOREIGN LANGUAGES

Advanced English

PUBLICATIONS

1. Dilci, G.M., The Role of Strike-Slip Faulting in Fracture Reservoirs: Kızılın Fault from SE Turkey as a Case Study, 2014, AAPG International Conference & Exhibition, Istanbul, Turkey, September 14-17, 2014
2. Dilci G.M., Aksu R., 2014. The Outcomes of the Field Surveys of 2013: The Geology and Petroleum System of the Surroundings of Gemrik and Karababa Highs. Turkish Petroleum Corporation, Achieved Report No: 5503

HOBBIES

Philosophy, History of Science, Economics of Natural Resources,
Volunteering (2014 – Present; Joint Disabled Persons Art Theatre)